andorkormanyos_7_22

andorkormanyos_7_22

DSc dissertation

Spin-orbit coupling effects in atomically thin materials and their heterostructures

Andor Kormányos
Eötvös Loránd University
Department of Physics of Complex Systems

Website: http://akormanyos.web.elte.hu/

Budapest, September 2022

andorkormanyos_7_22

Contents

List of Acronyms

vdW van der Waals

hBN hexagonal boron nitride

MLG monolayer graphene

BLG bilayer graphene

TLG trilayer graphene

TMDC transition metal dichalcogenide

2D two-dimensional

BZ Brillouin zone

DFT density functional theory

QPC quantum point contact

SOC spin-orbit coupling

E_F Fermi energy

irreps irreducible representations

AHE anomalous Hall effect

QHE quantum Hall effect

VHE valley Hall effect

SHE spin Hall effect

SVHE spin-valley Hall effect

QSHE quantum spin Hall effect

2DEG two-dimensional electron gas

2DHG two-dimensional hole gas

LED light-emitting diode

CP circular polarization

KR Kerr rotation

CSI charge-to-spin interconversion

SCI spin-to-charge interconversion

QD quantum dot

CB conduction band

VB valence band

WAL weak antilocalization

QD quantum dot

SdH Shubnikov-de Haas

LL Landau level

Chapter 1

Introduction

1.1 Atomically thin materials

Since the discovery of graphene, a one-atom thin, two-dimensional (2D) carbon material, atomically thin materials, such as mono [1, 2, 3] and few-layer graphene [4, 5, 6, 7], or few-layer transition metal dichalcogenides [8, 9, 10, 11] have been one of the most intensively studied field in solid states physics. The importance of the discovery of graphene was also recognized by a Nobel Prize in 2010 which was awarded for the "*groundbreaking experiments regarding the two-dimensional material graphene*". While graphene is a semimetal, in recent years atomically thin samples encompassing basically the whole range of electrical properties have been discovered, including metals [12], semiconductors [10, 13, 14], insulators [15], ferromagnets [16, 17], antiferromagnets [18], superconductors [12], and topological insulators [19, 20]. Moreover, the combination of topological properties with magnetism [21] has lead to an axion-topological state [22]. Initially, atomically thin samples were obtained from layered bulk materials, most often by mechanical or chemical exfoliation, that is, by removing few-layer thick flakes from the surface of a bulk sample. However, recently few-layer thin materials that do not have naturally occurring bulk counterpart [23, 24, 25] have also been synthesized. This can potentially further enlarge the design possibilities for synthetic materials with desirable properties.

In parallel with the discovery and synthesis or novel 2D materials, heterostructures of different monolayer and few-layer materials have also been attracting huge interest. This field is often referred to as *van der Waals engineering* [26, 27], because e.g., the electrical properties of the few-layer stacks can be affected by the weak, yet finite van der Waals (vdW) interaction between the constituent layers. One may use this term to describe (i) the fabrication of few-layer stacks of different 2D materials [26, 27], (ii) fabrication of few-layer stacks of the same 2D material where there is an interlayer twist angle between the individual layers [28, 29]. In both cases the resulting systems can posses functionalities and properties that the individual constituent layers do not have. Namely, in comparison with bulk samples, interface properties become crucial exactly because these heterostructures are atomically thin.

The interlayer twist angle itself has also emerged as a powerful knob to change the electronic properties of atomically thin materials [28, 29]. A new term called *twistronics* was coined to describe this emerging field. Currently, two main effect of the interlayer twist are known: it can imprint a long wavelength (with respect to the typical wavelength of electronic quasiparticles) effective potential, a so-called moiré potential, which can affect, e.g., the transport properties of graphene in graphene/hexagonal boron nitride (hBN) heterostructures [30, 31, 32]. Remarkably, it has become possible to achieve *in-situ* dynamical rotation and manipulation of the layers in these heterostructures [33]. The second effect of interlayer twist is even more dramatic: following the theoretical work of Ref. [34], it has been shown that in twisted graphene [29] and TMDC bilayers [35, 36], for certain interlayer twist angles dubbed *magic angles* [34], a strong reconstruction

of the band structure takes place. The most important consequence of this reconstruction is that almost dispersionless bands, so-called "flat bands" appear in the low energy spectrum. Since the kinetic energy of the electrons is suppressed in the flat bands, electron-electron interaction effects become dominant and, depending on other parameters, such as electron density and temperature, lead to a variety of interacting phases [29, 37, 38, 36, 39] and even superconductivity [29]. More generally, since these twisted vdW bilayers allow a great deal of tunability of their properties through gating, straining, external pressure and changing the twist angle, they offer a robust platform to study the interplay of strongly correlated physics and topology. Moreover, they can serve as a quantum simulator [40] to realize a large number of many-body quantum models. While much progress has been achieved with quantum simulators based on ultracold gases of bosonic and fermionic atoms [41], it remains a challenge to engineer Hamiltonians with tunable long-range interactions which are relevant in condensed-matter physics. Therefore twisted VdW systems can offer a complementary platform to the existing quantum simulators.

It is important to mention that atomically thin materials helped to bring into focus yet another set of interesting problems. Namely, charge carriers posses several degrees of freedom. Examples include the spin degree of freedom, which may be coupled to the orbital motion (spin-orbit coupling) or the valley, which is related to the minima in the dispersion of the bands. In the case of structures consisting of more than one layer, one can define in certain cases the layer degree of freedom, since the electrons may not be spread homogeneously over every layers. The effects related to the interplay of these degrees of freedom of the charge carriers will be central to this thesis.

Seeing the enormous interest in graphene shortly after its discovery, which was manifested in the appearance of dozens of manuscripts every week on the preprint server *arXiv*, one was inclined to think that such a level of interest in 2D materials was not going to last for long. This is indeed what happened and the number of publications have decreased to a more "sustainable" level over time. Yet, we now know, that there was going to be many more unexpected twists and turns (pun intended) in the story. To the extend that one can extrapolate from the past to the near future, it is to be expected that the field of 2D materials is going to give us many exciting discoveries is the coming years.

1.2 Graphene

As already mention, the 2D materials "revolution" started with the demonstration that it was possible to obtain a single atom thin layer from bulk graphite and measure its electrical properties [1, 2]. Subsequent theoretical and experimental studies showed that few-layers graphene has surprising electrical, optical and mechanical properties, such as a universal minimal conductivity at vanishing carrier density [42, 43, 44], Klein tunneling in $p-n$ junctions [45, 46, 47], Zitterbewegung [42, 48], unconventional quantum Hall effect [2], frequency independent optical conductivity [49, 50], unparalleled tensile strength [51] etc. Many of these properties can be understood by considering the single particle band structure as a first step. In the following we briefly review the most important features of the band structure of monolayer, bilayer and trilayer graphene.

1.2.1 Monolayer graphene

As shown in Fig. 1.1, in first approximation monolayer graphene (MLG) consist of a flat 2D layer of carbon atoms arranged into a hexagonal lattice. There are two basis atoms, denoted by A and B, in the unit cell. In reality, graphene is not completely flat, instead, it hosts ripples [52], which are surface waves of typically 0.5 nm amplitude and 5 nm wavelength, as illustrated in Fig. 1.1(b). Nevertheless, a simple tight-binding (TB) model, based on the assumptions that MLG is perfectly flat and that it is sufficient to take into account only nearest neighbor hopping, can be already be used as a starting point to explain a wide range of experimental observations.

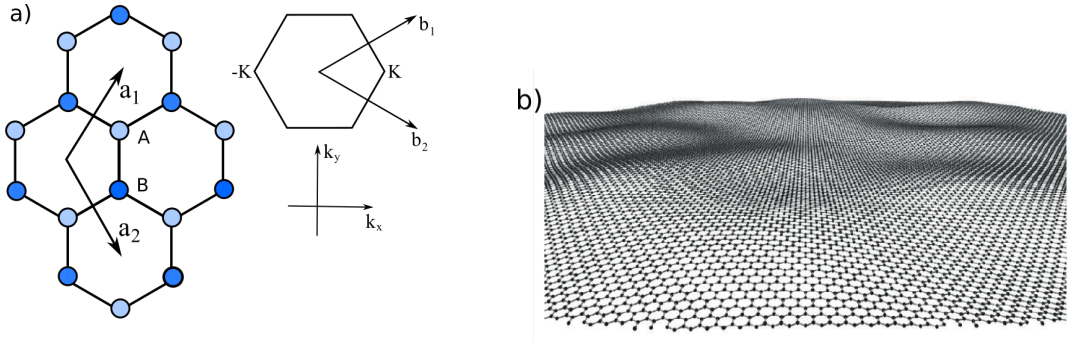

Figure 1.1: a) Schematics of the graphene lattice. The two carbon atoms in the unit cell are denoted by A and B, the primitive lattice vectors by $\mathbf{a}_1$ and $\mathbf{a}_2$. The inset shows the Brillouin zone of graphene, with reciprocal primitive lattice vectors $\mathbf{b}_1$ and $\mathbf{b}_2$ and the coordinate system in the wavenumber space. The low-energy states can be found at the $\mathbf{K}$ and $-\mathbf{K}$ points. b) A more realistic view of a graphene sheet, which host ripples and therefore it is not completely flat. Adapted from Ref. [52].

In the approximation where the non-orthogonality of the adjacent atomic orbitals is neglected, the Hamiltonian following from the TB approach reads

$$H_{mlg} = \begin{pmatrix} \varepsilon_p & -\gamma_0 f(\mathbf{k}) \\ -\gamma_0 f^*(\mathbf{k}) & \varepsilon_p \end{pmatrix}. \tag{1.1}$$

Here $\gamma_0 \approx 2.67$ eV is the hopping amplitude between the $2p_z$ atomic orbitals of nearest neighbor A and B carbon atoms and ε_p is the energy of these atomic orbitals. It is customary to take $\varepsilon_p = 0$, i.e., all other energies are measured with respect to ε_p. The function $f(\mathbf{k})$ reads $f(\mathbf{k}) = e^{ik_y a/\sqrt{3}} + 2e^{-ik_y a/2\sqrt{3}} \cos(k_x a/2)$, where a is the length of the lattice vectors $\mathbf{a}_1$ and $\mathbf{a}_2$. The dispersion of the two bands described by H_{mlg} is given by $E(\mathbf{k}) = \pm\gamma_0 |f(\mathbf{k})|$. One can easily check that $f(\mathbf{k}) = 0$ for $(k_x, k_y)^T = (\tau\frac{4\pi}{3a}, 0)^T \equiv \tau\mathbf{K}$, where $\tau = \pm 1$, i.e., the valence and the conduction bands are degenerate at the $\tau\mathbf{K}$ points of the Brillouin zone (BZ). (As one can see in Fig. 1.1(a), there are six K points in the BZ, but only two are non-equivalent, which are denoted by $\tau\mathbf{K}$). In undoped graphene the Fermi energy (E_F) lies at this degeneracy point, therefore graphene is often called a zero-gap semiconductor. Expanding $f(\mathbf{k})$ for small wave vectors $\mathbf{q}$ around $\mathbf{K}$ one finds

$$H_{mlg}(\tau\mathbf{K} + \mathbf{q}) = \hbar v_F \begin{pmatrix} 0 & (\tau q_x + i q_y) \\ (\tau q_x - i q_y) & 0 \end{pmatrix}, \tag{1.2}$$

where $v_F = \sqrt{3}a\gamma_0/(2\hbar) \approx 10^6$m/s is the Fermi velocity. The eigenvalues and eigenfunctions of H_{mlg} are

$$E_{mlg}(\mathbf{q}) = \pm\hbar v_F |\mathbf{q}|, \qquad \Psi_\pm(\mathbf{q}) = \frac{1}{\sqrt{2}} \begin{pmatrix} e^{i\tau\varphi_\mathbf{q}/2} \\ \pm\tau e^{-i\tau\varphi_\mathbf{q}/2} \end{pmatrix}, \tag{1.3}$$

where $\varphi_\mathbf{q}$ is the polar angle of $\mathbf{q}$: $\mathbf{q} = |\mathbf{q}|(\cos\varphi_\mathbf{q}, \sin\varphi_\mathbf{q})^T$. As shown by Eq. (1.3), one finds that the dispersion of graphene is linear close to the $\tau\mathbf{K}$ points. Since the conduction (valence) band has a minimum (maximum) at $\tau\mathbf{K}$, these points are often referred to as *valleys* and τ is called the valley index (see Sect. 1.7 for further discussion of the valleys). Furthermore, since $\Psi_\pm(\mathbf{q})$ has two components, it is reminiscent of the wavefunction of a spin-$\frac{1}{2}$ particle. However, the two components of $\Psi_\pm(\mathbf{q})$ describe the relative weight of the Bloch wavefunctions on the A and B carbon atoms and therefore this degree of freedom in the wavefunction is called *pseudospin*. It is convenient to introduce the Pauli matrices σ_x, σ_y acting in this pseudospin space and write

$$H_{mlg}(\mathbf{q}) = \hbar v_F(\tau q_x \sigma_x - q_y \sigma_y) \tag{1.4}$$

Introducing the notation $\mathbf{p} = \hbar\mathbf{q}$ and performing a unitary transformation, the low-energy effective Hamiltonian of MLG can be cast into

$$H_{mlg}(\mathbf{p}) = v_F(\tau p_x\sigma_x + p_y\sigma_y), \tag{1.5}$$

which has the form of 2D massless Dirac equation. However, as already mention, it is the pseudospin degree of freedom and not the real spin that underlies Eq. (1.5). Nevertheless, similarly to relativistic physics, one can define the *chirality* of the quasiparticles. The chiral operator $\boldsymbol{\sigma}\cdot\hat{\mathbf{n}}$, where $\boldsymbol{\sigma} = (\sigma_x, \sigma_y)$ and $\hat{\mathbf{n}} = \mathbf{p}/|\mathbf{p}|$, commutes with H_{mlg} given in Eq. (1.5). Therefore $\Psi_\pm$ are eigenfunctions of the chirality operator with eigenvalues ± 1. An important consequence of the chirality of the low-energy quasiparticles in graphene is the following: a scattering potential, which does not break the symmetry of the $A-B$ sublattice, cannot lead to backscattering [53]. Namely, scattering into a state with opposite momentum would require a reversal of the pseudospin, which is forbidden.

1.2.2 Bilayer and trilayer graphene

The unit cell of graphite contains two layers of MLG, arranged in such a way that carbon atoms on sublattice A_1 in the first layer are directly below carbon atoms on sublattice B_2 in the second layer, see Fig. 1.2. This is called AB or Bernal stacking of the layers. Soon after the isolation of MLG, bilayer graphene (BLG) samples were also obtained [4]. It turns out that the electrical and transport properties of BLG differ from those of MLG [54, 4, 55] in important ways and electron-electron interaction effects tend to be much stronger [56], especially at low electron density and high magnetic fields. This gave further impetus for graphene research and motivated the study of few-layer graphene, such as trilayer graphene (TLG). Importantly, TLG and other few-layer graphene samples can have different *stacking order*, a property that is absent in monolayers. As it can be seen in Fig. 1.2, in the case of ABA stacking the B_2 atom in under the A_3 atom, while in ABC stacked TLG the B_2 atom in the second layer is under the hollow position of the hexagonal lattice of the third layer. ABC stacking can be understood as a naturally occurring stacking fault in graphite. While BLG samples show almost exclusively Bernal stacking, TLG samples of both ABA and ABC stackings have been experimentally [5, 6, 7, 57] and theoretically [58, 59, 60, 61] investigated. TLG is a good example of how the stacking order of the layers can affect the band structure and the electrical properties of few-layer materials.

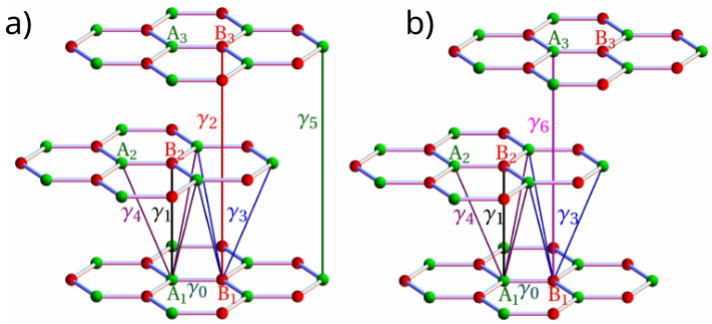

Figure 1.2: TB model of a) ABA and b) ABC stacked trilayer graphene. Bilayer graphene can be obtained by neglecting the uppermost, third layer. Adapted from Ref. [62].

Let us first briefly consider BLG. The primitive lattice vectors $\mathbf{a}_1$, $\mathbf{a}_2$ are the same as for MLG, but the unit cell of BLG contains four atoms. Therefore in a TB model similar to MLG, i.e., that takes into account one p_z orbital per atomic site, there will be four bands. The possible inter-layer

hopping amplitudes γ_1, γ_3 and γ_4 are illustrated in Fig. 1.2. The largest and most important of them is $\gamma_1 \approx 0.4\,\mathrm{eV}$, which describes the hopping between the atomic sites A_1 and B_2. The approximation where only this inter-layer hopping amplitude is included in the TB model (in addition to the intralayer hopping γ_0) is already sufficient to obtain the most important features of the band structure. In the basis of A_1,B_1,A_2,B_2 carbon atoms the TB Hamiltonian of BLG reads

$$H_{blg} = \begin{pmatrix} \varepsilon_p & -\gamma_0 f(\mathbf{k}) & 0 & \gamma_1 \\ -\gamma_0 f^*(\mathbf{k}) & \varepsilon_p & 0 & 0 \\ 0 & 0 & \varepsilon_p & -\gamma_0 f(\mathbf{k}) \\ \gamma_1 & 0 & -\gamma_0 f^*(\mathbf{k}) & \varepsilon_p \end{pmatrix}. \tag{1.6}$$

As in the case of MLG, the most important part of the spectrum is the vicinity of the $\tau\mathbf{K}$ points. The spectrum consists of two low-energy bands that are degenerate at the $\tau\mathbf{K}$ points and two higher energy, "split-off" bands at $E = \pm\gamma_1$, see Fig. 1.3(a). Expanding $f(\mathbf{k})$ for small wave vectors $\mathbf{q}$ around $\tau\mathbf{K}$ and projecting out the high energy degrees of freedom, using, e.g., Löwdin partitioning [63], one can again obtain a low-energy, effective 2×2 Hamiltonian. One finds [54]

$$H_{blg}(\mathbf{p}) = -\frac{1}{2m_{\mathrm{eff}}} \begin{pmatrix} 0 & (\tau p_x - i p_y)^2 \\ (\tau p_x + i p_y)^2 & 0 \end{pmatrix}, \tag{1.7}$$

where $m_{\mathrm{eff}} = \gamma_1 / 2v_F^2 \approx 0.03 m_e$ is the effective mass (m_e is the free electron mass). The eigenvalues and eigenstates of $H_{blg}(\mathbf{p})$ are

$$E_{blg}(\mathbf{p}) = \pm\frac{p^2}{2m_{\mathrm{eff}}}, \qquad \Psi_{\pm}(\mathbf{p}) = \frac{1}{\sqrt{2}} \begin{pmatrix} e^{i\tau 2\varphi_{\mathbf{p}}} \\ \mp e^{-i\tau 2\varphi_{\mathbf{p}}} \end{pmatrix}. \tag{1.8}$$

One can easily check that H_{blg} commutes with the chiral operator $\boldsymbol{\sigma} \cdot \hat{\mathbf{n}}$, hence the low energy quasiparticles of BLG are chiral as well. However, in contrast to MLG, backscattering is not forbidden, because it does not reverse the pseudospin. Furthermore, the dispersion is quadratic in momentum, similarly to quasiparticles described by the usual Schrödinger equation. Thus, charge carriers have both relativistic and non-relativistic properties in BLG. Another important difference with respect to MLG is that an external electric field can open a band gap [64], which makes possible the electrical confinement of charge carriers as well as interesting valleytronic effects (see Sec. 1.7).

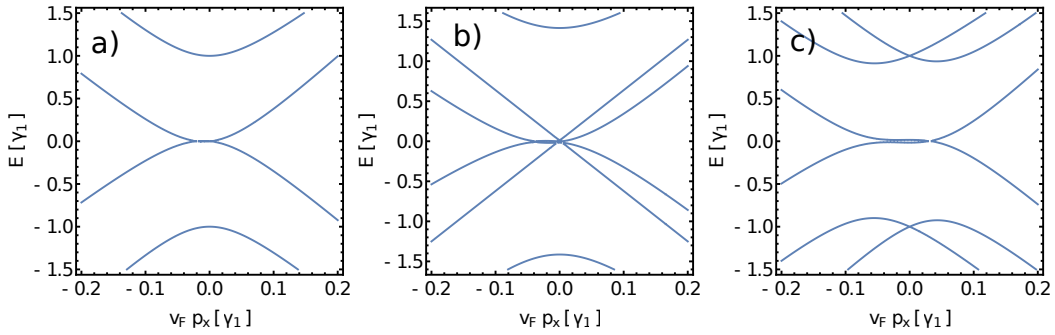

Figure 1.3: Band structure of a) AB stacked bilayer, b) ABA, and c) ABC stacked trilayer graphene. In these calculations all γ_i hopping parameters shown in Fig.1.2 are taken into account, their values are given in Ref. [60].

The TB approach can be extended to TLG graphene in a straightforward way [58, 59]. Importantly, the low-energy band structure depends on the stacking order. *ABA* stacked TLG has two linearly dispersing bands at low energies, as in MLG, and two quadratically dispersing bands, as in

BLG, see Fig. 1.3(b). On the other hand, the low-energy charge carriers in *ABC* stacked TLG are chiral quasiparticles with $\sim \pm|\mathbf{p}|^3$ dispersion. They can be described by the effective Hamiltonian

$$H_{ABC}(\mathbf{p}) = \frac{v_F^3}{\gamma_1^2} \begin{pmatrix} 0 & (\tau p_x - i p_y)^3 \\ (\tau p_x + i p_y)^3 & 0 \end{pmatrix}. \tag{1.9}$$

In addition, *ABC* graphene also has four split-off bands at $E \approx \pm\gamma_1$. The comparison of Fig. 1.3(b) and Fig. 1.3(c) shows clearly the effect of stacking order on the TLG band structure.

1.3 Transition metal dichalcogenides

Not long after the fabrication of the first monolayer a few-layer graphene samples it was realized that the bulk form of many materials consists of stacks of atomic layers held together by weaker interlayer interactions. These materials are amenable to obtain atomically thin samples and one of the first that came into the focus was the transition metal dichalcogenide (TMDC) [65, 66] family of materials. TMDCs can be described by the formula MX_2, where X is a chalcogen (S, Se or Te) and M is a metal from group IV (e.g., Ti, Zr, Hf) or group V (e.g., V, Nb, Ta) or group VI (e.g., Mo, W). Regarding electronic properties, they can be metallic (e.g., NbX_2 and TaX_2) or semiconducting (MoX_2 and WX_2), and some of them exhibit superconductivity, strong electronic correlations or charge density wave behavior [67, 68]. In this thesis we will only be concerned with the semiconductors MoS_2, $MoSe_2$, WS_2 and WSe_2 and henceforth, when we refer to TMDCs, we usually have these four materials in mind.

Most of the initial theoretical work in this field considered monolayer MoX_2 and WX_2. We introduce a minimal model to describe these monolayers in Sec. 1.3.1. While this minimal model was successfully used to interpret a number of optical and transport experiments, its limitations also became apparent over time. This motivated the work that will be presented in Chapt. 4. The interest in monolayers was also motivated by important experimental discoveries, and three of them will be briefly presented in Sec. 1.3.2. Albeit later than monolayers, bilayers of TMDCs have also started to attract both theoretical and experimental interest, their basic electronic structure and an interesting transport property will be the subject of Chapt. 7.

1.3.1 Minimal model of monolayer TMDCs

Monolayers of group-VI TMDCs are, with regards to their thickness, the ultimate 2D semiconductors [10, 11, 69], as they are only a few Ångstrom thin. Similarly to graphene, they have a hexagonal lattice structure, where the planes of the X atoms are separated by a plane of metal atoms, see Fig. 1.4(a). DFT band structure calculations showed that they are direct band gap materials, and the band edge can be found at the K and $-K$ points of the hexagonal BZ (Fig. 1.4(c)). Unlike graphene, however, these 2D crystals do not have inversion symmetry. One of the consequences of the lack of inversion symmetry is that the bands can be spin polarized by the SOC. Because of the resemblance to graphene, which is apparent when looking from above on the layers (see Fig. 1.4(b)), it is perhaps not surprising that the minimalist model used to describe the properties at the band edge is based on mimicking them as graphene with a staggered sublattice potential that breaks inversion symmetry. The minimal model of the band structure is given by the Hamiltonian [70]

$$H_{tmdc} = \hbar v_F(\tau q_x \sigma_x + q_y \sigma_y) + \Delta\sigma_z + \tau\frac{\lambda_{tmdc}}{2}(\sigma_z - 1)s_z. \tag{1.10}$$

Here v_F is the Fermi velocity of the TMDC, and the term is $\Delta\sigma_z$ appears due to the presence of a band gap. However, in Eq. (1.10) the pseudospin degree of freedom corresponds to the conduction band (CB) and valence band (VB), whereas in the case of MLG the pseudospin corresponded to the A and B sublattice. Monolayer TMDCs have a strong SOC, especially in the VB. This is

described by the third term of H_{tmdc}, where s_z is a spin Pauli matrix and the SOC constant λ_{tmdc} is e.g., ≈ 140 meV for monolayer MoS_2. The spin splitting described by this term can indeed be observed in the DFT band structure calculations around the K point in Fig. 1.4(c). (As we will see in Chapt. 4, the SOC can also be quite large in the CB, which is neglected in Eq. (1.10).) Time reversal symmetry requires that the spin-polarization is opposite in the K and the $-K$ valleys, thus the valley and the spin degree of freedoms are coupled: the SOC term depends on the product of the valley index τ and the spin operator s_z. An interesting consequence of this *spin and valley coupling* will be discussed in Sec. 1.7.3.

This minimal model can capture a number of optical and transport effects related to the valley degree of freedom, such as the valley dependent optical selection rules, which we will briefly discuss in Sec. 1.7. However, as it can be seen in Fig. 1.4(c), these materials have a relatively complicated band structure with several extrema (valleys) both in the valence and the conduction bands. Accordingly, the TB models [71, 72, 73] are significantly more complex than the graphene TB Hamiltonian, containing a large number of hopping parameters. The accumulation of experimental

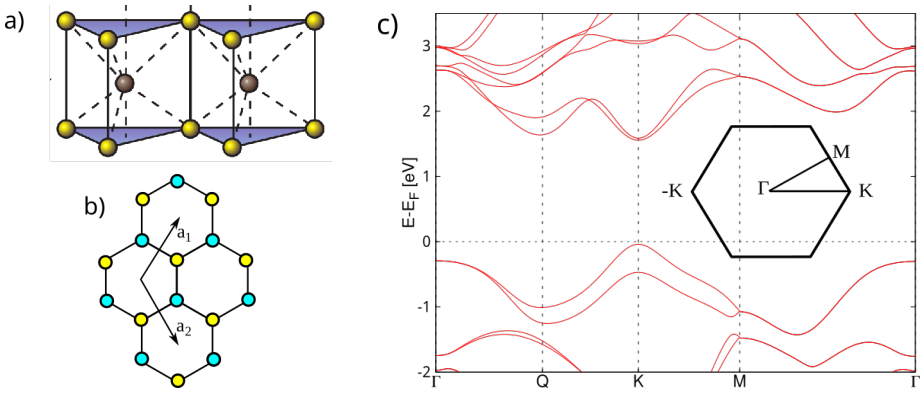

Figure 1.4: a) Schematics of the crystal structure of monolayer TMDCs. Adapted from Ref. [10]. b) Top view of the lattice. c) Overview of the band structure as obtained from DFT calculations along the Γ–K–M–Γ line in the BZ. Inset shows the schematics of the Brillouin zone. Adapted from Ref. [74].

data over time then called for theoretical models that are both detailed and compact, relying on a limited number of parameters while still offering an accurate description. This is the main motivation to introduce the so-called $\mathbf{k} \cdot \mathbf{p}$ methodology in Sec. 1.4, and the relevant results will be discussed in Chap. 4.

1.3.2 Three important experiments

In order to motivate the interest in monolayer TMDCs, we mention three discoveries which were very influential in the early days of this field. Further interesting experiments will be discussed in Sec. 1.7, after introducing the notion of *valleytronics*.

The first experiment concerns the change in the band structure of TMDCs. Namely, band gap is indirect in the bulk material while it is direct in the monolayer limit [9]. This results in a huge increase of the photoluminescence from the monolayers [8, 9] with respect to bulk, or even few layer samples, see Fig. 1.5(a). Moreover, the emitted light falls into the visible range of the spectrum. This opened the way for a relatively straightforward optical investigation and characterization of these materials. This was particularly important because the relatively strong disorder in the samples (compared to graphene) and problems with obtaining good electrical contacts made it initially difficult to perform e.g., transport studies. Obviously, the presence of strong photoluminescence has implications for TMDC based photonics and optoelectronics as well.

This first discovery also laid the foundations for the second one: the investigation of valley selective optical transitions. It was found that one can selectively address the electronic states either in the K or in the $-K$ valley [75, 76, 77] using circularly polarized light. We will briefly discuss this phenomenon, which lead to a renewed interest in the idea of valleytronics, in Sec. 1.7

The third important discovery was that monolayer TMDCs, since they are semiconductors, can be implemented in field-effect transistors [78, 79, 80] [see Fig. 1.5(b)] and logical devices [81, 82]. Although the mobility of the charge carriers (which would determine the speed of the operations) in TMDCs is much smaller than in graphene, the lack of band gap in the latter means that in a transistor setup the current through the graphene channel cannot be switched off. This limits the use of graphene for digital transistors. In contrast, a large current on/off ratio can be achieved if monolayer TMDCs are used as channel [78]. Moreover, it was expected that their extreme thinness allows more efficient control over switching and can help to reduce power dissipation.

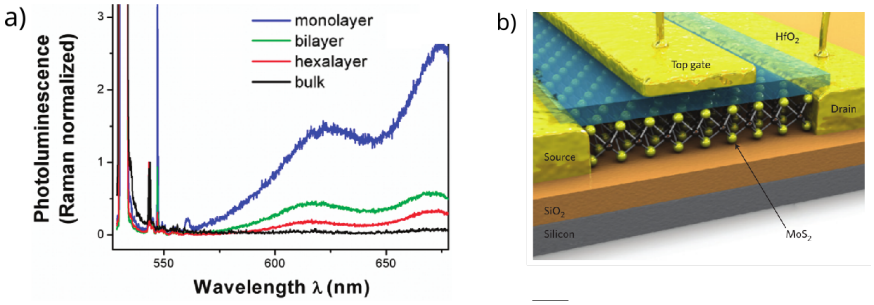

Figure 1.5: a) Photoluminescence spectra normalized by Raman intensity as a function of the wavelength λ of the emitted light for MoS_2 layers with different thickness. The photoluminescence efficiency is hugely increased for monolayers. The peaks below 550nm correspond to Raman scattering. Adapted from Ref. [9]. b) Schematic illustration of a monolayer MoS_2 field effect transistor. Adapted from Ref. [78].

1.3.3 Quantum dots in few-layer TMDCs

A quantum dot (QD) is a confined semiconductor or metallic region, where electrons can be added to or taken away in a controlled way due to the Coulomb interaction. Typically, a QD connects to a source and a drain contact through tunnel barriers so that transport measurements can be performed. QDs containing only a few electrons or even one electron can be achieved [83] using semiconductor hosts. This means that when the size of the QD is of the order of the wavelength of the confined electrons, it has a discrete energy spectrum and can behave as an artificial atom [84, 83]. The tremendous progress in the fabrication techniques makes it possible to manipulate the electron's charge or spin degree of freedom [85, 86], which makes QDs currently one of the leading platform for solid state qubits [87, 88, 89, 90, 91] and quantum computation. Indeed, proof-of-principle quantum algorithms has recently been demonstrated [92, 93] in QD arrays defined on a silicon wafer.

For our purposes the most important type of QDs are the ones fabricated in a semiconductor host and where the confinement potential is provided by electrostatic gates. Moreover, gate electrodes can shift the chemical potential of the dot and tune the coupling of the dot levels to the source and drain electrodes. Regarding 2D materials, currently the two main platforms to obtain gate such controlled QDs are BLG [94, 95, 96] and few-layer TMDCs [97]. To set the stage for Chapt. 6, we briefly discuss recent experimental results on gate controlled QDs in atomically thin TMDCs. We mention that QDs can be obtained by other methods of confinement as well, e.g., using etching [97].

Experiments on gate controlled quantum dots

The finite band gap in the TMDCs makes it possible to confine the charge carriers using similar fabrication techniques to those developed earlier for GaAs or Si. In this respect they offer a viable alternative to BLG, where a more complicated gate architecture is needed to open a band gap and achieve confinement simultaneously [95]. QDs has indeed been fabricated using monolayer [98, 99, 100] and few-layer [99, 101, 102, 103] TMDC samples. As shown in Figs. 1.6(a), the fabrication of QD devices actually involves the stacking of several thin layers, where e.g., hBN is used as an insulator, and graphene or graphite as gates.

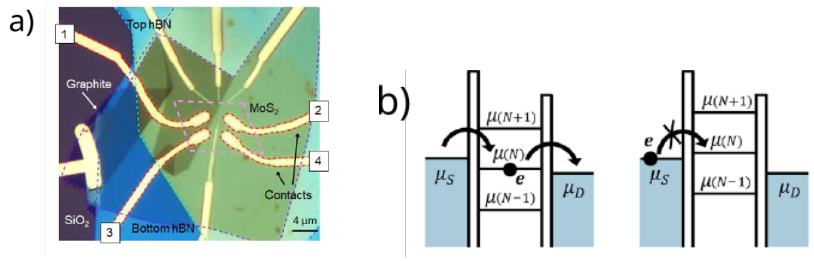

Figure 1.6: QDs in atomically thin TMDCs. a) Optical micrograph of a device based on monolayer MoS_2. The MoS_2 flake (pink dashed lines) is encapsulated between two hBN flakes. Graphite is used as a backgate and the electrical contacts to the MoS_2 flake are Ti/Au (yellow, numbered $1-4$). Adapted from Ref. [98]. b) Schematics of the Coulomb blockade effect in a QD. When the chemical potential $\mu(N)$ of the dot is tuned into the bias window $eV_{sd} = \mu_S - \mu_D$, the number of electrons can vary between $N-1$ and N, resulting in a single-electron tunneling current (left panel). If $\mu(N)$ is not in the bias window, the electron number is fixed in the QD and no current flows, known as Coulomb blockade (right panel). Adapted from Ref. [97].

The basic transport effect through QDs is the so-called Coulomb blockade [83], which means, in simple terms, that electrons are added on-by-one to the dot and then tunnel out. The chemical potential $\mu(N, V_i)$ of the dot depends on the number of electrons N on the dot and the gate voltages V_i (assuming a capacitive coupling between the dot and the gates). The strong Coulomb repulsion between the electrons prevents transport through the dot unless $\mu(N, V_i)$ is in the bias window determined by the source-drain voltage V_{sd}. In this case the number of electrons can vary between $N-1$ and N, resulting in a single-electron tunneling current. As shown in Fig. 1.7, transport measurements of the TMDC QD devices at low temperatures can show clear signatures of Coulomb blockade. Besides single dots, double quantum dots have also been realized in TMDCs [98, 104]. An example is shown in Fig. 1.7, where by changing the voltage on one of the gates it was possible to tune the device between hosting one larger QD or two smaller QDs. This demonstrates the tunability of gate defined TMDC QDs.

One of the motivations to study QDs in TMDCs is that the strong SOC and the valley degree of freedom, which we already mentioned in Sec. 1.3.1, would add interesting aspects to the QD physics. One should note that several experiments actually used few-layer TMDCs [99, 101, 102, 103] and not a monolayer to fabricate QD devices. This is important, because the band structure of few-layer TMDCs is sensitive to the number of layers: the position of the band edge can shift from the $\pm K$ point to the Q point in the CB or to the Γ point in the VB. Therefore in few-layer samples, instead of the $\pm K$ valleys, carriers from other valleys can be dominant. The degeneracy of the lowest energy electronic states at these points also changes depending on the layer number: for example, the K valley is two-fold (four-fold) degenerate, the Q point is six-fold (six or twelve-fold, depending on the stacking of the layers) degenerate, the Γ point is non-degenerate (two-fold degenerate) in monolayers (bilayers). The layer number should therefore affect the electronic states formed in the QDs as well as the transport through the QDs. However, a good control on

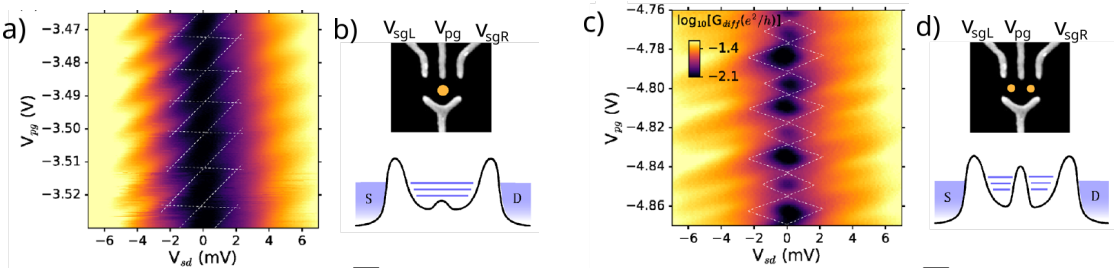

Figure 1.7: Gate defined single and double QD in monolayer MoS_2. a) Coulomb blockade diamond measurement in the single QD regime. c) The same as in a) in the double dot regime. Dark regions indicate low conductance, bright regions represent high conductance. b) and d) Upper panel: scanning electron microscope image of a QD device. Bright regions correspond to metallic electrodes, dark region is hBN. Lower panel: schematics of the electrostatic potential landscape without and with the middle barrier potential, which is determined by the gate V_{pg}. Changing V_{pg} allows to tune the device from single to double dot behavior. The gates V_{sgL} and V_{sgR} tune the tunnel barrier to the source and drain. Adapted from Ref. [98].

the number of confined electrons and clear signs of valley or SOC physics has not yet been achieved in TMDC QDs. This is partly due to the lower material quality of the TMDC flakes (compared to BLG) and partly to fabrication problems of electrical contacts to TMDCs [97].

1.4 $\mathbf{k}\cdot\mathbf{p}$ theory

We have seen in Sec. 1.2 that all the important properties of the band structure of few-layer graphene can be obtained using a relatively simple TB model. This is due to the simple chemical composition of graphite (consisting of only carbon atoms) and because it is sufficient to take into account a single atomic orbital. However, in more complicated compounds, such as TMDCs introduced in Sec. 1.3, there can be several different atoms in the unit cell and one would need to consider more then one atomic orbitals for each atom. Therefore TB models can become complicated and depend on a large number of hopping amplitudes. The parameterization of such a TB model, i.e., obtaining the actual values of the hopping amplitudes for a given material, is usually not easy. Currently, the probably most widely used methodology to calculate the band structure is based on density functional theory (DFT). The problem of determining a large number of parameters does not arise, the results are usually quite accurate, and the needed computational power, which is significantly larger than for TB models, is nowadays readily available. Nevertheless, DFT calculations can still be prohibitively expensive for certain problems, such as studying quantum dots (see Chapt. 6), and magnetic-field effects cannot be easily addressed by DFT-based techniques.

We will discuss now a relatively simple, yet powerful approach, the $\mathbf{k}\cdot\mathbf{p}$ methodology. Starting from the pioneering works of Luttinger and Kohn [105] to more recent monographs [106, 107], it has a long history in describing the band structure of III-V semiconductors in the vicinity of the Γ point of the BZ. It can give an accurate characterization of the dispersion, including important details such as band anisotropy or coupling between bands, and often in terms of a relatively small number of material parameters. This latter property can make it advantageous with respect to TB models. However, in contrast to TB models and DFT modeling, its use is more restricted: it is usually employed to describe the band structure in the vicinity of high-symmetry $\mathbf{k}$-space points in the BZ. In the case of semiconductors, which will be the main focus of this work, this is not necessarily a problem: the physics of semiconductors is mainly governed by charge carriers residing in the minima or maxima of the energy bands. Moreover, magnetic-field effects can also be taken into account in a rather straightforward way. Importantly, the $\mathbf{k}\cdot\mathbf{p}$ method can complement

DFT band structure calculations, whereby the material specific parameters appearing in the $\mathbf{k}\cdot\mathbf{p}$ methodology are extracted from DFT calculations (see Chap. 4 and 7). Furthermore, as we will see in Chap. 8, in the case of proximity induced material properties it can give physical insights that is not easy to obtain from other approaches.

1.4.1 Basic approach

In single-particle approximation, the physics of the electrons in the periodic potential $V(\mathbf{r})$ of a crystal is governed by the Schrödinger equation

$$\left[\frac{\hat{\mathbf{p}}^2}{2m_e} + V(\mathbf{r})\right]\Psi_{n,\mathbf{k}}(\mathbf{r}) = E_n(\mathbf{k})\Psi_{n,\mathbf{k}}(\mathbf{r}), \tag{1.11}$$

where n is the band index and the eigenfunctions of the Hamiltonian are Bloch functions: $\Psi_{n,\mathbf{k}}(\mathbf{r}) = \frac{1}{\sqrt{V}}e^{i\mathbf{kr}}u_{n,\mathbf{k}}(\mathbf{r})$, where $u_{n,\mathbf{k}}(\mathbf{r})$ is lattice periodic, which means that $u_{n,\mathbf{k}}(\mathbf{r}+\mathbf{R}_m) = u_{n,\mathbf{k}}(\mathbf{r})$ for arbitrary lattice vector $\mathbf{R}_m$. In the following, we assume that the motion of the electrons is confined to two dimensions, i.e., $\hat{\mathbf{p}} = (\hat{p}_x, \hat{p}_y)^T$ and for simplicity, we have neglected the SOC in Eq. (1.11) [the discussion of SOC effects is deferred to Sec. 1.4.3].

Substitution of $\Psi_{n,\mathbf{k}}(\mathbf{r})$ into Eq. (1.11) gives an equation for $u_{n,\mathbf{k}}(\mathbf{r})$:

$$\left[\frac{\hat{\mathbf{p}}^2}{2m_e} + V(\mathbf{r}) + \frac{\hbar\mathbf{k}\cdot\hat{\mathbf{p}}}{m_e} + \frac{\hbar^2\mathbf{k}^2}{2m_e}\right]u_{n,\mathbf{k}}(\mathbf{r}) = E_n(\mathbf{k})u_{n,\mathbf{k}}(\mathbf{r}). \tag{1.12}$$

We will mainly be interested in the properties of semiconductors, where the physically important electron states can be found around band extrema (minima and/or maxima). Let us denote by $\mathbf{k}_0$ the wave vector pointing to such an extrema in the BZ, and introduce the notation

$$\mathcal{H}(\mathbf{k}_0) = \left[\frac{\hat{\mathbf{p}}^2}{2m_e} + V(\mathbf{r}) + \frac{\hbar\mathbf{k}_0\cdot\hat{\mathbf{p}}}{m_e}\right]. \tag{1.13}$$

The lattice periodic part $u_{n,\mathbf{k}_0}(\mathbf{r})$ then satisfies the Schrödinger equation

$$\mathcal{H}(\mathbf{k}_0)u_{n,\mathbf{k}_0}(\mathbf{r}) = \varepsilon_n(\mathbf{k}_0)u_{n,\mathbf{k}_0}(\mathbf{r}), \tag{1.14}$$

where $\varepsilon_n(\mathbf{k}_0) = E_n(\mathbf{k}_0) - \frac{\hbar^2\mathbf{k}_0^2}{2m_e}$. It follows that Eq. (1.12) can be cast into the form

$$\left[\mathcal{H}(\mathbf{k}_0) + \frac{\hbar\mathbf{q}\cdot\hat{\mathbf{p}}}{m_e}\right]u_{n,\mathbf{k}_0+\mathbf{q}}(\mathbf{r}) = \varepsilon_n(\mathbf{k}_0+\mathbf{q})u_{n,\mathbf{k}_0+\mathbf{q}}(\mathbf{r}), \tag{1.15}$$

where we introduced the notation $\mathbf{k} = \mathbf{k}_0 + \mathbf{q}$. The band edge wavefunctions $u_{m,\mathbf{k}_0}(\mathbf{r})$ form a complete orthonormal basis [108], therefore one may use the expansion

$$u_{n,\mathbf{k}_0+\mathbf{q}}(\mathbf{r}) = \sum_m A_m^{(n)}(\mathbf{k}_0+\mathbf{q})u_{m,\mathbf{k}_0}(\mathbf{r}) \tag{1.16}$$

and calculate calculate the matrix elements of the operator $\mathcal{H}(\mathbf{k}_0)+\frac{\hbar\mathbf{q}\cdot\hat{\mathbf{p}}}{m_e}$ in the basis of the $u_{m,\mathbf{k}_0}(\mathbf{r})$ functions. Substituting Eq. (1.16) into Eq. (1.15), multiplying the resulting equation by $u^*_{m',\mathbf{k}_0}(\mathbf{r})$ from the left and integrating over the unit cell Ω, one finds the algebraic eigenvalue problem

$$\begin{pmatrix} \ddots & & & & \\ \cdots & \varepsilon_{m-1}(\mathbf{k}_0) & \mathbf{q}\cdot\boldsymbol{\gamma}_{m-1,m} & \mathbf{q}\cdot\boldsymbol{\gamma}_{m-1,m+1} & \cdots \\ \cdots & \mathbf{q}\cdot\boldsymbol{\gamma}_{m,m-1} & \varepsilon_m(\mathbf{k}_0) & \mathbf{q}\cdot\boldsymbol{\gamma}_{m,m+1} & \cdots \\ \cdots & \mathbf{q}\cdot\boldsymbol{\gamma}_{m+1,m-1} & \mathbf{q}\cdot\boldsymbol{\gamma}_{m+1,m} & \varepsilon_{m+1}(\mathbf{k}_0) & \cdots \\ & & & & \ddots \end{pmatrix}\begin{pmatrix} \vdots \\ A_{m-1} \\ A_m \\ A_{m+1} \\ \vdots \end{pmatrix} = \varepsilon(\mathbf{k}_0+\mathbf{q})\begin{pmatrix} \vdots \\ A_{m-1} \\ A_m \\ A_{m+1} \\ \vdots \end{pmatrix}, \tag{1.17}$$

where $\boldsymbol{\gamma}_{m',m} = \frac{\hbar}{m_e}\mathbf{p}_{m',m}$ and $\mathbf{p}_{m',m} = \int_\Omega d\mathbf{r}\, u^*_{m',\mathbf{k}_0}(\mathbf{r})\,\hat{\mathbf{p}}\,u_{m,\mathbf{k}_0}(\mathbf{r}) = \langle u_{m',\mathbf{k}_0}|\hat{\mathbf{p}}|u_{m,\mathbf{k}_0}\rangle$ are momentum matrix elements. We have dropped the band index n because it is arbitrary and to keep the derivation simple, we assumed that $\mathbf{p}_{m,m} = 0$. In general, the diagonal matrix elements $\mathbf{p}_{m,m}$ can be non-zero, in many cases, however, they turn out to be zero for reasons related to the symmetries of the system, as we will see, e.g., in Chap. 4. Apart from this, the derivation has so far been general and if the band-edge energies $E_m(\mathbf{k}_0)$ and the basis states $u_{m,\mathbf{k}_0}(\mathbf{r})$ and were known, by solving the secular equation (1.17) one could calculate the band structure in the whole BZ.

In the spirit of $\mathbf{k}\cdot\mathbf{p}$ theory, we now assume that the band-edge energies $E_m(\mathbf{k}_0)$ are known either from measurements (e.g., from optical spectroscopy, where interband transition energies can be measured) or from DFT band structure calculations. This, together with two additional observations listed below, is what can make $\mathbf{k}\cdot\mathbf{p}$ theory a workable approach:

- if one is interested in the dispersion of the bands in a small vicinity of $\mathbf{k}_0$, i.e., one considers $|\mathbf{q}| \ll |\mathbf{k}_0|$ and the $E_m(\mathbf{k}_0)$ are not (near)degenerate, then usually a few $u_{m,\mathbf{k}_0}(\mathbf{r})$ basis states can already be sufficient and therefore the matrix in Eq. (1.17) is of finite dimensions. We will denote this Hamiltonian matrix by $H_{\mathbf{k}\cdot\mathbf{p}}$. One is usually interested in the properties of the valence band (VB) and conduction band (CB), therefore one may take $u_{vb,\mathbf{k}_0}(\mathbf{r})$ and $u_{cb,\mathbf{k}_0}(\mathbf{r})$ as basis states, and few more $u_{m,\mathbf{k}_0}(\mathbf{r})$ corresponding to $E_m(\mathbf{k}_0)$ lower and/or higher than $E_{vb}(\mathbf{k}_0)$ and $E_{cb}(\mathbf{k}_0)$.

- for high symmetry $\mathbf{k}_0$ points in the BZ not only $\mathbf{p}_{m,m}$ are usually zero, but many of the off-diagonal $\mathbf{p}_{m',m}$ matrix elements as well. The non-zero $\mathbf{p}_{m',m}$ can be found using group theory considerations, which we will briefly explain in Sec. 1.4.2.

In this way one can obtain a Hamiltonian matrix $H_{\mathbf{k}\cdot\mathbf{p}}$ parameterized by a few non-zero parameters $\boldsymbol{\gamma}_{m',m}$. Since there are only a few $\boldsymbol{\gamma}_{m',m}$, it is easier to extract their values either from measurements or e.g., by fitting the band dispersion obtained by diagonalizing $H_{\mathbf{k}\cdot\mathbf{p}}$ to fully numerical DFT band structure calculations.

One may employ second-order perturbation theory to approximately diagonalize Eq. (1.17) for a given band n:

$$\varepsilon_n(\mathbf{k}_0+\mathbf{q}) = \varepsilon_n(\mathbf{k}_0) + \frac{\hbar^2}{m_e^2}\sum_{m'\neq n}\frac{|\mathbf{q}\cdot\boldsymbol{\gamma}_{n,m'}|^2}{E_n(\mathbf{k}_0)-E_{m'}(\mathbf{k}_0)}. \tag{1.18}$$

Using the definition $\frac{1}{(m_{\text{eff}})_{ij}} = \frac{1}{\hbar^2}\frac{\varepsilon_n(\mathbf{k}_0+\mathbf{q})}{\partial q_i \partial q_j}$, Eq.(1.18) allows to calculate the effective mass m_{eff} characterizing the band n. If the vector $\boldsymbol{\gamma}_{n,m'}$ has only one independent component denoted by $\gamma_{n,m'}$, which can happen for high symmetry $\mathbf{k}_0$ points in the BZ, then the effective mass is isotropic and one finds the well-known result [63, 109]:

$$\frac{m_e}{m_{\text{eff}}} = 1 + \frac{2}{m_e}\sum_{m'\neq n}\frac{|\gamma_{n,m'}|^2}{E_n(\mathbf{k}_0)-E_{m'}(\mathbf{k}_0)}. \tag{1.19}$$

1.4.2 Group theory considerations

Whether or not the matrix element $\mathbf{p}_{m',m}$ is zero or not depends on the crystal symmetries of the material, which is where group theoretical considerations can be useful. A detailed discussion of the symmetry properties of Bloch wavefunctions can be found in [109, 110], here we will only briefly outline how group theory can help to determine which $\mathbf{p}_{m',m}$ are non-zero. For simplicity, we will consider symmorphic crystals, where the symmetry group of the crystal contains only translations and point group operations but no glide plains or screw axis and we denote the point group describing the symmetries of the crystal by g_{cr}.

Since Eq. (1.14) is an effective Schrödinger equation for $u_{m,\mathbf{k}_0}(\mathbf{r})$, the first step is to consider the symmetry properties of $\mathcal{H}(\mathbf{k}_0)$. The first term has full rotational symmetry, while the second term only that of the crystal lattice, i.e., discrete rotations and reflections. Depending on $\mathbf{k}_0$, the

symmetry of $\mathcal{H}(\mathbf{k}_0)$ can be further lowered by the third term, $\frac{\hbar\mathbf{k}_0\cdot\hat{\mathbf{p}}}{m_e}$. To see this, let us denote by $\{G_a\}$ a group of some coordinate transformations G_a which leave $V(\mathbf{r})$ invariant. One may recall that the effect of a symmetry transformation $\mathcal{O}(G_a)$ on an arbitrary function $f(\mathbf{r})$ is given by $\mathcal{O}(G_a)f(\mathbf{r}) = f(\mathbf{R}(G_a^{-1})\mathbf{r}) = f([\mathbf{R}(G_a)]^{-1}\mathbf{r})$, where $\mathbf{R}$ is a matrix representation of the coordinate transformation. Furthermore, note that under symmetry transformations $\mathcal{O}(G_a)$ the operator $\hat{\mathbf{p}}$ transforms in the same way as the polar vector $\mathbf{r} = (x, y, z)^T$. One finds that the effect of the transformed operator $\mathcal{O}(G_a)\frac{\hbar}{m_e}\mathbf{k}_0\hat{\mathbf{p}}\,\mathcal{O}^{-1}(G_a)$ on an arbitrary function is

$$\mathcal{O}(G_a)\frac{\hbar}{m_e}\mathbf{k}_0\hat{\mathbf{p}}\,\mathcal{O}^{-1}(G_a)f(\mathbf{r}) = \mathcal{O}(G_a)\left[\frac{\hbar}{m_e}\mathbf{k}_0\hat{\mathbf{p}}f([\mathbf{R}(G_a)]\mathbf{r})\right] = \frac{\hbar}{m_e}\mathbf{k}_0\left([\mathbf{R}(G_a)]^{-1}\hat{\mathbf{p}}\right)f(\mathbf{r}). \quad (1.20)$$

On the other hand, because of the properties of the scalar product, $(\mathbf{R}(G_a)\mathbf{k}_0)\cdot(\mathbf{R}(G_a)\hat{\mathbf{p}}) = \mathbf{k}_0\cdot\hat{\mathbf{p}}$. Thus, one may write

$$\mathcal{O}(G_a)\left(\frac{\hbar}{m_e}\mathbf{k}_0\cdot\hat{\mathbf{p}}\right)\mathcal{O}^{-1}(G_a) = \mathcal{O}(G_a)\left(\frac{\hbar}{m_e}[\mathbf{R}(G_a)\mathbf{k}_0]\cdot[\mathbf{R}(G_a)\hat{\mathbf{p}}]\right)\mathcal{O}^{-1}(G_a) = \frac{\hbar}{m_e}(\mathbf{R}(G_a)\mathbf{k}_0)\cdot\hat{\mathbf{p}}. \quad (1.21)$$

This shows that for a given $\mathbf{k}_0$, of all the symmetries of the Hamilton operator in Eq. (1.11), it is of special interest to consider those which leave $\mathbf{k}_0$ invariant, because they will be be symmetries of the effective Hamilton operator $\mathcal{H}(\mathbf{k}_0)$. For the corresponding set of point group operations, formally, one may write $\mathcal{O}(G_a)\mathbf{k}_0 = \mathbf{k}_0 + \mathbf{G}_l$, where $\mathbf{G}_l$ is a reciprocal lattice vector. These $\mathcal{O}(G_a)$ point group operations form the group of the wave vector $\mathbf{k}_0$ and we will use the notation $g_{\mathbf{k}_0}$ for this group. In general, not all symmetry operation in g_{cr} satisfy the above condition, therefore $g_{\mathbf{k}_0}$ is usually a subgroup of g_{cr}. It is also easy to see that if $\mathbf{k}_0 = \mathbf{0}$ then $g_{\mathbf{k}_0}$ is equivalent to g_{cr}.

Importantly, if $g_{\mathbf{k}_0}$ is the symmetry group of $\mathcal{H}(\mathbf{k}_0)$, then the eigenfunctions $u_{m,\mathbf{k}_0}(\mathbf{r})$ will transform according to the irreducible representations (irreps) of $g_{\mathbf{k}_0}$. In other words, one can assign a label $u_{m,\mathbf{k}_0}(\mathbf{r}) \to u^{(\Gamma_{j\alpha})}_{m,\mathbf{k}_0}(\mathbf{r})$ to each eigenfunction of $\mathcal{H}(\mathbf{k}_0)$, where Γ_j denotes the irrep and if it is not one-dimensional, then the index α denotes the partners of the irrep. Once these labels are known for a set of $u_{m,\mathbf{k}_0}(\mathbf{r})$ of interest, this information can be used to find out which $\mathbf{p}_{m',m}$ are non-zero. By writing $\mathbf{p}_{m',m} = \langle u^{(\Gamma_{j'\alpha'})}_{m',\mathbf{k}_0}|\mathcal{H}'|u^{(\Gamma_{j\alpha})}_{m,\mathbf{k}_0}\rangle$, it is apparent that this question can be considered as a quantum mechanical selection rule with respect to the perturbation $\mathcal{H}' = \hat{\mathbf{p}}$. Let $u^{(\Gamma_{j'\alpha'})}_{m',\mathbf{k}_0}$ and $u^{(\Gamma_{j\alpha})}_{m,\mathbf{k}_0}$ transform as partners α' and α of irreps $\Gamma_{j'}$ and Γ_j of $g_{\mathbf{k}_0}$, and $\hat{\mathbf{p}}$ transform as Γ_l of $g_{\mathbf{k}_0}$. As it is known from group theoretical arguments [109, 110], the matrix element $\langle u^{(\Gamma_{j'\alpha'})}_{m',\mathbf{k}_0}|\hat{\mathbf{p}}|u^{(\Gamma_{j\alpha})}_{m,\mathbf{k}_0}\rangle$ transforms according to the direct product $\Gamma^*_{j'\alpha}\otimes\Gamma_l\otimes\Gamma_{j\alpha}$ of the irreps. If the decomposition of this direct product into irreps of $g_{\mathbf{k}_0}$ contains the fully symmetric representation Γ_1, then the matrix element is non-zero, otherwise it is zero. Examples of how the labels $\Gamma_{j\alpha}$ can be determined for a concrete material and set of bands will be given in Chaps. 3 and 4.

1.4.3 Spin-orbit coupling effects

The spin-orbit coupling can have very important effect on the energy band structure $E_n(\mathbf{k})$. It is well known, for example, that in semiconductors, such as GaAs, the SOC gives rise to the lifting of the four-fold degeneracy of the topmost valence band. The SOC can be similarly important in 2D materials, leading e.g., to a spin-orbit split bands in materials that lack inversion symmetry (see, e.g., Chapt. 4). In addition to the spin-splitting of the bands, a second important effect of SOC appears in the Zeeman splitting of electrons and holes, as well as interband excitations such as excitons. Namely, the Zeeman splitting will be characterized by effective g-factors that can differ substantially from the free-electron's value $g_e \approx 2.0$ (see further discussion in Chapt. 5).

Starting from the Dirac equation and developing a nonrelativistic approximation, the single-particle Schrödinger equation including the SOC can be written as [111, 109]

$$\left[\frac{\hat{\mathbf{p}}^2}{2m_e} + V(\mathbf{r}) + \frac{\hbar}{4m_e^2c^2}(\boldsymbol{\nabla}V(\mathbf{r})\times\hat{\mathbf{p}})\cdot\mathbf{s}\right]\Psi_{\nu,\mathbf{k}}(\mathbf{r}) = E_\nu(\mathbf{k})\Psi_{\nu,\mathbf{k}}(\mathbf{r}), \quad (1.22)$$

where $\mathbf{s} = (s_x, s_y, s_z)^T$ are Pauli matrices acting in spin-space and the Bloch wavefunction $\Psi_{\nu,\mathbf{k}}(\mathbf{r}) = e^{i\mathbf{kr}}u_{\nu,\mathbf{k}}(\mathbf{r})$ is a two-component spinor. In general, the spin quantum number $s = \{\uparrow, \downarrow\}$ itself is not a good quantum number when the SOC is taken into account. The bands are labeled by ν, which is a shorthand to denote the band index n and the irreducible *double group* representation $\tilde{\Gamma}_{j,\alpha}$. The use of $\tilde{\Gamma}_{j,\alpha}$ is the appropriate way to indicate the symmetry properties of the wavefunctions. The lattice periodic part $u_{\nu,\mathbf{k}}(\mathbf{r})$ satisfies the equation

$$\left[\frac{\hat{\mathbf{p}}^2}{2m_e} + V(\mathbf{r}) + \frac{\hbar}{4m_e^2c^2}\left(\boldsymbol{\nabla}V(\mathbf{r}) \times \hat{\mathbf{p}}\right) \cdot \mathbf{s} + \frac{\hbar}{m_e}\mathbf{k}\left(\hat{\mathbf{p}} + \frac{\hbar}{4m_ec^2}\left[\mathbf{s} \times \boldsymbol{\nabla}V(\mathbf{r})\right]\right)\right] u_{\nu,\mathbf{k}}(\mathbf{r}) = \varepsilon_\nu(\mathbf{k})u_{\nu,\mathbf{k}}(\mathbf{r}), \tag{1.23}$$

where $\varepsilon_\nu(\mathbf{k}) = E_\nu(\mathbf{k}) - \frac{\hbar^2\mathbf{k}^2}{2m_e}$. The procedure is now basically the same as in Sec. 1.4.1. One can write $\mathbf{k} = \mathbf{k}_0 + \mathbf{q}$ and introduce the spinfull basis states $u_{m,\mathbf{k}_0,s} = u^{(\Gamma_{j\alpha})}_{m,\mathbf{k}_0} \otimes |s\rangle$ where $|s\rangle$ is an eigenstate of the spin-operator $\hat{S} = \frac{\hbar}{2}s_z$. Note, that here the superscript $\Gamma_{j\alpha}$ refers to single group irreps of $g_{\mathbf{k}_0}$. One may then expand $u_{\nu,\mathbf{k}}(\mathbf{r})$ in terms of $u_{m,\mathbf{k}_0,s}(\mathbf{r})$ and calculate the matrix elements of the operator appearing in Eq. (1.23). One finds the following set of algebraic equations:

$$\sum_{m',s'}\left[\varepsilon_m(\mathbf{k}_0)\delta_{m,m'}\delta_{s,s'} + \mathbf{q}\cdot\boldsymbol{\gamma}_{m,m'}\delta_{s,s'} + \boldsymbol{\Delta}_{ms,m's'}\right]A^{(\nu)}_{m',s'} = \varepsilon_\nu(\mathbf{k})A^{(\nu)}_{ms}. \tag{1.24}$$

Apart from the term $\boldsymbol{\Delta}_{ms,m's'}$, Eq. (1.24) is the same as Eq. (1.17). In the derivation of Eq. (1.24) we neglected $\langle u_{m,\mathbf{k}_0,s}|\frac{\hbar}{4m_ec^2}\left[\mathbf{s}\times\boldsymbol{\nabla}V(\mathbf{r})\right]|u_{m',\mathbf{k}_0,s'}\rangle$ with respect to $\langle u_{m,\mathbf{k}_0,s}|\hat{\mathbf{p}}|u_{m',\mathbf{k}_0,s'}\rangle$, which is usually a good approximation. The effect of SOC is therefore given by the matrix elements $\boldsymbol{\Delta}_{ms,m's'} = \langle u_{m,\mathbf{k}_0,s}|\frac{\hbar}{4m_e^2c^2}\left(\boldsymbol{\nabla}V(\mathbf{r})\times\hat{\mathbf{p}}\right)\cdot\mathbf{s}|u_{m',\mathbf{k}_0,s'}\rangle = \langle u_{m,\mathbf{k}_0,s}|\mathcal{H}_{soc}|u_{m',\mathbf{k}_0,s'}\rangle$. The use of $u_{m,\mathbf{k}_0,s}$ basis is especially convenient when the typical scale of the SOC is smaller than the energy separation between states labeled by different $\Gamma_{j\alpha}$ indices and therefore the mixing of these states is weak.

In the so-called atomic approximation, $\mathcal{H}_{soc} = \frac{\hbar}{4m_e^2c^2}\left(\boldsymbol{\nabla}V(\mathbf{r})\times\hat{\mathbf{p}}\right)\cdot\mathbf{s}$ is written as $\mathcal{H}_{soc} = \lambda_{so}\hat{\mathbf{L}}\cdot\hat{\mathbf{S}}$, where $\hat{\mathbf{L}} = (\hat{L}_x, \hat{L}_y, \hat{L}_z)^T$ and $\hat{\mathbf{S}} = (\hat{S}_x, \hat{S}_y, \hat{S}_z)^T$ are vectors of angular momentum and spin operators, respectively, and λ_{so} is a constant indicating the strength of the SOC. This form of $\mathcal{H}_{soc}$ is exact in atomic physics, where $V(\mathbf{r}) \sim \frac{1}{|\mathbf{r}|}$ is a central potential, and therefore $\boldsymbol{\nabla}V(\mathbf{r}) \sim \frac{\mathbf{r}}{|\mathbf{r}|^3}$. Regarding solid state physics, λ_{so} is an effective parameter which depends on the chemical composition of the material and it is sometimes argued that the use of atomic approximation is justified because the largest contribution to the SOC comes from regions close to the atomic cores, where the Coulomb interaction is strongest. It is probably more rigorous to think of this form of $\mathcal{H}_{soc}$ as a convenient notation: regardless of the exact form of the crystal potential $V(\mathbf{r})$, from symmetry point of view the gradient $\boldsymbol{\nabla}V(\mathbf{r})$ transforms as a polar vector $\mathbf{r}$. Therefore, with respect to crystal symmetries, the operator $\left(\boldsymbol{\nabla}V(\mathbf{r})\times\hat{\mathbf{p}}\right)\cdot\mathbf{s}$ transforms in the same way as $\hat{\mathbf{L}}\cdot\hat{\mathbf{S}}$. This can be used to determine which matrix elements $\boldsymbol{\Delta}_{ms,m's'}$ are non-zero by extending the argument put forward about the matrix elements $\mathbf{p}_{m,m'}$ in Sec. 1.4.2. If the components $\hat{L}_{x,y,z}$ transform according to an irrep Γ_l of $g_{\mathbf{k}_0}$, then in order to determine whether the matrix elements $\langle u^{(\Gamma_{j'\alpha'})}_{m,\mathbf{k}_0}|\hat{L}_{x,y,z}|u^{(\Gamma_{j\alpha})}_{m',\mathbf{k}_0}\rangle$ are finite one needs to consider the direct product $\Gamma^*_{j'}\otimes\Gamma_l\otimes\Gamma_j$ and decompose it using the irreps of $g_{\mathbf{k}_0}$.

1.4.4 Magnetic field and external potential

Until now we considered problems where the translation invariance of the crystal was preserved and therefore it was natural to use Bloch wavefunctions as basis states. In many important problems, however, the translation invariance is broken. This can happen, e.g., if a magnetic field or an external electrical potential is applied to confine the motion of the charge carriers. Thus, one

considers the Schrödinger equation

$$\left[\frac{(\hat{\mathbf{p}}+e\mathbf{A})^2}{2m_e}+V(\mathbf{r})+\frac{\hbar}{4m_e^2c^2}\left(\boldsymbol{\nabla}V(\mathbf{r})\times(\hat{\mathbf{p}}+e\mathbf{A})\right)\cdot\mathbf{s}+U(\mathbf{r})+\frac{g_e}{2}\mu_B\mathbf{s}\cdot\mathbf{B}\right]\Psi(\mathbf{r})=E\Psi(\mathbf{r}), \tag{1.25}$$

where $\mathbf{A}(\mathbf{r})$ is the vector potential which gives rise to the magnetic field $\mathbf{B}$, and $U(\mathbf{r})$ is a slowly varying (on the scale of the crystal lattice) external scalar potential. It is assumed that $U(\mathbf{r})$ gives a negligible contribution to the SOC. The last term on the right-hand side of Eq.(1.25) is the Zeeman term describing the coupling of the spin degree of freedom to the magnetic field, $g_e \approx 2$ is the free electron gyromagnetic factor, and μ_B is the Bohr magneton.

The derivation of the $\mathbf{k}\cdot\mathbf{p}$ approximation becomes more involved in this case, for details we refer to the original work of Luttinger and Kohn [105] and recent discussions in Refs. [106, 107]. Following [63], here we only provide a short summary of the most important results. Since the functions $u_{m',\mathbf{k}_0}(\mathbf{r})$ form a complete orthonormal basis [108], one may use the expansion

$$\Psi(\mathbf{r})=\sum_{m',s'}\Psi_{m',s'}(\mathbf{r})u_{m',\mathbf{k}_0,s'}(\mathbf{r}), \tag{1.26}$$

where the expansion coefficients $\Psi_{m',s'}(\mathbf{r})$ are called envelope functions. They are supposed to vary slowly on the length scale of the lattice constant and modulate the quickly oscillating $u_{m',\mathbf{k}_0,s'}(\mathbf{r})$ functions. We insert Eq. (1.26) into Eq. (1.25), multiply from the left by $u^*_{m,\mathbf{k}_0,s}(\mathbf{r})$ and integrate over one unit cell. Since $\mathbf{A}(\mathbf{r})$, $U(\mathbf{r})$ and $\Psi_{m',s'}(\mathbf{r})$ are slowly varying, they can be taken out of the integral as constant factors. One finds

$$\sum_{m',s'}\left\{\left[E(\mathbf{k}_0)+\frac{(\hat{\mathbf{p}}+e\mathbf{A})^2}{2m_e}+U(\mathbf{r})\right]\delta_{m,m'}\delta_{s,s'}+\frac{1}{m_e}(\hat{\mathbf{p}}+e\mathbf{A})\cdot\boldsymbol{\gamma}_{m,m'}\delta_{s,s'}\right.$$
$$\left.+\boldsymbol{\Delta}_{ms,m's'}+\frac{g_e}{2}\mu_B\mathbf{S}\cdot\mathbf{B}\delta_{m,m'}\right\}\Psi_{m',s'}(\mathbf{r})=E\,\Psi_{m,s}(\mathbf{r}), \tag{1.27}$$

which is system of coupled differential equations for the envelope function components $\Psi_{m,s}(\mathbf{r})$. As one can see, there is a close similarity between Eq. (1.24) and Eq. (1.27). Formally, the latter can be obtained using the substitution $\mathbf{q}\to\hat{\mathbf{q}}=\frac{1}{\hbar}(\hat{\mathbf{p}}+e\mathbf{A})$ in the former and adding the terms $U(\mathbf{r})$ and $\frac{g_e}{2}\mu_B\mathbf{S}\cdot\mathbf{B}$ to the diagonal. This is sometimes called the Luttinger-substitution [109].

It is important to emphasize that this substitution should be performed in Eq. (1.24), which is, formally, infinite dimensional. In practice, from Eq. (1.24) various lower dimensional approximations or results are obtained using the method of Löwding partitioning [63]. An example of such "downfolding" procedure is the effective mass equation (1.18). On the other hand, the Luttinger substitution promotes the vector $\mathbf{q}$ into a vector operator $\hat{\mathbf{q}}$, and the components of the latter do not commute:

$$[\hat{q}_i,\hat{q}_j]=-i\frac{e}{\hbar}\varepsilon_{ijk}B_k, \tag{1.28}$$

where ε_{ijk} is the Levi-Civita symbol and B_k is a component of the magnetic field $\mathbf{B}$. Therefore, when applying the Löwding partitioning, one has keep in mind Eq. (1.28) as it can have important consequences. An example for this will be discussed in Chap.5.

1.5 Anomalous velocity and Berry curvature

In a seminal paper [112], Michael Berry studied the adiabatic evolution of an eigenstate of a quantum system due to some slowly varying parameters. He found that if the eigenstate remains non-degenerate during the evolution and the change of the parameter values is cyclic, i.e., it makes up a loop, then there will be a interesting phase difference between the eigenstate at the initial and at the final time. While part of the total phase difference is of dynamical origin, there will be another contribution, which is now commonly called the *Berry phase*. The Berry phase is of

geometric origin, meaning that it can be written as a line integral of a vector field over a loop in the parameter space and its value does not depend on the rate of change of the parameter values. One can show that the Berry phase can be expressed as surface integral of another vector field, the Berry curvature.

The Berry phase and Berry curvature influenced several fields of physics immensely, including solid state physics: it is closely related to the conductance quantization in the integer quantum Hall effect [113], it gives an important contribution to the anomalous Hall effect in ferromagnets [114], plays a central role in the modern theory of electric polarization [115, 116], to name a few important results. It is also a fundamental concept in topological band theory. In the following we give a brief introduction of the Berry curvature in crystalline materials and show that it can affect certain transport properties through the so-called anomalous velocity. The anomalous velocity will play an important role in Sect. 1.7 and later in Chapt. 7.

1.5.1 Anomalous velocity

Let us consider a non-degenerate band n in a crystalline material. It has been recently shown [117, 118] that if a weak electric field $\mathbf{E}$ is applied to the material, the group velocity $v_n(\mathbf{k})$ of the electrons in band n is not simply $\mathbf{v}_n(\mathbf{k}) = \frac{\partial \varepsilon_n(\mathbf{k})}{\hbar \partial \mathbf{k}}$, but there is another contribution, which is linear in the electric field:

$$\mathbf{v}_n(\mathbf{k}) = \frac{\partial \varepsilon_n(\mathbf{k})}{\hbar \partial \mathbf{k}} - \frac{e}{\hbar} \mathbf{E} \times \mathbf{\Omega}_n(\mathbf{k}). \tag{1.29}$$

The first term on the right-hand-side is the well-known group velocity and the second one is usually called the anomalous velocity. In addition to the electric field, the anomalous velocity depends on the Berry-curvature $\mathbf{\Omega}_n(\mathbf{k})$. It is given by the vector product [118]

$$\mathbf{\Omega}_n(\mathbf{k}) = \nabla_{\mathbf{k}} \times i \langle u_{n,\mathbf{k}} | \nabla_{\mathbf{k}} u_{n,\mathbf{k}} \rangle, \tag{1.30}$$

where $u_{n,\mathbf{k}}$ is the lattice-periodic part of the Bloch wavefunction $\Psi_{n,\mathbf{k}}$ and Im[...] denotes the imaginary part. The vector

$$\mathcal{A}(\mathbf{k}) = i \langle u_{n,\mathbf{k}} | \nabla_{\mathbf{k}} u_{n,\mathbf{k}} \rangle \tag{1.31}$$

is called the Berry connection.

One can make the following symmetry considerations [118]. Under time reversal $\mathbf{k} \to -\mathbf{k}$, which means that the first term on the right-hand-side of Eq. (1.29) changes sign, whereas $\mathbf{E}$ does not. One expects that $\mathbf{v}_n(\mathbf{k}) \to -\mathbf{v}_n(\mathbf{k})$ and this requires that

$$\mathbf{\Omega}_n(-\mathbf{k}) = -\mathbf{\Omega}_n(\mathbf{k}). \tag{1.32}$$

Under spatial inversion both $\mathbf{k}$ and $\mathbf{E}$ change sign. One expects that $\mathbf{v}_n(\mathbf{k}) \to -\mathbf{v}_n(\mathbf{k})$, which implies that

$$\mathbf{\Omega}_n(-\mathbf{k}) = \mathbf{\Omega}_n(\mathbf{k}). \tag{1.33}$$

It follows from Eqs. (1.32) and (1.33) that if both time-reversal and inversion symmetry are present then $\mathbf{\Omega}_n(\mathbf{k})$ vanishes everywhere in the BZ. However, if either time-reversal or inversion symmetry is broken, the anomalous velocity is not required to vanish.

We note that one may rewrite Eq. (1.30) by expressing $|\nabla_{\mathbf{k}} u_{n,\mathbf{k}}\rangle$ with the help of the Schrödinger equation $H(\mathbf{k})|u_{n,\mathbf{k}}\rangle = \varepsilon_n(\mathbf{k})|u_{n,\mathbf{k}}\rangle$ and making use of the fact that $|u_{m,\mathbf{k}}\rangle$ form a complete orthonormal basis, $\sum_m |u_{m,\mathbf{k}}\rangle\langle u_{m,\mathbf{k}}| = 1$. One finds that

$$\mathbf{\Omega}_n(\mathbf{k}) = -2\mathrm{Im} \sum_{n \neq m} \frac{\langle u_{n,\mathbf{k}} | \nabla_{\mathbf{k}} H(\mathbf{k}) | u_{m,\mathbf{k}} \rangle \times \langle u_{m,\mathbf{k}} | \nabla_{\mathbf{k}} H(\mathbf{k}) | u_{n,\mathbf{k}} \rangle}{[\varepsilon_m(\mathbf{k}) - \varepsilon_n(\mathbf{k})]^2}. \tag{1.34}$$

The form of $\mathbf{\Omega}_n$ given in Eq. (1.34) is significant for several reasons. Firstly, it shows that the Berry curvature is gauge-independent, i.e., a gauge transformation $u_{n,\mathbf{k}} \to e^{i\Phi(\mathbf{k})} u_{n,\mathbf{k}}$ does not

affect $\mathbf{\Omega}_n(\mathbf{k})$. This is important in numerical calculations, because the numerical algorithms that one can use to obtain the eigenstates of the Hamiltonian usually do not output phase factors $e^{i\Phi(\mathbf{k})}$ that are smooth functions of $\mathbf{k}$ everywhere in the BZ. Secondly, while Eq. (1.30) involves only the state $u_{n,\mathbf{k}}$, Eq. (1.34) shows that the Berry curvature in band n can be thought of as a result of an interaction between $u_{n,\mathbf{k}}$ and $u_{m,\mathbf{k}}$, i.e., between band n and other bands m in the band structure.

Thirdly, Eq. (1.34) suggest that $\mathbf{\Omega}_n(\mathbf{k})$ can be large if there is near-degeneracy in the band structure, i.e., when $\varepsilon_m(\mathbf{k}) \approx \varepsilon_n(\mathbf{k})$. This is indeed what was found for a number of materials [119, 120, 121] using DFT band structure calculations. An example is shown in Fig. 1.8 for a 2D material, monolayer MoS_2. One can see that the Berry curvature is strongly peaked at the $\pm K$ points of the BZ. Therefore, one may expect that $\mathbf{\Omega}_n$, and consequently transport effects related to

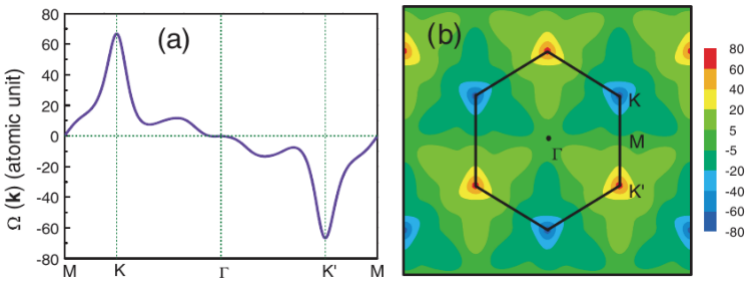

Figure 1.8: Berry curvature calculation for monolayer MoS_2 based on DFT band structure calculations. a) $\Omega_z(\mathbf{k})$ along high symmetry directions, and b) in the whole BZ. Here $\Omega_z(\mathbf{k}) = \sum_n \Omega_{z,n}(\mathbf{k})$, where n$\in$ valence bands. The main contribution actually comes from just one band, the highest energy valence band. Adapted from Ref. [121].

it can already be understood, at least qualitatively, if the band structure is known in the vicinity of those $\mathbf{k}_0$ wavenumber vectors where $\varepsilon_n(\mathbf{k}_0) \approx \varepsilon_{n+1}(\mathbf{k}_0)$ or $\varepsilon_n(\mathbf{k}_0) \approx \varepsilon_{n-1}(\mathbf{k}_0)$. In other words, one does not necessarily need to know the band structure in the whole BZ in order to account for Berry phase related effects. As discussed in Sec. 1.4, the $\mathbf{k} \cdot \mathbf{p}$ methodology can give an accurate characterization of the band dispersion $\varepsilon_n(\mathbf{k}_0 + \mathbf{q})$ and allows to calculate $u_{n,\mathbf{k}_0+\mathbf{q}}$. Thus, it can be an important tool to calculate the Berry curvature.

Historically, the role of the anomalous velocity component in transport effects first emerged in the discussion of the anomalous Hall effect (AHE) by Karplus and Luttinger in 1954 [122]. They showed that the velocity operator has off-diagonal (in the band index n) elements because the electric field, which is applied to drive a current, mixes different bands. However, the relation to the Berry curvature was not realized until much later. In general, several microscopic mechanism can contribute to the AHE, the one closely related to the anomalous velocity is usually called the *intrinsic* contribution.

Finally, we note that the notion of Berry connection and Berry curvature can be extended to degenerate or nearly degenerate bands as well. In this case the Berry curvature becomes a matrix with a non-Abelian gauge structure [118], first discussed by Ref. [123] in a different context. It turns out that the non-Abelian formulation is not needed for the problems we will be discussing in Chapt. 7, therefore we do not consider further details here.

1.5.2 Off-diagonal conductivity and Berry curvature

As one can see from Eq. (1.29), the anomalous velocity component is perpendicular to the electric field $\mathbf{E}$. In conductors the electric field would drive a current and semiclassical considerations would suggest that the anomalous velocity can lead to transverse, Hall effect-like transport phenomena. This intuition is confirmed by a linear response analysis based on the Kubo formula, which we will

now briefly discuss.

Let us consider a 2D system, which will be our main focus later. The Berry curvature has only one non-zero component in this case, which we will denote by $\Omega_{z,n}(\mathbf{k})$. By applying an in-plane electric field $\mathbf{E}$ one can drive a current in the system. The constituent relation between the current components j_ν ($\nu = \{x, y\}$) and the applied electric field E_μ is given by $j_\nu = \sigma_{\nu\mu}E_\mu$, where $\sigma_{\nu\mu}$ is the conductivity tensor. Using the Kubo formalism, the DC limit of the Hall conductivity (per spin) reads [124]:

$$\sigma_{xy} = e^2\hbar \sum_{n\neq m} \int \frac{d\mathbf{k}}{(2\pi)^2}[f(\varepsilon_n(\mathbf{k})) - f(\varepsilon_m(\mathbf{k}))]\frac{\mathrm{Im}\left[\langle u_{n,\mathbf{k}}|\hat{v}_x(\mathbf{k})|u_{m,\mathbf{k}}\rangle\langle u_{m,\mathbf{k}}|\hat{v}_y(\mathbf{k})|u_{n,\mathbf{k}}\rangle\right]}{[\varepsilon_n(\mathbf{k}) - \varepsilon_m(\mathbf{k})]^2}. \quad (1.35)$$

Here $f(\varepsilon_n(\mathbf{k})) = 1/(1+e^{(\varepsilon_n(\mathbf{k})-E_F)/k_BT})$ is the Fermi function and the velocity operator $\hat{\mathbf{v}}$ is defined by the commutator $\hat{\mathbf{v}} = \frac{i}{\hbar}[\mathcal{H}(\mathbf{k}), \mathbf{r}] = \frac{1}{\hbar}\nabla_{\mathbf{k}}\mathcal{H}(\mathbf{k})$, where the Hamiltonian $\mathcal{H}(\mathbf{k})$ was introduced in Eq. (1.13). Note, that the matrix elements of the velocity operator can be expressed using the identity

$$\frac{\langle u_{n,\mathbf{k}}|\nabla_{\mathbf{k}}H(\mathbf{k})|u_{m,\mathbf{k}}\rangle}{\varepsilon_m(\mathbf{k}) - \varepsilon_n(\mathbf{k})} = \langle u_{n,\mathbf{k}}|\nabla_{\mathbf{k}}|u_{m,\mathbf{k}}\rangle. \quad (1.36)$$

Substituting Eq. (1.36) into Eq. (1.35) one finds that

$$\sigma_{xy} = \frac{e^2}{\hbar}\sum_n \int \frac{d\mathbf{k}}{(2\pi)^2} f(\varepsilon_n(\mathbf{k}))\Omega_{z,n}(\mathbf{k}), \quad (1.37)$$

i.e., σ_{xy} depends on the integral of $\Omega_{z,n}(\mathbf{k})$ over the Fermi sea for each occupied band n . One can note that Eq. (1.37) could be obtained by calculating the transverse current due to the anomalous velocity defined in Eq. (1.29) and summing over the occupied bands. The integration in Eq. (1.37) involves the whole Fermi sea, while it is usually expected that transport properties of Fermi liquids at low temperatures should depend only on Fermi surface properties. Indeed, one can show that σ_{xy} can be expressed as a Fermi-surface property [125].

It follows from Eq. (1.37) that when E_F is in a band gap, the Hall conductivity contribution of the nth band is given by the integral of $\Omega_{z,n}(\mathbf{k})$ over the whole Brillouin zone. The number

$$C_n = \int_{BZ} \frac{d\mathbf{k}}{(2\pi)^2}\Omega_{z,n}(\mathbf{k}), \quad (1.38)$$

is an integer [126] called the first Chern number. The physical importance of the Chern number came to prominence when its relation to the off-diagonal conductance of the quantum Hall effect (QHE) was realized. Thouless et. al. [113] showed theoretically that $\sigma_{xy} = Ne^2/h$, and the integer N is given by $N = \sum_n C_n$, where the summation runs over the occupied bands and equals the number of occupied Landau levels.

1.6 Spintronics

Broadly speaking, the aim of *spintronics* is to use the spin of charge carriers to control equilibrium and non-equilibrium properties of materials in order to obtain new ways to store information and to operate logic devices [127]. From practical point of view, key ingredients of spintronics are the injection, transport, manipulation and detection of spin information. The implementation of these ingredients often involves trade-offs: for example, spin transport would require low a SOC material, whereas spin manipulation and detection can typically be achieved using materials with strong SOC.

The origins of spintronics go back to metals and semiconductor quantum wells [128, 129]. Atomically thin materials and their heterostructures have opened new opportunities in spintronics [127, 130, 131]. Graphene is a strong candidate for spintronics applications [127], due to its long spin-relaxation times [132, 133] and spin-diffusion lengths even at room temperature [134], which could

be used in spin-logic devices [135, 136, 137]. Many of the ideas developed earlier for 2D quantum wells based spintronics setups can be implemented in rather straightforward way using vdW heterostructures as well. However, new concepts have also been established, e.g., which make use of the twist angle between the layers, see Chapt. 8. Spintronics in atomically thin materials can overlap with another recent idea called *valleytronics*, which will be introduced in Sec. 1.7. Our main aim here is to briefly present some background for the topics that will be discussed in Chapt. 3, 7, and 8.

1.6.1 Graphene heterostructures for van der Waals spintronics

In heterostructures of graphene with TMDCs, topological insulators and 2D magnets the proximity of the atomic layers means that material properties can be imprinted across the interfaces. Although the vDW interactions are weak, the interlayer tunnel coupling can nevertheless change the energy dispersion or the spin texture in the layers. An important example is the so-called proximity induced SOC, whereby a material that has a strong intrinsic SOC can effectively change the SOC properties of an atomically thin layer which is brought in close contact with it. The concept of proximity SOC can potentially help to engineer many of the SOC related phenomena, such as spin relaxation, charge-to-spin conversion, spin-orbit torques [130, 131] etc in vdW systems.

MLG and BLG represent model systems for SOC proximity effects. The intrinsic SOC of MLG is weak, of the order of 10^{-2}meV [138], and opens a small gap in the dispersion at $\pm K$ points. The aim of achieving a strong proximity induced SOC is motivated by the fact that the weak intrinsic SOC of graphene hinders the control and tunability of possible spintronics devices. In order to increase the SOC in graphene, one of the most actively pursued direction is to interface it with materials that have strong intrinsic SOC, such as TMDCs [139, 140, 141, 142, 143]. TMDCs appear to be ideal material system to induce SOC, because they are chemically inert, they have strong intrinsic SOC (see Chap. 4) and they have little impact on graphene's electronic properties in the energy range relevant for transport studies. Following Refs. [144, 145], this is illustrated in Fig. 1.9, which shows DFT band structure calculations for two examples of MLG/TMDC heterostructures. The band structure of the heterostructures (upper row of Fig. 1.9) can be understood as a combination of the band structure of the TMDC layer, which has a finite band gap, and the linearly dispersing MLG bands. One can clearly see that the Dirac point of the MLG band structure is located within the band gap of the TMDC. Focusing on the electronic states close to the Dirac point, one finds that the spin degeneracy of the MLG bands is lifted (lower row of Fig. 1.9), which is a clear signature of the SOC induced by the TMDC in the MLG bands . Further details of the SOC in graphene will be discussed in Sec. 1.6.2. Here we make two important remarks:

- Although DFT calculation can underestimate the band gap of the TMDC layer and may not give precisely the position of the Dirac point of MLG within the band gap, there is experimental evidence [146, 147] that the picture shown in Fig. 1.9 is qualitatively correct.

- The results in Fig. 1.9 were obtained by assuming that the MLG and TMDC layers were perfectly aligned, i.e., for zero interlayer twist angle. One can expect that a finite twist angle between the layers can affect, e.g., the magnitude of the induced SOC. This will be the main topic of Chap. 8.

Experimental probes of the induced SOC

There are three main experimental techniques that have been used to investigate the SOC in graphene in recent years [148]. The first one is the so called charge-to-spin interconversion (CSI), and its inverse, the spin-to-charge interconversion (SCI) phenomena. An important example is the spin Hall effect (SHE), which will be briefly discussed in Sec. 1.6.3. We will mainly be interested in the *intrinsic* SHE, which depends on the band structure of the host material and is finite in the

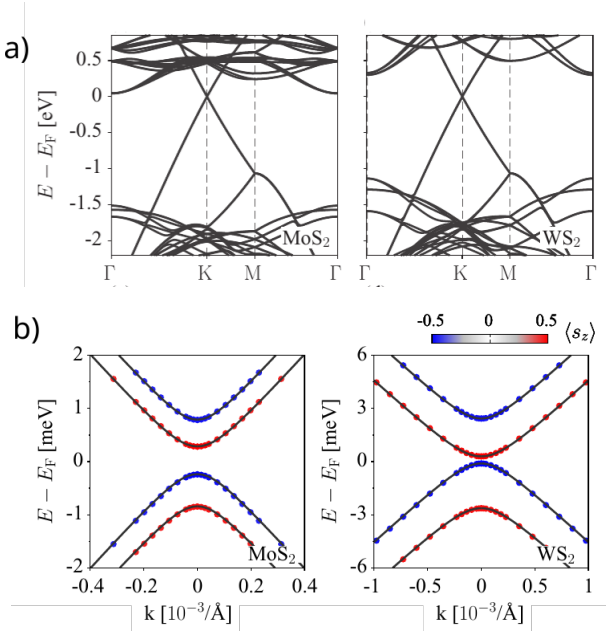

Figure 1.9: Band structure calculations for MLG/monolayer TMDC heterostructures. a) Overview of the band structure of MLG/MoS_2 and MLG/WS_2. One can recognize the linearly dispersing bands and the Dirac point of MLG in the band gap of the TMDCs. b) Band structure close to the Dirac point of MLG for the systems shown in a). The bands become spin polarized due to the induced SOC. Adapted from Ref. [145].

ballistic transport limit. We note that in graphene heterostructures the SHE is often accompanied by another CSI effect, the so-called Rashba-Edelstein or inverse spin galvanic effect [149, 150, 151].

In the presence of SOC the spin degree of freedom can be affected by the momentum scattering of the charge carriers. Materials in spintronics applications are usually characterized by the spin relaxation time τ_s and the spin diffusion length λ_s, which are related by the relation $\lambda_s = \sqrt{D_s \tau_s}$, where D_s is the spin diffusion coefficient. These parameters can be obtained from two different type of measurements: i) spin injection and Hanle precession in lateral spin valves and ii) weak (anti)localization measurements. If the momentum relaxation time τ_p and the microscopic mechanism of the spin relaxation (e.g., Elliott-Yafet and D'yakonov-Perel type) are known, one can estimate the strength of the SOC using the extracted spin-relaxation time. However, in addition to the SOC there can be several sources of spin relaxation in graphene (e.g., strain fields, magnetic impurities etc), and it remains difficult to unambiguously differentiate between different relaxation mechanism.

A way around this problem can be to consider the spin lifetime anisotropy $\zeta = \tau_s^{\perp}/\tau_s^{\parallel}$, which is defined as the ratio of the lifetime of spins pointing out of the graphene plane ($\tau_s^{\perp}$) to those pointing in-plane ($\tau_s^{\parallel}$). This is motivated by the realization that different spin relaxation mechanism yield different ζ values. In particular, assuming that the main spin relaxation channel is the induced SOC and the relaxation occurs in the D'yakonov-Perel regime [152, 153, 154], it was found [155] that $\zeta \approx \left(\frac{\lambda_{vZ}}{\lambda_R}\right)^2 \left(\frac{\tau_{iv}}{\tau_p}\right) + 1/2$, where τ_{iv} is the intervalley scattering time, λ_{vZ} and λ_R are the coupling constants of the valley Zeeman and Rashba type SOC (see Sec. 1.6.2). Since $\tau_{iv} \gg \tau_p$ in graphene, this suggest that ζ can be quite large if $\lambda_{vZ} \gtrsim \lambda_R$. Indeed, $\zeta \geq 10$ was found in two recent experiments [156, 157], which can be taken as a strong indication of the induced SOC.

The third main experimental technique that has been used is the weak localization (WL) and weak antilocalization (WAL) measurements. WL and WAL are quantum corrections to the classical

conductivity in diffusive systems due to the interference of backscattered electrons traversing time-reversed paths. In the case WAL, which can signal the presence of SOC, the interference between the time-reversed loops is destructive and the conductivity is increased compared to the classical value. The dependence of the conductivity on the magnetic field can be used to infer various charge and spin relaxation times. In its most general form [158] the WAL theory requires the fitting of six independent time scales [148]. Since obtaining a unique fit is difficult, usually simplified models are used which entail assumptions that may or may not be completely justified. This, in turn, complicates the interpretation of the experimental results. Nevertheless, WAL measurements provided convincing evidence of the induced SOC in graphene [139, 142, 159].

Finally, we mention that in TMDC/BLG heterostructures it was also possible to use the quantum Hall effect to gain information on the strength of the induced valley Zeeman SOC [160]. In summary, although its strength is difficult the determine quantitatively, the different experimental techniques did demonstrate that TMDCs can induce SOC in graphene, and it is ≈ 100 times stronger than graphene's intrinsic SOC.

1.6.2 Effective graphene Hamiltonian in proximitized heterostructures

Various aspects of the SOC in graphene will be one of the main topics of this thesis (see Chaps. 3 and 8). Here we first summarize the most important SOC terms that can appear in MLG, including both the intrinsic and the proximity induced SOC. The latter can be derived, e.g., in a heuristic way, by considering how external perturbations break the symmetries of the graphene sheet [161]. The microscopic mechanisms giving rise to the proximity induced SOC will be discussed in Chap. 8.

Intrinsic SOC

The Hamiltonian of the intrinsic SOC of pristine MLG at the $\pm K$ points of the BZ reads

$$H_{intr} = \lambda_I \tau \sigma_z s_z, \tag{1.39}$$

where, we remind, $\tau = \pm 1$ refers to the graphene valleys, σ_z to the sublattice, and s_z to the spin degrees of freedom. Carbon is a light element, therefore the intrinsic SOC is quite weak, in the τK valleys the energy scale of the SOC is $\lambda_I = 24 - 50\mu$eV [138]. By calculating the spectrum of $H_{mlg}(\mathbf{q}) + \mathcal{H}_{intr}$ one finds that $\mathcal{H}_{intr}$ opens a gap in the Dirac spectrum, but the bands remain spin degenerate due to the combined effect of time reversal and inversion symmetries.

Historically, H_{intr} motivated the prediction of the quantum spin Hall effect [162] and started the field of topological insulators. However, the small magnitude of λ_I has made impossible the direct experimental observation of this effect in MLG.

Bychkov-Rashba type SOC

The Rashba type SOC appears when the (horizontal) mirror symmetry with respect to the plane of the graphene sheet is broken by a substrate, external electric field or adatoms. If the system still has vertical mirror planes, i.e., it has C_{3v} symmetry, the corresponding SOC Hamiltonian reads

$$H_R = \frac{\lambda_R}{2}(\tau \sigma_x s_y - \sigma_y s_x), \tag{1.40}$$

where λ_R is the SOC strength. One can notice that H_R does not depend on the momentum. This is in contrast to III-V semiconductor quantum wells, where the Rashba SOC is linear in the momentum. H_R leads to a spin splitting of the otherwise spin degenerate graphene bands, but it does not open a gap at the $\tau\mathbf{K}$ point and the spin polarization $\langle \mathbf{s} \rangle$ of the bands is in-plane. When the Bychkov-Rashba type SOC is due to an out-of-plane electric field, microscopically it can be described by taking into account the hybridization of the π and σ orbitals of graphene [163].

If the mirror symmetry of graphene is broken by a substrate that itself has a hexagonal lattice, then for a general interlayer rotation angle the system has only a C_3 symmetry. It was recently realized [164, 165], that in this case the Rashba SOC in graphene reads

$$H_R = \frac{\lambda_R}{2} e^{i\frac{\Theta}{2}s_z}(\tau\sigma_x s_y - \sigma_y s_x)e^{-i\frac{\Theta}{2}s_z}, \tag{1.41}$$

i.e., the effect of lowering the symmetry from C_{3v} to C_3 corresponds to a rotation in spin-space. We will discuss the details of Eq. (1.41) and the meaning of the angle Θ in Chapt. 8.

Experimentally, by fitting the results of WAL measurements it was found that the value of proximity induced λ_R was $0.3 - 3.0\,\text{meV}$ in graphene/TMDC heterostructures [142].

valley Zeeman SOC

When the inversion symmetry of a heterostructure consisting of graphene and another 2D materials is broken, then the so-called valley Zeeman SOC is also allowed to appear by symmetries. It is given by the Hamiltonian

$$H_{vZ} = \lambda_{vZ}\tau s_z, \tag{1.42}$$

where λ_{vZ} is the SOC strength. It is similar to the intrinsic SOC given in Eq. (1.39), but it does not depend on the sublattice degree of freedom, i.e., on σ_z. H_{vZ} leads to a spin splitting of the bands at the $\tau\mathbf{K}$ points and to an out-of-plane spin polarization. An important example for a substrate which can induce this type of SOC are TMDCs.

Experimentally, the value of proximity induced λ_{vZ} was found to be $0.2 - 2.0\,\text{meV}$ [142] in graphene/TMDC heterostructures, i.e., its magnitude was similar to λ_R.

Effective graphene Hamiltonian

In general, all three types of SOC discussed above are present in heterostructures that involve graphene. Therefore the effective (emergent) Hamiltonian would read

$$H_{\text{eff}} = H_{mlg}(\mathbf{q}) + H_{intr} + H_R + H_{vZ}, \tag{1.43}$$

where $H_{mlg}(\mathbf{q})$ was defined in Eq. (1.4). Here the word "effective" refers to the fact that H_{eff} acts only on the spin and pseudospin degrees of freedom of the graphene sheet. The substrate, which would give rise to H_R and/or H_{vZ}, does not appear explicitly is this description. In graphene/TMDC heterostructures this approach is justified, because the graphene Dirac point is located within the TMDC band gap, as shown Fig. 1.9. Therefore, in many experimental setups the transport takes place only in the graphene layer and it is sufficient to consider $\mathcal{H}_{\text{eff}}$. As it is clear from the preceding discussions, $\lambda_I \ll \lambda_R, \lambda_{vZ}$, which means that $\mathcal{H}_R$ and $\mathcal{H}_{vZ}$ are the main SOC terms, but we kept $\mathcal{H}_{intr}$ for later reference, see Chap. 3.

We note that in Ref. [145] other terms were also included in H_{eff}, and we now briefly comment on them. The first such term is $H_{bg} = \Delta\sigma_z$, which would open a spin-independent band gap of 2Δ in the graphene spectrum. H_{bg} would be relevant for rotationally aligned graphene/hBN structures, where indeed there is experimental evidence [166] for a band gap opening. However, one can expect that if a heterostructure consist of layers that have incommensurate lattice constants, such as graphene/TMDC, such term should be absent (this argument does not preclude the existence of locally gapped regions in graphene). Ref. [145] fitted the DFT bands structure calculations shown in Fig. 1.9 with an effective Hamiltonian that included H_{bg} and obtained values of $\Delta \approx 0.5$ meV. The fact that Δ was found to be finite can be due to the finite computational supercell and the presence of atomic relaxation in these calculations. Finally, the SOC terms which are linear in momentum [145] are also neglected in Eq. (1.43). For typical graphene dopings these terms are much smaller than H_R and H_{vZ}, which are momentum independent.

1.6.3 The spin Hall effect

The SHE was originally proposed by D'yakonov and Perel 40 years ago [167] and it is one of the key phenomena in the field of spintronics. In the direct SHE, an electrical current flowing through a material can generate a transverse spin current, which is polarized perpendicular to the plane defined by the charge and spin current. This spin current can lead to spin-accumulation at the edges of the sample. A schematic illustration of the effect is shown in Fig. 1.10(a). The reciprocal effect also exists, which is called the inverse SHE (ISHE): a pure spin current can generate a transverse charge current. A prerequisite for (I)SHE is that the material must possess a strong SOC. This phenomenon is also important e.g., for proposals aiming to achieve energy efficient spin-logic devices [168]. In the last twenty years there has been an upsurge of interest in SHE. In this more recent setting the details of SHE were extensively discussed for III-V semiconductors and quantum wells, for a recent review see Ref. [129]. We now briefly summarize a few important results obtained in this this field.

A simple model for the SHE is a two-dimensional electron gas (2DEG) with Bychkov-Rashba SOC, which is described by the $\mathbf{k}\cdot\mathbf{p}$ Hamiltonian

$$H_R = \frac{\mathbf{p}^2}{2m_{\text{eff}}} + \frac{\lambda_R}{\hbar}(\mathbf{s}\times\hat{\mathbf{p}})_z. \tag{1.44}$$

Here m_{eff} is the effective mass, λ_R is the strength of the SOC, $\mathbf{s} = (s_x, s_y, s_z)^T$ is a vector of Pauli matrices acting in the spin space, and, with respect to Sec. 1.4.1, $\mathbf{p} = \hbar\mathbf{q}$. This model is an example for the *intrinsic* SHE, which depends on the properties of the band structure in a perfect crystal. One may define define [169] the spin current operator for out-of-plane polarized spins by $\mathbf{j}^z_{\text{spin}} = \frac{\hbar}{4}\{s_z, \mathbf{v}\}$, where $\{\dots\}$ denotes the anticommutator and $\mathbf{v} = \partial H(\mathbf{p})/\partial\mathbf{p}$. Assuming, e.g., charge current flowing in the y direction due to an electric field E_y and substituting $j^z_{\text{spin},x}$ into Eq. (1.35) one finds that $\sigma^s_{xy} = -j^z_{\text{spin},x}/E_y = \frac{e}{8\pi}$ in a broad range of the Fermi energy E_F. Since σ^s_{xy} is independent of material specific parameters, this results was called the "universal intrinsic spin Hall effect" [169]. We mention here that this contribution is canceled exactly by short-range disorder scattering [170, 171]. However, using a more general SOC model, which includes, e.g., the Dresselhaus type SOC [172] as well, the intrinsic contribution survives the disorder average [129].

Another example for the SHE can be found in bulk semiconductors, such as germanium [173]. In contrast to the previous case, where the Bychkov-Rashba SOC due to the structural asymmetry breaking of the semiconductor heterostructure played a role, here the intrinsic SOC gives rise to the effect in the valence band. The valence band is four-fold degenerate at the Γ point of the BZ, away from the Γ point the degeneracy of the heavy-hole and light-hole bands is lifted but due to the inversion symmetry, they remain spin-degenerate. Assuming that an electric field is applied in the z direction, for spin parallel with the x axis and flowing into the y direction the spin Hall conductivity is $\sigma^s_{xy} = \frac{e}{12\pi^2}(3k_F^{hh} - k_F^{lh})$, where k_F^{hh} and k_F^{lh} are the Fermi wavenumber of the heavy hole and light hole bands, respectively.

Regarding atomically thin materials, the first theoretical study of SHE in MLG was performed in Ref. [174]. In this work the effects of the intrinsic and the Rashba type SOC were considered using Green's function technique (the valley Zeeman SOC was not included into the model) and impurity scattering was neglected. It was found that both SOC terms can lead to finite SHE. Experimentally, however, it would be difficult to check these predictions: on the one hand, λ_I is very small, on the other hand, a later work [175] showed that the SHE based on the Rashba SOC would be suppressed by disorder, similarly to the situation in 2DEG. More recently Ref. [176] obtained important results for σ^s_{xy}, which are summarized in Fig. 1.10(b). They used large scale numerical calculations based on appropriately parameterized TB model of proximitized graphene and the Kubo formalism. As one can see, the SHE is finite in a narrow energy region near the charge neutrality point (CNP), therefore it can be controlled by tuning the carrier density. Another important result of the calculations of Ref. [176] is that σ^s_{xy} remained finite when intervalley

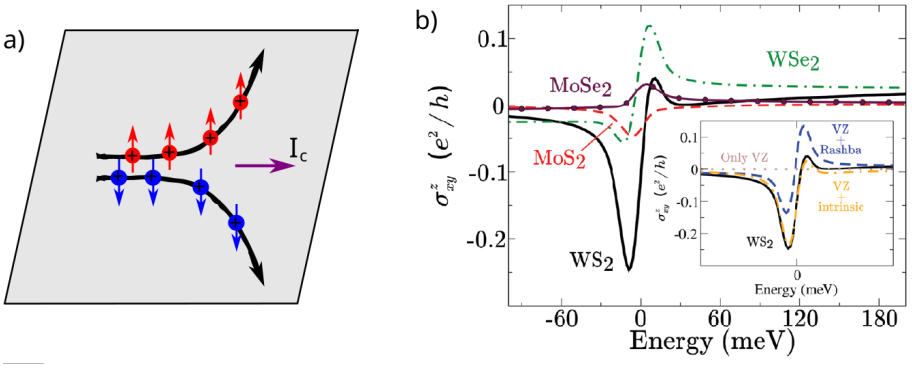

Figure 1.10: a) Schematic picture of the intrinsic SHE assuming p-doping. A charge current I_c generates a transverse spin current. b) Intrinsic spin Hall conductivity calculations for MLG on different TMDCs as a function of E_F. The inset indicates that the valley Zeeman SOC alone does not lead to finite σ^s_{xy}. Adapted from Ref. [177].

scattering of moderate strength was taken into account, which suggested that the SHE should be observable experimentally.

We also point out that beyond its relevance to spintronics, the SHE inspired and influenced several other ideas in the field of atomically thin materials, such as the valley Hall effect and the coupled valley and spin Hall effect, which will be discussed in Sec. 1.7.2 and Sec. 1.7.3, respectively.

Intrinsic and extrinsic contributions to the SHE

It is important to mention that in general several microscopic mechanism can contribute to the SHE (as well as to the AHE). We follow the terminology used in Ref. [129]. The first one, as already mentioned above, is called the *intrinsic* mechanism. It is generated by the SOC and depends on the properties of the band structure in a perfect crystal. For example, avoided crossings in the band structure often give rise to a large Berry curvature (see Sec. 1.5.1), which, in turn, can lead to a transverse spin current. All of the examples mentioned in the previous section rely on such intrinsic mechanism. The second possible contribution to the SHE is called *side-jump* mechanism. This can happen both when a not spin-orbit coupled wavepacket is scattered off a spin-orbit coupled disorder potential and when a spin-orbit coupled wavepacket scatters off a scalar potential. Both the intrinsic and the side-jump contributions are independent of the transport lifetime τ_{tr} of the Bloch states. The third possible contribution is called *skew-scattering*. It is linear in τ_{tr} and there can be several microscopic mechanism behind it, such as the relativistic Mott scattering, as proposed originally by Dyakonov and Perel [167]. Which of the contributions is the dominant one in a given sample depends on a number of factors, e.g., presence/absence of band crossings, the importance of the disorder and the strength of the SOC [129].

Experimental probes of the SHE

The first experiments to detect the SHE made use of optical methods. In Fig. 1.11 we show the setup used in Ref. [178]. It is based on a two-dimensional hole gas (2DHG) with strong SOC in a (Al,Ga)As/GaAs heterostructure. The p-doped region is in contact with n-doped regions at the 2DHG channel edges, where the electrons and holes can recombine leading to electroluminescence. The device therefore contains two light-emitting diode (LED)s on each side of the 2DHG channel. The spin polarization in the system is detected by measuring the circular polarization (CP) of the light. Due to optical selection rules, a finite CP along a given light propagation direction indicates that the spin-polarization of the charge carries in that direction is finite. When a current is driven

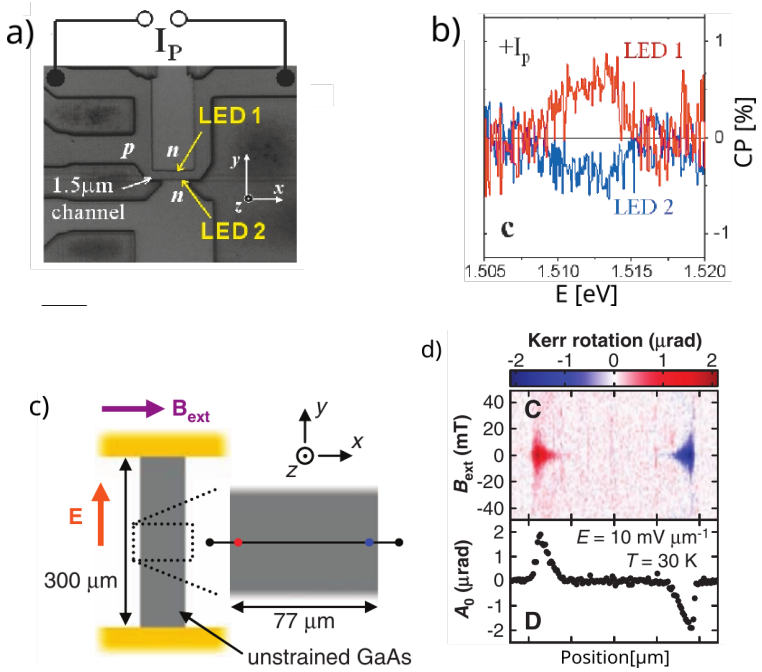

Figure 1.11: Optical detection of SHE. a) The scanning electron microscope image of the LED device used in Ref. [178]. A current I_p flows in the p-doped channel. The top (LED1) and bottom (LED2) n doped contacts are used to facilitate electroluminescence at the opposite edges of the 2DHG. b) CP of the electroluminescence stemming from LED1 and LED2. The electroluminescence has opposite polarization at opposite edges of the 2DHG channel. Adapted from Ref. [178]. c) Schematics of the thin film GaAs device used in Ref. [179], with an applied electric field E. The largest KR signal is detected close to the sample edges, indicated by the red and blue dots. d) Upper panel: magnetic field dependence of the KR signal. Lower panel: the KR signal measured along the line indicated in c). Adapted from Ref. [179].

through the p-doped channel, the emitted light into the z direction from the LEDs had a finite CP, indicating a finite spin-polarization $\langle s_z \rangle$ of the holes that recombine with the electrons. Moreover, $\langle s_z \rangle$ was found to be opposite at opposite edges of the 2DHG channel, in accordance with the phenomenology of the SHE. The analysis of the sample suggested that the effect is due to the intrinsic mechanism of the SHE.

Another well-know experiment measured the spatial dependence of the Kerr rotation (KR) of light [179] [Figs. 1.11 (c)-(d)]. A linearly polarized light beam was incident perpendicularly to the sample surface and the polarization axis of the reflected beam was measured. The rotation angle of the polarization is proportional to the magnetization of the electron spins along the laser propagation direction, therefore it can be used to detect the induced spin accumulation at the sample edges. As shown in Fig. 1.11(d), a finite and opposite KR signal was measured close to the two edges of the sample. This indicated the accumulation of $+z$ and $-$ polarized spins at opposite edges. The effect disappeared in small in-plane magnetic field, demonstrating that the phenomenon was indeed related to the spin degree of freedom. The analysis of the properties of the sample suggested that the extrinsic SHE was dominant in this experiment.

The results of Refs. [178, 179] demonstrated that the spin-polarization information can be turned into light-polarization in semiconductors, thus facilitating the detection of the former phenomenon. As we will see in Sec. 1.7.2, similar ideas can be used to probe phenomena related to the valley degree of freedom.

On the other hand, when metals or graphene is used as a spin transport channel, the detection

of the SHE relies on transport measurements. The device geometry would typically consist of a Hall cross with ferromagnetic injector and collector contacts in one of the arms [180]. In Fig. 1.12 we show a recent setup using proximitized graphene [151]. The device consists of a graphene Hall cross with a WS_2 flake covering part of one of the arms and inducing SOC in the graphene channel. Ferromagnetic injector/detector electrode(s), such as F1 (and others not shown) can be found across the other arm of the Hall cross. An electric field $\mathbf{E}$ along the graphene-WS_2 arm generates a spin current due to the SHE (red arrows). The spins diffuse into the other arm and are detected by measuring a non-local voltage V_{nl}^F at F1. V_{nl}^F is proportional to the local spin accumulation projected along the detector magnetization $\mathbf{M}_1$. In zero external magnetic field $V_{nl}^F = 0$ because the diffusing spins are orthogonal to $\mathbf{M}_1$. However, if a small in-plane magnetic field $\mathbf{B}_x$ is used to make the spins precess, V_{nl}^F will be non-zero.

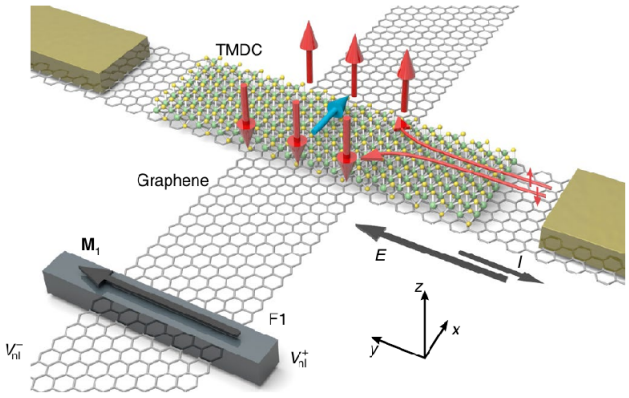

Figure 1.12: Graphene Hall bar to study the SHE. A TMDC flake covers one of the arms and a ferromagnetic electrode F1 is found in the other. The electric field $\mathbf{E}$ generates a current through the region with enhanced SOC in graphene. Out-of-plane spin accumulation (red arrows) is generated by the SHE and diffuses towards F1. In addition to the SHE, a non-equilibrium in-plane spin density is also generated (blue arrow). $\mathbf{M}_1$ denotes the magnetization direction of F1. Adapted from Ref. [151].

As indicated by the blue arrow in Fig. 1.12, another effect is also present in this device. Due to the finite Bychkov-Rashba type SOC in graphene, a non-equilibrium in-plane spin density is generated, which is polarized perpendicularly to the current. This is called the Rashba-Edelstein or inverse spin galvanic effect (ISGE)[129, 149], which we already mentioned in Sec. 1.6.1. In general both the SHE and the ISGE would have a contribution to the measured signal but the setup used in Ref. [151] made it possible to discriminate between the SHE and the ISGE.

1.7 Valleytronics

Valleys are local minima or maxima in the band structure of crystalline materials. For example, it is well-known that in the conduction band of bulk silicon there are six such degenerate electron pockets, or valleys. They can be found along the $\Gamma - X$ line of the BZ, at a relatively low symmetry point of the band structure, which makes it challenging to address the electronic states in different valleys separately. However, they can be important in relaxation processes for silicon donor based qubits [181]. Attempts for valley-dependent manipulation of electronic states have remained rather limited [182, 183, 184] until recently. Nevertheless, already Refs. [182, 183, 184] formulated the concept of *valleytronics*, which is build on the idea that the valley degree of freedom could carry and store information, similarly to the charge in conventional electronics or the spin in spintronics. The main motivation of valleytronics is to identify and study suitable systems that can complement

or even surpass existing technologies based on the charge or spin degree of freedom. Generally, a valleytronic material has a band structure that host two (or more) degenerate valleys that can be used to encode information, and at the same time, the different valleys should be addressable so that the information can be read and written.

1.7.1 Valleytronics in atomically thin materials

The discovery of atomically thin 2D materials has given a huge boost to the interest in valley related phenomena. Many of these materials, such as graphene or monolayer TMDCs, have a hexagonal lattice and the band edge of the valence and conduction bands can be found at the $+K$ and $-K$ points of the BZ. Thus, in analogy to a spin-1/2 system, charge carriers can be assigned a pseudospin number in these materials: those in the $+K$ valley can be labeled as valley pseudospin-up, and those in the $-K$ valley as pseudospin-down. Several 2D materials have been proposed as a suitable valleytronics system and correspondingly, there have been a number of suggestions for how to use and manipulate the valley pseudospin.

One of the first ideas was to use a quantum point contact (QPC), i.e., a short and narrow constriction (see Fig. 1.13), made of a zigzag graphene nanoribbon [185]. For low-enough Fermi energies the transmission through the QPC is valley polarized due to the peculiar dispersion of the propagating modes in the QPC. Whether states in the $+K$ or the $-K$ valley are transmitted can be tuned by locally raising the Dirac point in the constriction, therefore, this device can act as a valley filter. Two such valley filters in series, as shown in Fig. 1.13(a), can block the current if they have opposite polarities, demonstrating, in principle, that the QPC can function as a valley-valve. In practice, the fabrication of graphene constrictions that have zigzag edges proved to be difficult.

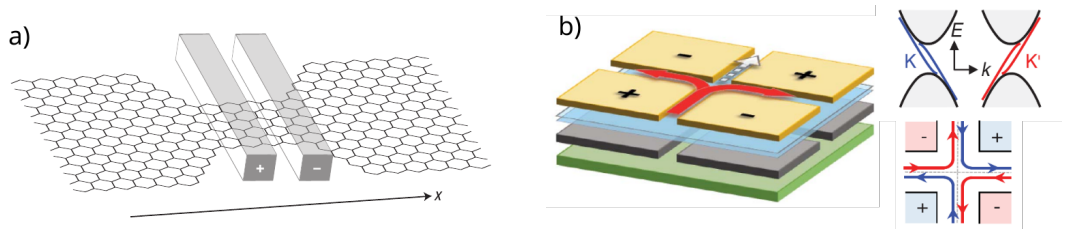

Figure 1.13: Valleytronics in graphene. a) Schematics of a valley valve device based on zigzag graphene nanoribbon constriction. When the local gates have opposite polarities, the current through the QPC can be blocked. Adapted from Ref. [185]. b) Schematics of a beam splitter and valley valve in BLG. Blue denotes the BLG layer, gold and gray rectangles are gate electrodes. Their polarity defines the direction of the out-of-plane electric field in each region. In the region between by the electrodes, so-called kink-states are formed, which have a particular chirality in each of the valleys (upper inset). Lower inset shows the chirality of the kink states in each of quadrant of the setup. Assuming that intervalley scattering is suppressed, the setup shown in the figure can be used as a beam splitter (red arrows in the main figure). At the same time, the current from the bottom to the top is blocked (white arrow), which is a valley valve effect. Adapted from Ref. [186].

Another idea is illustrated in Fig. 1.13(b). External out-of-plane electric field can open a band gap in BLG [64]. Between regions where the polarity of the electric field is opposite, so-called kink-states of topological origin can form [187] in the band gap. These states have a different chirality in each of the valleys. Assuming that the scattering between the $+K$ and $-K$ valleys is suppressed, one can use the kink states to obtain a simultaneous beam splitter and valley valve [188, 186].

As a third example, one can consider monolayer TMDCs. As we have already mentioned in Sec. 1.3, they are direct band gap semiconductors and the band gap can be found at the

$+K$ and $-K$ points. The selection rules for the optical transition between the valence and the conduction bands are valley dependent [189, 77] [see Fig. 1.14(a)]: electronic states in the $+K$ ($-K$) valley couple to right circularly polarized σ^+ (left circularly polarized σ^-) light. In this

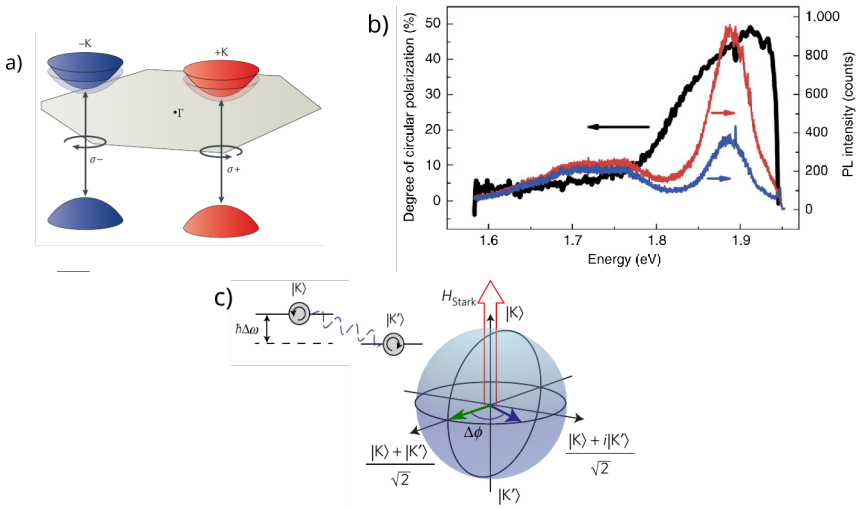

Figure 1.14: Valleytronics in monolayer TMDCs. a) Valleys at the $+K$ and $-K$ points of the hexagonal BZ of a monolayer TMDC. The optical interband transitions between the valence and the conduction bands (vertical black arrows) in the $+K$ ($-K$) valley are excited by σ^+ (σ^-) polarized light. Adapted from Ref. [190]. b) Circularly polarized photoluminescence of monolayer MoS_2. The red and blue curves correspond to the intensities of the emitted σ^+ and σ^- polarizations upon σ^+ excitation. Adapted from Ref. [77]. c) Optical valley pseudospin manipulation. A linearly polarized optical pulse excites a coherent superposition of $+K$ and $-K$ excitons denoted by the green arrow. (In this figure the notation K' is used for the $-K$ valley.) When a strong σ^+ polarized control pulse is applied, the energy of the K valley exciton is increased by $\hbar\Delta\omega$. If the duration of the control pulse is Δt, a dynamic phase difference $\Delta\phi = \Delta\omega\Delta t$ develops between the exciton components in the two valleys and the pseudospin is rotated (blue arrow). Adapted from Ref. [191].

case the information carriers are neutral or charged excitons, and as shown in Fig. 1.14(b), optical selection rules allow the optical preparation and read-out of the valley pseudospin by measuring the polarization of the photoluminescence [75, 76, 77]. The electronic states in the $+K$ and $-K$ valleys are degenerate, because they are related by time reversal symmetry. Breaking the degeneracy of the valleys can be important in order to provide an additional control over this pseudospin degree of freedom. This can be achieved, e.g., by an out-of-plane magnetic field, which we will discuss in Chapt. 5. All-optical control and rotation of the valley pseudospin has also been achieved [191]. As illustrated in Fig. 1.14(c), when a linearly polarized light is used for the excitation, a coherent superposition state of the excitons in the $+K$ and $-K$ valley is formed. This coherent state can be manipulated if the degeneracy of the valleys is lifted, which was achieved using the optical Stark effect [192, 193].

1.7.2 The valley Hall effect

We now discuss the valley Hall effect (VHE), which is related both to the off-diagonal conductivity introduced in Sec. 1.5 and to the valley degree of freedom. As a first example, let us consider MLG with broken inversion symmetry. Experimentally, this can be achieved in a hBN/graphene superlattice [194], where the MLG and the hBN layers are carefully aligned. The effective Hamiltonian

of the graphene layer is given by

$$H_{\text{eff}} = \hbar v_F(\tau q_x \sigma_x + q_y \sigma_y) + \Delta \sigma_z, \tag{1.45}$$

where Δ denotes the on-site energy difference of the A and B sublattice. If $\Delta \neq 0$, a band gap opens in the spectrum at the $\pm K$ points and this leads to a finite Berry curvature [195]

$$\Omega_z(\mathbf{q}) = \mp\tau \frac{v_F^2 \Delta}{2(v_F^2 \mathbf{q}^2 + \Delta^2)^{3/2}}, \tag{1.46}$$

where $-$ $(+)$ sign applies for electron (hole) doping. One can notice that $\Omega_z(\mathbf{q})$ has opposite sign in the two valleys. By injecting a (valley unpolarized) electrical current $\mathbf{j}_e$ along the $\hat{y}$ direction, the

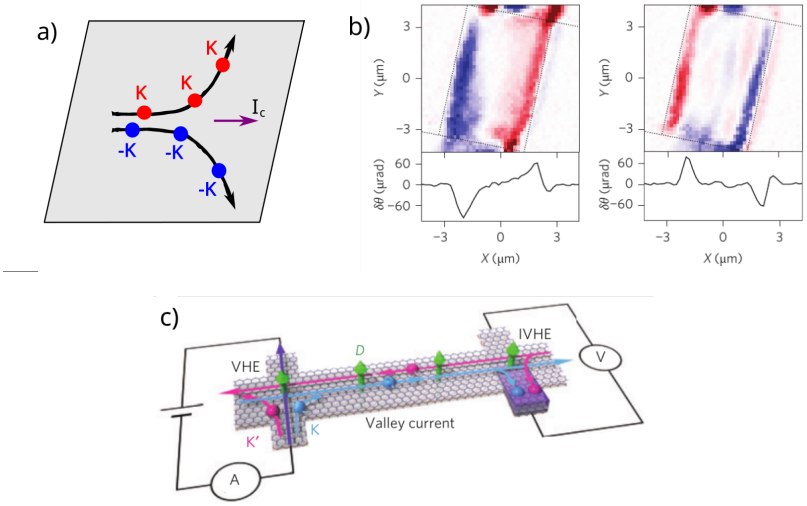

Figure 1.15: The valley Hall effect. a) Schematic picture of the VHE. **E** denotes the applied in-plane electric field. b) Kerr rotation spectroscopy of bilayer MoS_2. Thin dashed lines show the boundaries of the sample. The spatial map of the KR angle $\delta\theta$ indicates opposite valley polarization along the two edges of the sample. The comparison of the two figures suggest that the valley polarization flips when the direction of the in-plane electric field is changed. Lower figures show line cuts for $\delta\theta$. Adapted from Ref. [196]. c) Detection of the VHE in graphene using nonlocal resistance measurement. Due to the valley dependence of the Berry-curvature, the injected current at one of the terminals will lead to a valley population imbalance at a remote terminal, which can be detected due to the inverse VHE (the $-K$ valley is denoted by K' in this figure). The green arrows indicate the displacement field that is used to open a band gap in BLG. Adapted from Ref. [197].

electrons in the K and $-K$ valley will be deflected into the $\pm\hat{x}$ directions due to the anomalous velocity component, as shown schematically in Fig. 1.15(a). This leads to a transverse charge neutral valley current $\mathbf{j}_x^v = \mathbf{j}_{K,x} - \mathbf{j}_{-K,x}$, where one may define the currents $\mathbf{j}_{\tau K} = e\langle \tau \mathbf{v}(\mathbf{q}) \rangle$ as the average of the velocity operator (times the valley index τ) over $\mathbf{q}$ in the $\tau\mathbf{K}$ valleys. Because of the large separation of the K and $-K$ valleys in $\mathbf{k}$-space, the interlayer scattering is expected to be suppressed and therefore this current may extend over large distances. By writing $\mathbf{j}_x^v = \sigma_{xy}^{vH} \mathbf{E}_y$, using Eq. (1.37) and taking into account the spin-degeneracy, one finds a valley Hall conductivity $\sigma_{xy}^{vH} = 2e^2/h$ at zero temperature if E_F lies in the band gap (here σ_{xy}^{vH} is expressed in the same units as the electrical conductivity). Comparing the SHE and the VHE, it is worth noticing that the former, in general, does not require inversion symmetry breaking, while the latter does.

Experimental probes of the VHE

Based on earlier work on the SHE [198], it was proposed that the transverse valley current can be measured in a non-local setup, see Fig. 1.15(c). Far from the terminal where the electrical current is injected, $\mathbf{j}_x^v$ creates a difference $\delta\mu$ between the chemical potentials of the charge carriers in the K and $-K$ valleys which leads to a non-local voltage U_{nl} due to the inverse VHE. A large non-local resistance $R_{nl} = U_{nl}/|\mathbf{j}_e|$ was indeed measured when E_F was in the induced band gap of the MLG [194]. The same effect was later measured using BLG [199, 197], where a band gap can be opened by applying an out-of-plane electric field.

We note that the interpretation of these experimental results is not without controversy and alternative mechanism were suggested that can contribute to the non-local signal. These include possible dispersive edge states that reside close to the Dirac point in MLG/hBN structures [200] or point to the role of the spatially non-uniform gap produced by the Moiré interference pattern [201]. A recent experiment [202], which aimed to obtain local information on the current and heat distribution by using a superconducting interference device mounted on the tip of a scanning gate microscope, have lead to further surprising observations. It indicated the presence of charge accumulation and narrow conducting channels at the sample edges, thereby casting doubt on the bulk mechanism invoked in earlier works. However, the results of Ref. [202] corresponded to a single sample where the alignment between the MLG and the hBN layers was not addressed and it is unclear whether Ref. [202] is sufficient to explain all the observations of Ref. [194].

In TMDC samples the VHE was studied with the help of optoelectronic measurements. In the experiment of Ref. [203], which used monolayer MoS_2, a transverse voltage was measured when a circularly polarized light was shone one a Hall bar device. The voltage changed sign depending on whether σ^+ or σ^- polarized excitation was applied. The observation was interpreted using the valley dependent optical selection rules mentioned in Sec. 1.7.1 [see Fig. 1.14(a)]. In principle, one can induce a valley population imbalance by shining circularly polarized light on the sample. If an in-plane electric field is applied, the motion of the induced charge carriers will be affected by the Berry curvature, which is opposite in the two valleys. Because of the valley population imbalance the VHE is manifested through a charge Hall current in this setup. This is different from the transport measurement discussed above in connection with graphene, where a charge neutral valley current was induced. Although the observations were in qualitative agreement with the theoretical predictions [70], the microscopic mechanism behind the effect is not entirely clear because of the strong excitonic effects in this material.

In another recent measurement bilayer MoS_2 was used [196]. The inversion symmetry was broken by applying a backgate voltage and this gave rise to a finite Berry curvature in the $\pm K$ valleys. If a current is driven through the sample, this can lead to an accumulation of valley polarization along the edges, which can be probed by KR microscopy. Namely, as already mentioned in Sec. 1.7.1, σ^+ and σ^- polarized light selectively couples to the K and $-K$ valleys (see Fig. 1.14). Due to the valley polarization the dielectric function for the σ^+ and σ^- polarized states of light will be different. Correspondingly, a linearly polarized light will acquire a KR angle $\delta\theta$ [204]. Thus, in similar way to the measurements of the SHE in Ref. [179], the VHE and the concurrent valley accumulation can be converted into an optical effect enabling their detection. As shown in Fig. 1.15(b), the spatially resolved Kerr signal indeed indicates opposite valley polarization at opposite edges and it changes sign when the direction of the applied electric field is reversed, in agreement with the theoretical expectations.

Similarly to the case of hBN/graphene heterostructures, the interpretation of the measurements of Refs. [203, 196] relied on intrinsic properties of the TMDC band structure. Given that TMDC samples are, in general, more disordered than hBN/graphene samples, one may expect that disorder scattering should play an important role, but this has been only very recently discussed [205].

1.7.3 Coupled spin and valley Hall effect

Shortly after the isolation of monolayer MoS_2, it was suggested that p-doped monolayer TMDCs may host a combination of spin and valley Hall effects [70]. The crystal lattice of the monolayer TMDCs does not have inversion symmetry, therefore the Berry curvature is not required to vanish. Calculations of the Berry curvature based on DFT band structure calculations were already shown in Fig. 1.8. The results, which indicate a strongly enhanced Berry curvature in the $\pm K$ valleys, can be readily understood with the help of the minimal model introduced in Sec. 1.3.1. The first two terms in Eq. (1.10) have the appearance of the Hamiltonian of gapped MLG, c.f. Eq. (1.45). Looking back to the discussion in Sec. 1.7.2, this form of the effective Hamiltonian implies that there is a finite Berry curvature in the K and $-K$ valleys. Moreover, as shown schematically

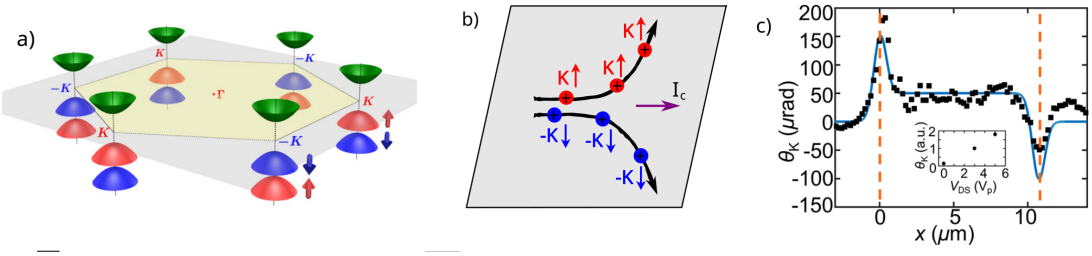

Figure 1.16: Coupled spin and valley Hall effect. a) Schematic of the band structure of monolayer TMDCs at the $\tau\mathbf{K}$ point of the BZ according to the minimal model given in Eq. (1.10). The valence band is split and spin-polarized, as indicated by the blue and red arrows. Adapted from Ref. [70]. b) Illustration of the coupled spin and valley Hall effect considering a p-doped sample. I_c denotes charge current. c) KR scans across the channel of the device in Ref. [204]. θ_K denotes the KR angle. Experimental data are indicated by black symbols, blue line shows the result of a model calculation. Adapted from Ref. [204].

in Fig. 1.16(a), the VB is split and spin-polarized due to the strong SOC. Because of the finite Berry curvature, this means that an applied electric field can give rise to a coupled spin-valley Hall effect (SVHE), which is schematically illustrated in Fig. 1.16(b). The effect is especially easy to see for moderate p-doping, when only the upper spin-orbit split VB is occupied by holes. In this case the spin σ^s_{xy} and valley σ^v_{xy} conductivities are the same, $\sigma^z_{xy} = \sigma^v_{xy} = \frac{1}{\pi}\frac{E_F}{2\Delta - \lambda_{tmdc}}$, where E_F is measured from the VB maximum [70].

The probably most convincing experimental demonstration of the SVHE can found in Ref. [204], see Figs. 1.16(c). The measurement technique was very similar to the one discussed in Sec. 1.7.2 to detect the VHE and the geometry is basically the same as the one used in Ref. [179] [see Fig. 1.11(c)]. When a charge current flows along the TMDC channel, the SVHE leads to the accumulation of spin and valley polarized carriers at the edges, which can be detected using KR spectroscopy. An important difference between the samples of Ref. [204] and Ref. [196] is that the former used monolayer WSe_2, while the latter bilayer MoS_2. Since the SOC is rather weak in the CB of bilayer MoS_2, it was assumed that in the n-doped and quite disordered samples of Ref. [196] the valley index of the carriers was more robust than the spin. Therefore Ref. [196] interpreted their experimental results in terms of the VHE. (Further discussion of the SHE and VHE in bilayer MoS_2 is presented in Chapt. 7.) In contrast, the SOC is strong in monolayer WSe_2, especially in the VB (see Chapt. 4) and therefore the spin as well as the valley should be preserved and the KR signal [Fig. 1.16(c)] was ascribed to the SVHE. Nevertheless, the rather low mobility of the sample suggests that disorder scattering was probably substantial, but its effect on the SVHE was not quantified. The analysis of the results indicated that the spin-valley polarization at the edges was around a few percent.

1.7.4 Brief overview of Hall effects

To conclude this section, it is instructive to have a brief recap of the different Hall effects mentioned in Secs. 1.5.2, 1.6.3 and 1.7.2. Although not discussed in this work, for comparison and because of their importance we also show schematic illustrations of the Hall effect (HE), quantum Hall effect (QHE), the quantum spin Hall effect (QSHE) [126] and the quantum anomalous Hall effect (QAHE) [206] in Fig. 1.17.

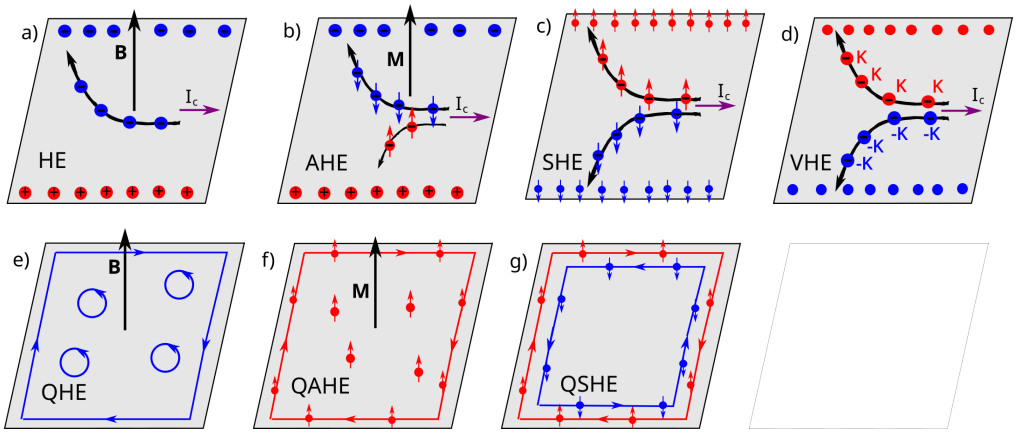

Figure 1.17: Schematics of different Hall effects. I_c denotes charge current. a) HE: charge carriers are deflected due to the Lorentz force. **B** denotes the external magnetic field. b) AHE: in ferromagnets, charge carriers with different spins are deflected due to SOC. The finite magnetization **M** means that there is an imbalance of different spins. c) intrinsic SHE: charge carriers with different spins are deflected due to SOC, which leads to spin accumulation at the edges. d) intrinsic VHE: charge carriers in different valleys are deflected due to Berry curvature, which leads to valley polarization accumulation at the edges. e) integer QHE: chiral edge state circulate the sample in strong magnetic field. f) QAHE: in magnetic topological insulators helical edge state(s) form. g) QSHE: in topological insulators pairs of counter-propagating helical edge states form.

In the case of HE, AHE, QHE and QAHE the time reversal symmetry is broken by either the external magnetic field (HE and QHE) or by the magnetization of the material (AHE and QAHE). In contrast, the time reversal symmetry is preserved for SHE, QSHE, and VHE. The presence of SOC is required for the existence of the AHE, SHE, and QSHE. The SOC leads to spin-dependent velocities and if there is difference between the populations of spin-up and spin-down electrons, as in ferromagnets, there can be a net transverse charge current leading to the AHE. If the population of different spins is the same, as in the case of SHE, then the net transverse charge current is zero. However, the transverse spin current can still be non-zero leading to spin accumulation at the edges of the sample. In the case of QSHE, pairs of counter-propagating helical edge states are formed. Regarding the VHE, it is the Berry curvature which plays the same role as the SOC for the SHE, i.e., it gives rise to a transverse charge neutral current and valley accumulation at the edges. The Berry curvature is also necessary for the intrinsic contribution to the AHE. It is important to mention that extrinsic, impurity scattering related contributions can be very important for SHE, AHE and VHE, while the QHE, AQHE and QSHE are rooted in intrinsic properties of the materials.

Considering the transverse conductivity σ_{xy}, in the case of HE and AHE it refers to the charge degree of freedom, which is a conserved quantity, while in SHE (VHE) it refers to the spin (valley) degree of freedom, which is subject to relaxation. σ_{xy} is not quantized for the effects shown in the upper row of Fig. 1.17, while it is quantized for QHE and QAHE [206] in units of e^2/h, and in units of $2e^2/h$ for QSHE [126].

Chapter 2

Structure and objectives

Atomically thin 2D materials offer an exciting opportunity to explore the interplay of spin, valley and layer degrees of freedom of charge carriers. An important objective of this thesis is to present examples of the interesting effects that are born out of this interplay. As a common thread we will use the spin, more precisely, the spin-orbit coupling in the rest of this thesis, but as we will see, the valley and layer degrees of freedom repeatedly appear in the discussions.

We start with the intrinsic SOC of ABC stacked trilayer graphene in Chapt. 3. This system provides an example of how group theory considerations, mentioned in Sec. 1.4.2, can be used to determine the general form of the SOC. We will also see that certain SOC constants can be considered as intralayer, while other as interlayer ones, indicating the importance of the layer degree of freedom. Next, in Chapt. 4 we discuss the electronic band structure of semiconductor monolayer TMDCs. We develop $\mathbf{k} \cdot \mathbf{p}$ models to describe the dispersion of the electronic bands at high symmetry points of the BZ. We also discuss the intrinsic SOC of monolayer TMDCs, which is important both for the optical and the electrical properties of these materials. Moreover, off-diagonal matrix elements of the SOC matrix, which affect certain details of the band structure, will play an important role in the induced SOC of graphene/TMDC heterostructures, which we consider in the final chapter of this thesis.

The developed $\mathbf{k} \cdot \mathbf{p}$ models can be used to study magnetic field effects in monolayer TMDCs. In Chapt. 5 we show that the degeneracy of the electronic states in the K and $-K$ valleys is broken by the magnetic field and this affects the Landau level spectrum. We also study the oscillations of the longitudinal conductance as a function of the magnetic field. By comparing our calculations with experimental results, we find that the single particle picture can be a useful starting point to interpret the measurements. However, the electron-electron interaction effects become important at low electron densities and low temperatures leading to effects that cannot be captured in single particle picture.

In most of the thesis we are concerned with bulk properties of 2D materials and their heterostructures. The one exception we make is the study of gate defined quantum dots in monolayer TMDCs in Chapt. 6. We consider single QDs to find out what kind of qubit states they can host. We also study double QDs and discuss the effects of the interplay between the strong intrinsic SOC of the TMDC host and the electron-electron interactions present in the QDs.

We touch on another topic of recent interest, namely, topological properties of materials in Chapt. 7. We investigate the properties of bilayer TMDCs and show how the interlayer coupling and the stacking order of the layers affect the Berry curvature. It is know from previous studies that the Berry curvature can give rise interesting transport phenomena, such as valley and spin Hall effects. We therefore investigate the spin and valley Hall effect in bilayer TMDCs, which presents an example for the interplay of spin, valley and layer degrees of freedom.

Finally, in Chapt. 8 we study the heterostructure of monolayer graphene with monolayer TMDCs. Here we are interested in two questions: i) the microscopic mechanism giving rise to

proximity induced SOC in graphene, and ii) the interlayer twist angle dependence of the induced SOC. We show that the strength of the induced SOC can be significantly enhanced at certain interlayer twist angles. We argue that our approach, which is based on virtual interlayer tunneling, can give insights into the physics of proximity induced SOC which cannot be easily obtained from other methodologies, such as tight binding or DFT calculations.

Chapter 3

Intrinsic spin-orbit coupling in ABC trilayer graphene

We have already mentioned in Sec. 1.6 that graphene is a good candidate for spintronics applications. However, since it is not possible to open a band gap in monolayer graphene with external gates, one cannot fabricate gate defined transport channels. BLG and ABC stacked trilayer graphene are more advantageous in this respect, because they allow the opening of a band gap by electrical gates. The understanding of SOC in few-layer graphene would be one of the first steps to study e.g., spin relaxation or weak localization in order to characterize the spin transport in gate defined channels.

Previous *ab initio* calculations on MLG [138, 207] and BLG [208] provided strong evidence that in order to understand the intrinsic SOC in *flat* graphene systems one has to go beyond the usual approach of considering only the p_z orbitals of the carbon atoms. This is sufficient to set up a TB model to describe the dispersion of the bands (see Sec. 1.2), but in the case of SOC the key step is to take into account the (nominally unoccupied) atomic d orbitals as well. As it was discussed in Ref. [163], in MLG the main contribution to the intrinsic SOC comes from the admixture of p_z orbitals with the d_{xz} and d_{yz} orbitals. The other d orbitals, namely, d_{z^2}, d_{xy} and $d_{x^2-y^2}$ play no role due to the fact that they are symmetric with respect to the mirror reflection $\sigma_h : (x, y, z) \to (x, y, -z)$, whereas p_z is antisymmetric.

Here we will derive the intrinsic SOC Hamiltonian for ABC trilayer graphene by generalizing the work of Ref. [163]. We will see that the multi-layer structure of ABC graphene plays an important role in the general form of the SOC matrix.

3.1 Calculation of the intrinsic SOC

Our aim is to calculate the non-zero matrix elements of the SOC operator $\mathcal{H}_{soc} = \lambda_{soc}\hat{\mathbf{L}} \cdot \hat{\mathbf{S}}$. We will show that the most important d orbitals to take into account are the d_{xz}, d_{yz} and d_{z^2} orbitals. While the former two have been considered in Ref. [163] in the context of monolayer graphene, the latter one is important to understand the SOC in AB stacked bilayer and ABC stacked trilayer graphene. As a first step, we will find suitable basis states by taking into account the symmetries of ABC TLG at the $\pm K$ points. They can help to simplify the calculations of the SOC matrix elements by making use of the group theory approach outlined in Sec. 1.4.3.

We have already introduced the TB model and the dispersion of the electronic bands of ABC trilayer graphene in Sec. 1.2.2. For convenience, the schematics of the lattice is displayed again in Fig. 3.1(a), while in Fig. 3.1(b) we show the most important hopping amplitudes in the TB description. The symmetries of the ABC TLG are described by the point group D_{3d}, which does not contain a horizontal mirror plane σ_h. This suggest that, in contrast to the case of MLG, all d

atomic orbitals should be considered in the discussion of the intrinsic SOC. When the d orbitals are also included into the TB basis in addition to the p_z orbitals, there will be six basis functions centered on each of the six carbon atoms in the unit cell. By describing the hopping amplitudes between the p_z and the d orbitals using, e.g., the Slater-Koster parameterization [209], one could obtain a TB Hamiltonian H_{ABC}, which would be a 36×36 matrix. After numerically diagonalizing this matrix one would find that the p_z orbitals hybridize with (some of) the d orbitals. One could then use these eigenstates to calculate the matrix elements of $\mathcal{H}_{soc}$ everywhere in the BZ. However, we are only interested in the intrinsic SOC at the $\pm K$ points of the BZ, where the low energy states can be found. Therefore the first step will be to approximately diagonalize the TB Hamiltonian H_{ABC} at the $\pm K$ points.

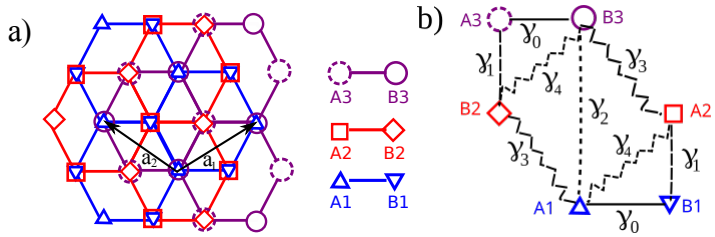

Figure 3.1: a) Schematics of the lattice structure of ABC TLG. Atoms on layer $j = \{1, 2, 3\}$ are indicated with different symbols. $\mathbf{a}_1$ and $\mathbf{a}_2$ are the two lattice vectors. b) Side view of the unit cell showing the most important TB hopping amplitudes between the p_z orbitals. Adapted form Ref. [210].

3.1.1 Basic notations

According to band theory, each state at the K point belongs to one of the irreducible representations of the small group of the K point [109], which is D_3 in this case. This group has two one-dimensional irreducible representation, denoted by Γ_{A_1} and Γ_{A_2} respectively, and a two-dimensional one denoted by Γ_E, see Table 3.1. The matrix elements of H_{ABC} between basis states corresponding to different irreducible representations of D_3 are zero [109]. In other words, for $\mathbf{k} = \tau\mathbf{K}$ the orbital Hamiltonian H_{ABC} can be block-diagonalized by choosing suitable linear combinations of atomic p_z and d orbitals such that the new basis functions transform as the irreducible representations of the group D_3. We first introduce some important notations, and then we will obtain the suitable basis states.

(D_3)	E	$2C_3$	$3C_2$
Γ_{A_1}	1	1	1
Γ_{A_2}	1	1	-1
Γ_E	2	-1	0

Table 3.1: Character table of the group 32 (D_3).

One can use as basis the Bloch wavefunctions

$$\Psi_\nu^{\eta j}(\mathbf{r}, \mathbf{k}) = \frac{1}{\sqrt{N}} \sum_n e^{i\mathbf{k}\cdot(\mathbf{R}_n + \mathbf{t}_\eta)} \Phi_\nu^j(\mathbf{r} - (\mathbf{R}_n + \mathbf{t}_\eta)), \tag{3.1}$$

where the wave vector $\mathbf{k}$ is measured from the Γ point of the BZ, $\eta j = \{A1, A2, A3, B1, B2, B3\}$ is a composite index for the sublattice $\eta = \{A, B\}$ and layer $j = \{1, 2, 3\}$ indices and Φ_ν^j denotes the atomic orbitals of type $\nu = \{p_z, d_{z^2}, d_{xz}, d_{yz}, d_{xy}, d_{x^2-y^2}\}$ in layer j. The summation runs

over all Bravais lattice vectors $\mathbf{R}_n$, whereas the vectors $\mathbf{t}_\eta$ give the position of atom η in the two-dimensional unit cell. We use a coordinate system where the primitive lattice vectors are $\mathbf{a}_1 = \frac{a}{2}(\sqrt{3},1)$ and $\mathbf{a}_2 = \frac{a}{2}(-\sqrt{3},1)$, the positions of the atoms in the unit cell are $\mathbf{t}_{A1} = \mathbf{t}_{B3} = (0,0)$, $\mathbf{t}_{A2} = \mathbf{t}_{B1} = \frac{a}{2}\left(-\frac{1}{\sqrt{3}},1\right)$ and $\mathbf{t}_{A3} = \mathbf{t}_{B2} = \frac{a}{2}\left(\frac{1}{\sqrt{3}},1\right)$ where $a = 0.246\,\mathrm{nm}$ is the lattice constant. The K and $-K$ points of the Brillouin zone can be found at $\tau\mathbf{K} = (0, \tau\frac{4\pi}{3a})$, $\tau = \pm 1$.

The small group of D_3 contains threefold rotations by $\pm 2\pi/3$ around an axis perpendicular to the graphene layers. Since the atomic orbitals $d_{xz}, d_{yz}, d_{xy}, d_{x^2-y^2}$ themselves do not possess this symmetry, instead of $\Psi_\nu^{\eta j}(\mathbf{r},\mathbf{k})$ given in Eq. (3.1) we will use Bloch states which depend on $\frac{1}{\sqrt{2}}(d_{xz} \pm i d_{yz}) \sim \mp Y_2^{\pm 1}$, $\frac{1}{\sqrt{2}}(d_{x^2-y^2} \pm i d_{xy}) \sim Y_2^{\pm 2}$ (rotating orbitals), where Y_l^m are spherical harmonics. Taking into account that $p_z \sim Y_1^0$ and $d_{z^2} \sim Y_2^0$, the Bloch states we use as basis will be denoted by $\Psi_{l,m_l}^{\eta j}(\mathbf{r},\mathbf{k})$, where $l = 1,2$ and $m_1 = 0$, whereas m_2 can take all allowed values $m_2 = -2 \ldots 2$. Often, we will need a linear combination of two of these basis functions where both of the basis functions have the same quantum number l but one of them is centered on the A sublattice and the other one is on the B sublattice, e.g., $\frac{1}{\sqrt{2}}[\Psi_{1,0}^{A1}(\mathbf{r},\mathbf{k}) - \Psi_{1,0}^{B3}(\mathbf{r},\mathbf{k})]$. As a shorthand notation, we will denote the symmetric combination of two such basis functions by $\Psi_{l,m,m'}^{j,j'}(\mathbf{r},\mathbf{k}) = \frac{1}{\sqrt{2}}[\Psi_{l,m}^{Aj}(\mathbf{r},\mathbf{k}) + \Psi_{l,m'}^{Bj'}(\mathbf{r},\mathbf{k})]$ and the anti symmetric one with $\overline{\Psi_{l,m,m'}^{j,j'}(\mathbf{r},\mathbf{k})} = \frac{1}{\sqrt{2}}[\Psi_{l,m}^{Aj}(\mathbf{r},\mathbf{k}) - \Psi_{l,m'}^{Bj'}(\mathbf{r},\mathbf{k})]$. The first upper index j in $\Psi_{l,m,m'}^{j,j'}$ always denotes the layer index of the atomic orbital on the A sublattice, the second upper index j' is the layer index for the orbital centered on the B sublattice, the first lower index l is the common angular momentum quantum number, and finally, the second and the third lower indices m, m' give the magnetic quantum number in the same manner as the upper indices give the layer index. To lighten the notation, we will usually suppress the dependence of the Bloch functions on $(\mathbf{r},\mathbf{k})$ and use the bra-jet notation, e.g., $|\Psi_{1,0,0}^{1,3}\rangle$, $|\overline{\Psi_{1,0,0}^{1,3}}\rangle$.

3.1.2 Approximate eigenstate

A group-theoretical analysis of the problem shows that by taking a suitable linear combinations of the above discussed basis functions, H_{ABC} is block-diagonal. It has two 6×6 blocks which we denote by $H_{\Gamma_{A_1}}$ and $H_{\Gamma_{A_2}}$, they correspond to basis states with Γ_{A_1} and Γ_{A_2} symmetry. Furthermore, there is a 24×24 block H_{Γ_E} corresponding to states with Γ_E symmetry. By inspection one can find that the basis states with Γ_{A_1}, Γ_{A_2} and Γ_E symmetries are those listed in Table 3.2.

Γ_{A_1}	$\lvert\overline{\Psi_{1,0,0}^{1,3}}\rangle$, $\lvert\Psi_{2,1,-1}^{3,1}\rangle$, $\lvert\Psi_{2,0,0}^{1,3}\rangle$, $\lvert\Psi_{2,-2,2}^{3,1}\rangle$, $\lvert\Psi_{2,-1,1}^{2,2}\rangle$, $\lvert\Psi_{2,2,-2}^{2,2}\rangle$
Γ_{A_2}	$\lvert\Psi_{1,0,0}^{1,3}\rangle$, $\lvert\overline{\Psi_{2,1,-1}^{3,1}}\rangle$, $\lvert\overline{\Psi_{2,0,0}^{1,3}}\rangle$, $\lvert\overline{\Psi_{2,-2,2}^{3,1}}\rangle$, $\lvert\overline{\Psi_{2,-1,1}^{2,2}}\rangle$, $\lvert\overline{\Psi_{2,2,-2}^{2,2}}\rangle$
Γ_E	$\{\lvert\Psi_{1,0,0}^{2,1}\rangle, \lvert\Psi_{1,0,0}^{3,2}\rangle\}$, $\{\lvert\overline{\Psi_{1,0,0}^{2,1}}\rangle, \lvert\overline{\Psi_{1,0,0}^{3,2}}\rangle\}$ $\{\lvert\Psi_{2,0}^{A2}\rangle, \lvert\Psi_{2,0}^{B2}\rangle\}$, $\{\lvert\Psi_{2,1}^{A2}\rangle, \lvert\Psi_{2,-1}^{B2}\rangle\}$, $\{\lvert\Psi_{2,-2}^{A2}\rangle, \lvert\Psi_{2,2}^{B2}\rangle\}$ $\{\lvert\Psi_{2,0}^{A3}\rangle, \lvert\Psi_{2,0}^{B1}\rangle\}$, $\{\lvert\Psi_{2,-1}^{A3}\rangle, \lvert\Psi_{2,1}^{B1}\rangle\}$, $\{\lvert\Psi_{2,2}^{A3}\rangle, \lvert\Psi_{2,-2}^{B1}\rangle\}$ $\{\lvert\Psi_{2,1}^{A1}\rangle, \lvert\Psi_{2,-1}^{B3}\rangle\}$, $\{\lvert\Psi_{2,-1}^{A1}\rangle, \lvert\Psi_{2,1}^{B3}\rangle\}$, $\{\lvert\Psi_{2,2}^{A1}\rangle, \lvert\Psi_{2,-2}^{B3}\rangle\}$ $\{\lvert\Psi_{2,-2}^{A1}\rangle, \lvert\Psi_{2,2}^{B3}\rangle\}$

Table 3.2: Basis functions for the irreducible representations of the small group of the K point for ABC trilayer graphene. The basis functions for the $-K$ point can be obtained by complex-conjugation.

As a concrete example let us consider $H_{\Gamma_{A_1}}$. We show how one can extract an effective basis state in which p_z atomic orbitals with large weight and d orbitals with small weights are admixed.

The basis states transforming as the irreducible representation Γ_{A_1} are shown in the first row of Table 3.2. The TB Hamiltonian $H_{\Gamma_{A_1}}$ can be further divided into 3×3 blocks:

$$H_{\Gamma_{A_1}} = \begin{pmatrix} H_{pd}^{A_1} & W^{A_1} \\ (W^{A_1})^\dagger & H_{dd}^{A_1} \end{pmatrix}. \tag{3.2}$$

Explicitly, the upper left block $H_{pd}^{A_1}$, corresponding to the basis states $|\overline{\Psi_{1,0,0}^{1,3}}\rangle, |\Psi_{2,1,-1}^{3,1}\rangle$ and $|\Psi_{2,0,0}^{1,3}\rangle$, reads

$$H_{pd}^{A_1} = \begin{pmatrix} \varepsilon_p - \gamma_2 & \frac{3}{\sqrt{2}} V_{pd\pi} & V_{pd\sigma}^{A1,B3} \\ \frac{3}{\sqrt{2}} V_{pd\pi} & \varepsilon_d & 0 \\ V_{pd\sigma}^{A1,B3} & 0 & \varepsilon_d + V_{dd\sigma}^{A1,B3} \end{pmatrix}. \tag{3.3}$$

Here ε_p and ε_d is the energy of the p_z and the d orbitals, $V_{pd\pi}$, $V_{pd\sigma}$ and $V_{dd\sigma}$ are Slater-Jouster parameters [209] and the the upper indices $A1$, $B3$ on the parameters indicate the atomic sites between which the hopping takes place. The parameter $V_{pd\pi}$ describes hopping between A and B type atoms within the same graphene layer and we assume that its value is the same in all three layers. We assume that the skew hopping between the p_z and d orbitals are much smaller than both $V_{pd\pi}$ and the vertical hopping $V_{pd\sigma}^{A1,B3}$. Then the matrix elements in W^{A_1} of the Hamiltonian (3.3) can be neglected: they describe either remote direct hoppings between the first and the third layer or skew hoppings between the p_z and d orbitals located on different atoms in different layers. (The skew hopping amplitude between the p_z orbitals on different layers are denoted by γ_3 and γ_4 in Fig. 3.1 and they will not be neglected). This is not a crucial assumption but it simplifies the lengthy algebra that follows. Therefore $W^{A_1} \approx 0$ and $H_{dd}^{A_1}$ is decoupled from $H_{pd}^{A_1}$. The matrix $H_{pd}^{A_1}$, given in Eq. (3.3) describes the hybridization between the p_z orbital based basis vector $|\overline{\Psi_{1,0,0}^{1,3}}\rangle$ and the basis vectors $|\Psi_{2,1,-1}^{3,1}\rangle$, $|\Psi_{2,0,0}^{1,3}\rangle$ involving d_{xz}, d_{yz} and d_{z^2} orbitals. The energy of the atomic d orbitals is much larger than the energy of the p_z orbitals. Since $\varepsilon_d \gg \varepsilon_p$, we next perform a transformation $\tilde{H}_{pd}^{A_1} = e^{-S} H_{pd}^{A_1} e^{S}$ to approximately block-diagonalize $H_{pd}^{A_1}$ into a 1×1 and a 2×2 block by eliminating the matrix elements between $|\overline{\Psi_{1,0,0}^{1,3}}\rangle$ on one hand and $|\Psi_{2,1,-1}^{3,1}\rangle$, $|\Psi_{2,0,0}^{1,3}\rangle$ on the other hand. (A detailed discussion of this method can be found in e.g., Ref. [63].) The matrix S is anti-Hermitian: $S^\dagger = -S$ and only its nondiagonal blocks S_{pd} and $-S_{pd}^\dagger$ are non-zero. In first order of the coupling matrix elements $V_{pd\pi}$ and $V_{pd\sigma}^{A1,B3}$ one finds that

$$S_{pd}^{(1)} = -\left(\frac{\bar{V}_{pd\pi}}{\delta\varepsilon_{pd} - \gamma_2}, \frac{V_{pd\sigma}^{A1,B3}}{\delta\varepsilon_{pd} - \tilde{\gamma}_2} \right). \tag{3.4}$$

where $\bar{V}_{pd\pi} = \frac{3}{\sqrt{2}} V_{pd\pi}$, $\delta\varepsilon_{pd} = \varepsilon_p - \varepsilon_d$ and $\tilde{\gamma}_2 = \gamma_2 + V_{dd\sigma}^{A1,B3}$. While the above transformation is usually used to obtain effective Hamiltonians, one can also obtain the new basis in which $\tilde{H}_{pd}^{A_1}$ is block-diagonal. Making the approximation[1] $e^{-S} \approx 1 - S$ we find that the purely p_z-like state $|\overline{\Psi_{1,0,0}^{1,3}}\rangle$ is transformed into

$$|\Psi_{\Gamma_{A_1}}^{p_z}\rangle = |\overline{\Psi_{1,0,0}^{1,3}}\rangle + \frac{\bar{V}_{pd\pi}}{\delta\varepsilon_{pd} - \gamma_2} |\Psi_{2,1,-1}^{3,1}\rangle + \frac{V_{pd\sigma}^{A1,B3}}{\delta\varepsilon_{pd} - \tilde{\gamma}_2} |\Psi_{2,0,0}^{1,3}\rangle, \tag{3.5}$$

i.e. it is admixed with two other basis vectors containing d_{xz}, d_{yz} and d_{z^2} orbitals. Note, however, that $\frac{\bar{V}_{pd\pi}}{\delta\varepsilon_{pd} - \gamma_2}, \frac{V_{pd\sigma}^{A1,B3}}{\delta\varepsilon_{pd} - \tilde{\gamma}_2} \ll 1$. The upper index p_z in $|\Psi_{\Gamma_{A_1}}^{p_z}\rangle$ is meant to indicate that in this state p_z

[1] The approximation $e^{-S} \approx 1 - S$ can be justified by the numerical calculations of Ref. [163]. There it was shown that in the case of monolayer graphene graphene $\frac{3}{2} \frac{V_{pd\pi}}{(\varepsilon_p - \varepsilon_d)} \approx 0.0871$. Since γ_2 is a small energy scale compared to $\delta\varepsilon_{pd} = \varepsilon_p - \varepsilon_d$, we find that $\tilde{V}_{pd\pi}/(\delta\varepsilon_{pd} - \gamma_2) \ll 1$. Furthermore, since $V_{pd\sigma}^{A1,B3}$ and $V_{dd\sigma}^{A1,B3}$ corresponds to hopping between $A1$ and $B3$ atoms which are at larger distance than the A and B atoms within the same graphene layer, one can expect that $V_{pd\sigma}^{A1,B3} < V_{pd\pi}$ and $V_{dd\sigma}^{A1,B3} \propto \gamma_2$, hence both matrix elements of $S_{pd}^{(1)}$ in Eq. (3.4) are much smaller than unity.

orbitals have the largest weight. Since $|\Psi^{p_z}_{\Gamma_{A_1}}\rangle$ corresponds to a 1×1 and hence diagonal block of $\tilde{H}^{A_1}_{pd}$, it is an approximate eigenvector of $H^{A_1}_{pd}$ with energy $\tilde{\varepsilon}_{A_1}$. The explicit expression of $\tilde{\varepsilon}_{A_1}$ is not important, one can show that $\tilde{\varepsilon}_{A_1} \gtrsim \varepsilon_p$. There are two other states with Γ_{A_1} symmetry which could be obtained by diagonalizing the the remaining 2×2 block of $\tilde{H}^{A_1}_{pd}$. In these states $|\Psi^{3,1}_{2,1,-1}\rangle$ and $|\Psi^{1,3}_{2,0,0}\rangle$ would have large weight and their energy is $\approx \varepsilon_d$. This means that they are far away in energy from $|\Psi^{p_z}_{\Gamma_{A_1}}\rangle$ and therefore play no role in our further considerations. The same applies to the states that could be obtained by diagonalizing the block $H^{A_1}_{dd}$ of $H_{\Gamma_{A_1}}$.

Similar considerations can be made for the blocks $H_{\Gamma_{A_2}}$ and H_{Γ_E} of H_{ABC}. In the end one obtains the six approximate, low-energy eigenstates of H_{ABC} shown in Table 3.3. We will refer to the basis formed from the physically important approximate eigenvectors $\{|\Psi_{\Gamma_{A_1}}\rangle, |\Psi_{\Gamma_{A_2}}\rangle, |\Psi_{\Gamma_{E_{1,1}}}\rangle, |\Psi_{\Gamma_{E_{1,2}}}\rangle, |\Psi_{\Gamma_{E_{2,1}}}\rangle, |\Psi_{\Gamma_{E_{2,2}}}\rangle\}$ as the "symmetry basis" henceforth. (The symmetry basis for the $-K$ point can be obtained by complex-conjugation.) Looking at these basis states one can see that the d_{xz}, d_{yz}, and d_{z^2} orbitals hybridize with the p_z orbital. We remind that in the case of MLG only d_{xz} and d_{yz} orbitals are admixed with the p_z orbital [163]. As it will be shown in Sec. 3.1, the admixture of d_{z^2} orbitals is crucial to obtain the non-diagonal elements of the SOC Hamiltonian.

$$
\begin{aligned}
|\Psi_{\Gamma_{A_1}}\rangle &= |\overline{\Psi^{1,3}_{1,0,0}}\rangle + \tfrac{3}{\sqrt{2}}\tfrac{V_{pd\pi}}{\delta\varepsilon_{pd}-\gamma_2}|\Psi^{3,1}_{2,1,-1}\rangle + \tfrac{\tilde{V}_{pd\sigma}}{\delta\varepsilon_{pd}-\tilde{\gamma}_2}|\Psi^{1,3}_{2,0,0}\rangle \\
|\Psi_{\Gamma_{A_2}}\rangle &= |\Psi^{1,3}_{1,0,0}\rangle - \tfrac{3}{\sqrt{2}}\tfrac{V_{pd\pi}}{\delta\varepsilon_{pd}+\gamma_2}|\overline{\Psi^{3,1}_{2,1,-1}}\rangle - \tfrac{\tilde{V}_{pd\sigma}}{\delta\varepsilon_{pd}+\tilde{\gamma}_2}|\overline{\Psi^{1,3}_{2,0,0}}\rangle \\
|\Psi_{\Gamma_{E_{1,1}}}\rangle &= |\Psi^{2,1}_{1,0,0}\rangle + \tfrac{1}{\delta\varepsilon_{pd}+\gamma_1}\left[\tfrac{V_{pd\sigma}}{\sqrt{2}}|\overline{\Psi^{2,1}_{2,0,0}}\rangle - \tfrac{3V_{pd\pi}}{2}|\overline{\Psi^{1,2}_{2,1,-1}}\rangle\right] \\
|\Psi_{\Gamma_{E_{1,2}}}\rangle &= |\Psi^{3,2}_{1,0,0}\rangle + \tfrac{1}{\delta\varepsilon_{pd}+\gamma_1}\left[\tfrac{V_{pd\sigma}}{\sqrt{2}}|\overline{\Psi^{3,2}_{2,0,0}}\rangle - \tfrac{3V_{pd\pi}}{2}|\overline{\Psi^{2,3}_{2,1,-1}}\rangle\right] \\
|\Psi_{\Gamma_{E_{2,1}}}\rangle &= |\overline{\Psi^{2,1}_{1,0,0}}\rangle + \tfrac{1}{\delta\varepsilon_{pd}-\gamma_1}\left[\tfrac{3V_{pd\pi}}{2}|\Psi^{1,2}_{2,1,-1}\rangle - \tfrac{V_{pd\sigma}}{\sqrt{2}}|\Psi^{2,1}_{2,0,0}\rangle\right] \\
|\Psi_{\Gamma_{E_{2,2}}}\rangle &= |\overline{\Psi^{3,2}_{1,0,0}}\rangle + \tfrac{1}{\delta\varepsilon_{pd}-\gamma_1}\left[\tfrac{3V_{pd\pi}}{2}|\Psi^{2,3}_{2,1,-1}\rangle - \tfrac{V_{pd\sigma}}{\sqrt{2}}|\Psi^{3,2}_{2,0,0}\rangle\right]
\end{aligned}
$$

Table 3.3: The "symmetry basis functions" (see the text for explanation) in terms of Slater-Koster parameters. Here $\tilde{V}_{pd\sigma} = V^{A1,B3}_{pd\sigma}$.

3.1.3 SOC matrix elements

We can now proceed to calculate the matrix elements of $\mathcal{H}_{soc} = \lambda_{soc}\hat{\mathbf{L}}\cdot\hat{\mathbf{S}}$. One can introduce the spinful symmetry basis functions by $|\Psi_\mu\rangle \to |\Psi_\mu\rangle \otimes |s\rangle$, where $s = \{\uparrow,\downarrow\}$ denotes the spin degree of freedom. Noting that $\mathbf{L}\cdot\mathbf{S} = L_z s_z + L_+ s_- + L_- s_+$, where $L_\pm = L_x \pm iL_y$ and $s_\pm = \frac{1}{2}(s_x \pm is_y)$, where $s_{x,y,z}$ are spin Pauli matrices, it is straightforward to calculate the matrix elements $(H^{ABC}_{soc})_{\mu,\nu} = \langle\Psi_\mu|\mathcal{H}_{soc}|\Psi_\nu\rangle$ in the symmetry basis shown in Table 3.3.

The results of the calculations are given in Table 3.4. One finds that the number of SOC constants in ABC trilayer graphene is seven. Previous calculations employed various approximations and therefore Ref. [211] found five SOC constant, while Ref. [62] used a single SOC constant. By expressing the seven SOC constants in terms of Slater-Koster parameters (see Ref. [210] for explicit expressions), one can show that $\lambda^{E_1}_{1/3}, \lambda^{E_2}_{1/3}, \lambda^{E_1}_{2/3}$ and $\lambda^{E_2}_{2/3}$ are related to interlayer SOC, i.e., they corresponds to matrix elements where the basis functions have a large weight on different layers. In this sense the layer degree a freedom affects the intrinsic SOC of ABC graphene. The $\lambda_{3/3}$ parameter ensures that the otherwise fourfold degeneracy of the high-energy split-off states at the K point (see Sec. 1.2.2) is lifted, as it is dictated by general group-theoretical considerations based on the double group representation of D_3. These five parameters are proportional to the product $V_{pd\pi}V_{pd\sigma}$ of Slater-Koster parameters and they could not be obtained considering only the d_{xz}, d_{yz}

H_{soc}^{ABC}	$\Psi_{\Gamma_{A_1}}$	$\Psi_{\Gamma_{A_2}}$	$\Psi_{\Gamma_{E_{1,1}}}$	$\Psi_{\Gamma_{E_{1,2}}}$	$\Psi_{\Gamma_{E_{2,1}}}$	$\Psi_{\Gamma_{E_{2,2}}}$
$\Psi_{\Gamma_{A_1}}$	0	$\lambda_{1/2}s_z$	$\lambda_{1/3}^{E_1}s_+$	$\lambda_{1/3}^{E_1}s_-$	$-\lambda_{1/3}^{E_2}s_+$	$\lambda_{1/3}^{E_2}s_-$
$\Psi_{\Gamma_{A_2}}$	$\lambda_{1/2}s_z$	0	$-\lambda_{2/3}^{E_1}s_+$	$\lambda_{2/3}^{E_1}s_-$	$\lambda_{2/3}^{E_2}s_+$	$\lambda_{2/3}^{E_2}s_-$
$\Psi_{\Gamma_{E_{1,1}}}$	$\lambda_{1/3}^{E_1}s_-$	$-\lambda_{2/3}^{E_1}s_-$	0	0	$\lambda_{3/3}^{z}S_z$	$\lambda_{3/3}s_+$
$\Psi_{\Gamma_{E_{1,2}}}$	$\lambda_{1/3}^{E_1}s_+$	$\lambda_{2/3}^{E_1}s_+$	0	0	$\lambda_{3/3}s_-$	$\lambda_{3/3}^{z}s_z$
$\Psi_{\Gamma_{E_{2,1}}}$	$-\lambda_{1/3}^{E_2}s_-$	$\lambda_{2/3}^{E_2}s_-$	$\lambda_{3/3}^{z}\,s_z$	$\lambda_{3/3}s_+$	0	0
$\Psi_{\Gamma_{E_{2,2}}}$	$\lambda_{1/3}^{E_2}s_+$	$\lambda_{2/3}^{E_2}s_+$	$\lambda_{3/3}s_-$	$\lambda_{3/3}^{z}s_z$	0	0

Table 3.4: Intrinsic spin-orbit Hamiltonian H_{soc}^{ABC} in the symmetry basis at the K point of the BZ.

orbitals. The remaining two SOC parameters, $\lambda_{1/2}$ and $\lambda_{3/3}^z$ are proportional to $V_{pd\pi}^2$ and describe SOC in the plane of a graphene layer. In MLG there is one intrinsic SOC parameter, here there are two, because the two carbon atoms in the top and the bottom graphene layers are not equivalent due to their different interlayer couplings.

Since the lattice of Bernal stacked BLG has the same symmetry group as the ABC trilayer, the above considerations can be easily applied to AB stacked BLG as well. The importance of the bilayer result H_{soc}^{AB} is that it can be compared with the numerical calculations of Ref. [208]. In the case of BLG, there are four SOC parameters, which we will denote by $\lambda_{\mathrm{I}2}$, λ_0, λ_4^{bi} and $\lambda_{\mathrm{I}1}$. It is useful to give their explicit expression in terms of Slater-Koster hopping parameters:

$$\begin{aligned} \lambda_0 &= 3\sqrt{3}\,\xi_d\,\frac{V_{pd\pi}V_{pd\sigma}}{\delta\varepsilon_{pd}^2-\tilde{\gamma}_1^2}\frac{\tilde{\gamma}_1}{\varepsilon_{pd}}, \qquad \lambda_{\mathrm{I}1}=\frac{9}{2}\,\xi_d\,\frac{V_{pd\pi}^2}{\delta\varepsilon_{pd}^2}, \\ \lambda_4^{bi} &= 3\sqrt{3}\,\xi_d\,\frac{V_{pd\pi}V_{pd\sigma}}{\delta\varepsilon_{pd}^2-\tilde{\gamma}_1^2}, \qquad \lambda_{\mathrm{I}2}=\frac{9}{2}\,\xi_d\,\frac{V_{pd\pi}^2}{\delta\varepsilon_{pd}^2-\gamma_1^2}, \end{aligned} \tag{3.6}$$

where ξ_d is the angular momentum resolved atomic SOC strength and $\tilde{\gamma}_1=\gamma_1+V_{dd\sigma}$. Looking at the expressions given in (3.6), one can make the following observations: (i) Since $\delta\varepsilon_{pd}=\varepsilon_p-\varepsilon_d<0$ and $\tilde{\gamma}_1>0$, one can expect that the sign of λ_0 and λ_4^{bi} will be different; (ii) $|\lambda_0|<|\lambda_4^{bi}|$ because $\frac{\tilde{\gamma}_1}{|\varepsilon_{pd}|}<1$; (iii) $\lambda_{\mathrm{I}1}$ and $\lambda_{\mathrm{I}2}$ have the same sign and they are approximately of the same magnitude because $\gamma_1^2/\delta\varepsilon_{pd}^2\ll 1$.

In order to obtain the values of the four SOC parameters of BLG, Ref. [208] used the fitting of their TB model to DFT band structure calculations. In such multi-parameter fitting it is usually difficult to ascertain whether the resulting parameter set is unique. Considerations that can give constraints on the values of the fit parameters can help to assess the result of the fitting procedure. By fitting the band structure obtained from DFT calculations, the authors of Ref. [208] found the following values for the bilayer SOC parameters: $2\lambda_{\mathrm{I}1}=24\mu$eV, $2\lambda_{\mathrm{I}2}=20\mu$eV, $\lambda_0=5\mu$eV, $\lambda_4=-12\mu$eV. These numbers are in agreement with the considerations made below Eq. (3.6). In addition, if one assumes that $V_{pd\pi}V_{pd\sigma}<0$, then according to Eqs. (3.6) three of the parameters ($\lambda_{\mathrm{I}1}$, $\lambda_{\mathrm{I}2}$, λ_0) should have the same sign, which would again agree with the results of Ref. [208]. These considerations illustrate how the approach to calculate the SOC parameters outlined in this chapter can complement other methods, such as *ab-initio* calculations.

Based on this comparison between Eqs. (3.6) and the BLG results of Ref. [208], one can also estimate the values of five of the seven SOC parameters of ABC trilayer graphene. To this end one needs to transform H_{soc}^{ABC} obtained in the symmetry basis into the the basis of effective p_z orbitals. This leads to four SOC constants λ_1, λ_2, λ_3 and λ_4 which are linear combinations of $\lambda_{1/3}^{E_1}$, $\lambda_{1/3}^{E_2}$, $\lambda_{2/3}^{E_1}$ and $\lambda_{2/3}^{E_2}$ obtained in the symmetry basis. The other three constants, $\lambda_{1/2}$, $\lambda_{3/3}$ and $\lambda_{3/3}^z$, are

not affected by the basis change. One can make the following estimates: $2\lambda_{1/2} \approx 2\lambda^z_{3/3} \approx 20\mu$eV, $|\lambda_{3/3}| \approx |\lambda_1| \approx 10\mu$eV and $|\lambda_2| \approx 5\mu$eV. We cannot estimate the values of λ_3 and λ_4 in this way because their depend on Slater-Koster parameters whose values are not known. Nevertheless, one would expect that they are much smaller than λ_1 and λ_2 because they depend on the presumably weak $p-d$ hopping between the $A1$ and $B3$ sites.

3.2 Low-energy effective description

One can neglect the weak $\mathbf{k}$ dependence of the SOC [109], and therefore the total Hamiltonian of the system can be written as $H_{ABC} = H^{ABC}_{\mathbf{k}\cdot\mathbf{p}} + H^{ABC}_{soc}$. Here $H^{ABC}_{\mathbf{k}\cdot\mathbf{p}}$ is the $\mathbf{k}\cdot\mathbf{p}$ Hamiltonian obtained without taking into account the SOC, see, e.g., Refs. [59, 60] for the explicit expression of this 6×6 matrix. Regarding transport properties, one is primarily interested in the low-energy physics, for which the use of H_{ABC} is not convenient. Namely, as it is shown in Fig. 1.3(c), this model includes four bands which are split-off from the Fermi energy of the (undoped) ABC TLG by the large energy scale $\approx \pm\gamma_1$. Employing the Löwding-partitioning method [63], one can derive an effective low-energy Hamiltonian. The two-component (including the spin, four-component) Hamiltonian $H^{\text{eff}}_{ABC} = H^{\text{eff}}_{el} + H^{\text{eff}}_{soc}$ describes the hopping between atomic sites $A1$ and $B3$ and the SOC in the low-energy subspace. We introduce the notation $\pi = -(ip_x + \tau p_y)$, where $\tau = 1(-1)$ for valley K $(-K)$ and the momenta p_x, p_y are measured from the K $(-K)$ point of the BZ. We treat γ_1 as a large energy scale with respect to $v_0\pi$, $|\gamma_3|$, γ_4, γ_2 and keep only the leading order for the terms involving γ_2, v_3 and v_4 (the velocities v_i are given by $v_i = (\sqrt{3}/2)a\gamma_i/\hbar$). The electronic part is given by

$$
\begin{aligned}
\hat{H}^{\text{eff}}_{el} &= \hat{H}_{chir} + \hat{H}_{3w} + \hat{H}_{\gamma_2} + \hat{H}_{v_4}, \\
\hat{H}_{chir} &= \frac{v_0^3}{\gamma_1^2}\begin{pmatrix} 0 & \left(\pi^\dagger\right)^3 \\ \pi^3 & 0 \end{pmatrix}, && \text{(3.7a)} \\
\hat{H}_{3w} &= -\frac{v_0 v_3}{\gamma_1}[\pi^\dagger\pi + \pi\pi^\dagger]\begin{pmatrix} 0 & 1 \\ 1 & 0 \end{pmatrix}, && \text{(3.7b)} \\
\hat{H}_{\gamma_2} &= \gamma_2\left(1 - \frac{1}{2}\frac{v_0^2}{\gamma_1^2}[\pi^\dagger\pi + \pi\pi^\dagger]\right)\begin{pmatrix} 0 & 1 \\ 1 & 0 \end{pmatrix}, && \text{(3.7c)} \\
\hat{H}_{v_4} &= -\frac{2v_0 v_4}{\gamma_1}\begin{pmatrix} \pi^\dagger\pi & 0 \\ 0 & \pi\pi^\dagger \end{pmatrix}. && \text{(3.7d)}
\end{aligned}
$$

In the derivation of Eqs. (3.7) we did not assume that π and $\pi^\dagger$ commute, therefore this form of H^{eff}_{el} is valid in the presence of an external magnetic field as well. In zero magnetic field, when $\pi\pi^\dagger = \pi^\dagger\pi = p^2$, the Hamiltonian (3.7) simplifies to the corresponding results in Refs. [59, 60]. The leading terms of the effective SOC Hamiltonian are

$$
\begin{aligned}
H^{\text{eff}}_{soc} &= H^{mlg}_{soc} + H^{(1)}_{soc}, \\
H^{mlg}_{soc} &= \tau\,\lambda_{1/2} s_z \sigma_z, && \text{(3.8a)} \\
H^{(1)}_{soc} &= -\tau\,\tilde{\lambda}_1\,\frac{v_0}{\gamma_1}\,[s^\tau_-\pi^\dagger + s^\tau_+\pi]\sigma_z. && \text{(3.8b)}
\end{aligned}
$$

Here the Pauli matrix σ_z acts in the space of $\{A1, B3\}$ sites and $\tilde{\lambda}_1 = \lambda_1 + \lambda_3(v_3/v_0) + \lambda_2(v_4/v_0) \approx \lambda_1$. The term H^{mlg}_{soc} is the well-known SOC Hamiltonian of monolayer graphene [162] and describes the leading contribution to the SOC. $H^{(1)}_{soc}$ is the most important momentum dependent term close to the τK points. One can note that $\tilde{\lambda}_1$ depends on the interlayer SOC matrix elements of the original SOC matrix of ABC TLG. In zero external magnetic field H^{eff}_{ABC} can be easily diagonalized. Similarly to MLG [162] and BLG [211, 208], the main effect of the SOC on the spectrum of ABC TLG is to open a (small) band gap while preserving the spin degeneracy of the bands.

Given the small energy scale associated with the SOC parameters, their experimental detection does not appear to be easy. It is encouraging, however, that in monolayer graphene it was possible to detect the band gap opened by the intrinsic SOC using a microwave technique [212].

3.3 Summary

In summary, we studied the intrinsic SOC in ABC trilayer graphene. Assuming that the most important contribution to the SOC in flat graphene systems comes from the admixture of p_z and d atomic orbitals and using a combination of group-theoretical and tight-binding approaches, we derived the intrinsic SOC Hamiltonian. We found that three of the five d atomic orbitals need to be taken into account: the d_{xz}, d_{yz} and d_{z^2} orbitals. We showed that the intrinsic SOC in ABC graphene is characterized by seven SOC constants. Four of them can be characterized as interlayer SOC, one SOC parameter ensures that a four-fold degeneracy of the spin-off bands is lifted and two SOC parameters describe the (slightly) different SOC on the A and B carbon atoms in the top and bottom graphene layers. The results could also be used to derive the intrinsic SOC Hamiltonian of BLG. The comparison of the obtained expressions for BLG with the results of fitting to DFT calculations [208] helped us to estimate the values of the SOC constants for ABC trilayer graphene. In order to better see the implications of these results we derived a low-energy effective Hamiltonian. This shows that the interlayer SOC parameters determine the leading momentum dependent SOC term in the effective model.

The results discussed in this chapter were published in Ref. [210].

Chapter 4

$\mathbf{k} \cdot \mathbf{p}$ Hamiltonian for monolayer transition metal dichalcogenides

As already mentioned in Sec. 1.3.1, monolayer TMDCs have a relatively complicated band structure with several extrema (valleys) both in the valence and the conduction bands, see Fig. 1.4(c). The strong interest in this material motivated that an accurate yet reasonably simple model that can describe the most important features of the band structure should be developed. Here we briefly describe the $\mathbf{k} \cdot \mathbf{p}$ approach that we used [74, 213, 214] to derive effective Hamiltonians for all important extrema of the valence and conduction bands (at the K, Q, Γ, and M points of the BZ). Once the general form of a $\mathbf{k} \cdot \mathbf{p}$ Hamiltonian is established, the material specific parameters appearing in the Hamiltonian can be obtained by analyzing various measurements probing the electrical and optical properties of the material. A faster approach, which can usually give reasonably accurate material parameters is the fitting of the $\mathbf{k} \cdot \mathbf{p}$ model to DFT band structures calculations. This approach was employed in Refs. [74, 213, 214] discussed below. These DFT calculations are, however, not subjects of this thesis.

To illustrate the main steps involved in setting up an effective $\mathbf{k} \cdot \mathbf{p}$ Hamiltonian, in Sec. 4.1 we give a brief account of a seven-band $\mathbf{k} \cdot \mathbf{p}$ model of monolayer TMDCs for the $\pm K$ points of the BZ. We will see how our model goes beyond the minimal model of Ref. [70] (see Sec. 1.3.1) and allows to understand further important details of the physics of monolayer TMDCs. The $\mathbf{k} \cdot \mathbf{p}$ model derived here will also be be used as a starting point in other chapters of this thesis. The $\pm K$ points are a relatively high symmetry point in the BZ, which makes it easier to set up a $\mathbf{k} \cdot \mathbf{p}$ model. At the end of this chapter we will consider the Q point as an example for a $\mathbf{k} \cdot \mathbf{p}$ Hamiltonian at a lower symmetry point in the BZ.

4.1 $\mathbf{k} \cdot \mathbf{p}$ Hamiltonian at the $\pm K$ point

The $\mathbf{k} \cdot \mathbf{p}$ method relies on the use of the symmetries of the crystal structure in order to determine the non-zero matrix elements of the Hamiltonian matrix $H_{\mathbf{k} \cdot \mathbf{p}}$, see Sec. 1.4.1 The two most important symmetries for our purposes are the rotational symmetry by $2\pi/3$ around an axis perpendicular to the plane of the layer (we denote it by C_3) and the reflection σ_h with respect to horizontal mirror plane that contains the metal atoms. The various matrix elements appearing in the theory are calculated with the help of Bloch wave functions of the bands that are taken into account in the model at a given BZ point. We will use the notation $|\Psi_\mu^b\rangle$ for the Bloch wave functions, where b is the band index and μ denotes the irreducible representation of the pertinent point group, which is C_{3h} in this case. Table 4.1 shows the notations of the irreps and the characters of the point group. We set up a seven-band model (without spin) which contains every band between the third band below the VB (which we denote by VB-3) and the second band above the CB (denoted

$\overline{6}\,(C_{3h})$	E	C_3	C_3^2	σ_h	S_3	$\sigma_h C_3^2$
A'	1	1	1	1	1	1
A''	1	1	1	-1	-1	-1
E_1'	1	ω	ω^2	1	ω	ω^2
E_2'	1	ω^2	ω	1	ω^2	ω
E_1''	1	ω	ω^2	-1	$-\omega$	$-\omega^2$
E_2''	1	ω^2	ω	-1	$-\omega^2$	$-\omega$

Table 4.1: Character table of the group $\overline{6}$ (C_{3h}). Here $\omega = e^{2i\pi/3}$.

by CB+2), i.e., we take the basis $\{|\Psi^{\mathrm{vb}-3}_{\mathrm{E}_2'}\rangle, |\Psi^{\mathrm{vb}-2}_{\mathrm{E}_1''}\rangle, |\Psi^{\mathrm{vb}-1}_{\mathrm{E}_2''}\rangle, |\Psi^{\mathrm{vb}}_{\mathrm{A}'}\rangle, |\Psi^{\mathrm{cb}}_{\mathrm{E}_1'}\rangle, |\Psi^{\mathrm{cb}+1}_{\mathrm{A}''}\rangle, |\Psi^{\mathrm{cb}+2}_{\mathrm{E}_1'}\rangle\}$.

Two important questions can be raised at this point:

i) What is the motivation to include seven bands in the model and not more (or less)?

ii) How can we find out which irreducible representation of the group C_{3h} is relevant for a given band at a given $\mathbf{k}$-space point?

To answer the first question, we note that a natural starting point would be to use a two-band model which includes the VB and the CB, as in in Ref. [70]. While this model can explain, e.g., the optical selection rules for the strongest excitonic transition, it turns out that it cannot describe a number of other effects. Here we briefly mention a few examples. i) Features that appear in DFT band structure calculations, such as the different effective masses in the VB and the CB or the details of the spin-splitting in the CB (see Sec. 4.1.2). In $\mathbf{k}\cdot\mathbf{p}$ theory these effects can be understood as arising from the coupling of the VB and CB to other bands. ii) The Bychkov-Rashba type SOC induced by an external electric field. We will briefly discuss this effect in Sec. 4.1.3. iii) The valley g-factor, which describes the strength of the coupling of the valley degree of freedom to a perpendicular magnetic field. This will be discussed in Chapt. 5. iv) Interesting interference effects in optical transitions are also naturally explained by going beyond the two-band model, see Ref. [215]. Therefore the choice of the number of bands is motivated by the range of physics that one wishes to describe.

Regarding the second question, many DFT codes can calculate the projection of the Kohn–Sham wave functions of each energy band onto atomic orbitals Φ_ν^η, where $\eta = \{\mathrm{M}, \mathrm{X1}, \mathrm{X2}\}$ denotes whether the given orbital is centred on the metal (M) or one of the chalcogen (X1, X2) atoms in the unit cell, and the lower index $\nu = \{s, p_x, p_y, p_z, d_{z^2}, d_{xy}, d_{xz}, d_{yz}, d_{x^2-y^2}\}$ indicates the type of the orbital. An example for such a calculation is shown in Fig. 4.1. The procedure we will follow is then similar to the one in Chapt. 3. Motivated by the fact that the system has a three-fold rotational symmetry, one may use linear combinations of these orbitals to form spherical harmonics Y_l^m. One can then consider the transformation properties of the Bloch wave functions formed with these spherical harmonics:

$$\Psi^\eta_{l,m}(\mathbf{k},\mathbf{r}) = \frac{1}{\sqrt{N}} \sum_{\mathbf{R}_n} e^{i\mathbf{k}\cdot(\mathbf{R}_n+\mathbf{t}_\eta)}\, Y_l^m(\mathbf{r} - [\mathbf{R}_n + \mathbf{t}_\eta]). \tag{4.1}$$

Here the summation runs over all lattice vectors $\mathbf{R}_n$, $\mathbf{t}_M$ and $\mathbf{t}_{X1} = \mathbf{t}_{X2}$ give the positions of the metal and chalcogen atoms in the 2D unit cell, and the wavevector $\mathbf{k}$ is measured from the Γ point of the BZ. By inspection one can then find out how the Bloch wave functions $\Psi^\eta_{l,m}(\mathbf{k},\mathbf{r})$ transform at, e.g., the $\mathbf{k} = K$ point of the BZ under the symmetry operations σ_h and C_3.

The symmetry adapted Bloch wavefunctions are listed in Table 4.2. The d atomic orbitals of the M atoms are either even ($\{d_{z^2}, d_{xy}, d_{x^2-y^2}\}$) or odd ($\{d_{xz}, d_{yz}\}$) with respect to σ_h. Similarly, one can also form linear combinations of $\Psi^{X1}_{l,m}(\mathbf{k},\mathbf{r})$ and $\Psi^{X2}_{l,m}(\mathbf{k},\mathbf{r})$ from the p orbitals of the $X1$ and $X2$ atoms which are either even or odd with respect to σ_h. The Bloch wavefunctions

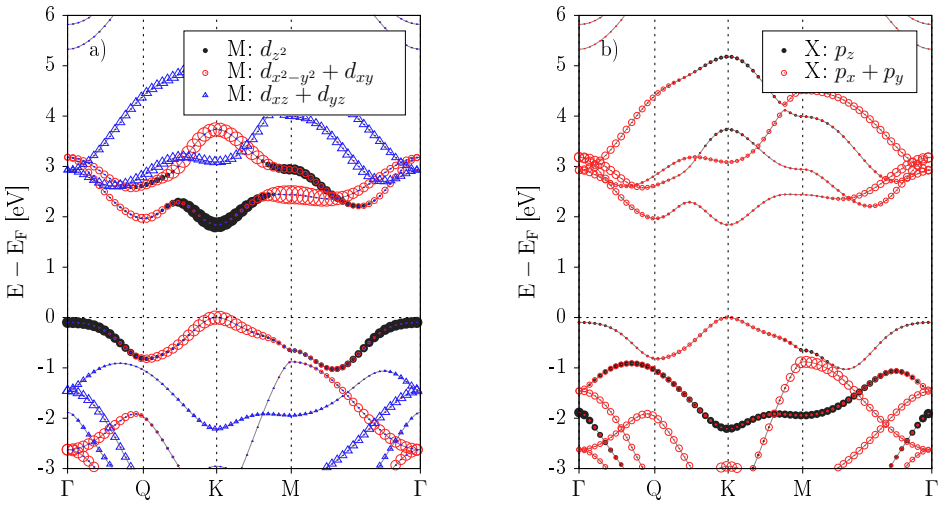

Figure 4.1: Atomic orbital weights in the energy bands of MX_2. a) d orbitals of the metal atom, and b) p orbitals of the chalcogen atoms. The size of each symbol is proportional to the weight of the atomic orbital. SOC was neglected in these calculations. Adapted from Ref. [74].

shown in Table 4.2 are also eigenstates of the rotation operation $\hat{C}_3$ with an eigenvalue $\lambda^{\eta}_{l,m}$: $\hat{C}_3|\Psi^{\eta}_{l,m}\rangle = \lambda^{\eta}_{l,m}|\Psi^{\eta}_{l,m}\rangle$. At the $\mathbf{k} = K$ or $-K$ points, $\lambda^{\eta}_{l,m}$ can take on one of the following three values: 1, $e^{i\frac{2\pi}{3}}$, $e^{-i\frac{2\pi}{3}}$. Note that $\hat{C}_3$ acts on both the spherical harmonics part $Y^m_l(\mathbf{r})$ and on the plane-wave component $e^{i\mathbf{k}\cdot(\mathbf{R}_n+\mathbf{t}_\eta)}$ in $\Psi^{\eta}_{l,m}(\mathbf{k},\mathbf{r})$ [109], because in a rotated coordinate system the vectors $\mathbf{t}_M$ and $\mathbf{t}_X$ are also transformed. Once the eigenvalues of $\hat{\sigma}_h$ and $\hat{C}_3$ with respect to $|\Psi^{\eta}_{l,m}(\mathbf{k} = \pm K, \mathbf{r})\rangle$ are known, a symmetry label, e.g., A', E' etc, of an irreducible representation of the point group C_{3h} can be assigned to each $|\Psi^{\eta}_{l,m}\rangle$. These are also listed in Table 4.2. In the single-particle picture hybridisation between different Bloch wavefunctions should preserve symmetry properties; hence, e.g., the CB at the K point can be thought of as a linear combination of $c_1|\Psi^M_{2,0}\rangle + c_2\frac{1}{\sqrt{2}}\left(|\Psi^{X1}_{1,1}\rangle + |\Psi^{X2}_{1,1'}\rangle\right)$, where c_1, c_2 are, in general, complex coefficients.

4.1.1 The $\mathbf{k}\cdot\mathbf{p}$ matrix

The $\mathbf{k}\cdot\mathbf{p}$ matrix elements, which characterise the coupling of the bands away from the $\pm K$ points, are calculated using the Hamiltonian

$$\mathcal{H}_{\mathbf{k}\cdot\mathbf{p}} = \frac{1}{2}\frac{\hbar}{m_e}(q_+\hat{p}_- + q_-\hat{p}_+) = \mathcal{H}^-_{\mathbf{k}\cdot\mathbf{p}} + \mathcal{H}^+_{\mathbf{k}\cdot\mathbf{p}}, \tag{4.2}$$

where $\hat{p}_\pm = \hat{p}_x \pm i\hat{p}_y$ are momentum operators and $q_\pm = q_x \pm iq_y$ are wavenumbers measured from the $\pm K$ point. The operator $\mathcal{H}_{\mathbf{k}\cdot\mathbf{p}}$ is symmetric with respect to σ_h: $\sigma_h^{-1}\mathcal{H}_{\mathbf{k}\cdot\mathbf{p}}\sigma_h = \mathcal{H}_{\mathbf{k}\cdot\mathbf{p}}$. Therefore non-zero matrix elements $\langle\Psi^b_\mu|\mathcal{H}_{\mathbf{k}\cdot\mathbf{p}}|\Psi^{b'}_{\mu'}\rangle$ only exist if the orbital parts of $|\Psi^b_\mu\rangle$ and $|\Psi^{b'}_{\mu'}\rangle$ are either both even or both odd with respect to σ_h. As Table 4.2 shows, both the VB and the CB are even with respect to σ_h, therefore a minimal model would use these two bands. A natural extension of this model is to include one more band, which, regarding its energy, is below the VB, and one, which is above the CB. One finds that the first even band below the VB is the VB-3 and the first even band above the CB is the CB$+2$ band. Thus we arrive at a four-band model containing $\{|\Psi^{\mathrm{vb}}_{\mathrm{A}'}\rangle, |\Psi^{\mathrm{cb}}_{\mathrm{E}'_1}\rangle, |\Psi^{\mathrm{vb}-3}_{\mathrm{E}'_2}\rangle, |\Psi^{\mathrm{cb}+2}_{\mathrm{E}'_1}\rangle\}$.

Furthermore, the matrix elements of $\mathcal{H}_{\mathbf{k}\cdot\mathbf{p}}$ are constrained by the symmetries of the states with respect to $\hat{C}_3$. In order to see how $\hat{C}_3$ constrains the matrix elements, let us consider, as an example, the states $|\Psi^{\mathrm{vb}}_{A'}\rangle$ and $|\Psi^{\mathrm{cb}+2}_{E'_2}\rangle$. The relation $\langle\Psi^{\mathrm{vb}}_{A'}|\hat{p}_+|\Psi^{\mathrm{cb}+2}_{E'_2}\rangle = \langle\Psi^{\mathrm{vb}}_{A'}|\hat{C}_3^\dagger\hat{C}_3\,\hat{p}_+\,C_3^\dagger C_3|\Psi^{\mathrm{cb}+2}_{E'_2}\rangle$ should

irrep	basis functions	band
A'	$\lvert\Psi^M_{2,-2}\rangle,\ \frac{1}{\sqrt{2}}\left(\lvert\Psi^{X1}_{1,-1}\rangle + \lvert\Psi^{X2}_{1,-1}\rangle\right)$	VB
A''	$\lvert\Psi^M_{2,1}\rangle,\ \frac{1}{\sqrt{2}}\left(\lvert\Psi^{X1}_{1,-1}\rangle - \lvert\Psi^{X2}_{1,-1}\rangle\right)$	CB+1
E'_1	$\lvert\Psi^M_{2,0}\rangle,\ \frac{1}{\sqrt{2}}\left(\lvert\Psi^{X1}_{1,1}\rangle + \lvert\Psi^{X2}_{1,1}\rangle\right)$	CB
E'_2	$\lvert\Psi^M_{2,2}\rangle,\ \frac{1}{\sqrt{2}}\left(\lvert\Psi^{X1}_{1,0}\rangle - \lvert\Psi^{X2}_{1,0}\rangle\right)$	VB−3 CB+2
E''_1	$\lvert\Psi^M_{1,0}\rangle,\ \frac{1}{\sqrt{2}}\left(\lvert\Psi^{X1}_{1,1}\rangle - \lvert\Psi^{X2}_{1,1}\rangle\right)$	VB−2
E''_2	$\lvert\Psi^M_{2,-1}\rangle,\ \frac{1}{\sqrt{2}}\left(\lvert\Psi^{X1}_{1,0}\rangle + \lvert\Psi^{X2}_{1,0}\rangle\right)$	VB−1

Table 4.2: Basis functions at the K point of the BZ for the irreducible representations of the C_{3h}. The rightmost column shows the band where a given basis function has large weight. The basis functions for the $-K$ point can be obtained by complex-conjugation. Adapted from Ref. [213].

hold. Since $\langle\Psi^{\mathrm{vb}}_{A'}|\hat{C}_3^\dagger = \langle\Psi^{\mathrm{vb}}_{A'}|$, $\hat{C}_3\hat{p}_\pm\hat{C}_3^\dagger = e^{\mp i2\pi/3}\hat{p}_\pm$ and $\hat{C}_3|\Psi^{\mathrm{cb}+2}_{E'_2}\rangle = e^{-i2\pi/3}|\Psi^{\mathrm{cb}+2}_{E'_2}\rangle$, one obtains that $\langle\Psi^{\mathrm{vb}}_{A'}|\mathcal{H}^+_{\mathbf{k}\cdot\mathbf{p}}|\Psi^{\mathrm{cb}+2}_{E'_2}\rangle = e^{-i4\pi/3}\langle\Psi^{\mathrm{vb}}_{A'}|\mathcal{H}^+_{\mathbf{k}\cdot\mathbf{p}}|\Psi^{\mathrm{cb}+2}_{E'_2}\rangle$, which means that this matrix element must vanish. By contrast, $\langle\Psi^{\mathrm{vb}}_{A'}|\mathcal{H}^-_{\mathbf{k}\cdot\mathbf{p}}|\Psi^{\mathrm{cb}+2}_{E'_2}\rangle$ is allowed to be finite and one can prove that it is a real number. In the same way all non-zero matrix elements of $\mathcal{H}_{\mathbf{k}\cdot\mathbf{p}}$ can be determined, and one finds that the $\mathbf{k}\cdot\mathbf{p}$ Hamiltonian at the K point is given by

$$H_{\mathbf{kp}} = \begin{pmatrix} \varepsilon_{vb} & \gamma_3 q_- & \gamma_2 q_+ & \gamma_4 q_+ \\ \gamma_3 q_+ & \varepsilon_{cb} & \gamma_5 q_- & \gamma_6 q_- \\ \gamma_2 q_- & \gamma_5 q_+ & \varepsilon_{vb-3} & 0 \\ \gamma_4 q_- & \gamma_6 q_+ & 0 & \varepsilon_{cb+2} \end{pmatrix}, \tag{4.3}$$

where γ_i are the matrix elements of $\mathcal{H}_{\boldsymbol{k}\cdot\boldsymbol{p}}$ in the above mentioned basis and $\varepsilon_{vb}, \varepsilon_{cb}, \varepsilon_{vb-3}, \varepsilon_{cb+2}$ are band-edge energies. The Hamiltonian in Eq. (4.3) will also be the starting point for the calculations that consider the effects of a perpendicular magnetic field in Chapt. 5.

So far we have only considered the $\mathbf{k}\cdot\mathbf{p}$ matrix elements in the basis $\{|\Psi^{\mathrm{vb}}_{\mathrm{A}'}\rangle, |\Psi^{\mathrm{cb}}_{\mathrm{E}'_1}\rangle, |\Psi^{\mathrm{vb}-3}_{\mathrm{E}'_2}\rangle, |\Psi^{\mathrm{cb}+2}_{\mathrm{E}'_1}\rangle\}$, where the basis functions are even with respect the σ_h. One could derive a similar result to Eq. (4.3) using the other, odd basis states $\{|\Psi^{\mathrm{vb}-2}_{\mathrm{E}''_1}\rangle, |\Psi^{\mathrm{vb}-1}_{\mathrm{E}''_2}\rangle, |\Psi^{\mathrm{cb}+1}_{\mathrm{A}''}\rangle\}$. But there are no matrix elements between the even and the odd block of $H_{\mathbf{k}\cdot\mathbf{p}}$, therefore the odd states, at this point, do not affect the low energy physics, which involves the VB and the CB. However, the odd bands do become important when we consider the SOC in Sec. 4.1.2.

4.1.2 Spin-orbit coupling

The next step is to take into account the intrinsic SOC. According to DFT band structure calculations [74], it is a significant energy scale both in the VB (150−400 meV) and in the CB (3−50 meV), which leads to the spin-splitting of the bands around the $\pm K$ point. One can introduce the spinful symmetry basis functions by $|\Psi^b_\mu, s\rangle = |\Psi^b_\mu\rangle \otimes |s\rangle$, where $s = \{\uparrow, \downarrow\}$ denotes the spin degree of freedom. As already explained in Sec. 1.4.3, the task is then to find the non-zero matrix elements

of the operator $\hat{\mathbf{L}}\cdot\hat{\mathbf{S}}$. Note, that this Hamiltonian can have non-zero matrix elements between even and odd states, which is due to the fact that the $\hat{L}_\pm$ operators are antisymmetric with respect to σ_h. Therefore it is natural to enlarge our basis of four even states by those odd states which, regarding their energy, lie between VB−3 and CB+2: these are $\{|\Psi^{\mathrm{vb}-2}_{\mathrm{E}''_1}, s\rangle, |\Psi^{\mathrm{vb}-1}_{\mathrm{E}''_2}, s\rangle, |\Psi^{\mathrm{cb}+1}_{\mathrm{A}''}, s\rangle\}$. Thus, we work with a basis that consists of 7 (or 14, if the spin degree of freedom is explicitly counted) basis states.

The non-zero matrix elements of $\hat{\mathbf{L}}\cdot\hat{\mathbf{S}}$ can again be obtained by considering the transformation properties of the basis states and angular-momentum operators with respect to the mirror operation σ_h and the rotation $\hat{C}_3$. To this end one may use that $\hat{\mathbf{L}}\cdot\hat{\mathbf{S}} = \hat{L}_z s_z + \hat{L}_+ s_- + \hat{L}_- s_+$, where $\hat{L}_\pm = \hat{L}_x \pm i\hat{L}_y$ and $s_\pm = \frac{1}{2}(s_x \pm i s_y)$, where $s_{x,y,z}$ are spin Pauli matrices. For the K valley one finds the result shown in Table 4.3 [214]. The matrix elements at the $-K$ point can be obtained

H^{intr}_{soc}	$\lvert\Psi^{vb}_{A'}, s\rangle$	$\lvert\Psi^{cb}_{E'_1}, s\rangle$	$\lvert\Psi^{vb-3}_{E'_2}, s\rangle$	$\lvert\Psi^{cb+2}_{E'_2}, s\rangle$	$\lvert\Psi^{vb-2}_{E''_1}, s\rangle$	$\lvert\Psi^{vb-1}_{E''_2}, s\rangle$	$\lvert\Psi^{cb+1}_{A''}, s\rangle$
$\lvert\Psi^{vb}_{A'}, s\rangle$	$s_z\Delta_v$	0	0	0	$s_-\Delta_{v,v-2}$	$s_+\Delta_{v,v-1}$	0
$\lvert\Psi^{cb}_{E'_1}, s\rangle$	0	$s_z\Delta_c$	0	0	0	$s_-\Delta_{c,v-1}$	$s_+\Delta_{c,c+1}$
$\lvert\Psi^{vb-3}_{E'_2}, s\rangle$	0	0	$s_z\Delta_{v-3}$	$s_z\Delta_{v-3,c+2}$	$s_+\Delta_{v-3,v-2}$	0	$s_-\Delta_{v-3,c+1}$
$\lvert\Psi^{cb+2}_{E'_2}, s\rangle$	0	0	$s_z\Delta^*_{v-3,c+2}$	$s_z\Delta_{c+2}$	$s_+\Delta_{c+2,v-2}$	0	$s_-\Delta_{c+2,c+1}$
$\lvert\Psi^{vb-2}_{E''_1}, s\rangle$	$s_+\Delta^*_{v,v-2}$	0	$s_-\Delta^*_{v-3,v-2}$	$s_-\Delta^*_{c+2,v-2}$	$s_z\Delta_{v-2}$	0	0
$\lvert\Psi^{vb-1}_{E''_2}, s\rangle$	$s_-\Delta^*_{v,v-1}$	$s_+\Delta^*_{c,v-1}$	0	0	0	$s_z\Delta_{v-1}$	0
$\lvert\Psi^{cb+1}_{A''}, s\rangle$	0	$s_-\Delta^*_{c,c+1}$	$s_+\Delta^*_{v-3,c+1}$	$s_+\Delta^*_{c+2,c+1}$	0	0	$s_z\Delta_{c+1}$

Table 4.3: SOC matrix of TMDCs at the K point in the seven-band model.

by taking into account the time-reversal symmetry, which dictates that the wave functions at K and $-K$ are connected by complex conjugation.

We want to make the following points regarding the SOC matrix in Table 4.3: i) In contrast to the minimal model introduced in Sec. 1.3.1, the SOC is not zero in the CB, i.e., $\Delta_c \neq 0$. This is due to the small, but finite chalcogen p-orbital weight in the CB, which can be seen in Fig. 4.1(b) and also indicated in Table 4.2. ii) Moreover, there are off-diagonal elements in the SOC matrix between certain even and odd states. Together with Δ_c, they can help to understand certain details of the DFT calculations regarding the SOC in the CB. We will briefly discuss this question in Sec. 4.1.3, after introducing the low-energy effective model. iii) As it will be shown in Chapt.8, these off-diagonal matrix elements can give rise to the Bychkov-Rashba type proximity induced SOC in graphene.

Until now we discussed the intrinsic SOC of monolayer TMDCs. Previous works on GaAs quantum wells showed that there the Bychkov-Rashba type SOC could be tuned [216, 217] by external electric gates providing an important knob to control their spin related properties. This motivated the study of the effects of a perpendicular external electric field $\mathcal{E}_z$ in monolayer TMDCs. The same basis that we used to consider the intrinsic SOC can also be used to consider the effects of a $\mathcal{E}_z$. We assume that the external electric field is homogeneous and that its strength is given by $\mathcal{E}_z$, which can be described by the Hamiltonian $U(z) = e\mathcal{E}_z z$. It breaks the mirror symmetry σ_h of the monolayer and therefore there are non-zero matrix elements between even and odd basis states of the seven-band model. The matrix elements between states of the same symmetry are zero. It can be shown that $\mathcal{E}_z$ has two effects [214]: (i) it can induce Bychkov-Rashba type SOC, and (ii) it can change the energy of the band edge. We will briefly discuss the induced Bychkov-Rashba

SOC in Sec. 4.1.3. The change in the energy of the band edge is a very small effect for realistic electric fields which can be neglected.

4.1.3 Low-energy effective Hamiltonian

In practice, working with a 7×7 (or 14×14, if the spin degree of freedom is explicitly counted) $H_{\mathbf{k}\cdot\mathbf{p}}$ Hamiltonian is not very convenient. However, in most cases one can use a low-energy effective two-band Hamiltonian that describes the dispersion of the VB and the CB and the coupling between these two bands. An effective Hamiltonian can be obtained from $H_{\mathbf{k}\cdot\mathbf{p}} + H_{\mathrm{soc}}^{intr}$ by means of Löwdin partitioning (see, e.g., Ref. [63]), which implicitly accounts for the various inter-band couplings in the original, seven-band model.

One finds that the low-energy effective Hamiltonian $H_{\mathrm{eff}}^{\tau,s} = H_0 + H_{\mathbf{k}\cdot\mathbf{p}}^{\tau,s} + H_{\mathrm{soc}}^{\tau,s}$ is the sum of three terms. The first one is the free-electron term $H_0 = \frac{\hbar^2\mathbf{q}^2}{2m_e}$. It is usually neglected in the $\mathbf{k}\cdot\mathbf{p}$ models on GaAs because of the light effective mass of this material, but in general this term can be added to the effective Hamiltonian. The second term describes the dispersion of the VB and the CB at the $\pm K$ points. $H_{\mathbf{k}\cdot\mathbf{p}}^{\tau,s}$ is given by

$$H_{\mathbf{k}\cdot\mathbf{p}}^{\tau,s} = H_{\mathrm{D}}^{\tau,s} + H_{\mathrm{as}}^{\tau,s} + H_{3w}^{\tau,s}, \tag{4.4}$$

where

$$H_{\mathrm{D}}^{\tau,s} = \begin{pmatrix} \varepsilon_{\mathrm{vb}} & \tau\cdot\gamma_{\tau,s}q_-^{\tau} \\ \tau\cdot\gamma_{\tau,s}^{*}q_+^{\tau} & \varepsilon_{\mathrm{cb}} \end{pmatrix}, \tag{4.5}$$

$$H_{\mathrm{as}}^{\tau,s} = \begin{pmatrix} \alpha_{\tau,s}\mathbf{q}^2 & 0 \\ 0 & \beta_{\tau,s}\mathbf{q}^2 \end{pmatrix}, \tag{4.6}$$

$$H_{3w}^{\tau,s} = \begin{pmatrix} 0 & \kappa_{\tau,s}(q_+^{\tau})^2 \\ \kappa_{\tau,s}^{*}(q_-^{\tau})^2 & 0 \end{pmatrix}. \tag{4.7}$$

Here $q_{\pm}^{\tau}$ is defined as $q_{\pm}^{\tau} = q_x \pm i\tau q_y$, $\varphi_{\mathbf{q}} = \arctan(q_y/q_x)$, $\varepsilon_{\mathrm{vb}}$ and $\varepsilon_{\mathrm{cb}}$ are band-edge energies, $\gamma_{\tau,s}$, $\alpha_{\tau,s}$, and $\beta_{\tau,s}$ are material parameters. Due to time-reversal symmetry these parameters depend on the product $\tau\cdot s$. Concrete values for $\gamma_{\tau,s}$, $\alpha_{\tau,s}$, $\beta_{\tau,s}$ and $\kappa_{\tau,s}$ for each MX_2 material can be obtained e.g., by fitting a DFT band structure calculations [74]. $H_{\mathrm{D}}^{\tau,s}$ is basically the massive Dirac fermion model introduced in Ref. [70] and already presented in Sec. 1.3.1. It is linear in q_+ and q_-, it describes an isotropic dispersion around the band edge and it does not break the electron-hole symmetry. The value of $\gamma_{s,\tau}$ depends on the SOC, but this dependence is weak. The diagonal Hamiltonian $H_{\mathrm{as}}^{\tau,s}$ contains terms which are quadratic in $q_{\pm}$. It breaks the electron-hole symmetry because in general $\alpha_{\tau,s} \neq \beta_{\tau,s}$. This means that in contrast to the minimal model in Eq. (1.10), the effective masses in the CB and the VB are different. We note that the observation of photoluminescence peak splitting in magnetic field [218, 219, 220, 221] indicated that electron-hole symmetry is indeed broken. Off-diagonal terms quadratic in $q_{\pm}$ appear in $H_{3w}^{\tau,s}$. In combination with $H_{\mathrm{D}}^{\tau,s}$, it leads to the trigonal warping of the energy contours, which was observed in ARPES measurements [222, 223, 224]. The trigonal warping also plays an important role in the explanation of the electroluminescence experiments of Ref. [225]. Further terms of the low energy model, which are cubic in $q_{\pm}$, are listed in Ref. [74]. This discussion indicates the limitations of the minimal model introduced in Sec. 1.3.1 in the interpretation of a number of experimental results.

The SOC of the effective model is given by the Hamiltonian $H_{\mathrm{soc}}^{\tau,s} = H_{intr} + H_{BR}$. It is the sum of H_{intr}, which stems from the intrinsic SOC, and the Bychkov-Rashba H_{BR} term, which is finite if an external electric field is applied. H_{intr} reads

$$H_{\mathrm{intr}} = \begin{pmatrix} \tau\Delta_{\mathrm{vb}}s_z & 0 \\ 0 & \tau\Delta_{\mathrm{cb}}s_z \end{pmatrix}, \tag{4.8}$$

i.e., it is diagonal in spin space. H_{intr} describes the spin-orbit splitting of the CB and the VB, which is due to the absence of inversion symmetry in monolayer TMDCs. Note that Δ_{vb} and Δ_{cb}

in Eq. (4.8) are not the same as Δ_{v} and Δ_{c} in Table 4.3. This is especially important [214] in the CB: here $\Delta_{cb} \approx \Delta_c + \frac{|\Delta_{c,c+1}|^2}{(\varepsilon_{cb}-\varepsilon_{cb+1})} - \frac{|\Delta_{c,v-1}|^2}{(\varepsilon_{cb}-\varepsilon_{vb-1})}$. Since $|\varepsilon_c - \varepsilon_{v-1}|$ is much larger than $|\varepsilon_{cb} - \varepsilon_{cb+1}|$, one may write $\Delta_{cb} \approx \Delta_c + \frac{|\Delta_{c,c+1}|^2}{(\varepsilon_{cb}-\varepsilon_{cb+1})}$. Since $\Delta_c > 0$ at the K point (the corresponding Bloch wave function is an eigenfunction of $\hat{L}_z$ with positive eigenvalue, see Table 4.2) and $(\varepsilon_{cb} - \varepsilon_{cb+1}) < 0$, Δ_{cb} can be either positive of negative, depending on whether the first of the second contribution dominates. DFT band structure calculations indeed suggest that the sign of Δ_{cb} is different in

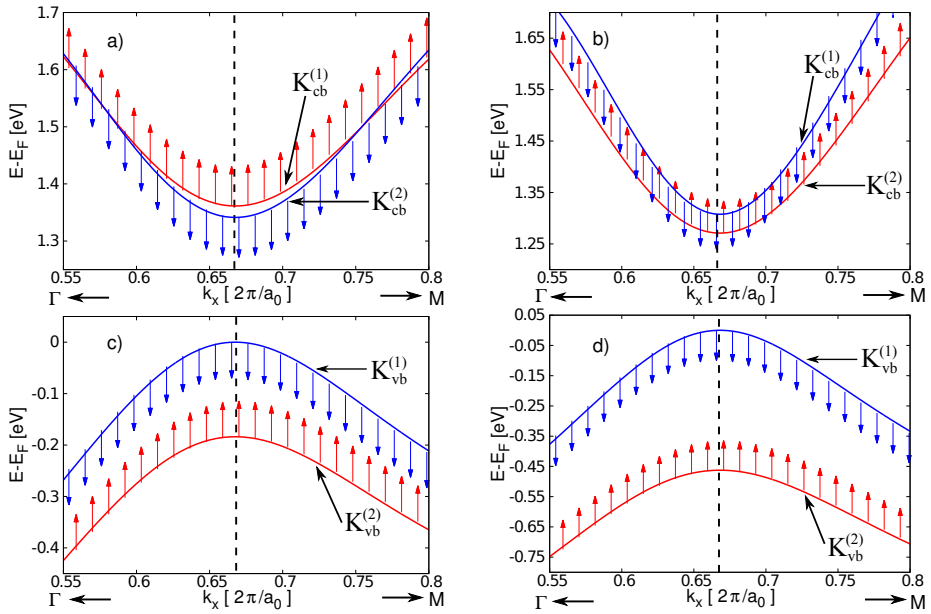

Figure 4.2: Spin polarisation and dispersion of the spin-orbit split CB and VB in the vicinity of the K point from DFT calculations. Arrows show the direction of the spin expectation values (red: spin-up, blue: spin-down). a) and c) shows the situation for MoX_2; b) and c) for WX_2 compounds. Note that the order of spin-up and spin-down bands in the CB is different for MoX_2 and WX_2. The vertical dashed line shows the position of the K point. The actual calculations were performed for $MoSe_2$ and WSe_2. Adapted from Ref. [74].

the MoX_2 and the WX_2 compounds, see Fig. 4.2. A plausible explanation for the results shown in Fig. 4.2 is that for MoX_2 materials the first, X-p orbital related term is larger, whereas in the case of WX_2, which contains a heavier metal, the second term is larger. Regarding the VB, there $\Delta_{vb} \approx \Delta_v$ and the sign is the same for both the MoX_2 and the WX_2 compounds [74].

We note that the the relative sign of Δ_{cb} and Δ_{vb} matters in optical transitions, which can be easily seen by looking at Fig. 4.2. If the sign is different, then the lowest energy exciton is bright, meaning that it can relax through photoluminescence. If the sign is the same, then the highest-energy spin-split VB and the lowest-energy spin-split CB have opposite spin polarization and optical transitions, since they preserve the spin, are not possible between these two bands. However, it may happen that the electron of the slightly higher-energy bright exciton flips its spin due to other processes and relaxes into the lower energy spin-split CB band. Since it cannot then recombine with the hole left behind in the VB leading to photoluminescence, this exciton is called dark [226, 227]. (More generally, excitonic states can also be dark because of momentum mismatch [226]). Dark excitons are important in e.g., exciton relaxation processes [228].

As one can see from Eq. (4.8), the effective intrinsic SOC Hamiltonian of both the CB and the VB are diagonal in spin-space. This is no longer the case if a perpendicular external electric field $\mathcal{E}_z$ is applied to the monolayers, which induces a Bychkov-Rashba SOC. The Hamiltonian of the Bychkov-Rashba SOC projected onto the CB can be obtained by employing the Löwdin

transformation. It reads [214]

$$\begin{aligned} H_{\mathrm{BR}}^{cb} &= \lambda_{\mathrm{BR}}^{cb,i}\left(s_y q_x - s_x q_y\right) + \lambda_{\mathrm{BR}}^{cb,r}\left(s_x q_x + s_y q_y\right) \\ &= \begin{pmatrix} 0 & (\lambda_{BR}^{cb})^* q_- \\ \lambda_{BR}^{cb} q_+ & 0 \end{pmatrix}. \end{aligned} \tag{4.9}$$

Here s_x and s_y are spin Pauli matrices. The first term in Eq. (4.9) is the well-known Bychkov-Rashba [229, 230] Hamiltonian, which is also present in GaAs and other III-V semiconductor compounds. The second term in Eq. (4.9) is also allowed by symmetry in monolayer TMDCs because the pertinent symmetry group at the K point in the presence of an external electric field is C_3, whereas it is C_{3v} in III-V semiconductor quantum wells. The Bychkov-Rashba SOC in the VB has the same form as in the CB with a different coupling constant λ_{BR}^{vb}. In terms of $\mathbf{k}\cdot\mathbf{p}$ band parameters λ_{BR}^{cb} can be estimated by [214]

$$\lambda_{BR}^{cb} \approx \frac{\gamma_3^* \xi_{v,c+1} \Delta_{c,c+1}^*}{(\varepsilon_{cb} - \varepsilon_{vb})(\varepsilon_{cb} - \varepsilon_{cb+1})}, \tag{4.10}$$

where $\xi_{v,c+1}$ is a matrix element shown of the potential $U(z) = e\mathcal{E}_z z$ describing the electric field. An estimate for the magnitude of λ_{BR} in TMDCs shows that for the electric field values of $\mathcal{E}_z \leq 10^{-2}$ V/Å, where the perturbation theory approach can be expected to work, $|\lambda_{BR}|$ is smaller by an order of magnitude than in InAs [231] or InSb [232] quantum wells. It is worth pointing out that the Bychkov-Rashba SOC given in Eq. (4.9) also appears in the so-called Janus-TMDCs [233], which possess a strong built-in electric field and therefore a much larger SOC of this form.

4.2 $\mathbf{k}\cdot\mathbf{p}$ Hamiltonian at the Q points

Similar considerations to the ones in Sec. 4.1 can be used to derive a $\mathbf{k}\cdot\mathbf{p}$ Hamiltonian for the Γ, Q and M points int the BZ as well, see Ref. [74]. These models are, in general, less developed than the one for the $\pm K$ points, because most of the theoretical and experimental attention focused on the valleytronics related physics associated with the $\pm K$ points. As an example, we now consider the six Q_i points in the CB [see Fig. 4.3(a)] which are important regarding relaxation processes. This is especially the case in the WX_2 compounds, where the energy difference between the band edge at the $\pm K$ points and at the Q_i points is relatively small [74]. This allows phonon scattering between the $\pm K$ and the Q_i valleys to be effective which affects, e.g., the electron mobility [234, 235]. The Q_i valleys also play a role in the dynamics of the K valley excitons [236]. Therefore we now briefly discuss the $\mathbf{k}\cdot\mathbf{p}$ Hamiltonian at the Q_i points. The discussion will also show how the $\mathbf{k}\cdot\mathbf{p}$ methodology and DFT calculations can complement each other in order to obtain a relatively simple and transparent model.

Due to the low symmetry of the Q_i points in the BZ and because there are many nearby bands in energy, there is a large number of $\mathbf{k}\cdot\mathbf{p}$ matrix elements that would need to be taken into account in a detailed multi-band $\mathbf{k}\cdot\mathbf{p}$ model. Such a model would therefore offer less physical insight and for this reason we use the theory of invariants [237, 238] to derive a simplified low-energy effective $\mathbf{k}\cdot\mathbf{p}$ Hamiltonian. The pertinent symmetry group is C_{1h}; for convenience, its character table is shown in Table 4.4 [109]. As an example, let us consider the Q_1 and Q_4 minima, which can be

	C_{1h}		E	σ_h
A'	$k_x^2,\ k_y^2,\ k_x k_y$	$s_z,\ k_x,\ k_y$	1	1
A''		$z,\ s_x,\ s_y$	1	−1

Table 4.4: Character table and invariants for the group C_{1h}.

found along the Γ–K and Γ–$(-K)$ directions, respectively. This direction is parallel to the k_x

component of $\mathbf{k}$. Using Table 4.4, the most general Hamiltonian, up to second-order in $\mathbf{k}$ and taking SOC into account, reads:

$$H_Q^{\tau,s} = \frac{\hbar^2 k_x^2}{2m_{Q,x}^{\tau,s}} + \frac{\hbar^2 k_y^2}{2m_{Q,y}^{\tau,s}} + \frac{\hbar^2 k_x k_y}{2m_{Q,xy}^{\tau,s}} + \Delta_Q s_z \tau_z + a_1 k_x s_z + a_2 k_y s_z + b_1 k_x \tau_z + b_2 k_y \tau_z + E_Q. \quad (4.11)$$

Here we used the following notations. The Q_i-point minima are pairwise connected by time-reversal symmetry and to describe this one can introduce the matrix τ_z, whose eigenvalues, $\tau = \pm 1$ label individual members of the pairs of valleys. $s = \pm 1$ are the eigenvalues of the spin Pauli matrix s_z. $1/m_{(Q,x,y,xy)}^{\tau,s}$ are effective masses, one can show that they depend on the product $\tau \cdot s$. E_Q is the band-edge energy if SOC is neglected, Δ_Q is the spin-splitting at the Q point, and $a_{1,2}$ and $b_{1,2}$ are material parameters. According to DFT calculations [see Fig. 4.3(b)], close to the Q point the

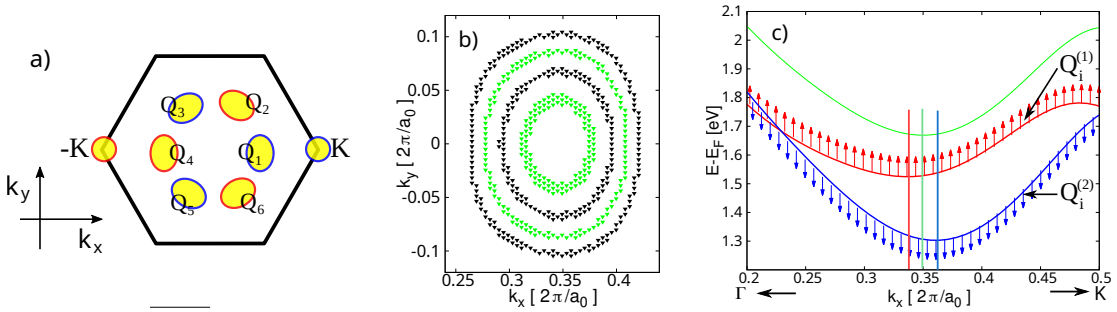

Figure 4.3: a) Schematics of the position of the $\pm K$ valleys and the six Q_i valleys in the BZ. b) Energy contours at the Q point obtained from DFT calculations for MoS_2. SOC is not taken into account. The energy difference between the energy contours is 0.04 eV. c) Band structure of WSe_2 along the Γ–K direction around the Q point with SOC (red and blue lines) and without SOC (green line). The bands without SOC are shifted in energy for clarity. Vertical bars indicate the k_x values at which the corresponding curve has a minimum. Adapted from Ref. [74].

energy contours are in a good approximation ellipses whose axes are parallel to k_x and k_y, which means that $1/m_{(Q,xy)}^{\tau,s} = 0$. The effect of the terms $\sim b_1, b_2$ in Eq. (4.11) is to shift the minimum of the dispersion, and the terms $\sim a_1, a_2$ describe the same effect but the shift can also depend on the spin polarization of the bands. Introducing the wavenumbers q_x and q_y, which are measured from $\mathbf{k} = (\tau k_Q, 0)$, i.e., from the Q_1 (Q_4) point, one can set $b_1 = b_2 = 0$ and write

$$H_Q^{\tau,s} = \frac{\hbar^2 (q_x + s_z \cdot \tilde{q}_{Q,x})^2}{2m_{Q,x}^{\tau,s}} + \frac{\hbar^2 (q_y + s_z \cdot \tilde{q}_{Q,y})^2}{2m_{Q,y}^{\tau,s}} + \Delta_Q s_z \tau_z + E_{KQ}. \quad (4.12)$$

As one can see by looking at Fig. 4.3(c), the dispersion given by Eq. (4.12) captures the most important features in the DFT band structure calculations: the bands are spin-split by the SOC, the effective masses of the spin-polarized bands are different, and the minima of dispersions of the spin-split bands are shifted, which is described by the parameters $\tilde{q}_{s,x}$ and $\tilde{q}_{Q,y}$. DFT calculations indicate that $\tilde{q}_{Q,y}$ is zero and $\tilde{q}_{Q,x}$ always very small [74].

4.3 Summary

In summary, we presented the derivation of $\mathbf{k} \cdot \mathbf{p}$ Hamiltonians at high symmetry points of the BZ of monolayer TMDCs. Firstly, we set up a seven-band model (fourteen-band model, if the spin-degree is explicitly counted) for the $\pm K$ points, which takes into account the coupling between the VB and CB as well as couplings of these two bands to other, in energy more remote bands. We

used this model to obtain an effective two-band model that describes the dispersion and the SOC in the CB and the VB. We pointed out the implications of our model with respect to a previously derived minimal model and also how it can give a plausible explanation for the different spin-orbit splitting in the CB of MoX_2 and WX_2 materials. Besides the effects of the intrinsic SOC, we discussed the Bychkov-Rashba SOC as well and showed that the BR Hamiltonian contains an extra term compared to the corresponding Hamiltonian valid for III-V semiconductors. As a second example for $\mathbf{k} \cdot \mathbf{p}$ approach, we derived a Hamiltonian to describe the dispersion of the CB at the Q_i points. We directly wrote down the terms that are allowed by symmetry in the Hamiltonian and showed how the general form of the Hamiltonian can be simplified by taking into account the results of DFT calculations.

The results discussed in this chapter were published in Refs. [74, 213, 214]. A further work [239], closely related to the low-energy effective Hamiltonian in Eq. (4.4) but not discussed in this thesis, considered the edge states in finite samples.

Chapter 5

Shubnikov-de Haas oscillations in monolayer TMDCs

Magnetic field is an important tool to probe material properties. For example, the Shubnikov-de Haas (SdH) oscillations can provide information about the cross-sectional area of the Fermi surface and the effective mass of the carriers. The measurement of the SdH oscillations of the longitudinal resistance were performed in boron-nitride encapsulated mono– and few-layer MoS_2 [240, 241] and in mono– and bilayer WSe_2 [242]. Furthermore, the magnetic field breaks the degeneracy of the electronic states in the inequivalent K and $-K$ valleys of the BZ. This is due to the fact the electronic states in K and $-K$ valleys are related by time-reversal symmetry (TRS). Therefore, if TRS is broken by the magnetic field, the degeneracy of the states can be lifted. In commonly reachable magnetic fields the energy difference between the K and $-K$ valley states is rather small, of the order of few meV. Because of the disorder broadening of the electronic states, for a long time it was difficult to resolve such a small energy scale in transport experiments, but this has recently become possible [241]. On the other hand, optical techniques, such as magnetoluminescence[218, 221, 220, 219, 243], were also used to obtain information on the valley degeneracy breaking.

Here we first briefly overview the most important steps to calculate the Landau level (LL) spectrum in monolayer semiconductor TMDCs using a multi-band $\mathbf{k}\cdot\mathbf{p}$ model. We then use the LL spectrum and the self-consistent Born approximation to calculate the SdH oscillations of the longitudinal conductance σ_{xx}. This can help to understand many features of recent magnetotransport measurements, but the experimental results also indicate the limitations of this approach when electron-electron interaction effects become important.

5.1 Landau levels in monolayer TMDCs

We consider monolayer TMDCs, where the band edge can be found at he $\pm K$ points of the BZ. As already mentioned in Sec. 1.4.4, in order to take into account the effects of a perpendicular magnetic field $\mathbf{B}_z$ in a $\mathbf{k}\cdot\mathbf{p}$ Hamiltonian, one may use the co-called Kohn-Luttinger prescription. This means that one can replace the wavenumbers $\mathbf{q} = (q_x, q_y)$ appearing in the seven-band $\mathbf{k}\cdot\mathbf{p}$ model introduced in Sec. 4.1 by operators $\hat{\mathbf{q}}$: $\mathbf{q} \to \hat{\mathbf{q}} = \frac{1}{i}\nabla + \frac{e}{\hbar}\mathbf{A}$, where $\mathbf{A}^T = (0, B_z x, 0)$ is the vector potential in Landau gauge and $e > 0$ is the magnitude of the electron charge. We note that it is important to perform the Kohn-Luttinger prescription in the original, seven-band model, which contains the wavenumbers q_x, q_y in linear-order, and not in an effective low-energy model where products of q_x, q_y appear in certain terms. This is because the operators $\hat{q}_x$, $\hat{q}_y$ do not commute and therefore their order is important.

Since working with a seven-band model is not very convenient, one may want to obtain an effective model $H_{\text{eff}}^{\tau,s}$ that involves fewer bands and describes the physics in the CB and the VB.

This can be again done using Löwdin-partitioning method [63]. The original seven band $\mathbf{k}\cdot\mathbf{p}$ model depended on the wavenumbers $q_\pm = q_x \pm i q_y$. Therefore, in the process of obtaining the low-energy effective Hamiltonian one has to take care because the operators $\hat{q}_+ = \hat{q}_x + i\hat{q}_y$ and $\hat{q}_- = \hat{q}_x - i\hat{q}_y$ do not commute: $[\hat{q}_-, \hat{q}_+] = \frac{2eB_z}{\hbar}$, where B_z is the strength of the magnetic field and $[\ldots]$ denotes the commutator. In this way one can obtain, e.g., an 2×2 (4×4 if spin is taken into account) effective Hamiltonian $H_{\text{eff}}^{\tau,s}(B_z)$ that corresponds to Eq. (4.4) derived for zero-magnetic field. The explicit form of $H_{\text{eff}}^{\tau,s}(B_z)$ is given in Ref. [244]. Taking $B_z > 0$ for concreteness, the operators a and $a^\dagger$ defined as $\hat{q}_- = \frac{\sqrt{2}}{l_B} a$, $\hat{q}_+ = \frac{\sqrt{2}}{l_B} a^\dagger$, where $l_B = \sqrt{\hbar/(eB_z)}$ is the magnetic length, satisfy the bosonic commutation relation $[a, a^\dagger] = 1$. Therefore one can calculate the matrix elements of $H_{\text{eff}}^{\tau,s}$ in a large, but finite harmonic oscillator basis and diagonalize the resulting matrix to obtain the spectrum. An example for such a calculation is shown in Fig. 5.1. One can notice that the LLs

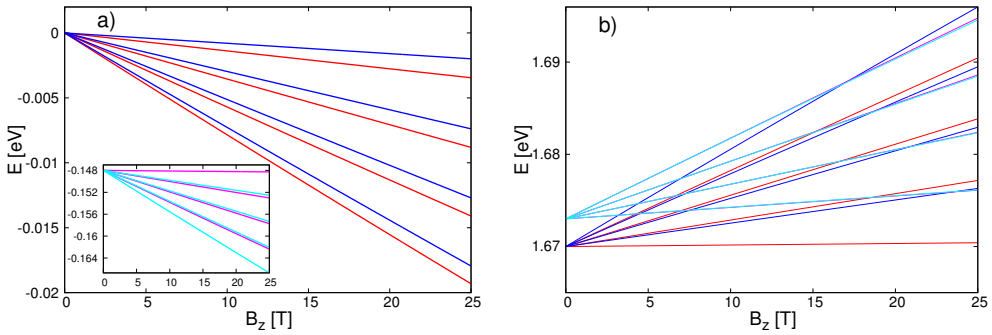

Figure 5.1: Numerically calculated LL spectrum of monolayer MoS_2. a) The first few LLs in the higher spin-orbit split VB. Red lines: the K valley ($\tau = 1$), blue lines: the $-K$ valley ($\tau = -1$). The inset shows the LLs in the lower spin-orbit split VB. b) The first few LLs in the CB. LLs both in the lower spin-orbit split band and in the higher spin-orbit split band are shown. Red and purple lines: the K valley, blue and cyan: the $-K$ valley. For the calculations we used the material parameters given in Ref. [74]. Adapted from Ref. [244].

in different valleys are not degenerate. The magnitude of this *valley degeneracy breaking* (VDB) is different in the VB and CB and for the lower-in-energy and higher-in-energy spin-orbit split bands. One can also observe that in the CB the lowest LL is in valley K, whereas in the VB it is in valley $-K$. We note that LL calculations based on the minimal model of Eq. (1.10) do not capture the VDB and hence, as we will see in Sec. 5.3, they are in contradiction with experimental measurements.

The results shown in Fig. 5.1 were obtained using a model that describes the low-energy physics in the subspace spanned by the VB and CB and takes into account the coupling between these two bands explicitly. One may perform a further Löwdin partitioning step to obtain an effective model that corresponds to the CB or the VB alone. One finds that the LL energies are given by

$$E_{n,\text{vb}}^{\tau,s} = \varepsilon_{\text{vb}}^{\tau,s} + \hbar\omega_{\text{vb}}^{(\tau,s)}\left(n + \frac{1}{2}\right) + \frac{1}{2} g_e \mu_B B_z s + \frac{1}{2} g_{vl,\text{vb}}^{(s)} \mu_B B_z \, \tau, \tag{5.1a}$$

$$E_{n,\text{cb}}^{\tau,s} = \varepsilon_{\text{cb}}^{\tau,s} + \hbar\omega_{\text{cb}}^{(\tau,s)}\left(n + \frac{1}{2}\right) + \frac{1}{2} g_e \mu_B B_z s + \frac{1}{2} g_{vl,\text{cb}}^{(s)} \mu_B B_z \, \tau. \tag{5.1b}$$

Here $n = 0, 1, 2, \ldots$ is an integer denoting the LL index, $\varepsilon_{\text{vb(cb)}}^{\tau,s} = \varepsilon_{\text{vb(cb)}} + \tau\Delta_{\text{vb(cb)}} s_z$ are the band edge energies in the VB (CB) for a given spin-orbit split band s, $\omega_{\text{vb\,(cb)}}^{(\tau,s)} = \frac{eB_z}{m_{\text{vb\,(cb)}}^{(\tau,s)}}$ are cyclotron frequencies, where $m_{\text{vb\,(cb)}}^{(\tau,s)}$ are effective masses in the VB (CB). The second term, which corresponds to a harmonic oscillator spectrum, is due to the fact that in the simplest approximation

the dispersion is parabolic at the band edge and this leads to a harmonic oscillator spectrum in quantizing magnetic field. The third term is the Zeeman coupling of the spin degree of freedom to the magnetic field with the free-electron g-factor $g_e \approx 2$. The spin-index s to be used in the evaluation of this term follows from the spin-polarization of the given spin-orbit split band, see Fig. 4.2. The VDB is described by the last term in Eqs. (5.1). As one can see, the VDB is *linear* in magnetic field. The strength of the coupling of the valley degree of freedom to the magnetic field are given by the valley g-factors $g^{(s)}_{vl,\mathrm{vb}}$ and $g^{(s)}_{vl,\mathrm{cb}}$. As indicated by the subscript vb and cb, they are, in general, different in the VB and the CB. One can show that they depend on the (virtual) inter-band transitions to higher energy bands that have been projected out. The valley g-factors can be expressed in terms of the band-structure parameters $\alpha_{\tau,s}$, $\beta_{\tau,s}$ and $\gamma_{\tau,s} \approx \gamma$ discussed in Sect. 4.1.3 and the band gaps $E^{\downarrow}_{\mathrm{bg}}$, $E^{\uparrow}_{\mathrm{bg}}$ corresponding to the spin-orbit split bands. One finds that

$$g^{(s)}_{vl,\mathrm{vb}} = 4\frac{m_e}{\hbar^2}\left(\alpha_s + \frac{|\gamma|^2}{E^{(s)}_{bg}}\right), \tag{5.2a}$$

$$g^{(s)}_{vl,\mathrm{cb}} = 4\frac{m_e}{\hbar^2}\left(\frac{|\gamma|^2}{E^{(s)}_{bg}} - \beta_s\right). \tag{5.2b}$$

Using Eqs. (5.1), the valley splitting can be written as $\delta E^{(i)}_{cb(vb)} = g^{(i)}_{\mathrm{eff},cb(vb)}\mu_B B_z$ where the effective g-factor is given by $g^{(i)}_{\mathrm{eff},cb(vb)} = (g_e s\tau + g^{s}_{vl,cb(vb)})$ and $i = 1(2)$ denotes the higher-in-energy (lower-in-energy) spin-orbit split band, see Fig. 5.2 (note, that the spin polarization in the CB is different in MoX_2 and WX_2 compounds, see Sec. 4.1.3). The effective g-factors $g_{\mathrm{eff},cb(vb)}$ can be calculated once the band-structure parameters appearing Eq. (5.2) are determined by, e.g., fitting the $\mathbf{k}\cdot\mathbf{p}$ model to DFT band-structure calculations. As an example, we show the results of such calculations for monolayer MoS_2 and WSe_2 in Table 5.1, which are based on the material parameters given in Ref. [74]. As one can see from Eqs. (5.2), $g^{(s)}_{vl}$ depends explicitly on the band-

	$E^{\downarrow}_{\mathrm{bg}}$	$E^{\uparrow}_{\mathrm{bg}}$	$g^{\downarrow}_{vl,\mathrm{vb}}$	$g^{\uparrow}_{vl,\mathrm{vb}}$	$g^{(1)}_{\mathrm{eff},\mathrm{vb}}$	$g^{(2)}_{\mathrm{eff},\mathrm{vb}}$	$g^{\downarrow}_{vl,\mathrm{cb}}$	$g^{\uparrow}_{vl,\mathrm{cb}}$	$g^{(1)}_{\mathrm{eff},\mathrm{cb}}$	$g^{(2)}_{\mathrm{eff},\mathrm{cb}}$
MoS_2										
DFT	1.66 eV	1.838 eV	0.98	0.96	−1.02	2.96	−2.11	−2.05	−0.05	−4.11
GW	2.8 eV	2.978 eV	2.57	2.38	0.57	4.38	−0.52	−0.6	1.4	−2.52
WSe_2										
DFT	1.337eV	1.766eV	−0.38	−0.23	−2.38	1.77	−2.71	−2.81	−4.71	−0.81
GW	2.457eV	2.886eV	2.55	1.9	0.55	3.9	−0.67	0.13	−2.67	2.13

Table 5.1: Valley g-factors in MoS_2 and WSe_2. In the first row the g-factors are obtained using the DFT band gap, in the second row the g-factors are calculated with a band gap taken from *GW* calculations. Adapted from Ref. [244].

gap $E^{(s)}_{bg}$ of a given spin s. It is known that $E^{(s)}_{bg}$ is underestimated in DFT calculations, therefore we calculate two sets of $g^{(s)}_{vl}$: the first one using $E^{(s)}_{bg}$ from DFT and the second one using $E^{(s)}_{bg}$ extracted from more advanced GW calculations. The results shown in Fig. 5.1 were obtained with the former parameter set. As shown in Table 5.1, the calculated g-factors depend quite significantly on the choice of the parameter set, we expect that the g-factors obtained by using the DFT and the GW parameter sets should bracket the actual experimental values.

5.2 Shubnikov-de Hass oscillations of the longitudinal conductivity

The results in Sec. 5.1 provide the starting point for the calculation of the SdH oscillations of the magnetoconductance in monolayer TMDCs. The calculations, detailed in Ref. [244], rely on two main assumptions. The first one is that one can neglect inter-valley scattering and also intra-valley scattering between the spin-orbit split bands. One can argue that in the VB, if no magnetic impurities are present, for realistic values of E_F the inter-valley scattering should be strongly suppressed because it would also require a simultaneous spin-flip, since the bands are spin-polarized. In the CB, especially if E_F is high enough so that electronic states in both spin-orbit split CB bands are occupied, the inter-valley scattering is not forbidden by spin selection rules. However, one can expect that it should be suppressed due to the large momentum transfer that it would require. On the other hand, the intra-valley scattering between the spin-split bands in the CB should be absent due to the specific form of the intrinsic SOC. The second assumption is that we only consider the effect of random disorder potential $V(\mathbf{r})$ with short range correlations $\langle V(\mathbf{r})V(\mathbf{r}')\rangle = \lambda_{sc}\delta(\mathbf{r}-\mathbf{r}')$. This assumption is widely used in the interpretation of SdH oscillations, as it facilitates to obtain analytical results [245]. We note that according to Refs. [240, 246], evidence for the presence of short range scatterers in monolayer MoS_2 has indeed been recently found. While short-range scatterers can, in general, cause inter-valley scattering, a recent study shows that the scattering probability for this process is low [247].

Using these assumptions it is straightforward to extend the theory of Ando [245] to the SdH oscillations of monolayer TMDCs. Ando's theory was developed for a two-dimensional electron gas with parabolic dispersion and short-range scatterers. As it has been shown above, the LLs in monolayer TMDCs can be described by a formula which is the same as for a simple parabolic band except that it contains a term which describes a linear-in-magnetic field valley-splitting. Since we assume that one can neglect inter-valley and intra-valley inter-band scattering, the total conductance will be the sum of the conductances of individual bands with valley and spin indices τ, s. This simple model allows us to focus on the effects of the intrinsic SOC and valley degeneracy breaking on the SdH oscillations.

We treat impurity scattering in the self-consistent Born approximation (SCBA) and use the Kubo-formalism to calculate the longitudinal conductivity σ_{xx} (for a recent discussion see, e.g., Refs. [248, 249]). The complex self-energy of the charge carriers due to the impurity scattering is denoted by $\Sigma_R^{\tau,s} = \Sigma_r^{\tau,s} + i\Sigma_i^{\tau,s}$. For short range scatterers $\Sigma_R^{\tau,s}$ in a given band (τ, s) does not depend on the LL index n. It is given by the implicit equation

$$\Sigma_r^{\tau,s} + i\Sigma_i^{\tau,s} = \frac{\lambda_{sc}}{2\pi l_B^2}\sum_{n=0}^{\infty}\frac{1}{E - E_n^{\tau,s} - (\Sigma_r^{\tau,s} + i\Sigma_i^{\tau,s})}, \tag{5.3}$$

where $E_n^{\tau,s}$ is the energy of the LLs given by Eqs (5.1a)-(5.1b). We note that the term $\lambda_{sc}/2\pi l_B^2$ on the right-hand side of Eq. (5.3) can be written as $\frac{\lambda_{sc}}{2\pi l_B^2} = \frac{1}{2\pi}\hbar\omega_c^{(i)}\frac{\hbar}{\tau_{sc}^i}$, where $1/\tau_{sc}^{(i)} = \lambda_{sc}m^{(i)}/\hbar^3$ is the scattering rate calculated in the Born-approximation in zero magnetic field.

The self-energy are then used to calculate the disorder-averaged retarded $G_R^{\tau,s}$ and advanced $G_A^{\tau,s}$ Green's functions. They are given by $G_{R,A}^{\tau,s}(n,E) = [E - E_n^{\tau,s} - \Sigma_{R,A}^{\tau,s}]^{-1}$ and they are diagonal in the indices τ, s. Moreover, in the LL representation they are also diagonal in the LL index n. The conductivity $\sigma_{xx}^{\tau,s}$ in a single valley and band is then calculated as

$$\sigma_{xx}^{\tau,s} = \frac{e^2}{\pi^2\hbar}\int dE\left(-\frac{\partial f(E)}{\partial E}\right)\sigma_{xx}^{\tau,s}(E), \tag{5.4}$$

where $f(E)$ is the Fermi function and

$$\sigma_{xx}^{\tau,s}(E) = (\hbar\omega_c^{(i)})^2\sum_{n=0}^{\infty}(n+1)\mathrm{Re}[G_A^{\tau,s}(n,E)G_R^{\tau,s}(n+1,E) - G_A^{\tau,s}(n,E)G_A^{\tau,s}(n+1,E)]. \tag{5.5}$$

The total conductivity is then given by $\sigma_{xx} = \sum_{\tau,s} \sigma_{xx}^{\tau,s}$, where the summation runs over occupied sub-bands for a given total electron (hole) density n_e (n_h). As shown in Fig. 5.2, in p-doped samples there is one occupied band per valley, while for n-doping there can be two occupied bands per valley.

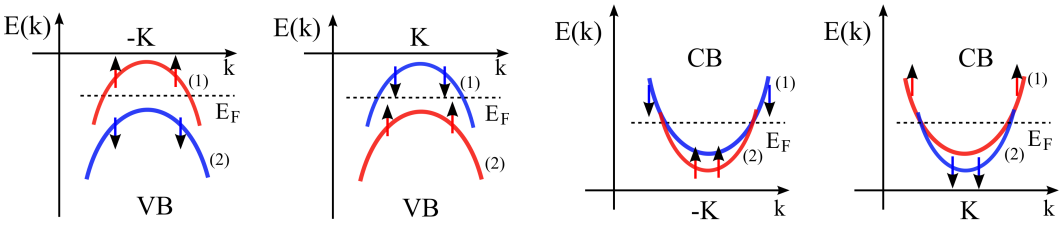

Figure 5.2: Schematics of the dispersion in the VB and in the CB around the K and $-K$ points of the band structure. The spin-orbit split bands are denoted by red and blue lines, different colours indicate different spin-polarization. The arrows show the spin-polarization for MoS_2. For typical values of p (n) doping, E_F (denoted by a dashed line) would intersect only the upper spin-orbit split band in the VB (both spin-orbit split bands in the CB). The index (1) and (2) denote the upper and lower spin-split band.

In general, one has to determine $\Sigma_R^{\tau,s}$ by solving Eq. (5.3) numerically. In particular, this is the case if there are only a few occupied LLs below the Fermi energy, either because of the low electron density or because of the high magnetic field. In the so-called semiclassical limit, when there are many occupied LLs below E_F, i.e., $\hbar\omega_c^{(i)} \ll E_F$, one can derive an analytical result for $\sigma_{xx}^{\tau,s}$, see Refs. [245, 248] for the details of this calculation. Assuming that only a single spin-orbit split band is occupied in each of the valleys, which is, practically, always the case for p-doped samples, one finds

$$\sigma_{xx}/\sigma_0 = \frac{2}{1+(\omega_{\rm vb}^{(1)}\tau_{sc}^{(1)})^2}\left[1 - \frac{4(\omega_{\rm vb}^{(1)}\tau_{sc}^{(1)})^2}{1+(\omega_{\rm vb}^{(1)}\tau_{sc}^{(1)})^2} e^{-\frac{\pi}{(\omega_{\rm vb}^{(1)}\tau_{sc}^{(1)})}} \cos\left(\frac{2\pi E_F}{\hbar\omega_{\rm vb}^{(1)}}\right)\mathcal{A}_1\,\mathcal{B} + \frac{g_{\rm eff}^{(i)}}{2}\frac{\mu_B B_z}{E_F}\frac{4(\omega_{\rm vb}^{(1)}\tau_{sc}^{(1)})^2}{1+(\omega_{\rm vb}^{(1)}\tau_{sc}^{(1)})^2} e^{-\frac{\pi}{(\omega_{\rm vb}^{(1)}\tau_{sc}^{(1)})}} \sin\left(\frac{2\pi E_F}{\hbar\omega_{\rm vb}^{(1)}}\right)\mathcal{A}_2\,\mathcal{B}\right]. \tag{5.6}$$

Here $\sigma_0 = \frac{e^2\tau_{sc}^{(1)}}{2\pi\hbar^2}E_F = \frac{e^2\tau_{sc}^{(1)}}{m_{\rm vb}^{(1)}}\frac{n_h}{2}$ is the zero field conductivity per single valley and band, n_h is the total charge density and we assumed $\Sigma_r^{\tau,s} \ll \Sigma_i^{\tau,s} \ll E_F$. The amplitudes $\mathcal{A}_{1,2}$ and $\mathcal{B}$ are given by

$$\mathcal{A}_1 = \cos\left(\frac{\pi}{2}g_{{\rm eff},vb}^{(1)}\frac{m_{\rm vb}^{(1)}}{m_e}\right), \qquad \mathcal{A}_2 = \sin\left(\frac{\pi}{2}g_{{\rm eff},vb}^{(1)}\frac{m_{\rm vb}^{(1)}}{m_e}\right), \tag{5.7}$$

and

$$\mathcal{B} = \frac{2\pi^2 k_B T/\hbar\omega_{\rm vb}^{(1)}}{\sinh\left(2\pi^2 k_B T/\hbar\omega_{\rm vb}^{(1)}\right)}, \tag{5.8}$$

where k_B is the Boltzmann constant and T is the temperature. One can see that Eqs. (5.6)-(5.8) are similar to the well known expression derived in Ref. [245] for a 2DEG. The valley-splitting, which leads to the appearance of the amplitudes $\mathcal{A}_{1,2}$, plays an analogous role to the Zeeman spin-splitting in 2DEG. The term proportional to $\mu_B B_z/E_F$ in Eq. (5.6) is usually much smaller than the first term. The amplitude $\mathcal{B}$ in Eq. (5.8) is the so-called Dingle-factor and describes the temperature dependent damping of the conductivity oscillations.

As an example, a fit of the oscillatory part of Eq. (5.6) to the measurement results of Ref. [242] performed in p-doped monolayer WSe_2 is shown in Figure 5.3. The theoretical results were fitted

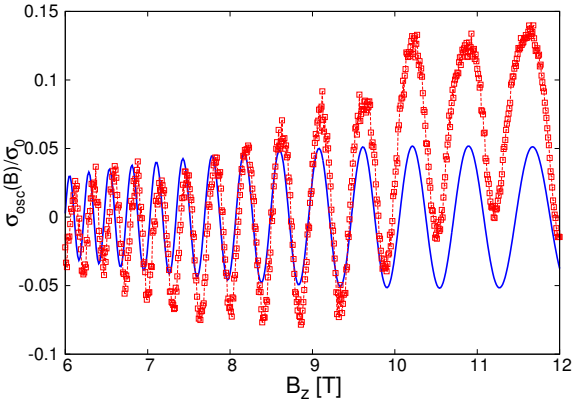

Figure 5.3: Experiment results of Ref. [242] (red) and the theoretical fit (blue).

in the range $6 - 10\,\mathrm{T}$. Once the amplitude $\mathcal{A}_1$ is extracted from the fit, one can also obtain $g^{(1)}_{eff,\mathrm{vb}}$ if the effective mass $m^{(1)}_{\mathrm{vb}}$ is known. In Ref. [242] the $m^{(1)}_{\mathrm{vb}}$ was extracted by measuring the temperature dependence of the SdH oscillations amplitude [see Eq. (5.8)] and it was found that $m^{(1)}_{\mathrm{vb}} = -0.45 m_e$, where m_e is the free electron mass. From the fitted value of $\mathcal{A}_1^{fit}$ the effective g-factor is calculated as $g^{(1)}_{\mathrm{eff,vb}} = \pm 2.52$. The magnitude is in reasonable with the theoretical value shown in Table 5.1, the sign of the $g^{(1)}_{\mathrm{eff,vb}}$ cannot be determined from the SdH measurements.

As already mentioned, Eq. (5.6) was derived for charge densities where only one spin-orbit split subband is occupied in each of the K and $-K$ valleys. For strong n-doping one can reach the regime where both spin-orbit split bands are occupied. This was indeed the case in the measurements on n-doped monolayer MoS_2, which will be discussed in Sect. 5.3. An expression similar to Eq. (5.6) can be derived for this situation [244] as well. Since the bands are spin-polarized, the total conductance is simply given by the sum of the conductances coming from the two spin-orbit split sub-bands: $\sigma_{xx} = \sigma^{(1)}_{xx} + \sigma^{(2)}_{xx}$. The analysis shows that the intrinsic SOC can affect the amplitude of the oscillations and it also leads to a phase difference between the oscillations coming from the two spin-orbit split sub-bands.

Finally, we briefly comment on the relevance of the other valleys in the band structure for the SdH oscillations in monolayer TMDCs. Regarding p-doped samples, the Γ point is significantly lower in energy than the $\pm K$ point, therefore it is unlikely to affect the SdH oscillations for realistic dopings. The situation might be more complicated for n-doped samples, especially for WS_2 and WSe_2. For these two materials the states in the six Q valleys are likely to be close in energy with the states in the $\pm K$ valleys. Therefore the Q valleys could be populated for finite n-doping and contribute to the SdH oscillations.

5.3 Interactions and magnetotransport in monolayer MoS_2

Transport measurements in monolayer TMDCs were for a long time affected by the relatively low mobilities (strong disorder) of the samples. This made the comparison between theoretical and experimental results difficult. Recently, new fabrication techniques have made it possible to obtain much higher quality samples [250, 251, 252, 241], and therefore magnetotransport measurements can be more directly compared to the theoretical calculations. It turns out that in cleaner samples electron-electron interaction effects, which were neglected in Sec. 5.2, become important, especially at low temperatures.

That interactions may play a significant role should not come as a surprise. The importance of the electron-electron interaction effects is indicated by the dimensionless Wigner-Seitz radius

$r_s = 1/(\sqrt{\pi n_e} a_B^*)$. Here n_e is the electron density, $a_B^* = a_B(\kappa m_e/m^*)$ is the effective Bohr radius, m^* is the effective mass, κ is the dielectric constant and a_B is the Bohr radius. In the experiments of Ref. [241] discussed below, the value of r_s was in the range of $r_s = 9.8 - 7.5$, meaning that the system is in a regime where interactions are important [253, 111]. Compared to e.g., the 2DEG in GaAs quantum wells, the effective mass in monolayer TMDCs is much larger, which leads to a larger Wigner-Seitz radius. This means that the ratio of the average kinetic energy and the Coulomb energy of the electron gas is smaller in monolayer TMDCs than in GaAs quantum wells, indicating the relative importance of interaction effects in the former system.

To illustrate the complex interplay of the energy scales related to electron-electron interaction, disorder and temperature, we start the discussion by comparing the magnetoconductance data measured in n-doped monolayer MoS_2 at two different temperatures, $T = 100\,\mathrm{mK}$ and $T = 1.7\,\mathrm{K}$, see Fig. 5.4. The longitudinal resistance was recorded in a four-terminal setup as a function of

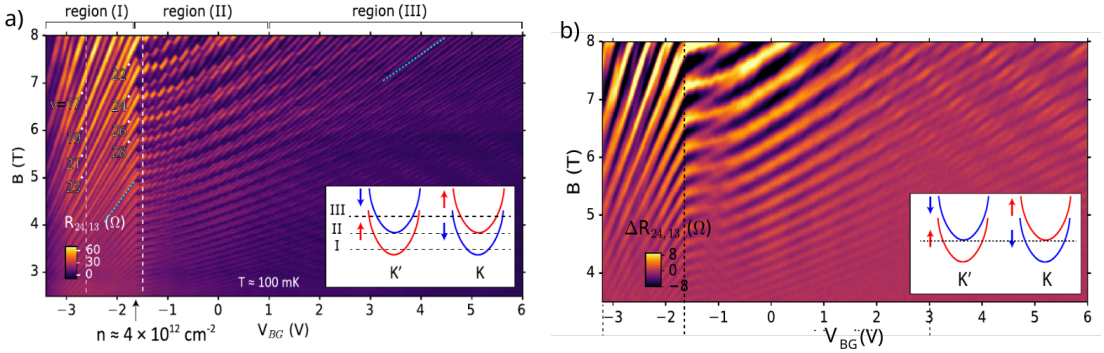

Figure 5.4: SdH measurements in monolayer MoS_2. (a) Four-terminal resistance $R_{24;13}$ as a function of the backgate V_{BG} and magnetic field at $T \approx 100$ mK. One can see a pronounced change in the slope (cyan dashed lines) of the Landau fan diagram at $V_{BG} \approx -1.6$ V, corresponding to electron density $n_e \approx 4 \times 10^{12}$ cm^2 (black arrow). The Landau fan diagram can be divided into three different regions: (I) $V_{BG} < -1.6$ V, (II) $-1.6 < V_{BG} < 1$ V, and (III) $V_{BG} > 1$ V. Inset: Sketch of the conduction band minima at the K and $-K$ valleys in the first Brillouin zone of monolayer MoS_2 (The $-K$ valley is denoted by K' in this figure). Because of the strong spin-orbit interaction, the spin degeneracy is lifted and spin and valley degrees of freedom are locked. Black dashed lines represent the Fermi energy corresponding to regions (I), (II), and (III), respectively. (b) The same as in (a) but measured at $T \approx 1.7$ K. The vertical dashed line indicates the backgate voltage at which the upper spin-orbit split CB starts to fill, see the inset. Adapted from Ref. [241].

perpendicular magnetic field B_z and backgate voltage V_{BG}. At $T = 100\,\mathrm{mK}$ a rather complex structure of brighter and darker ridges, corresponding to higher and lower resistance can be observed [Fig. 5.4(a)]. As V_{BG} (i.e., n_e) is changed, three regions can be distinguished, they will be discussed in more details below. Although at $T = 1.7\,\mathrm{K}$ [Fig. 5.4(b)] many of the details that can be seen at $T = 100\,\mathrm{mK}$ are washed out, the main features remain quite robust. It is these main features that can be explained by an extended single particle picture [251, 254]. In this picture electron-electron interaction effects are accounted for by assuming i) an electron density *dependent* valley g-factor g_{vl}, and ii) in good approximation electron density *independent* effective mass m^*. (We note that a weaker dependence of m^* on the electron density than that of the spin-susceptibility was predicted in Ref. [253]). With these additional assumptions one can make use of the results of Sec. 5.2 to interpret the measurements shown in Fig. 5.4.

We now discuss the measurements taken at $T = 1.7\,\mathrm{K}$ [Fig. 5.4(b)]. To understand how the results of Sec. 5.2 can be useful, note that in linear order the measured resistivity oscillations $\delta\rho_{xx}$ are given by the oscillations $\delta\sigma_{xx}$ of the conductivity [255]. For small amplitudes of the oscillations

$\delta\rho_{xx}/\rho \ll 1$ therefore one can use Eq. (5.6) to write

$$\delta\rho_{xx} \propto -R_0 \exp\left(-\frac{\pi}{\omega_{cb}\tau_q}\right)\cos\left(\frac{2\pi\nu_e}{d}\right)\cos\left(\pi\frac{E_{vz}}{E_c}\right). \tag{5.9}$$

Here R_0 is related to the zero field resistance, τ_q is the quantum scattering time, $\nu = \frac{hn_e}{eB_z}$ is the filling factor, n_e is the electron density, h is the Planck's constant and $d = 2$ stands for the two valleys, each hosting a band that is non-degenerate in spin. Moreover, $E_c = \hbar\omega_{cb}$ and $E_{vz} = g_{vl}\mu_B B_z$ are the cyclotron and the valley Zeeman energy, respectively. Although Eq. (5.6) was derived having p-doped samples in mind, it can also be used for n-doped samples as long as there is only one spin non-degenerate occupied band in each of the valleys. Amplitude factors that are smooth functions of the magnetic field in Eq. (5.6) are not explicitly taken into account in Eq. (5.9), it is a common practice that a smooth background is subtracted from the measurements. The term $\cos\left(\pi\frac{E_{vz}}{E_c}\right)$ is the amplitude factor $\mathcal{A}_1$ given in Eq. (5.7). The term $\sim \frac{g_{\rm eff}^{(i)}}{2}\frac{\mu_B B_z}{E_F}$ appearing in Eq. (5.6) is neglected because it is expected to be small for the magnetic field range used in these measurements.

Note, it follows from Eq. (5.9) that if $E_{\rm vz}/E_{\rm c}$ is approximately even (odd), the minima in $\delta\rho_{xx}$ should be at even (odd) ν, as sketched in Fig. 5.5(a). Indeed, measurements in Fig. 5.5(b) for $n_{SdH} = 3.8 * 10^{12}{\rm cm}^{-2}$ and $n_{SdH} = 4.3 * 10^{12}{\rm cm}^{-2}$ show minima at even and odd filling factors, respectively. A transition even→odd or odd→even ν minima can happen if $g_{\rm vl}$ is electron density dependent due to interaction effects. The transition corresponds to the case when $E_{\rm vz}/E_{\rm c}$ becomes a half integer, i.e., $\frac{m^* g_{\rm vl}}{2m_e} = l + 1/2$, where $l = 0, 1, 2\ldots$. However, Eq. (5.9) cannot be valid for densities close to the transition because it would imply vanishing $\delta\rho_{xx}$. Looking at the SdH oscillation trace measured at $n_{tr}^{(1)} = 3.0 * 10^{12}{\rm cm}^{-2}$ and $n_{\rm tr}^{(2)} = 4.1 * 10^{12}{\rm cm}^{-2}$ [see Fig. 5.5(b)], it is also clear that $\delta\rho_{xx}$ cannot be described by a single harmonic in the inverse magnetic field $1/B$. In order to gain further insight, we calculated $\delta\rho_{xx}$ numerically using Eqs. (5.3)-(5.5). The comparison of the measurements and the calculated SdH curves is shown in Fig. 5.5(b) for several densities. We used $g_{\rm vl}$, $\tau_{\rm q}$ and R_0 as adjustable parameters to reproduce the lineshape and the amplitude of the oscillations. As one can see, a qualitatively good agreement can be obtained between the calculations and the measurements made at $T \approx 1.7\,{\rm K}$. We found that for densities close to $n_{\rm tr}^{(1)}$ the lineshape of the oscillations depends quite sensitively on whether one assumes the same $\tau_{\rm q}$ for both valleys. A much better agreement between calculations and measurements was found using different valley scattering times $\tau_{K,q}$ and $\tau_{-K,q}$. Assuming $g_{\rm vl} > 0$, we found that $\tau_{K,q} < \tau_{-K,q}$, implying that the scattering time is shorter for the valley where, at a given total density $n_{\rm SdH}$ and $E_{\rm F}$, the charge density is lower due to the valley Zeeman effect and the concomitant charge re-distribution between the valleys. The $g_{\rm vl}$ values that gave the best fits were density dependent and we found $g_{\rm vl} > 10$ for all densities considered. This suggests a significant enhancement of the magnitude of $g_{\rm vl}$ due to electron-electron interaction as compared to the single particle values calculated in Sec. 5.1.

Furthermore, as indicated in Fig. 5.4(a) with cyan dashed lines [one in region (I), the other in region (III)], there is a change in the slope of the SdH minima by about a factor of two. Such a change can be expected if the density of states doubles. Additional data not shown here indicates that the Hall mobility μ and the four terminal resistance $\rm R_{24,13}$ at zero magnetic field exhibit a pronounced change in slope at the same point. One can attribute these observations to the occupation of the upper spin-orbit split bands in the K and $-K$ valleys, as shown schematically in the insets of Fig. 5.4. The sudden change in the slope of the SdH minima happens for $n_{tr}^{(2)} \approx 4.1 * 10^{12}{\rm cm}^{-2}$. Assuming a 2D density of states $DOS = m^*/\pi\hbar^2$ (implying a two-fold degeneracy corresponding to the valley), using the experimentally determined effective mass of $m^* = 0.65m_e$ and the density $n_{tr}^{(2)}$, one can calculate that the Fermi energy is $E_F \approx 15\,{\rm meV}$ when the upper spin-orbit split bands start to be filled. This gives us an estimate of the intrinsic spin-orbit interaction $2\Delta_{cb}^*$ for K-valley electrons in monolayer MoS_2. This value of $2\Delta_{cb}^*$ is about five times larger than the results of DFT band structure calculations [74]. The apparent enhancement of the spin-

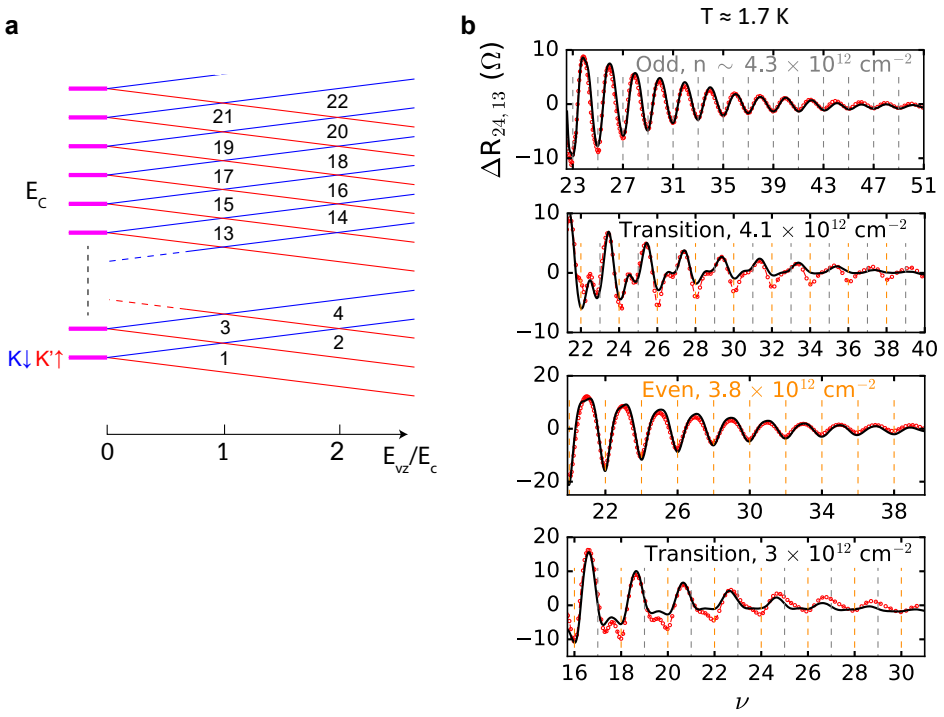

Figure 5.5: Density dependent g-factor in monolayer MoS_2. (a) LL structure highlighting the interplay between even and odd filling factors as $E_{\mathrm{vz}}/E_{\mathrm{c}}$ increases. Even (odd) $E_{\mathrm{vz}}/E_{\mathrm{c}}$ corresponds to even (odd) filling factor sequence. The red and blue lines indicate valley $-K$ spin-up and valley K spin-down LLs (the $-K$ valley is denoted by K' in this figure). (b) Measurements of the four terminal resistance $\Delta R_{24,13}$ at $T \approx 1.7K$, after subtracting a smooth background, as a function of LL filling factors at different electron densities (black solid line). By increasing the electron density, one can see transitions between even and odd filling factor sequences in the minima. Red dotted lines represent numerical calculations using Eqs. (5.3)-(5.5). Adapted from Ref. [241].

orbit splitting of the bands might be due to an exchange interaction driven band renormalization. Moreover, as shown in Fig. 5.5(b), although the upper spin-orbit split bands start to be filled, at $T \approx 1.7\,\mathrm{K}$ the measurements can still be fitted nicely assuming that only the lower spin-orbit split bands give visible contributions to the SdH oscillations.

The effect of the LLs corresponding to the upper spin-orbit split bands become apparent at lower temperatures. One can see the distinctive "waviness" of the lines in Fig. 5.4(a) measured at $T \approx 100\,\mathrm{mK}$. Comparison with Fig. 5.4(b) suggests, that LLs corresponding to the lower spin-orbit split bands are affected by the LLs originating from the upper spin-orbit split bands. The interaction effects start to be visible already at $T \approx 500\,\mathrm{mK}$. For $V_{BG} > 3\,\mathrm{V}$, corresponding to high densities, one can observe a string of bright spots surrounded by fainter lines that show clear anticrossings, see Fig. 5.6(a). It is tempting to interpret the bright spots as crossings between LLs residing in the same valley but belonging to different spin-orbit split bands, while the resolved anticrossings may be due to LLs belonging to different valleys, as shown in Fig. 5.6(b). This interpretation is motivated by the extended single particle picture. Due to the spin-orbit coupling, LLs in different valleys and different spin-orbit split bands should have the same spin-polarization and therefore they can anticross e.g., due to exchange interaction induced band repulsion. On the other hand LLs residing in the same valley but different spin-orbit split bands would have different spin polarization and therefore they can cross. These observations (and others not discussed here) clearly indicate that the single particle picture becomes insufficient at very low temperatures.

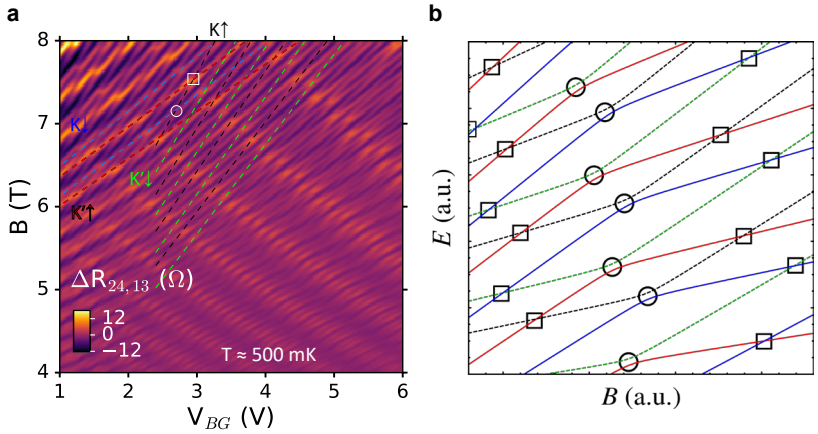

Figure 5.6: Interaction effects in the LL spectrum of monolayer MoS_2 . (a) $\Delta R_{24,13}$ measurements as a function of V_{BG} and magnetic field in region (III) at $T \approx 500\,\mathrm{mK}$. For $V_{BG} > 3\,\mathrm{V}$, by increasing the electron density one can observe both crossings (bright spots) and anticrossings between LLs. For $V_{BG} < 3\,\mathrm{V}$, the bright spots appear to be weak anticrossings between not fully spin polarized LLs. (b) Schematic of the LL interaction effects in the CB of monolayer MoS_2. LLs residing in the same valley can cross (squares). LLs residing in different valleys and different spin-orbit split bands anticross (circles). Adapted from Ref. [241].

5.4 Summary

In summary, we calculated the Landau level spectrum of monolayer TMDCs by making use of the $\mathbf{k} \cdot \mathbf{p}$ model developed in Chapt. 4. We found that the LLs in the K and $-K$ valleys are not degenerate. This valley degeneracy breaking is linear in the magnetic field and can be characterized by an effective valley g-factor. We then used the LL spectrum to extend previous results for the Shubnikov-de Haas oscillations of the longitudinal magnetoconductance σ_{xx} to the case of monolayer TMDCs. In particular, we considered the effects of valley degeneracy breaking and the intrinsic SOC of the TMDCs on σ_{xx}. Our results relied on single-particle considerations and they proved to be useful in the interpretation of the SdH measurements in monolayer MoS_2 for temperatures $1 < T \lesssim 1.7\mathrm{K}$. However, the measurement also gave clear indications that the single-particle picture is not sufficient at lower temperatures and at low dopings, when the signatures of strong electron-electron interactions become apparent. The electron-electron interaction leads to, e.g., avoided crossings between LLs and further theoretical work is needed to understand the LL phenomena in this regime.

The results of Secs. 5.1-5.2 were published in Ref. [244], while the discussions of Sec. 5.3 can be found in Ref. [241]. A further work [218], not discussed in this thesis, studied experimentally and theoretically the valley degeneracy breaking in magnetoluminescence. It was one of the first reports [218, 221, 220, 219, 243] of this phenomenon. The theoretical considerations in [218] relied on calculations similar to those in Sec. 5.1.

Chapter 6

Quantum dots in monolayer TMDCs

We have already mentioned in Sec. 1.3.3 that one can use electrostatic gates to create quantum dots in TMDCs. This is in contrast to MLG, where confinement of the charge carriers by electrostatic gates is not possible. Compared to III-V semiconductors, such as GaAs [256, 85], TMDCs have several isotopes with vanishing nuclear spin, thus lacking hyperfine interactions with the electronic spin. This means that TMDC based QDs may offer a platform to host qubits with longer coherence time than III-V semiconductors. Moreover, monolayer TMDCs comprise an additional valley pseudospin. Although these two features (i.e., isotope with vanishing nuclear spin and valley pseudospin) are common to several other materials, such as Si/SiGe quantum wells [257, 258], carbon nanotubes [259, 260], or BLG [94, 95, 96], what sets monolayer TMDCs apart is that they host strong spin-orbit coupling as well.

First, we consider a simple model for QDs defined by electrostatic gates in monolayer TMDCs. Note, that the typical size of such nanostructure (several tens of nanometers) and the presence of the confining potential means that, e.g., DFT calculations would be impracticable for this problem. However, one can make use of the $\mathbf{k}\cdot\mathbf{p}$ approach introduced in Chapt. 4. We also take into account the effect of external magnetic field and show that the interplay of magnetic field and confinement provides a possible realization of combined spin-valley qubits. We then discuss double quantum dots (DQDs) and in particular, the effects of strong SOC and Coulomb interaction on the low-energy states.

6.1 Single quantum dot in the non-interacting limit

We assume n-doped samples and make use of the $\mathbf{k}\cdot\mathbf{p}$ Hamiltonian obtained for the $\pm K$ point of the BZ, where the band edge can be found in monolayer TMDCs. We will be interested in the magnetic field dependence of the QD spectrum and discuss which eigenstates can be used as two-level systems for qubits. We consider relatively small QDs, which can be treated in the ballistic limit.

As already mentioned in Chapter 5, the effective Hamiltonian of the CB in external magnetic field can be obtained in two steps: first making the Kohn-Luttinger prescription in the seven-band model, followed by projecting out all other bands using the Löwdin-partitioning. The resulting Hamiltonian can be cast into the following form:

$$H_{cb} = \tau\Delta_{cb}s_z + \frac{\hbar^2\hat{q}_+\hat{q}_-}{2m_{\text{eff}}^{\tau,s}} + \frac{1}{2}g_{\text{eff},cb}\mu_B B_z. \tag{6.1}$$

Here the operators are defined as $\hat{q}_\pm = \hat{q}_x \pm i\hat{q}_y$, where $\hat{\mathbf{q}} = \frac{1}{i}\nabla + \frac{e}{\hbar}\mathbf{A}$, and $\mathbf{A}$ is the vector potential describing the magnetic field, see Sec. 5.1. Moreover, $m_{\text{eff}}^{\tau,s}$ is the effective mass and $g_{\text{eff},cb}$ is the valley g-factor. One may add the Bychkov-Rashba type SOC H_{BR}^{τ} (see Sect. 4.1.2) to H_{cb}, but since it introduces a relatively small energy scale, it can be treated as a perturbation. One can

take into account the electrostatic confinement by adding the term $V_{\rm dot}(r)$ to H_{cb}, so that the Hamiltonian reads $H_{\rm dot} = H_{cb} + V_{\rm dot}(r)$.

As a simple example, we consider a circular QD with hard wall boundary conditions, because their spectrum can be obtained relatively easily and can illustrate some important features of the spectrum of more general cases. The confinement is described by the potential $V_{dot}(r) = 0$ for $r \leq R_d$ and $V_{dot}(r) = \infty$ if $r > R_d$. In order to preserve the rotational symmetry of the system around the z axis one may use the axial gauge to describe the magnetic field, where $A_\phi = B_z r/2$ and $A_r = 0$. H_{dot} then commutes with the angular momentum operator $\hat{L}_z$ and the eigenfunctions of H_{dot} will be eigenfunctions of $\hat{L}_z$ as well. Therefore a quantum number $l = 0, \pm 1, \pm 2, \ldots$ can be assigned to the eigenvalues and eigenfunctions.

In order to find the eigenfunctions and eigenvalues of H_{dot}, one may re-write the operators $\hat{q}_\pm$ in cylindrical coordinates and introduce the operators $\hat{\alpha}_\pm$ by the relations $\hat{q}_- = \frac{-i\sqrt{2}}{l_B}\hat{\alpha}_-$ and $\hat{q}_+ = \frac{i\sqrt{2}}{l_B}\hat{\alpha}_+$, where $l_B = \sqrt{\frac{\hbar}{eB_z}}$ is the magnetic length. The eigenfunctions of the operators $\hat{\alpha}_+$ and $\hat{\alpha}_-$, which are (i) regular at $\rho = 0$ and (ii) also eigenfunctions of $\hat{L}_z$, are $g_{a,l}(\rho, \varphi) = e^{il\varphi}\rho^{\frac{|l|}{2}}e^{-\frac{\rho}{2}}M(a, |l|+1, \rho)$, where $\rho = \frac{1}{2}\left(\frac{r}{l_B}\right)^2$ and $M(a, |l|+1, \rho)$ is the confluent hypergeometric function of the first kind [261]. Since the intrinsic SOC is diagonal in the spin space, one may use the Ansatz $\Psi_l^\uparrow(\rho, \varphi) = \begin{pmatrix} 1 \\ 0 \end{pmatrix} g_{a,l}(\rho, \varphi)$ and $\Psi_l^\downarrow(\rho, \varphi) = \begin{pmatrix} 0 \\ 1 \end{pmatrix} g_{a,l}(\rho, \varphi)$ to solve the Schrödinger equation $H_{\rm dot}\Psi = E\Psi$. The bound state solutions of the QD problem are determined by the condition that the wave function has to vanish at the wall of the QD, i.e., at $r = R_d$. The task can be therefore re-formulated as finding, for a given magnetic field B_z and quantum number l, the roots of $M(a_l, |l|+1, \rho[r = R_d]) = 0$ as a function of a_l. For each l, there can be several such roots, which correspond to a radial quantum number n. Once the nth root $a_{n,l}$ is known, the energy of the bound state $E_{n,l}^{\tau,s}$ can be expressed in terms of $a_{n,l}$, the magnetic field and the material parameters appearing in Eq. (6.1). The roots of the equation $M(a_l, |l|+1, \rho[r = R_d]) = 0$ can be found numerically.

An example of the calculation of the lowest QD bound state energies is shown in Figure 6.1. At zero magnetic field there is an effective time reversal symmetry acting within each valley and

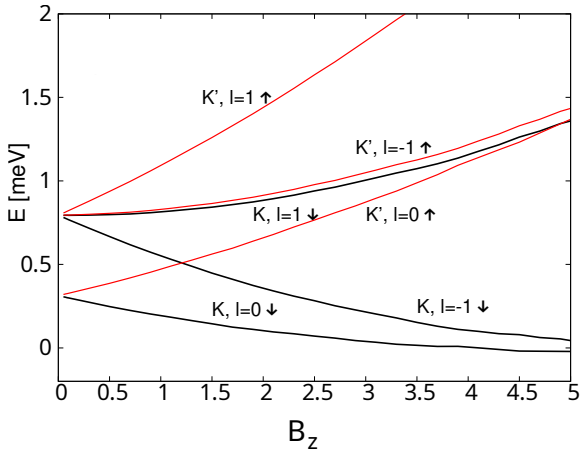

Figure 6.1: The first few bound states of a MoS_2 QD of radius $R_d = 40\,\text{nm}$ as a function of the perpendicular magnetic field $B_z > 0$. Labels show the valley, orbital quantum number l, and spin state for each level. The valley $-K$ is denoted by K' in this figure. All states have the lowest, $n = 1$ radial quantum number. Adapted from Ref. [214].

therefore states with angular momentum $\pm l$ within the same valley are degenerate. Not surprisingly, the valley degeneracy breaking introduced in Sec. 5.1 also appears in the QD spectrum and

for finite magnetic field all levels are both *valley and spin* split. When the magnetic fields becomes larger, so that $l_B \lesssim R_d$, the dot levels start to merge into Landau levels. One can also see that for $B_z \gtrsim 1\,\mathrm{T}$ the lowest energy states reside in the K valley. We emphasize that, in contrast to gapped monolayer [262, 263, 264] and bilayer [263, 264] graphene, the energy states are spin polarized. This suggest that QDs in MoS_2 can be used as simultaneous valley and spin filters.

The Bychkov-Rashba SOC turns the crossings between states $|l,\uparrow\rangle$ and $|l+1,\downarrow\rangle$, $l \geq 0$ in the same valley into avoided crossings. This can be shown by rewriting $\tilde{H}_{BR}^{\tau}$ in terms of the operators α_- and α_+ and calculating their effect on the non-perturbed eigenstates. For the low-lying energy states shown in Fig. 6.1, the effect of the Bychkov-Rashba SOC is to introduce a level repulsion between these states and higher energy ones which lie outside of the energy range of this figure. One can show that for magnetic fields $\lesssim 10\,\mathrm{T}$ and electric fields $E_z \lesssim 10^{-2}\,\mathrm{V/\AA}$ the level repulsion is much smaller than the intrinsic spin-orbit splitting Δ_{cb} and therefore one can neglect it.

Considerations for qubit states

We now briefly discuss which eigenstates of the QDs can be used as two-level systems for qubits. Firstly, we note that one would need to use relatively small QDs in order to make the mean level spacing (at zero magnetic field) larger than the thermal energy $k_B T$. This is because of the relatively large effective mass in the CB compared to, e.g., GaAs quantum wells. Assuming a chaotic QD with mean level spacing $\delta = 2\pi\hbar^2/(m_{\mathrm{eff}} A)$ where A is the area of the dot, taking $R = 40\,\mathrm{nm}$ and the effective mass of MoS_2 $m_{\mathrm{eff}} = 0.45 m_e$, one finds $\delta \approx 0.2\,\mathrm{meV}$ which corresponds to $T = 2.3\,\mathrm{K}$. In this respect TMDCs with smaller m_{eff}, such as WS_2 and WSe_2 [74], might be more advantageous. Secondly, by looking at the QD spectrum shown in Fig. 6.1, the most realistic approach appears to be to use the lowest Kramer's pairs around $B = 0$, e.g., $|l = 0; K'; \uparrow\rangle$ and $|l = 0; K; \downarrow\rangle$, as a combined spin-valley qubit [265, 266]. The external magnetic field can be used to tune the energy splitting of this two-level system and the exchange interaction would provide the necessary coupling to adjacent spin-valley qubits for the realization of two-qubit gates.

6.2 Double quantum dots

We will now discuss double quantum dots (DQDs) and the effect of Coulomb interaction on the low energy states. Restricting the considerations to the case when there are two electrons in the two QDs leads to a relatively simple problem where analytical calculations can be made and the insight gained in this way may serve as a basis for the interpretation of the results of more complicated situations, where only numerical calculations are feasible. One may note that the system of DQDs in carbon nanotubes [267, 268] shares similarities with the case in TMDCs, but the interplay of the exchange interaction with the strong SOC have not been studied previously.

We introduce the notation (n_L, n_R), which means that there are n_L electrons in the left QD and n_R electrons in the right QD. Furthermore, we will use the following notations. The operators $c_{j\tau\sigma}^{(\dagger)}$ annihilate (create) an electron in QD j with valley τ and spin σ indices. Here $j = L$ (R) refers to the left (right) QD, $\tau = K$ $(\overline{K})$ indicates the positive (negative) valley and $\sigma = \uparrow$ $(\downarrow)$ specifies spin up (spin down). The schematic energy diagram of the system is shown in Fig. 6.2. The Hubbard Hamiltonian describes the on-site Coulomb repulsion between electrons in the same QD:

$$H_U = \frac{U}{2} \sum_{j=L,R} n_j(n_j - 1), \tag{6.2}$$

where $U > 0$ is the positive charging energy of the dot and the number operator is defined as $n_j = \sum_{\tau=K,\bar{K}} \sum_{\sigma=\uparrow,\downarrow} c_{j\tau\sigma}^{\dagger} c_{j\tau\sigma}$. The energy difference ε between the dots is specified by a detuning term:

$$H_\varepsilon = \frac{\varepsilon}{2}(n_L - n_R). \tag{6.3}$$

Spin and valley preserving electron tunneling between the dots is described by

$$H_t = \sum_{\tau,\sigma} \left(t\, c^\dagger_{R\sigma\tau} c_{L\sigma\tau} + \text{h.c.} \right), \tag{6.4}$$

where t is the tunneling coefficient. The intrinsic SOC of the TMDC is modeled by $H_\Delta = \Delta\tau_z\sigma_z$, where τ_i (σ_i) is the ith Pauli matrix acting on the valley (spin) ($i = x, y, z$), while Δ is the SOC constant, which can be either positive or negative. Then the SOC Hamiltonian for the DQD system reads

$$H_\Delta = \Delta \sum_{j,\tau,\sigma} c^\dagger_{j\tau\sigma} (\tau_z)_{\tau\tau} (\sigma_z)_{\sigma\sigma} c_{j\tau\sigma}. \tag{6.5}$$

This implies that the Kramer's pair states in the set $\mathcal{P} = \left\{ |K\uparrow\rangle, |\overline{K}\downarrow\rangle \right\}$ are shifted by the energy $+\Delta$, while the Kramer's pair states in the set $\mathcal{N} = \left\{ |K\downarrow\rangle, |\overline{K}\uparrow\rangle \right\}$ are shifted by the energy $-\Delta$. We also assume that the spin-orbit splitting is the same for both dots, which is usually the case for dots created on the same material, although a more general case can also be treated [269]. The total Hamiltonian is given by

$$H_{\text{tot}} = H_U + H_\varepsilon + H_t + H_\Delta. \tag{6.6}$$

In the following discussions we will assume a small detuning and weak tunneling, i.e., $|t| \ll |U \pm \varepsilon|$.

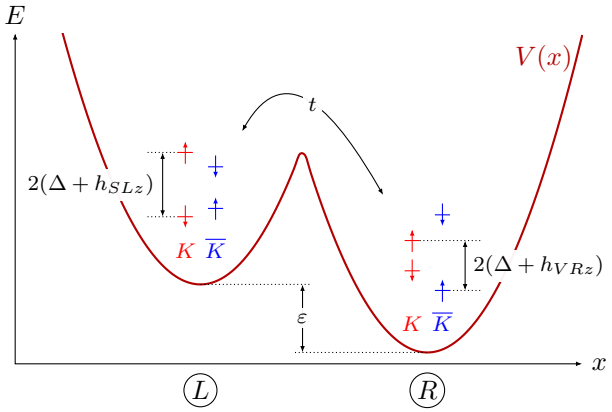

Figure 6.2: Schematic energy diagram of the DQD system. $V(x)$ (dark red line) represents the double-well potential that defines the left (L) and right (R) QDs. The energy levels of the valley and spin states inside the dots are shown here with a positive detuning $\varepsilon > 0$. Spin states in valley K ($\overline{K}$) are coloured in red (blue). The energy levels are shifted by a symmetric spin-orbit splitting (Δ) and by inhomogeneous spin and valley Zeeman terms along the z-direction, with coupling constants h_{SLz}/h_{SRz} and h_{VLz}/h_{VRz} respectively. Electrons are allowed to tunnel from one dot to the other with tunneling coefficient t. Adapted from Ref. [269].

The possible charge configurations in this DQD system are $(2,0)$, $(1,1)$ and $(0,2)$. Because of the spin and valley degrees of freedom and due to the Pauli exclusion principle, there are 28 linearly independent states: 6 $(2,0)$-states, 16 $(1,1)$-states and 6 $(0,2)$-states. As we will see, the basic physics of the system can be described in terms of virtual tunneling between the $(1,1)$-states and the $(2,0)$, $(0,2)$-states. Due to the Pauli exclusion principle, not all the states in the $(1,1)$-subspace are allowed to tunnel to $(0,2)$ or $(2,0)$-states, but only those which are antisymmetric in spin and valley [268]. We now introduce a basis consisting of states that are symmetric or antisymmetric in both spin and valley: $|s_V s_S\rangle_{(n_L,n_R)}$, where s_V (s_S) indicates the exchange symmetry of valley (spin) degree of freedom (DOF) and (n_L, n_R) is the charge configuration. The exchange symmetry can be either that of a singlet (S) or that of a triplet (T_-, T_0, T_+); see Table 6.1 for the definitions

	$\|S\rangle$	$\|T_-\rangle$	$\|T_0\rangle$	$\|T_+\rangle$
Spin	$\frac{\|\uparrow\downarrow\rangle - \|\downarrow\uparrow\rangle}{\sqrt{2}}$	$\|\downarrow\downarrow\rangle$	$\frac{\|\uparrow\downarrow\rangle + \|\downarrow\uparrow\rangle}{\sqrt{2}}$	$\|\uparrow\uparrow\rangle$
Valley	$\frac{\|K\overline{K}\rangle - \|\overline{K}K\rangle}{\sqrt{2}}$	$\|\overline{K}\overline{K}\rangle$	$\frac{\|K\overline{K}\rangle + \|\overline{K}K\rangle}{\sqrt{2}}$	$\|KK\rangle$

Table 6.1: Definitions of singlet and triplet states taking into account spin and valley.

of these states. The spin-orbit coupling term H_Δ is not diagonal in this basis. In order to work with a basis that makes H_Δ diagonal, one can substitute the states $|ST_0\rangle$, $|T_0S\rangle$, $|SS\rangle$ and $|T_0T_0\rangle$ with the following states in the $(1,1)$-subspace:

$$|n_\pm\rangle = (|ST_0\rangle \pm |T_0S\rangle)/\sqrt{2}, \tag{6.7a}$$

$$|\overline{n}_\pm\rangle = (|T_0T_0\rangle \pm |SS\rangle)/\sqrt{2}. \tag{6.7b}$$

Here $|n_\pm\rangle$ ($|\overline{n}_\pm\rangle$) are antisymmetric (symmetric) spin-valley states, which are superpositions of only positive (subscript $+$) or negative (subscript $-$) Kramer's pairs. Note that $|n_\pm\rangle$ ($|\overline{n}_\pm\rangle$) are odd (even) under time-reversal. For these states there is no defined exchange symmetry for spin or valley alone. States analogous to $|n_\pm\rangle$ can be defined in the $(2,0)$ and $(0,2)$-subspaces as well.

Low-energy subspace when Coulomb energy dominates

The spin-orbit coupling H_Δ shifts the states formed by two elements of the negative (positive) Kramer's pair by -2Δ ($+2\Delta$), while it leaves unchanged those states formed by one element of the negative Kramer's pair and one element of the positive Kramer's pair. Taking into account the Coulomb interaction as well, one can show that the whole $(1,1)$ charge sector is the *low energy subspace* (no $(2,0)$ or $(0,2)$-state is lower in energy than any $(1,1)$-state) if the condition

$$4|\Delta| < U - |\varepsilon| \tag{6.8}$$

is fulfilled. This means that the tunneling out from the $(1,1)$-sector into $(2,0)$ and $(0,2)$-states is strongly suppressed. However, virtual tunneling processes need to be taken into account. Since we assumed that the tunneling is spin- and valley-preserving, the antisymmetric $(1,1)$-states can tunnel only to their $(0,2)$ and $(2,0)$ counterpart states that have the same spin and valley configuration. Therefore there is no transition from a negative Kramer's pair to a positive Kramer's pair and vice versa and the energy differences between initial and final states in a virtual tunneling process do not depend on Δ. After projecting out the high-energy $(2,0)$ and $(0,2)$ subspaces, one obtains the following *effective Hamiltonian* for the low-energy subspace:

$$H_{\text{eff}} = -JP_{\text{as}} + \Delta\Sigma. \tag{6.9}$$

Here $J = \frac{4|t|^2U}{U^2-\varepsilon^2}$ is the exchange energy and $P_{\text{as}} = (3 - \boldsymbol{\sigma}_L \cdot \boldsymbol{\sigma}_R - \boldsymbol{\tau}_L \cdot \boldsymbol{\tau}_R - (\boldsymbol{\sigma}_L \cdot \boldsymbol{\sigma}_R)(\boldsymbol{\tau}_L \cdot \boldsymbol{\tau}_R))/8$ is the projection operator over the whole antisymmetric subspace of the $(1,1)$ sector [270] ($\boldsymbol{\sigma}_j$, $\boldsymbol{\tau}_j$ are vectors of Pauli matrices acting on spin and valley, respectively.) Furthermore, $\Delta\Sigma = H_\Delta|_{(1,1)} = \Delta\,(\tau_{Lz}\sigma_{Lz} + \tau_{Rz}\sigma_{Rz})$, where $H_\Delta|_{(1,1)}$ is the restriction of H_Δ to the $(1,1)$-subspace. The spectrum of the Hamiltonian H_{eff} is shown schematically in Fig. 6.3. Assuming $\Delta > 0$, the ground state is $|n_-\rangle$ because it is the only state that is shifted down by both $-J$ and -2Δ. Thus, the ground state space is one-dimensional. Note, that the dimensionality of the ground state space changes from one to six if $\Delta = 0$. As shown in Figs. 6.3, there are five groups of excited states with various degrees of degeneracy and whose relative distances in energy depend on Δ and J. Further analysis shows that each antisymmetric state is separated from its symmetric counterparts by the same energy J.

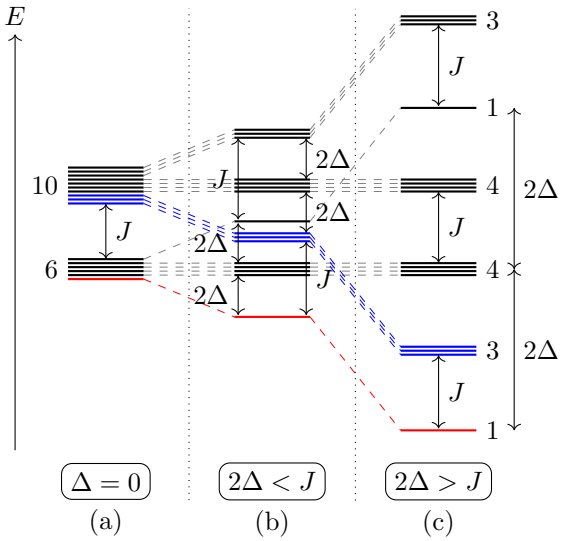

Figure 6.3: Level structure of $(1,1)$-states at fixed (small) detuning for different ratio of Δ and the exchange coupling J. It is assumed that $4|\Delta| < U - |\varepsilon|$. Horizontal lines illustrate the energy levels and degenerate levels are shown as a group of thick lines close together with a number indicating the degree of degeneracy. The coloured energy levels display states inside the $\mathcal{N} \times \mathcal{N}$-sector, see the text for definition. The red energy levels indicate the antisymmetric state $|n_-\rangle$, while the blue energy levels are the symmetric states $|\overline{n}_-\rangle$, $|T_+T_-\rangle$, $|T_-T_+\rangle$. (a) When the SOC splitting is zero, the higher (lower) manifold of states correspond to the symmetric (asymmetric) states, separated by the exchange energy J. (b) For $\Delta \neq 0$ and $2\Delta < J$ both symmetric and antisymmetric energy levels are separated in three groups, $|n_-\rangle$ becomes the ground state and the first excited states are antisymmetric. (c) When $2\Delta > J$, the $\mathcal{N} \times \mathcal{N}$-sector becomes the low-energy subspace and the first excited states are symmetric. Adapted from Ref. [269].

Low energy subspace when SOC dominates

In the derivation of Eq. (6.9) we assumed that $4|\Delta| < U - |\varepsilon|$. The available experiments on QDs created in monolayer WSe_2 [99, 100] and MoS_2 [98] indicate that $U \approx 2\,\text{meV}$ for QDs having a radius of around 100 nm. Since the intrinsic SOC is relatively strong even in the CB, the above mentioned condition does not seem to be satisfied for monolayer TMDC QDs. (According to DFT calculations $2\Delta = 3\,\text{meV}$ in MoS_2 and $2\Delta = 30\,\text{meV}$ in WSe_2 [74].) In other words, Δ is expected to be the dominant energy scale in these QDs.

When $4|\Delta| > U - |\varepsilon|$, the states $|n_-\rangle_{(2,0)}$ and $|n_-\rangle_{(0,2)}$ in the $(2,0)$ and $(0,2)$ charge configurations have lower energy than most of the states in the $(1,1)$ configuration. Nevertheless, it turns out that in order to give an effective description of the system it is possible to focus on a smaller subspace inside the $(1,1)$-sector. For weak tunneling $|t| \ll |U \pm \varepsilon|$ and $2\Delta > J$, the low energy subpace of the $(1,1)$ charge configuration is spanned by the states in $\mathcal{N} \times \mathcal{N}$, where the $\mathcal{N} = \left\{|K\downarrow\rangle, |\overline{K}\uparrow\rangle\right\}$ Kramer's pair states were defined above Eq. (6.6). One can identify the negative Kramer's pair $\mathcal{N}$ as a spin-1/2 degree of freedom with $|\widetilde{\uparrow}\rangle \equiv |\overline{K}\uparrow\rangle, |\widetilde{\downarrow}\rangle \equiv |K\downarrow\rangle$. One can now use the analogy with the known case of the effective Hamiltonian for two spinful electrons in two QDs, each QD having a single available energy level. For weak tunneling between the QDs, and taking into account the detuning and the Hubbard potential, the effective Hamiltonian for the latter system is given by $H_{\text{eff}} = J\boldsymbol{S}_L \cdot \boldsymbol{S}_R$ [85]. Here J is the exchange energy defined below Eq. (6.9), and $\boldsymbol{S}_j$ is the vector of spin operators acting in the jth QD. Similarly, by defining the operators, $\widetilde{\sigma}_z = \sigma_z$, $\widetilde{\sigma}_x = \tau_x\sigma_x$, $\widetilde{\sigma}_y = \tau_x\sigma_y$, the Hamiltonian of the system restricted to the sub-space

$\mathcal{N} \times \mathcal{N}$ reads

$$H_{\text{eff, } \mathcal{N}\times\mathcal{N}} = J\widetilde{\boldsymbol{S}}_L \cdot \widetilde{\boldsymbol{S}}_R, \tag{6.10}$$

where $\widetilde{S}_{ji} = \frac{1}{2}\widetilde{\sigma}_{ji}$ is the spin operator proportional to the new Pauli operator $\widetilde{\sigma}_i$, $i = x, y, z$, acting on QD $j = L, R$. In other words, the description of the low-energy physics in this case is formally identical to the Heisenberg exchange interaction between two spin-only qubits in a material which does not have two valleys. This renders the Kramer's pair an ideal implementation of a qubit in TMDCs. Namely, a recipe for a CNOT gate with these states is readily available from the original Loss and DiVincenzo proposal for spin-only qubits [271]. If, in addition, the τ_x operation could be effectively implemented (for theoretical proposals see, e.g., Refs. [272, 273]), then one would have a full set of single qubit operations.

Further cases

Although we will not consider them in details, more general setups can can also be studied [269]. For example, the SOC strength may not be the same in the two dots. In this case one can use the following more general SOC Hamiltonian: $H_{\Delta_L,\Delta_R} = \sum_j \Delta_j \sum_{\tau,\sigma} c^\dagger_{j\tau\sigma}(\tau_z)_{\tau\tau}(\sigma_z)_{\sigma\sigma}c_{j\tau\sigma}$, where Δ_L and Δ_R are the spin-orbit splittings in the left and right QD respectively. Such asymmetric SOC would change the exchange coupling constant J. One can also take into account the coupling of spin and valley to an external magnetic field. The corresponding spin Zeeman term is given by $H_S = \sum_j \boldsymbol{h}_{Sj} \cdot \sum_{\tau,\sigma_1,\sigma_2} c^\dagger_{j\tau\sigma_1}(\boldsymbol{\sigma})_{\sigma_1\sigma_2}c_{j\tau\sigma_2}$, where $\boldsymbol{h}_{SL}$ and $\boldsymbol{h}_{SR}$ are two vectors of coupling constants for left and right QD, respectively, and $\boldsymbol{\sigma}$ is the vector of Pauli matrices acting on spin. The valley Zeeman term is reads $H_V = \sum_j h_{Vjz} \sum_{\tau,\sigma} c^\dagger_{j\tau\sigma}(\tau_z)_{\tau\tau}c_{j\tau\sigma}$ where h_{VLz} and h_{VRz} describe the valley splittings in the left and right dot. One can show that H_S and H_V would mix a large number of the basis states used in the previous discussions and lead to a more complicated low-energy effective theory.

6.3 Summary

In summary, we studied the physics of single and double quantum dots in monolayer TMDCs. First, we considered a simple model of a circular QD in the non-interacting limit. We calculated the spectrum of the QD as a function of magnetic field. We pointed out that the valley degeneracy breaking discussed in Chapt. 5 appears in the QD spectrum and this offers the possibility to use the lowest energy Kramer's pair as spin-valley qubit. We then considered TMDC DQDs assuming that each QD hosts a single energy level and there are two electrons in the two QDs. In the limit of small detuning we derived effective Hamiltonians for the low-energy subspace in the $(1, 1)$ charge configuration of this system. When the Coulomb interaction dominates the intrinsic SOC, we take into account all states of the $(1, 1)$ charge configuration to construct the effective Hamiltonian. In the opposite case, when the intrinsic SOC is large, it is sufficient to consider only the lowest energy Kramer's pair. One can define spin-valley operators and in terms of these operators the effective low-energy Hamiltonian is formally identical to the Heisenberg exchange Hamiltonian between two spins.

The results of Sec. 6.1 were published in Ref. [214], while the results on DQDs in Sec. 6.2 can be found in Ref. [269].

Chapter 7

Spin and valley Hall effect in bilayer MoS_2

Bilayers of TMDCs have attracted comparatively less attention than monolayers. Nevertheless, several intriguing experimental observations, such as electrical tuning of valley magnetic moment [274], spin-layer locking [275], and finite valley Hall effect [196] have recently been reported in bilayer TMDCs. The observation of the VHE is interesting because it can be related to the Berry curvature, i.e., a topological property of the band structure. Another important property of bilayer TMDCs is that they can exists in different stacking orders. As it was discussed in Sec. 1.2.2 using the example of trilayer graphene, the stacking order can have an important effect on the electronic properties. Bilayer MoS_2 therefore offers an interesting system to study several phenomena introduced in Chap. 1.

In the following we first present the stacking order dependent $\mathbf{k} \cdot \mathbf{p}$ Hamiltonians for the $\pm K$ valley of bilayer TMDCs [276]. Similarly to Chap. 4, the material parameters of the $\mathbf{k} \cdot \mathbf{p}$ model were extracted from DFT calculations which are not subjects of this thesis. The $\mathbf{k} \cdot \mathbf{p}$ Hamiltonians will be the starting point to consider the Berry curvature properties of the valence and conduction bands. These properties have novel aspects compared to earlier examples discussed, e.g., for (few-layer)graphene. Finally, one can expect that the Berry curvature leads to spin and valley Hall effects in ballistic samples, and we discuss a particularly interesting scenario in this respect.

7.1 Stacking dependent $\mathbf{k} \cdot \mathbf{p}$ Hamiltonian for the $\pm K$ valley

Bulk MoS_2 occurs in nature in two polytypes: the so-called 2H and 3R polytypes. The unit cell of the 2H polytype contains two monolayer units which are rotated with respect to each other by 180°. In the case of the 3R polytype there are three monolayers in the unit cell which are shifted with respect to each other. Experimentally, bilayer samples both have been exfoliated from both bulk polytypes [274, 277]. The schematic crystal structure of the 2H and 3R bilayers can be seen in Fig. 7.1. As it will be shown below, the difference in the stacking is reflected in the form of the corresponding $\mathbf{k} \cdot \mathbf{p}$ Hamiltonians.

Motivated by the development of the theory for BLG [54], whereby the TB Hamiltonian could be written in terms of the TB Hamiltonians of the individual monolayers and certain interlayer hopping terms, one may ask if the $\mathbf{k} \cdot \mathbf{p}$ Hamiltonian for bilayer TMDCs can be written in terms of the $\mathbf{k} \cdot \mathbf{p}$ Hamiltonian of monolayers that we discussed in Chap. 4. It turns out that this is indeed possible. Furthermore, as in the case of monolayers, one can derive a separate $\mathbf{k} \cdot \mathbf{p}$ Hamiltonian for each high-symmetry point of the BZ. We note that the BZ of the bilayer is the same hexagonal BZ as for the monolayer[1]. We also remind that in monolayer TMDCs the d_{z^2} atomic orbitals of

[1] It is not true, however, that the K point of a monolayer would necessarily map onto the K point of the bilayer.

the metal atoms have the largest weight in the CB and the $d_{x^2-y^2} \pm id_{xy}$ orbitals in the VB at the $\pm K$ point of the BZ. These orbitals are mostly localized to the monolayers, therefore interlayer hybridization in bilayers should be weak at the $\pm K$ point and mainly due to the chalcogen p-orbitals. Therefore one may expect that, at least for the $\pm K$ valley, one can write the bilayer $\mathbf{k} \cdot \mathbf{p}$ Hamiltonian in the following way:

$$H_{bl} = \begin{pmatrix} H_{ml}^{(1)} & H_{il}^{(\gamma)} \\ (H_{il}^{(\gamma)})^{\dagger} & H_{ml}^{(2)} \end{pmatrix} \tag{7.1}$$

Here $H_{ml}^{(i)}$ is the effective $\mathbf{k} \cdot \mathbf{p}$ Hamiltonian of the ith monolayer and $H_{il}^{(\gamma)}$ describes the interlayer coupling. The index γ denotes the *stacking configuration* of the bilayer, to be discussed below. We note that similarly to $H_{ml}^{(i)}$, $H_{il}^{(\gamma)}$ can be obtained from considerations based on the symmetry of the bilayer.

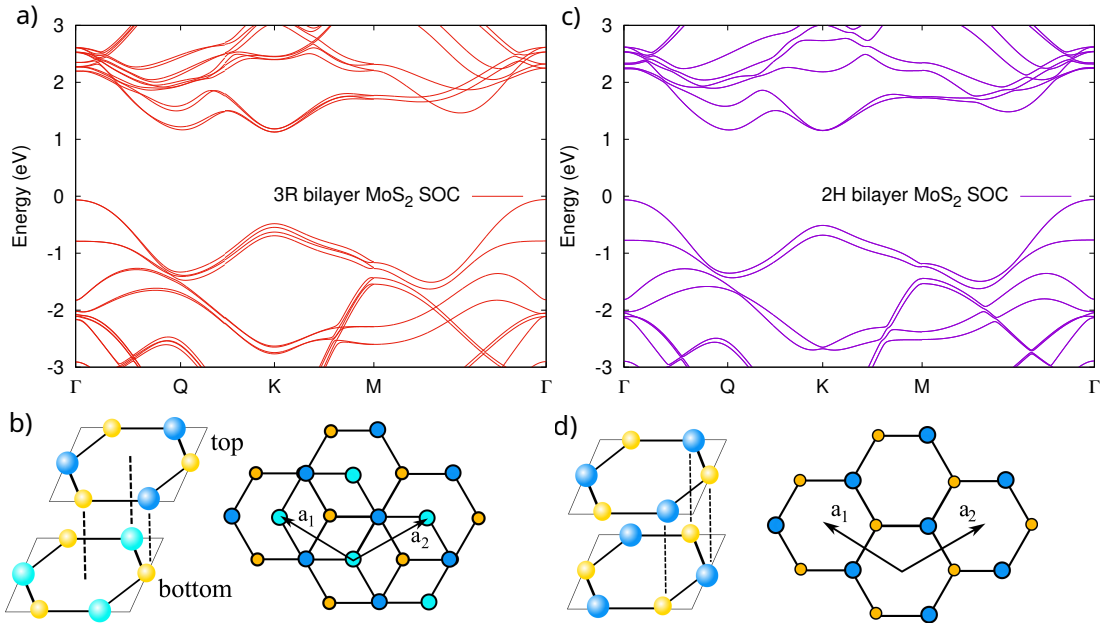

Figure 7.1: a) and c): Band structure of 3R and 2H stacked bilayer MoS_2, respectively, from DFT calculations. b) and d): Schematic crystal structure in side view and in top view of 3R and 2H stacked bilayer MoS_2, respectively. Adapted from Ref. [276].

As a first step in the derivation of the $\mathbf{k} \cdot \mathbf{p}$ Hamiltonians we neglect the SOC and show that the difference in the stacking order is reflected in the form of the $\mathbf{k} \cdot \mathbf{p}$ model. We will come back to the effects of intrinsic SOC in Sec. 7.3.

3R stacking

For 3R bilayers both $H_{ml}^{(1)}$ and $H_{ml}^{(2)}$ should be taken as the monolayer TMDC Hamiltonian at the K point. In order to keep the bilayer model simple, one may use the minimal $\mathbf{k} \cdot \mathbf{p}$ model of monolayer TMDCs given in Eq. (4.5). The interlayer coupling Hamiltonian reads

$$H_{il}^{(3R)} = \begin{pmatrix} \gamma_{cc} q_{-} & 0 \\ 0 & \gamma_{vv} q_{-} \end{pmatrix}. \tag{7.2}$$

In the case of AB stacked bilayers, the K point of one of the monolayers map onto the K point of the bilayer, however, for the other monolayer it is the $-K$ point of the monolayer BZ that maps onto the K point of the bilayer.

As one can see, the coupling between the VB and the CB of the top and bottom layers is $\mathbf{q}$ dependent and it is characterized by coupling constants γ_{vv} and γ_{cc}, respectively. Thus the minimal model for the band structure of 3R bilayers at the K point reads:

$$H_K^{3R} = \begin{pmatrix} \varepsilon_{cb}^b & \gamma_3\, q_+ & \gamma_{cc}\, q_- & 0 \\ \gamma_3\, q_- & \varepsilon_{vb}^b & 0 & \gamma_{vv}\, q_- \\ \gamma_{cc}\, q_+ & 0 & \varepsilon_{cb}^t & \gamma_3 q_+ \\ 0 & \gamma_{vv} q_+ & \gamma_3 q_- & \varepsilon_{vb}^t \end{pmatrix}. \tag{7.3}$$

The crystal structure of 3R bilayers is not inversion symmetric which means that the band edge energies ε_{cb}^b and ε_{cb}^t for the CB in the bottom and top layers can be different, and the same is true for the VBs. According to DFT calculations [276], the band-edge energy differences $\delta E_{cc} = (\varepsilon_{cb}^b - \varepsilon_{cb}^t)/2$ and $\delta E_{vv} = (\varepsilon_{vb}^b - \varepsilon_{vb}^t)/2$ are around 30 meV. The difference between δE_{cc} and δE_{vv} is a rather small energy scale which can be neglected for certain problems, see Sec. 7.2. Therefore we introduce here the notation δE_{ll} for the interlayer band-edge energy difference of 3R bilayers.

2H stacking

For 2H bilayers $H_{ml}^{(1)}$ can be chosen as the monolayer Hamiltonian at the K point of the monolayer BZ, while $H_{ml}^{(2)}$ should be taken as the monolayer Hamiltonian at the $-K$ point. The interlayer coupling is given by

$$H_{il}^{(2H)} = \begin{pmatrix} \gamma_{cc}\, q_- & 0 \\ 0 & t_\perp \end{pmatrix}. \tag{7.4}$$

Here $t_\perp$ describes the momentum independent interlayer tunnelling between the VBs of the constituent monolayers and was introduced in Refs. [278, 274]. The CBs of the monolayers are also coupled, albeit with a weaker, momentum dependent coupling given by the matrix element $\gamma_{cc}\, q_-$ in Eq (7.4). Thus the minimal model for the band structure of 2H bilayers at the K point reads:

$$H_K^{2H} = \begin{pmatrix} \varepsilon_{cb} + U_g & \gamma_3\, q_+ & \gamma_{cc}\, q_- & 0 \\ \gamma_3\, q_- & \varepsilon_{vb} + U_g & 0 & t_\perp \\ \gamma_{cc}\, q_+ & 0 & \varepsilon_{cb} - U_g & \gamma_3 q_- \\ 0 & t_\perp & \gamma_3 q_+ & \varepsilon_{vb} - U_g \end{pmatrix}. \tag{7.5}$$

The diagonal blocks correspond to Eq. (4.5), i.e., the first term of the monolayer TMDC Hamiltonian, but we also assume that a homogeneous external electric field is applied which adds a potential difference $\pm U_g$ between the layers. The electric field breaks the inversion symmetry and will be important for the Berry curvature calculations in Sec. 7.2.

Remarks

One may note the following:

1. The off-diagonal elements in Eqs. (7.2) and (7.4) are, strictly speaking, non-zero, but for simplicity they have been neglected. We have checked that the DFT band structure can be fitted very well using this model.

2. The above construction of the bilayer $\mathbf{k}\cdot\mathbf{p}$ Hamiltonian relied on the assumption that the monolayer units are only weakly coupled at the $\pm K$ points of the BZ. The same approach may not be useful for all high symmetry points: DFT band structure calculations indicate that, e.g., the monolayer bands are strongly hybridised at the Γ point of bilayer TMDCs. While it is possible to establish a $\mathbf{k}\cdot\mathbf{p}$ Hamiltonian for the Γ point, it may not be particularly useful to write this Hamiltonian in terms of monolayer Hamiltonians.

As we will see in Secs. 7.2, the differences in the crystal structure, and consequently, in the effective Hamiltonians of 2H and 3R bilayers lead to important differences in the Berry-curvature properties as well.

7.2 Berry curvature calculations

We now calculate both analytically and numerically the Berry curvature $\Omega_z(\mathbf{q})$ in the $\pm K$ valleys. To this end we use the 4×4 $\mathbf{k} \cdot \mathbf{p}$ models shown in Eqs. (7.3) and (7.5). As we show below, these models allow to take into account both *intralayer* and *interlayer* contributions to $\Omega_z(\mathbf{q})$. The existence of both of these contributions is an interesting property of bilayer TMDCs. In bilayer graphene, e.g., only the interlayer contribution is finite. The analytical calculations for the Berry curvature were obtained by deriving a perturbation series for $\Omega_z(\mathbf{q})$. This approach allowed to work with 2-spinors instead of the 4-spinors that are the eigenstates of the 4×4 $\mathbf{k} \cdot \mathbf{p}$ models and therefore made the analytical calculations easier.

In the case 3R bilayers, one can treat the interlayer coupling as perturbation which modifies the Berry curvature calculated for each layer separately. One finds that $\Omega_z^{(b)}$ ($\Omega_z^{(t)}$) for the bottom (top) layer can be written as $\Omega_z^{(b)} \approx \Omega_z^{(0)} - \Omega_z^{(1,1)}$ ($\Omega_z^{(t)} \approx \Omega_z^{(0)} + \Omega_z^{(1,1)}$), where

$$\Omega_z^{(0)}(\mathbf{q}) = \pm\frac{\tau}{2}\left(\frac{\gamma_3}{\delta E_{bg}}\right)^2 \frac{1}{\left(1+\left(\frac{\gamma_3|\mathbf{q}|}{\delta E_{bg}}\right)^2\right)^{3/2}} \tag{7.6a}$$

is the well-known result for a gapped-graphene two-band model [118, 189]. Here $|\mathbf{q}|$ is the magnitude of $\mathbf{q}$ and we used the notation $\delta E_{bg} = E_{bg}/2$ for half of the monolayer bandgap. The contribution $\Omega_z^{(1,1)}$ reads

$$\Omega_z^{(1,1)}(\mathbf{q}) \approx \frac{\tau}{(2\delta E_{ll})^2}\left(\lambda_1 \pm \frac{\lambda_2}{\left(1+\left(\frac{\gamma_3|\mathbf{q}|}{\delta E_{bg}}\right)^2\right)^{1/2}}\right), \tag{7.6b}$$

and it is due to the interlayer coupling. Here $\lambda_1 = \gamma_{cc}^2 + \gamma_{vv}^2$, $\lambda_2 = \gamma_{cc}^2 - \gamma_{vv}^2$ and the $+$ $(-)$ sign corresponds to the CB (VB).

In 2H bilayers Ω_z vanishes because of the presence of time reversal and inversion symmetry, see Sec. 1.5.1. However, by applying an external electric field, the inversion symmetry can be broken and the Berry curvature will be finite. As mentioned, the effect of a finite external electric field can be taken into account by an interlayer potential $\pm U_g$ in H_K^{2H}. For the physically relevant case of $U_g \ll \delta E_{bg}$ it proves to be useful to treat the intralayer coupling between the CB and VB in each layer as a perturbation. One finds that in the CB the Berry curvature is given by $\Omega_{z,cb} = \Omega_{z,cb}^{(0)} + \Omega_{z,cb}^{(1,1)}$, where

$$\Omega_{z,cb}^{(0)}(\mathbf{q}) = \mp\frac{\tau}{2}\frac{\gamma_{cc}^2 U_g}{\left(U_g^2 + (\gamma_{cc}|\mathbf{q}|)^2\right)^{3/2}} \tag{7.7a}$$

is due to the interlayer coupling of the CBs. The second contribution reads

$$\Omega_{z,cb}^{(1,1)}(\mathbf{q}) \approx \pm\frac{\tau}{2}\left(\frac{\gamma_3}{\delta E_{bg}}\right)^2 \lambda_3 \frac{U_g}{\left(U_g^2 + (\gamma_{cc}|\mathbf{q}|)^2\right)^{1/2}}, \tag{7.7b}$$

where, using the notation $\tilde{\varepsilon}_{vb} = \sqrt{t_\perp^2 + U_g^2}$, the constant λ_3 is given by $\lambda_3 = 1 + \frac{3}{4}\left(\frac{\tilde{\varepsilon}_{vb}}{\delta E_{bg}}\right)^2$. The upper (lower) sign in Eqs. (7.7a)-(7.7b) and below in Eq. (7.8) corresponds to the band that have larger weight in the layer at $+U_g$ $(-U_g)$ potential. $\Omega_{z,cb}^{(1,1)}(\mathbf{q})$ is non-zero even if we set $\gamma_{cc} = 0$, i.e., this term describes a Berry curvature contribution due to the intralayer coupling of the CB and the VB. One can note that the interlayer ($\Omega_{z,cb}^{(0)}$) and intralayer ($\Omega_{z,cb}^{(1,1)}$) contributions have opposite sign in each valley. For the VB one finds that $\Omega_{z,vb}^{(0)} = 0$ and the first non-zero term is

$$\Omega_{z,vb}^{(1,1)} = \mp 2\tau\frac{\gamma_3^2 U_g}{\tilde{\varepsilon}_{vb}(E_{bg} \mp \tilde{\varepsilon}_{vb})^2}, \tag{7.8}$$

which is in agreement with Ref. [274] for $\tilde{\varepsilon}_{vb} \ll E_{bg}$.

The comparison of the analytical results given in Eqs. (7.6)-(7.8) with the results of numerical calculations is summarized in Fig. 7.2. The numerical calculations of $\Omega_z(\mathbf{q})$ were performed by employing the FHS method [279] and we used material the parameters of bilayer MoS_2 [276]. As

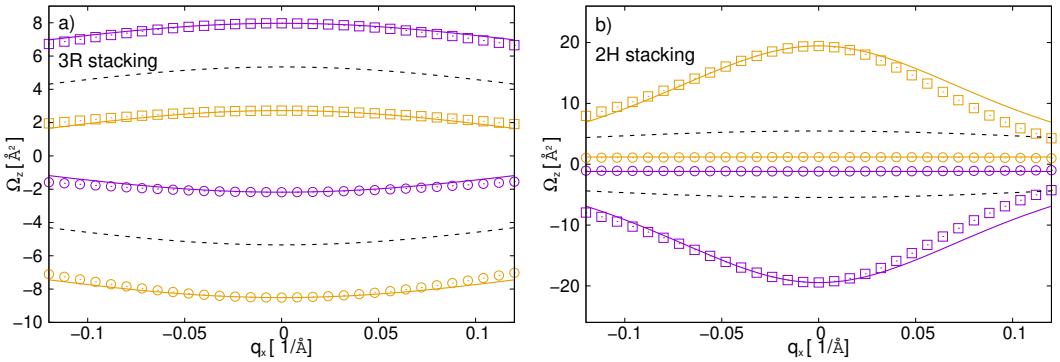

Figure 7.2: Calculation of $\Omega_z(\mathbf{q})$ in the K valley for a) 3R stacked, and b) 2H stacked bilayer MoS_2. Solid lines show analytical results, symbols show numerical calculations. The dashed line indicates the Berry curvature $\Omega_z^{(0)}(\mathbf{q})$ for monolayer MoS_2. The results for CBs are indicated by □ and for VBs by ◯. In a), brown colour corresponds to bands in the bottom layer, purple to bands in the top layer. In c) brown colour corresponds to the layer at $-U_g$ potential, purple to the layer at $+U_g$. In the calculations we used $U_g = 10\,\text{meV}$. Adapted from Ref. [276].

one can see the analytical and numerical results are in good agreement. It is also clear that the Berry curvature in both types of bilayer is substantially different from the monolayer case. This shows that the contributions due to interlayer coupling, described in Eqs. (7.6b) and (7.7a), play an important role. One can note that although the band structure of 3R and 2H stacked bilayers look rather similar in Fig. 7.1, the comparison of Figs. 7.2(a) and 7.2(b) reveals several important differences between their Berry curvature properties.

Discussion

Considering first the 3R bilayers, $\Omega_z(\mathbf{q})$ is significantly larger for the CB of the top layer than for the CB of the bottom layer, while the converse is true for the VBs [Fig. 7.2(a)]. The analytical calculations reveal that this happens because the interlayer and the intralayer contributions to $\Omega_z(\mathbf{q})$ are of the same order of magnitude and they can either reinforce or weaken each other. For example, in the CB one finds for $\mathbf{q} = 0$ that $\Omega_{z,cb} = \Omega_{z,cb}^{(0)} + \Omega_{z,cb}^{(1,1)} = \frac{\tau}{2}[(\gamma_3/\delta E_{bg})^2 \mp (\gamma_{cc}/\delta E_{ll})^2]$, where $-$ $(+)$ sign is for the bottom (top) layer. Therefore the interlayer coupling reduces $\Omega_{z,cb}$ for the bottom layer and enhances it for the top layer. We point out that an external electric field, depending on its polarity, could both decrease and increase δE_{ll}. Therefore one can expect that $\Omega_z^{(1,1)}$, hence Ω_z is *tunable*. (Note, that δE_{bg} and hence $\Omega_z^{(0)}$ would be difficult to change by electric field.)

For 2H bilayers, on the other hand, the Berry-curvature is *CB-coupled*: its magnitude is much larger in the CB than in the VB [Fig. 7.2(b)], independently of the layer index. This is due to the fact that close to the $\pm K$ points, where $\gamma_{cc}|\mathbf{q}| \ll U_g$, the main contribution to $\Omega_z(\mathbf{q})$ in the CB comes from the interlayer coupling. This contribution scales as $(\gamma_{cc}/U_g)^2$ and can be quite large for small U_g. Therefore $\Omega_{z,cb}$ is gate tunable, similarly to the situation in 3R bilayers. In contrast, using Eq. (7.8) and realistic material parameters, one can expect that the Berry curvature, albeit gate tunable, will be rather small in the VB.

The results in Fig. 7.2 clearly show the effect of stacking order on the Berry-curvature properties. It is also clear that both intralayer and interlayer contributions to the Berry curvature can be

important. Moreover, bilayers of TMDCs also offer an example for systems, where a topological property, in this case the Berry curvature, is tunable by external electric field.

7.3 Spin-orbit coupling effects

We start the discussion of the SOC by reminding that 2H bilayers have inversion symmetry, while the 3R bilayers do not. A consequence of the presence/absence of inversion symmetry is that the bands of 2H bilayers are spin-degenerate, whereas the SOC can lift the spin-degeneracy of the bands of 3R bilayers. DFT band structure calculations which take into account the SOC are shown in Figs. 7.1(a) and 7.1(c) for 3R and 2H bilayer MoS_2, respectively. Comparing these two figures one can observe that the bands of 3R bilayers are split by the intrinsic SOC around the K and Q points. Because of the presence of an additional symmetry, bands remain spin-degenerate for both stacking along the $\Gamma - M$ line.

In general, the SOC in bilayer TMDCs is more complex than in monolayers. In addition to the SOC in the constituent monolayers, certain interlayer terms are also allowed by symmetry considerations. However, the DFT calculations of Ref. [276] suggest that for bilayer MoS_2 it is sufficient to take into account only the intrinsic SOC of the constituent monolayers and one can neglect interlayer SOC terms. The effects of the SOC in the $\pm K$ valleys are summarized in Fig. 7.3.

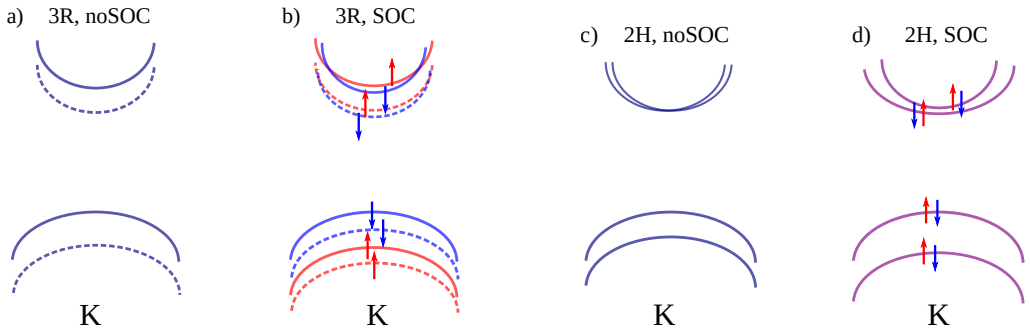

Figure 7.3: Schematic representation of SOC effects in the band structure of bilayer MoS_2 at the K point. a) For 3R bilayers, close to the $\pm K$ points the layer index is an approximately good quantum number for each of the bands both in the CB and the VB. Neglecting the SOC (noSOC) the lowest CB is mostly localized to the top layer (dashed line), while the next CB band (solid line) to the bottom layer. The opposite is true for the two highest energy VBs. The bands are shifted in energy due to the interlayer band edge energy differences $2\delta E_{cc}$ and $2\delta E_{vv}$. b) When SOC is taken into account for 3R bilayers, each of the bands becomes split and spin polarized. Red corresponds to $\uparrow$, blue to $\downarrow$ spin polarization. The spin-orbit splitting Δ_{cb} of the two lowest CBs is much smaller than the inter-layer splitting δE_{cc}. The situation is different for the VBs: here $\Delta_{vb} \gtrsim \delta E_{vv}$ and therefore the spin-polarized bands have an alternating layer index. c) For 2H bilayers, if the SOC is neglected (noSOC), the two lowest energy CBs are degenerate at the $\pm K$ points and weakly split away from the $\pm K$ points due to the interlayer coupling. The energy splitting of the two highest energy VBs is $2t_\perp$. Both layers contribute with equal weight to each of the bands. d) When SOC is taken into account for 2H bilayers, there are two two-fold degenerate and spin-unpolarized bands separated by an energy $2\Delta_{cb}$ at the $\pm K$ point in the CB. A combined layer and spin index can be assigned to each of the four CB bands at the $\pm K$ point, away from the $\pm K$ points both layers contribute to each of the bands, but with different weights. In the VB both layers contribute to each of the bands, even at the $\pm K$ points. Only if $\Delta_{vb} \gg t_\perp$ do the bands become approximately layer polarized [278]. Adapted from Ref. [276].

To set the stage for Sec. 7.4, here we discuss 2H bilayers in some details. If SOC is neglected and inversion symmetry is not broken, the CB is doubly degenerate, while the VB is non-degenerate at the $\pm K$ point [Fig. 7.3(c)]. If now spin is taken into account but SOC is neglected, this would mean a four-fold degeneracy of the CB. However, the SOC partially lifts this four-fold degeneracy and leads to two-fold degenerate bands, see Fig. 7.3(d). This remaining spin-degeneracy of the bands is due to the inversion symmetry. The SOC of 2H bilayers can be described by the Hamiltonian $H^{2H}_{so,cb} = \Delta_{cb}\tau_z\sigma_z s_z$ ($H^{2H}_{so,vb} = \Delta_{vb}\tau_z\sigma_z s_z$) in the CB (VB) of the bilayer. Here the Pauli matrix σ_z indicates that within a given valley the SOC has a different sign [278] in the two layers: this can be understood from the fact that the layers are rotated by 180° with respect to each other. Note that this form of the intrinsic SOC implies that the out-of-plane component of the spin is conserved. In the CB the splitting between the two-fold degenerate bands is basically given by the SOC strength $2\Delta_{cb}$ of monolayer TMDCs. In the VB the main effect of the SOC is to increase the energy splitting of the two highest bands from $2t_\perp$ to $2\sqrt{\Delta^2_{vb} + t^2_\perp}$.

The SOC affects the Berry curvature as well. The corresponding formulas can be obtained from Eqs. (7.7a) and (7.7b) by making the substitution $U_g \to \Delta_{cb}$ and using $\tilde{\varepsilon}_{vb} = \sqrt{\Delta^2_{vb} + t^2_\perp}$ in the expression for λ_3. One can label Ω_z by a spin index $s = \uparrow, \downarrow$ and write $\Omega^{\uparrow}_{z,cb} = \Omega^{(0)}_{z,cb} + \Omega^{(1,1)}_{z,cb}$, where the upper (lower) sign appearing in Eqs. (7.7a) and (7.7b) corresponds to the band at energy $\varepsilon_{cb} + \tau\Delta_{cb}$ ($\varepsilon_{cb} - \tau\Delta_{cb}$) for $\mathbf{q} = 0$. Regarding the $\downarrow$ bands, one finds $\Omega^{\downarrow}_{z,cb}(\mathbf{q}) = -\Omega^{\uparrow}_{z,cb}(\mathbf{q})$.

7.4 Spin and Valley Hall effects in 2H bilayer MoS_2

As discussed in Sec. 1.5, if the Berry curvature is finite, the charge carriers can acquire an anomalous transverse velocity component, which can give rise to various Hall effects in the ballistic limit. It turns out that 2H bilayer MoS_2 may host a particularly interesting scenario in this respect. Since few-layer MoS_2 on dielectric substrate is often found to be n-doped [280], we will focus on the Hall effects in the CB and we restrict the discussion to the intrinsic, Berry curvature related contribution.

Following the discussions in Sec. 1.5.2 and Sec. 1.7.2, one can define the valley Hall conductivity $\sigma^{vH}_{xy,n}$ of band n as [70]

$$\sigma^{vH}_{xy,n} = \frac{e^2}{\hbar}\int \frac{d\mathbf{q}}{(2\pi)^2}\left[f^{\uparrow}_n(\mathbf{q})\Omega^{\uparrow}_{z,n}(\mathbf{q}) + f^{\downarrow}_n(\mathbf{q})\Omega^{\downarrow}_{z,n}(\mathbf{q})\right] \tag{7.9}$$

where $f^{\uparrow,\downarrow}_n(\mathbf{q})$ is the Fermi-Dirac distribution function for charge carriers with spin $\uparrow, \downarrow$ and $\Omega^{\uparrow,\downarrow}_{z,n}(\mathbf{q})$ denotes the corresponding Berry curvatures. As mentioned above, the out-of-plane component of the spin is a good quantum number in bilayer TMDCs. Similarly, the the contribution- to the spin Hall conductivity $\sigma^{sH}_{xy,n}$ can be defined (in units of $e/2$, [70])

$$\sigma^{sH}_{xy,n} = \int \frac{d\mathbf{q}}{(2\pi)^2}\left[f^{\uparrow}_n(\mathbf{q})\Omega^{\uparrow}_{z,n}(\mathbf{q}) - f^{\downarrow}_n(\mathbf{q})\Omega^{\downarrow}_{z,n}(\mathbf{q})\right]. \tag{7.10}$$

In the evaluation of Eqs. (7.9) and (7.10) the integration is restricted to the K valley. This assumes that the Berry curvature is strongly peaked in the $\pm K$ valleys. Since we only study the Hall effects in the CB, we will neglect the band index n in the following.

In our case the formulas for $\Omega_z(\mathbf{q})$ were derived in Sec. 7.2 and the effect of the SOC was explained in Sec. 7.3. Let us start with the qualitative discussion of the effects of the interlayer potential the U_g. When $U_g = 0$, i.e., there is no out-of-plane external electric field applied, and if the SOC is neglected, then both σ^{vH}_{xy} and σ^{sH}_{xy} vanishes because the Berry curvature is zero, see Eqs. (7.7a)-(7.7b). If the SOC is not neglected, then the Berry curvature is finite even for $U_g = 0$. Since each band is spin-degenerate [Fig. 7.4(a)], $f^{\downarrow}_n(\mathbf{q}) = f^{\uparrow}_n(\mathbf{q})$ and one finds that σ^{vH}_{xy} vanishes in this limit. However, σ^{sH}_{xy} is non-zero. This is allowed because both the (in-plane) electric field and the spin current transform in the same way under time-reversal and inversion symmetries [173].

On the other hand, for $U_g \neq 0$ both σ_{xy}^{vH} and σ_{xy}^{sH} will be finite. The finite interlayer potential difference leads to the breaking of inversion symmetry and splitting of the spin-degenerate bands, see Fig. 7.4(b). Each band can be labelled by a spin index $\uparrow, \downarrow$ and by an index $\pm$ depending on whether the band edge is at $\pm U_g$ potential for $\mathbf{q} = 0$. When $U_g = \Delta_{cb}$ [Fig. 7.4(c)], the $(+,\downarrow)$ and $(-,\downarrow)$ bands become degenerate. This degeneracy is lifted if U_g is further increased [Fig. 7.4(d)]. As we will show below, the contribution to the Hall conductivity which is due to the interlayer coupling changes sign going from $U_g < \Delta_{cb}$ to $U_g > \Delta_{cb}$. At the $-K$ point, by time reversal symmetry, the $(+,\uparrow)$ and $(-,\uparrow)$ bands can become degenerate as a function of U_g.

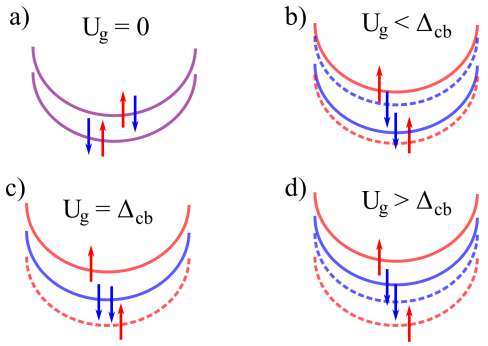

Figure 7.4: Schematic evolution of the four low-energy CB bands as a function of the interlayer potential U_g at the K point of the BZ. Spin-degenerate bands are shown with purple, $\uparrow$ polarized with red and $\downarrow$ polarized with blue. Solid line corresponds to bands at $+U_g$, dashed line to bands at $-U_g$ potential. Adapted from Ref. [276].

In the following we will assume that $E_F > 2(U_g + \Delta_{cb})$ for all U_g values considered, i.e., E_F is large enough so that both layers and all four low-energy CBs are occupied and contribute to the valley and spin Hall effects. In MoS_2, given the relatively small $\Delta_{cb} \approx 3$meV value of the SOC, we expect that this situation is realistic. Moreover, we assume that $U_g \neq \Delta_{cb}$ and that E_F is of the order of few tens of meV. The latter condition ensures that it is sufficient to consider only the $\pm K$ valleys, see below the discussion on the Q valleys. The case $U_g = \Delta_{cb}$ requires slightly different considerations [276] because two bands become degenerate [Fig. 7.4(c)]. Under the above listed assumptions and after summing up the contributions of all four bands shown in Fig. 7.4, one finds that

$$\sigma_{xy}^{vH} \approx \frac{e^2}{\hbar}\left[\frac{\varepsilon_{cc}}{2\pi}\frac{U_g}{U_g^2 - \Delta_{cb}^2} - \rho_{2d} U_g \left(\frac{\gamma_3}{\delta E_{bg}}\right)^2 \lambda_4(U_g)\right], \tag{7.11}$$

and

$$\sigma_{xy}^{sH} \approx -\left[\frac{\varepsilon_{cc}}{2\pi}\frac{\Delta_{cb}}{U_g^2 - \Delta_{cb}^2} + \rho_{2d}\Delta_{cb}\left(\frac{\gamma_3}{\delta E_{bg}}\right)^2 \lambda_4(U_g)\right]. \tag{7.12}$$

Here $\varepsilon_{cc} = \frac{2m_{\text{eff}}}{\hbar^2}\gamma_{cc}^2$, $\rho_{2d} = m_{\text{eff}}/2\pi\hbar^2$ is the 2D density of states per spin and valley, and $\lambda_4(U_g) = \left(1 + \frac{3}{4}\frac{\Delta_{vb}^2 + t_\perp^2 + U_g^2}{\delta E_{bg}^2}\right)$.

One can see that σ_{xy}^{vH} vanishes for $U_g \to 0$, but σ_{xy}^{sH} remains finite. When $U_g \approx \Delta_{cb}$ the first term on the r.h.s of Eqs. (7.11) and (7.12), which is related to the interlayer contribution to the Berry curvature, is larger than the second term. Moreover, this term changes sign as U_g is changed from $U_g < \Delta_{cb}$ to $U_g > \Delta_{cb}$ and one can expect that this leads to a sign change in σ_{xy}^{vH} and σ_{xy}^{sH}. It is interesting to note that in lattice Chern insulators such a sign change of the off-diagonal conductivity was associated with a topological transition [126, 281]. In our case the sign change of σ_{xy}^{vH} and σ_{xy}^{sH} happens when the $\downarrow$ ($\uparrow$) bands become degenerate at the K ($-K$) point and then the degeneracy is lifted again as the amplitude of the electric field is increased further. However, the true band gap of the system, between the VB and CB, does not close, nor does the gap close

and re-open for the $(\uparrow, +)$ and $(\uparrow, -)$ bands. Therefore i) σ_{xy}^{vH} and σ_{xy}^{sH} are not quantized, and ii) those contributions to σ_{xy}^{vH} and σ_{xy}^{sH}, which are related to the intralayer coupling of the CBs and the VBs, do not change sign as a function of U_g.

The Q valleys

As one can see in, e.g., Figs. 7.1(a) and (b), the local minimum of the CB at the Q points of the BZ is almost degenerate with the K valley. According to the DFT band structure calculations of Ref. [276], the band edge is at the $\pm K$ point for both stackings, but the difference δE_{QK} between the band edge at the $\pm K$ and Q points is only $\delta E_{QK} \approx 10\,\text{meV}$. Regardless of the exact value of δE_{QK} in DFT calculations, it is of interest to understand if the six Q valleys can affect the valley Hall conductivity. The calculations of Ref. [282] indicate that the Berry curvature is very small at the Q point of monolayer TMDCs, therefore it is only the inter-layer contribution that needs to be considered in bilayers. To this end we derived a $\mathbf{k} \cdot \mathbf{p}$ Hamiltonian for the Q points as well. However, we found that the Berry curvature is significantly smaller in the Q valley than in the K valley for bilayer MoS_2. Therefore, as long as intervalley scattering between the K and Q valleys is not strong, the Q valleys should have only a minor effect on the valley Hall and spin Hall conductivities.

7.5 Summary

In summary, we have studied the Berry curvature properties and the corresponding and the valley and spin Hall conductivities of bilayer TMDCs, in particular, of bilayer MoS_2. We have considered both 3R and 2H stacked bilayers and found intralayer as well as interlayer contributions to the Berry curvature. Such a situation, where both types of contributions are finite, has not been discussed before for layered materials. We pointed out that the stacking order has important effects on the Berry curvature. Due to the interlayer contribution, the Berry curvature is gate tunable. We studied the consequences of the Berry curvature for n-doped 2H MoS_2 bilayers. We found that the valley Hall conductivity is finite if the inversion symmetry is broken by an out-of-plane external electric field. Furthermore, if the intrinsic SOC of the constituent layers is taken into account, the spin Hall conductivity is also finite. Regarding the valley and spin Hall effects, the interplay of SOC and finite interlayer potential can lead to a change in the sign of the interlayer contribution, while the intralayer contribution does not change sign. These results highlight the effects of stacking order, intralayer and interlayer couplings of the energy bands in shaping the Berry curvature properties of a material. One can expect that these findings can be relevant for a wide range of van der Waals materials.

The results presented in this chapter were published in Ref. [276].

Chapter 8

Induced spin-orbit coupling in twisted graphene-TMDC heterobilayers

As we discussed in Sec. 1.6.1, experiments on TMDC/graphene heterostructures have found clear evidence of induced SOC in the graphene layer. This finding was also supported by early DFT calculations of Refs. [139, 144, 145]. A direct comparison of [139, 144, 145] and the measurements discussed in Sec. 1.6.1 is not straightforward, among others, because in contrast to the theoretical calculations, in the experiments the layers were not intentionally aligned. In general, there is a twist angle between the graphene and the TMDC layers in the prepared samples, as observed e.g., in Ref. [146]. This detail was not considered in the early theoretical calculations: they assumed perfectly aligned layers. One may expect that the twist angle can affect the strength of the induced SOC. This could be one of the reasons why the SOC strength extracted from the measurements varied quite a lot between different experiments (other reasons can be the different sample preparation methods and differences in the assumptions that were used to interpret the measurements). Indeed, a recent development in the field of atomically thin materials has been the understanding that a rotation angle between the layers can have a profound effect on the electronic properties [28, 29]. This has given rise to the flourishing field of "twistronics", which aims to understand how the twist angle can be used to tailor the properties of the heterostructures of atomically thin materials.

In the following, we present our theoretical work on the microscopic mechanism and interlayer twist angle dependence of the induced SOC in graphene/TMDC heterostructures. As we will show, the interlayer twist angle can be an important tool to tune the induced SOC in graphene.

8.1 Hamiltonian of the graphene/TMDC heterostructure

We consider a heterostructure consisting of a monolayer graphene and a monolayer TMDC. As shown in Fig. 8.1(a), there can be an arbitrary twist angle θ between the layers. We will describe the induced SOC in terms of virtual band-to-band tunneling between graphene and the monolayer TMDC substrate. This perturbation approach is motivated by previous DFT calculations [144, 145] which show that the Dirac point of the graphene layer can be found in the band gap of the TMDC layer and the linear dispersion of graphene close to the Dirac point is preserved, see Sec. 1.6.1. The total Hamiltonian has three parts, describing the isolated graphene and TMDC layers and the interlayer tunneling, respectively: $H_{\rm tot} = H_{\rm gr} + H_{\rm tmdc} + H_{\rm T}$. We assume that in graphene/TMDC heterostructures the relaxation of the graphene and/or TMDC lattice can be neglected. Therefore one can use the Bloch states of the graphene and the TMDC layers to investigate the effects of the

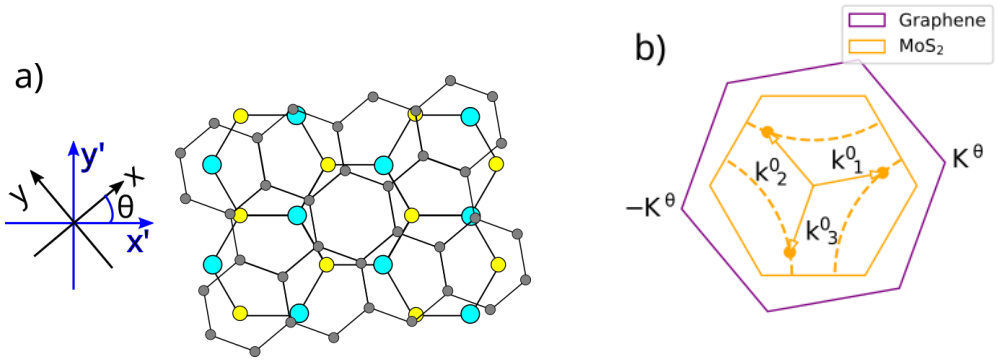

Figure 8.1: a) Schematics of a twisted graphene/TMDC bilayer with twist angle θ between the layers. The orientation of the coordinate systems $x-y$ ($x'-y'$) is fixed to the graphene (TMDC) layer. b) The Brillouin zone (BZ) of graphene (purple) and the TMDC (orange) for a finite twist angle. Backfolded TMDC BZ vectors satisfying the quasi-momentum conservation for the rotated Dirac point of graphene $\boldsymbol{K}^\theta$ are also shown. The dashed lines indicate the full paths of the backfolded vectors in the range of twist angles $\theta \in [0, \pi/3]$. Adapted from Ref. [283].

weak tunneling between the layers.

Interlayer tunneling

Following the approach of Ref. [284], one finds that the interlayer tunneling matrix element $U_{Xb}(\boldsymbol{k}, \boldsymbol{k}') = {}_{\mathrm{gr}}\langle X, \boldsymbol{k}^\theta | H_{\mathrm{T}} | b, \boldsymbol{k}' \rangle_{\mathrm{tmdc}}$ between orbital X of graphene and band b of the TMDC reads

$$U_{Xb}(\boldsymbol{k}^\theta, \boldsymbol{k}') = \sum_{\boldsymbol{G},\boldsymbol{G}'} \delta_{\boldsymbol{k}^\theta + \boldsymbol{G}^\theta, \boldsymbol{k}' + \boldsymbol{G}'} t_b(\boldsymbol{k}' + \boldsymbol{G}') \times e^{i\boldsymbol{G}^\theta \cdot (\boldsymbol{t}_X^\theta + \boldsymbol{r}_0) - i\boldsymbol{G}' \cdot \boldsymbol{t}_{X'}}. \tag{8.1}$$

Here we used the following notations. $\boldsymbol{r}_0$ denotes a possible shift between the graphene and the TMDC layers, and $\boldsymbol{t}_X$ ($\boldsymbol{t}_{X'}$) are vectors pointing to orbital X (X') in the graphene (TMDC) unit cell. $\boldsymbol{k}^\theta$ is a wavenumber in the first Brillouin zone (BZ) of graphene and $\boldsymbol{k}'$ is in the first BZ of the TMDC. $\boldsymbol{G}$, $\boldsymbol{G}'$ are reciprocal lattice vectors of graphene and TMDC, respectively. In the derivation of Eqs. (8.1) the Slater-Koster two-center approximation [285] has been used, whereby the tunneling matrix element between orbitals that can be found at positions $\boldsymbol{R}_X^\theta$ and $\boldsymbol{R}_{X'}$ depends only on $(\boldsymbol{R}_X^\theta - \boldsymbol{R}_{X'})$, i.e., $\langle \boldsymbol{R}_X^\theta | H_{\mathrm{T}} | \boldsymbol{R}_{X'} \rangle = T_{XX'}(\boldsymbol{R}_X^\theta - \boldsymbol{R}_{X'})$. The Fourier transform of $T_{XX'}(\boldsymbol{R})$ will be denoted by $t_{XX'}(\boldsymbol{q})$. The state of an electron in band b of the TMDC can be written as a linear combination of single orbital Bloch states: $|b, \boldsymbol{k}'\rangle_{\mathrm{tmdc}} = \sum_{X'} c_{bX'}(\boldsymbol{k}') |X', \boldsymbol{k}'\rangle_{\mathrm{tmdc}}$. Here X' runs over the relevant atomic orbitals of the TMDC and the complex amplitudes $c_{bX'}(\boldsymbol{k}')$ are different for each band b. In real space, we take into account tunneling processes between graphene and the closest layer of chalcogen atoms in the TMDC. This approximation allows to obtain a simple and effective parametrization of the interlayer tunneling using just two real parameters, as shown below in Eq. (8.4). We note that this approximation can be extended to take into account the tunneling between graphene and the metal atoms of the TMDC layer in a straightforward way [283]. Since we assume that the tunneling to the d atomic orbitals is suppressed, the sum over atomic orbitals in the expression of $|b, \boldsymbol{k}'\rangle_{\mathrm{tmdc}}$ runs over the three p orbitals of the nearest chalcogen layer when one calculates $U_{Xb}(\boldsymbol{k}^\theta, \boldsymbol{k}')$. Accordingly, the Fourier transform $t_b(\boldsymbol{k}' + \boldsymbol{G}')$ of the tunneling amplitude between orbital X of graphene and band b of the TMDC reads

$$t_b(\boldsymbol{k}' + \boldsymbol{G}') = \sum_{X'} c_{bX'}(\boldsymbol{k}')\, t_{X'}(\boldsymbol{k}' + \boldsymbol{G}'). \tag{8.2}$$

This quantity does not depend explicitly on X, because both atomic orbitals taken into account in the unit cell of graphene are of the same kind.

The term $\delta_{\boldsymbol{k}^\theta+\boldsymbol{G}^\theta,\boldsymbol{k}'+\boldsymbol{G}'}$ expresses quasi-momentum conservation and its meaning is further explained in Fig. 8.1(b). If the graphene layer is rotated with respect to the TMDC layer by a twist angle θ, the BZ of graphene is also rotated. Since the relevant low energy states in graphene are at the $\tau\mathbf{K}$ points of the BZ and assuming low doping one may take $\boldsymbol{k}^\theta = \tau\boldsymbol{K}^\theta$. It was pointed out in Refs. [34, 284] that one can expect $|t_b(\boldsymbol{q})|$ to decay very fast as function of $|\boldsymbol{q}|$. This can be used to restrict the summation in Eq. (8.1) to only three terms, as we now explain. Namely, one may consider only those vectors $\boldsymbol{k}'$ in the TMDC BZ that respect the quasi-momentum conservation $\tau\boldsymbol{K}^\theta + \boldsymbol{G}^\theta = \boldsymbol{k}' + \boldsymbol{G}'$ such that $|\boldsymbol{k}' + \boldsymbol{G}'|$ is minimal. For these $\boldsymbol{k}' + \boldsymbol{G}'$ vectors the corresponding $|t_b(\boldsymbol{k}' + \boldsymbol{G}')|$ will be the largest. These two conditions, i.e., quasi-momentum conservation and that $|\boldsymbol{k}' + \boldsymbol{G}'|$ is minimal, are satisfied for three distinct vectors $\tau\boldsymbol{k}'_j$, $j = 1, 2, 3$ of the TMDC BZ, see Fig. 8.1(b). The $\tau\boldsymbol{k}'_j$ vectors are related by $2\pi/3$ rotations.

For later reference we introduce the the tunneling matrix

$$\left(T(\tau\boldsymbol{k}'_j)\right)_{Xb} = e^{i\tau\boldsymbol{G}^\theta_j\cdot\boldsymbol{r}_0} t_b(\tau\boldsymbol{k}'_j) e^{i\tau\phi^X_j}, \tag{8.3}$$

where the phase ϕ^X_j is defined as $\phi^X_j = \boldsymbol{t}^\theta_X \cdot \boldsymbol{G}^\theta_j$. One can show that the band tunneling strength in Eq. (8.2) can be parameterized by two real numbers, $t_\parallel$ and $t_\perp$. For an arbitrary interlayer twist angle θ it can be written in the following way:

$$t_b(\tau\boldsymbol{K}^\theta) = i\tau[c_{bx}(\tau\boldsymbol{k}'_1)\cos\theta + c_{by}(\tau\boldsymbol{k}'_1)\sin\theta]\; t_\parallel + c_{bz}(\tau\boldsymbol{k}'_1)\; t_\perp. \tag{8.4}$$

In order to compute the band tunneling strength, Eq. (8.4) requires the knowledge of the amplitudes $c_{bp}(\tau\boldsymbol{k}'_j)$, $p = x, y, z$, which are intrinsic properties of the TMDC. We have obtained their values for MoS_2 from the tight-binding model of Ref. [73]. Finally, using DFT calculations of aligned graphene/MoS_2 structures [144], one can estimate $t_\parallel \approx t_\perp \approx 100$ meV.

Bilayer Hamiltonian

Using the results of Sec. 8.1 one can set up the following Hamiltonian for the graphene/TMDC heterostructure:

$$H = \left(\begin{array}{c|ccc} H^{\mathrm{gr},\theta}_{\tau\boldsymbol{K}}(\delta\boldsymbol{k}) & T(\tau\boldsymbol{k}'_1) & T(\tau\boldsymbol{k}'_2) & T(\tau\boldsymbol{k}'_3) \\ \hline T^\dagger(\tau\boldsymbol{k}'_1) & H^{\mathrm{tmdc}}_{\tau\boldsymbol{k}'_1}(\delta\boldsymbol{k}) & 0 & 0 \\ T^\dagger(\tau\boldsymbol{k}'_2) & 0 & H^{\mathrm{tmdc}}_{\tau\boldsymbol{k}'_2}(\delta\boldsymbol{k}) & 0 \\ T^\dagger(\tau\boldsymbol{k}'_3) & 0 & 0 & H^{\mathrm{tmdc}}_{\tau\boldsymbol{k}'_3}(\delta\boldsymbol{k}) \end{array}\right). \tag{8.5}$$

Here $\delta\boldsymbol{k}$ is a small displacement, $|\delta\boldsymbol{k}| \ll |\boldsymbol{K}|$, measured from the backfolded vectors $\tau\boldsymbol{k}'_j$. $H^{\mathrm{gr},\theta}_{\tau\boldsymbol{K}}(\delta\boldsymbol{k}) = e^{-i\tau_z\frac{\sigma_z}{2}\theta} H^{\mathrm{gr}}_{\tau\boldsymbol{K}}(\delta\boldsymbol{k}) e^{i\tau_z\frac{\sigma_z}{2}\theta}$ is the rotated graphene orbital Hamiltonian, where $H^{\mathrm{gr}}_{\tau\boldsymbol{K}}(\delta\boldsymbol{k}) = v_F(\tau_z\sigma_x\delta k_x - \sigma_y\delta k_y)$, see Sec. 1.2.1. Note, that we express the Hamiltonian Eq. (8.5) in the coordinate system aligned with the TMDC layer [see Fig. 8.1(a)]. $H^{\mathrm{tmdc}}_{\tau\boldsymbol{k}'_j}(\delta\boldsymbol{k})$ denotes the Hamiltonian of the TMDC and contains the dispersion of those bands that we take into account, e.g., in the simplest case the VB and the CB. The dispersion of the bands can be obtained, e.g., using the $\mathbf{k}\cdot\mathbf{p}$ method or taken from TB calculations. In our work $H^{\mathrm{tmdc}}_{\tau\boldsymbol{k}'_j}(\delta\boldsymbol{k})$ also includes the effects of the intrinsic SOC of the TMDC on the band structure. We used the TB model of Ref. [73] to obtain $H^{\mathrm{tmdc}}_{\tau\boldsymbol{k}'_j}(\delta\boldsymbol{k})$. Finally, $T(\tau\boldsymbol{k}'_j)$ are interlayer tunneling matrices describing the tunneling from the $\tau\boldsymbol{K}^\theta$ point of graphene to the $\tau\boldsymbol{k}'_j$ points of the TMDC BZ for each band b taken into account in $H^{\mathrm{tmdc}}_{\tau\boldsymbol{k}'_j}$. They were defined explicitly in Eq. (8.3). We use the approximation where the tunneling matrices do not depend on the value of the small wave vector $\delta\boldsymbol{k}$ and assume spin-independent tunneling, therefore $T(\tau\boldsymbol{k}'_j)$ is diagonal in spin space.

8.2 Analytical results for the induced SOC

The bilayer Hamiltonian (8.5) can serve as a starting point for further perturbation theory steps. The small parameters in the perturbation theory are the interlayer tunneling amplitudes $t_b(\tau \boldsymbol{k}'_j)$. As we show below, these calculations can help to understand how the intrinsic properties of the monolayer TMDC determine the induced SOC in graphene.

One may use the Löwdin partitioning to derive an effective graphene Hamiltonian

$$H_{\text{eff}}^{gr,\theta} = e^{-i\tau_z \frac{\sigma_z}{2}\theta} H_{\tau \boldsymbol{K}}^{\text{gr}}(\delta \boldsymbol{k}) e^{i\tau_z \frac{\sigma_z}{2}\theta} + H_R^{gr} + H_{vZ}^{gr}, \tag{8.6}$$

where H_R^{gr} and H_{vZ}^{gr} denote the Hamiltonian of the induced Bychkov-Rashba and valley Zeeman SOC. One may also perform a unitary transformation $e^{i\tau_z \frac{\sigma_z}{2}\theta} H_{\text{eff}}^{gr,\theta} e^{-i\tau_z \frac{\sigma_z}{2}\theta}$, which leaves H_{vZ} unchanged and one finds

$$H_{\text{eff}}^{gr} = H_{\tau \boldsymbol{K}}^{\text{gr}}(\delta \boldsymbol{k}) + e^{i\tau_z \frac{\sigma_z}{2}\theta} H_R^{gr} e^{-i\tau_z \frac{\sigma_z}{2}\theta} + H_{vZ}^{gr}. \tag{8.7}$$

valley Zeeman SOC

Using second-order perturbation theory the correction to the graphene Hamiltonian reads

$$\delta H_{Xs,X's}^{\text{gr},\tau} = \sum_{j,b} \frac{[T(\tau \boldsymbol{k}'_j)]_{X,b} \, [T(\tau \boldsymbol{k}'_j)]^{\dagger}_{b,X'}}{E_D^{\text{gr}} - E_{bs}^{\text{tmdc}}(\tau \boldsymbol{k}'_j + \delta \boldsymbol{k})}, \tag{8.8}$$

where $X, X' = A, B$ refers to the graphene sublattices, $s = \uparrow, \downarrow$ is the spin index. The energy of the Dirac point of graphene is denoted by E_D^{gr} and without the loss of generality, one can fix $E_D^{\text{gr}} = 0$. $E_{bs}^{\text{tmdc}}(\tau \boldsymbol{k}'_j + \delta \boldsymbol{k})$ is the energy of band b of the TMDC at the BZ point $\tau \boldsymbol{k}'_j + \delta \boldsymbol{k}$ and s is the spin index. Note, that since the tunneling matrices $[T(\tau \boldsymbol{k}'_j)]_{X,b}$ are spin-preserving, $\delta H_{X\uparrow,X'\downarrow}^{\text{gr},\tau} = 0$.

By expanding E_{bs}^{tmdc} up to linear order in $\delta \boldsymbol{k}$ one can show that the diagonal matrix elements $X = X'$ describe the induced valley Zeeman type SOC in graphene:

$$H_{vZ} = \lambda_{vZ} \, \tau s_z, \tag{8.9}$$

where s_z is a Pauli matrix for spin. The SOC strength λ_{vZ} is given by

$$\lambda_{vZ} = 3 \sum_b \frac{|t_b(\tau \boldsymbol{K}^{\theta})|^2 \Delta_{0,b}(\boldsymbol{k}'_1)}{E_b^2(\boldsymbol{k}'_1) - \Delta_{0,b}^2(\boldsymbol{k}'_1)}, \tag{8.10}$$

where $E_b(\boldsymbol{k}'_1)$ is the energy of band b (ignoring SOC) computed with respect to the Dirac point of graphene. Furthermore, $\Delta_{0,b}(\boldsymbol{k}'_1)$ is the spin-orbit splitting of band b at $\boldsymbol{k}'_1$ due to the diagonal part of the intrinsic SOC of the TMDC, see Sec. 4.1.2. According to Eq. (8.10), the strength of the induced valley Zeeman SOC has three main contributions from each band b: it is proportional to the magnitude square of the tunneling strength $|t_b|^2$ and to the spin splitting $\Delta_{0,b}$, while it is inversely proportional to the energy difference $E_b^2 - \Delta_{0,b}^2$. The induced valley Zeeman type SOC can be understood as follows: the bands of the TMDC layer are, in general, spin-split due to the intrinsic SOC of the TMDC and this is then imprinted on the bands of the proximity graphene layer as well. Eq. (8.10) shows explicitly how λ_{vZ} depends on the intrinsic properties of the TMDC substrate and the twist angle θ between the layers. Namely, θ determines the wavenumber $\boldsymbol{k}'_1$ and as well as the tunneling strength $t_b(\tau \boldsymbol{K}^{\theta})$ through Eq. (8.4). As a simple example, in Fig. 8.2 we show how $\Delta_{0,b}(\boldsymbol{k}'_1)$ and the tunneling amplitudes to the CB and VB change as a function of θ for MoS_2. We defer the numerical calculations of λ_{vZ} to Sec. 8.3.

We note that the off-diagonal elements $X \neq X'$ of Eq. (8.8) describe the renormalization of graphene's Fermi velocity due to the coupling to the TMDC layer. We found that this is a small effect and therefore do not discuss it here.

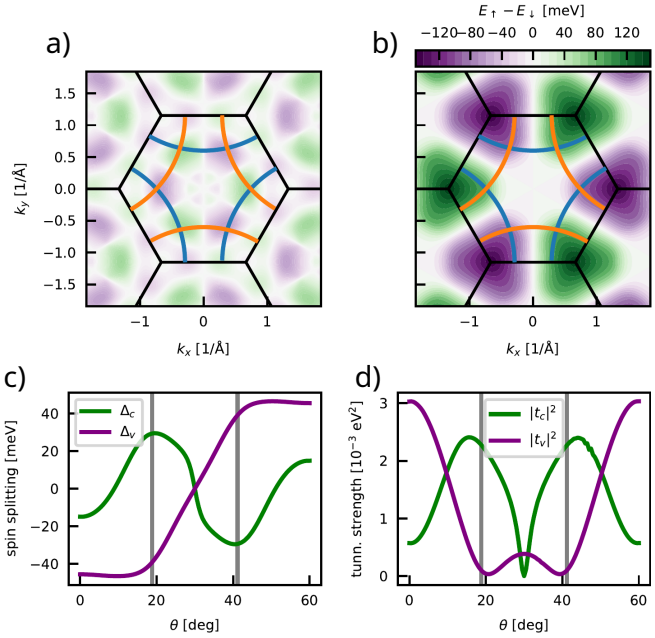

Figure 8.2: Spin-orbit splitting in the (a) conduction and (b) valence band of MoS_2 in the whole BZ. Blue (orange) arcs indicate the paths of the three backfolded vectors $\boldsymbol{k}'_j$ ($-\boldsymbol{k}'_j$) for Dirac point $\boldsymbol{K}$ ($-\boldsymbol{K}$). c) Spin-orbit splitting along the blue paths in (a) (green line) and in (b) (purple line). d) $|t_b(\tau \boldsymbol{K}^\theta)|^2$ for a tunneling process between graphene and the CB (green line) and VB (purple line) of MoS_2. Adapted from Ref. [165].

Bychkov-Rashba SOC

Traditionally, the Rashba SOC in graphene was understood in terms of the symmetry breaking effect of a perpendicular electric field [286, 138]. However, the DFT calculation of Ref. [145] indicated that a finite Bychkov-Rashba SOC is induced in graphene in graphene/TMDC bilayers even if the external electric field is zero. We show that this can be understood in terms of virtual interlayer tunneling processes that are facilitated by off-diagonal spin-flipping elements of the intrinsic SOC matrix of the TMDC layer. In general, such matrix elements can be non-zero between pairs of bands if one of the bands is symmetric (even) and the other one is antisymmetric (odd) with respect to reflection on the horizontal mirror plane of the TMDC. We have already encountered such matrix elements in Sec. 4.1.2, in the context of the SOC Hamiltonian at the $\pm K$ point of the BZ.

The Hamiltonian of the induced Bychkov-Rashba type SOC can be obtained from third-order perturbation theory:

$$(\delta H_R^{gr})_{Xs,X's'} = \sum_{j,b,b',s'',s'''} \frac{\left(T(\tau \boldsymbol{k}'_j)\right)_{Xs,bs''} (H_{\mathrm{soc}})_{bs'',b's'''} \left(T^\dagger(\tau \boldsymbol{k}'_j)\right)_{b's''',X's'}}{[E_D^{\mathrm{gr}} - E_b^{\mathrm{tmdc}}(\tau \boldsymbol{k}'_j)][E_D^{\mathrm{gr}} - E_{b'}^{\mathrm{tmdc}}(\tau \boldsymbol{k}'_j)]}. \tag{8.11}$$

where s, s', s'' are spin indices, $b \neq b'$ are band indices running over the bands of the TMDC layer and $(H_{\mathrm{soc}})_{bs,b's'}$ denotes spin-flip off-diagonal elements of the intrinsic SOC matrix. The details of the calculations for H_R^{gr} can be found in Ref. [165, 283]. One can show that the Hamiltonian of the induced Rashba SOC can be written as

$$H_R^{gr} = -\frac{\lambda_R(\boldsymbol{k}'_1)}{2} e^{i\frac{s_z}{2}\vartheta_R(\boldsymbol{k}'_1)} \left(\tau_z \sigma_x s_y + \sigma_y s_x\right) e^{-i\frac{s_z}{2}\vartheta_R(\boldsymbol{k}'_1)}. \tag{8.12}$$

This form of H_R^{gr} was also obtained in Ref. [164]. As one can see, the Bychkov-Rashba type SOC is characterized by two constants: $\lambda_R(\boldsymbol{k}'_1)$ and $\vartheta_R(\boldsymbol{k}'_1)$. $\lambda_R(\boldsymbol{k}'_1)$ denotes the strength of the induced

SOC. $\vartheta_R(\boldsymbol{k}'_1)$ is quantum phase which depends on the interlayer tunneling and on the spin-flip off-diagonal matrix elements of the intrinsic SOC of the TMDC. Note that both $\lambda_R(\boldsymbol{k}'_1)$ and $\vartheta_R(\boldsymbol{k}'_1)$ depend implicitly on the interlayer twist angle θ through $\boldsymbol{k}'_1$. Similarly to Eq. (8.10), one can derive explicit expressions for $\lambda_R(\boldsymbol{k}'_1)$ and $\vartheta_R(\boldsymbol{k}'_1)$ in terms of the interlayer tunneling and the band structure of the TMDC layer. They are rather complicated and hence not shown here, but can be evaluated numerically and the results will be reported in Sec. 8.3.

The terms containing ϑ_R appear because for a general interlayer twist angle the symmetry of the heterostructure is lowered from C_{3v} to C_3. Thus, the form of the Bychkov-Rashba Hamiltonian given in Eq. (8.11) is valid not only for graphene/TMDC heterostructures, but for a wide range of twisted heterostructures consisting of hexagonal layers. This includes heterostructures of graphene with semiconductor [287, 288], ferromagnetic [289], and topological insulator [290, 291] structures. However, the physical significance of ϑ_R was not appreciated before and the relation of ϑ_R to the interlayer twist angle θ was not discussed. Our numerical calculations for graphene/TMDC twisted bilayers indicate that ϑ_R can acquire finite values, see Sec. 8.3. It is important to note that for $\theta = l\pi/6$, $l = 0, 1, 2\ldots$ the vertical mirror planes of the graphene and the TMDC lattice line up and the system, as a whole, has C_{3v} symmetry. One can show that in this case H_R simplifies to $H_R = (-1)^{n+1}\frac{\lambda_R(\theta)}{2}(\tau_z\sigma_x s_y - \sigma_y s_x)$, where n is an integer. This is the form of H_R which was used previously in the literature [162, 145]. We found that the integer n can be, in general, both even and odd [see Fig.8.5], which means that $\lambda_R(\theta)$ can acquire a negative sign as θ is changed.

As already mentioned above Eq. (8.7), it is convenient to change to the coordinate system fixed to the graphene layer using the transformation $e^{-i\tau_z\frac{\sigma_z}{2}\theta}H_R^{gr}e^{i\tau_z\frac{\sigma_z}{2}\theta}$. From the explicit form of the transformed Rashba Hamiltonian one finds that the non-zero matrix elements are $\propto \lambda_R e^{\pm i(\vartheta_R+\theta)}$, i.e., the sum of the geometric angle θ and the quantum phase ϑ_R plays an important role. Looking at Eqs. (8.12) and (8.7) one may get the impression that the phase factors $e^{\pm i(\vartheta_R+\theta)}$ are not important because they come about due to a unitary transformation. Indeed, the phase factors $e^{\pm i(\vartheta_R+\theta)}$ do not change the band structure. However, one can easily show that when $\vartheta_R+\theta \neq n\pi$, the spin-orbit field $\mathbf{s}(\mathbf{q}) = (\langle\hat{s}_x\rangle, \langle\hat{s}_y\rangle, \langle\hat{s}_z\rangle)^T$ is not tangential to the Fermi surface, which is the case for the usual Bychkov-Rashba SOC. However, the orientation of $\mathbf{s}(\mathbf{q})$ can have a concrete physical consequence and we will comment on this in Sec. 8.3.

8.3 Numerical calculations

In Sec. 8.1 we introduced a simplified model whereby the interlayer tunneling between the graphene and the TMDC layer depended only on the p atomic orbitals of the nearest chalcogen layer. This model can be extended to take into account the tunneling between graphene and the the d orbitals of the metal atoms of the TMDC layer as well. In the numerical calculations shown below both type of tunneling was taken into account, for details see Ref. [283].

In addition to tunneling amplitudes $t_b(\tau\mathbf{k}'_j)$, there are further parameters that enter the numerical calculations, which we now briefly discuss.

- *The value of the band gap E_g of the TMDC.* One can take E_g either from experiments (when available) or from previous theoretical works. We use the TB model of Ref. [73] to calculate the band structure, the SOC Hamiltonian matrix elements and the interlayer tunneling amplitude, therefore we also used the E_g of this model. Although this model itself is based on DFT calculations, the value of E_g is different from what one can extract from the calculations of Ref. [145] that were performed for MLG/TMDC supercells. For example, in the case of MoS_2 the model of Ref. [73] has a band gap that is 17% larger than the corresponding E_g given in Ref. [145]. See Table 8.1 for the E_g values used in this work.

- *The position of the Dirac point of graphene within the band gap of the TMDC.* We describe the energy of the Dirac point of graphene in the band gap of the TMDC by a number $f_G \in [0, 1]$. The value of f_G is a linear function of the position of the Dirac point in the

TMDC band gap. When $f_G = 0$, the Dirac point is aligned with the TMDC valence band edge, for $f_G = 1$ the Dirac point has the same energy as the TMDC conduction band edge. We used the f_G values taken from DFT calculations, when available, its value could also be taken from experiments [146, 147]. See Table 8.1 for the f_G values used in this work.

- *The number of bands in the model for the TMDC layer.* The explicit expression to calculate λ_{vZ} involve a sum over the contributions of TMDC bands, see Eq. (8.10). Similarly, in order to calculate ϑ_R and λ_R, one needs to sum over pairs of even (e) and odd (o) bands. In Ref. [165] we used the approximation that only the CB and the VB were taken into account for λ_{vZ}, and three pairs of e-o bands for λ_R. As it is shown in Sec. 8.3.1 below, this already leads to qualitatively good results in many cases. It turns out [283] that due to band crossings and near-degeneracies of certain e bands, more pairs of e and o bands need to be taken into account in the calculation of λ_R for $\theta \approx \pi/6$. The TB model that we use involves 11 bands of the TMDC layer. Unless otherwise indicated, we use the contributions of all 11 bands to calculate λ_{vZ}, and 30 pairs of e and o bands for the ϑ_R and λ_R calculations.

- *The TB model of the TMDC.* We note that a comparison of the DFT band structure calculations and the corresponding results of the TB model indicates that the TB model is less accurate for the bands above the band gap [73]. This can add further uncertainty to the results, especially in the case graphene/MoS_2, where $f_G = 0.974$, i.e., the relative contributions of e-o band pairs above E_g is larger than the contribution coming from the valence bands.

	E_g (DFT)	E_g (exp)	f_G (DFT)	f_G (exp)
MoS_2	1.807 eV[73]	2.0 eV[146]	0.974 [145]	0.55 [146]
WSe_2	1.638 eV[73]	1.95 eV[147]	0.161 [145]	0.426 [147]

Table 8.1: Band gap E_g and MLG Dirac point energy position f_G parameters extracted from DFT calculations and angle resolved photoluminescence (ARPES) experiments.

8.3.1 Twist angle dependence of λ_{vZ} and λ_R

We now present the results of numerical calculations for λ_{vZ} and λ_R. We consider two heterostructures, MLG/MoS_2 and MLG/WSe_2.

In Fig. 8.3(a) we show calculations for λ_{vZ} vs θ for graphene/MoS_2 using the DFT parameters for E_g and f_G (see Table 8.1). The dashed curve in Fig. 8.3(a) corresponds to the case when only the p atomic orbitals of the chalcogen atoms are taken into account in the interlayer tunneling and the summation in Eq. (8.10) is restricted to the CB and the VB. The thin solid line is obtained by considering both the p orbitals of the chalcogen atoms and the d orbitals of the metal atoms in the interlayer tunneling and, as in the previous case, only tunneling to the VB and the CB is taken into account. The thick solid line shows the result when contributions of all 11 bands of the TB model are summed up in the evaluation of Eq. (8.10). As one can see, the λ_{vZ} vs θ dependence is qualitatively the same in all three cases. The results suggests that λ_{vZ} is highly tunable by the interlayer twist angle θ and going from $\theta = 0$ to $\theta \approx 20^\circ$ it is significantly increased. The peak in λ_{vZ} around $\theta = 20^\circ$ is expected for multiple reasons. First of all, note that for the particular f_G value used in the calculations, the dominant contribution to λ_{vZ} comes from the CB of the TMDC layer. Close to $\theta = 20^\circ$ both the spin splitting $\Delta_{0,c}(\boldsymbol{k}'_1)$ and tunneling strength $t_c(\boldsymbol{K}^\theta)$ reach their largest absolute values, see Figs. 8.2(c) and (d), respectively. For $\Delta_{0,c}(\boldsymbol{k}'_1)$ this happens because the backfolded points $\boldsymbol{k}'_j$ in the TMDC BZ can be found very close to the Q valley of the CB, which has large spin splitting. Moreover, the energy distance between the Dirac point of graphene and the bottom of the Q valley is also smaller than for other $\boldsymbol{k}'_1$ points in the BZ. These consideration,

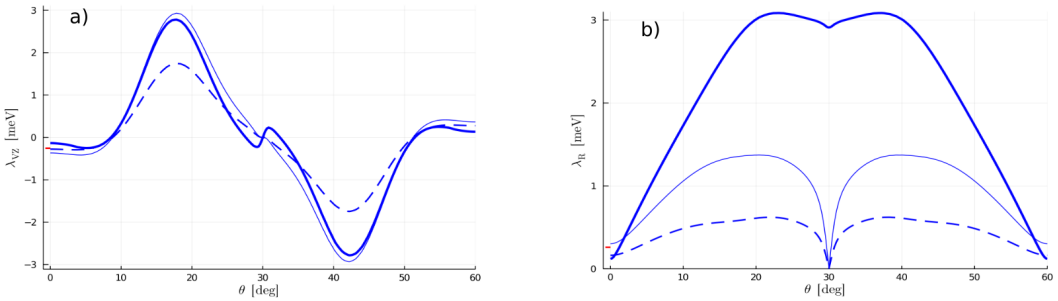

Figure 8.3: a) λ_{vZ} and b) λ_R for MLG/MoS_2 as a function of interlayer twist angle θ using the DFT parameters given in Table 8.1. Different lines correspond to different tunneling amplitudes and number of bands in the calculations, see text for details. Adapted from Ref. [283].

together with Eq. (8.10) can explain the enhancement of λ_{vZ} for $\theta = 20°$. On the other hand, λ_{vZ} vanishes for $\theta = 30°$. In this case the backfolded points $\boldsymbol{k}'_j$ lie on the Γ–M line [see Fig. 8.2(a)-(b)] and the spin-orbit splitting of all TMDC bands is zero along this line.

In Fig. 8.3(b) we show similar calculations for λ_R vs θ, using the DFT parameters for E_g and f_G. The meaning of the dashed and thin solid lines is the same as in Fig. 8.3(a) and the contribution of three pairs of even and odd bands have been used. The larger tunneling strength when both types of tunneling is taken into account leads to overall larger values of λ_R, but the θ dependence of the two results agree, including the deep minimum at $\theta = 30°$. However, when all possible even-odd pairs of bands are included in the calculation (thick solid line), this minimum becomes a small dip and the value of λ_R is significantly enhanced. This happens because of band crossings and near-degeneracies of certain e bands which means that more pairs of e and o bands need to be taken into account.

The above discussions illustrate how the interlayer tunneling, band-edge energy difference, the band structure and the intrinsic SOC of the TMDC layer determine the twist angle dependence of the induced SOC in graphene.

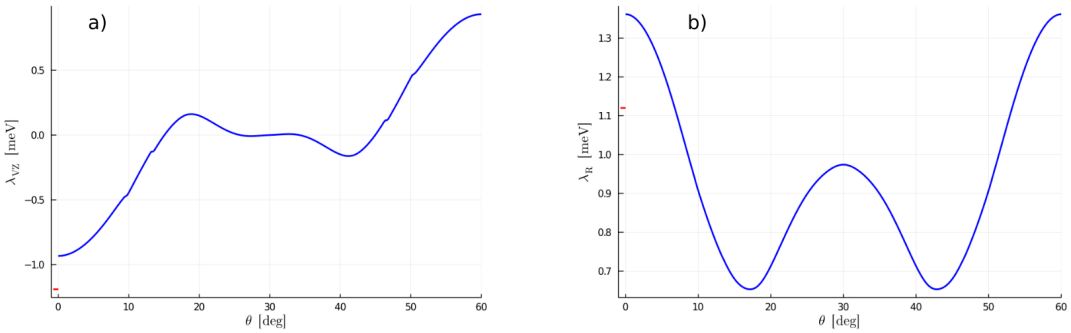

Figure 8.4: a) λ_{vZ} and b) λ_R for MLG/WSe_2 as a function of interlayer twist angle θ using the DFT parameters given in Table 8.1. Adapted from Ref. [283].

Similar calculations to the MLG/MoS_2 case can also be performed for MLG/WSe_2. The twist angle dependence of λ_{vZ} and λ_R are shown in Fig. 8.4. Contributions from all bands or pairs of bands of the TB model are taken into account. Importantly, one can see that both $\lambda_{vZ}(\theta)$ and $\lambda_R(\theta)$ are different from the corresponding results of the MLG/MoS_2 heterostructure shown in Fig. 8.3. For example, $\lambda_{vZ}(\theta)$ is a roughly monotonous function of θ and it does not have a large peak at $\theta \approx 20°$. This is mainly due to the fact that the Dirac point of graphene is closer to the VB of WSe_2 and we used $f_G = 0.161$ in these calculations versus $f_G = 0.976$ in Fig. 8.3. Therefore

in this case the valence bands give larger contributions to the induced SOC.

8.3.2 Twist angle dependence of ϑ_R

The results for the $\vartheta_R + \theta$ vs θ dependence for MoS_2 and WSe_2 are shown in Figs. 8.5(a) and (b), respectively. We used the parameters given in Table 8.1. In the case of MLG/MoS_2 one can see

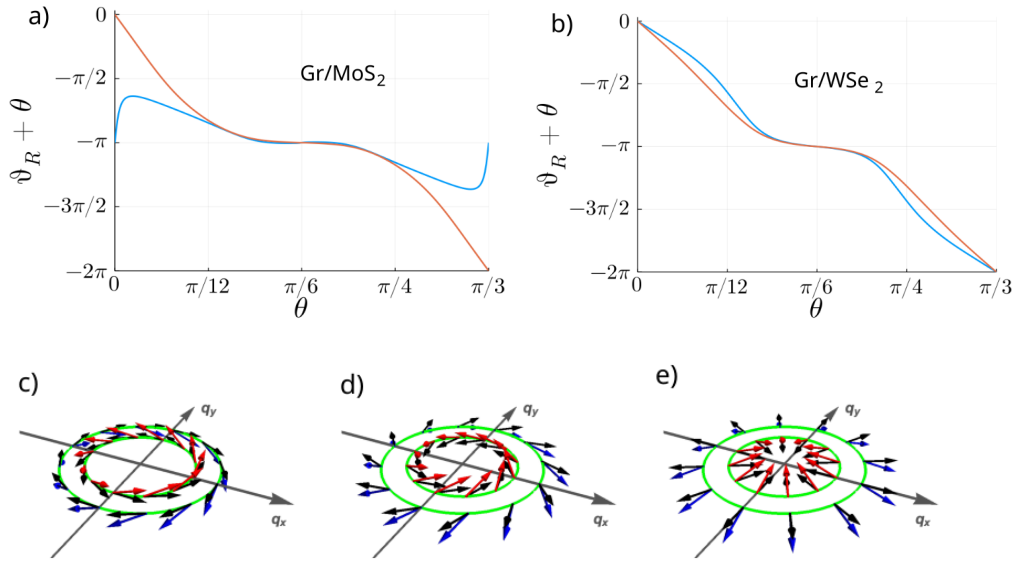

Figure 8.5: Twist angle dependence of ϑ_R and the spin-orbit field $\mathbf{s}(\mathbf{q})$. a) and b) $\vartheta_R + \theta$ as a function of θ for MoS_2 and WSe_2, respectively. Blue (red) curves were calculated using DFT (experimental) parameters, see main text for details. $\mathbf{s}(\mathbf{q})$ for c) $\theta = 0$, d) $\theta = 7°$ and e) for $\theta = 15°$, using the ϑ_R vs θ dependence shown in Fig. 8.5(b). The green circles indicate the Fermi surfaces for the two spin subbands. $\mathbf{s}(\mathbf{q})$ lies in the plane if only Rashba SOC is induced in graphene (black arrows), whereas it acquires a non-zero $\langle \hat{s}_z \rangle$ component if the valley Zeeman type SOC is finite as well (blue and red). Adapted from Ref. [283].

that $\vartheta_R + \theta$ remains in a limited range around π as θ varies from 0 to $\pi/3$ [Fig. 8.5(a)] when the DFT parameter set is used. However, for parameters extracted from ARPES measurements $\vartheta_R + \theta$ covers the entire range $[0, 2\pi]$. For MLG/WSe_2 one finds that $\vartheta_R + \theta$ covers the whole range of $[0, 2\pi]$ [Fig. 8.5(b)] and the results obtained from the two parameter sets qualitatively agree. The difference between the results for the two materials is mainly due to the different energy alignment of the Dirac point in the TMDC band gap.

In Figs. 8.5(c)-(e) we show the calculations for the spin-orbit field $\mathbf{s}(\mathbf{q}) = (\langle \hat{s}_x \rangle, \langle \hat{s}_y \rangle, \langle \hat{s}_z \rangle)^T$ as a function of θ. We considered two cases: i) when both the Bychkov-Rashba and the valley Zeeman SOC is taken into account and therefore all three components of $\mathbf{s}(\mathbf{q})$ are non-zero, ii) only the Bychkov-Rashba SOC is considered, which means that $\langle \hat{s}_z \rangle = 0$ and $\langle \hat{s}_x \rangle, \langle \hat{s}_y \rangle \neq 0$. When $\theta = l\pi/6$, $l = 0, 1, 2 \ldots$ then the heterostructure has a C_{3v} symmetry and $(\langle \hat{s}_x \rangle, \langle \hat{s}_y \rangle)^T$ is perpendicular to the wave vector $\mathbf{q}$ [Figs 8.5(c)]. This is the case known from numerous studies on 2DEG. However, for a general θ this is not any more the case, and the vector $(\langle \hat{s}_x \rangle, \langle \hat{s}_y \rangle)^T$ is rotated by an angle $\vartheta_R + \theta$ with respect to the tangential direction. This means that it has both tangential and perpendicular component to the Fermi surface and according to our calculations even a "hedgehog"-like spin polarization shown in Fig. 8.5(e) can occur.

We note that recently two experimental works [292, 293] based on charge-to-spin conversion type experiments have reported observations which suggest that the spin polarization can indeed

be of the more general type shown in Fig. 8.5(d).

8.4 Quantum interference effects in trilayers

Our methodology makes it possible to study twisted TMDC/graphene/TMDC trilayers as well, which would be difficult by other methods. In such trilayer structures there are in general two twist angles, denoted by $\theta^{(b)}$ and $\theta^{(t)}$, for the bottom and top TMDC layers. This allows an even broader control of the induced SOC in graphene.

Since the layers are only weakly coupled, the effective graphene Hamiltonian is $H^{gr}_{\text{eff}} = H_{\tau\mathbf{K}}(\delta\mathbf{k}) + H^{(t)}_{soc} + H^{(b)}_{soc}$, where the indices t and b refer to the contribution of the top and bottom TMDC layers, respectively. Note, that $H^{(b)}_{soc} = H^{(b)}_{vZ} + H^{(b)}_{R}$ and $H^{(t)}_{soc} = H^{(t)}_{vZ} - H^{(t)}_{R}$, i.e., $H^{(b)}_{R}$ and $H^{(t)}_{R}$ have a different sign. As a simple physical explanation, consider the case when the two TMDC layers are perfectly aligned and $\theta^{(b)} = \theta^{(t)}$. Then the graphene layer corresponds to a horizontal mirror plane of the whole stack, which dictates that the Rashba SOC must vanish.

One can define the complex Rashba coefficient for the trilayer system (tls) by

$$\bar{\lambda}^{(tls)}_{R} = \lambda^{(b)}_{R} e^{i\left(\vartheta^{(b)}_{R} + \theta^{(b)}\right)} - \lambda^{(t)}_{R} e^{i\left(\vartheta^{(t)}_{R} + \theta^{(t)}\right)}, \tag{8.13}$$

and we introduce the notations $\lambda^{(tls)}_{R} = \left|\bar{\lambda}^{(tls)}_{R}\right|$ and $\vartheta^{(tls)} = \text{Arg}\left[\bar{\lambda}^{(tls)}_{R}\right]$. In terms of these quantities the induced Rashba type SOC can be written as $H^{(tls)}_{R} = \frac{\lambda^{(tls)}_{R}}{2} e^{i\frac{s_z}{2}\vartheta^{(tls)}} \left(\tau_z \sigma_x s_y - \sigma_y s_x\right) e^{-i\frac{s_z}{2}\vartheta^{(tls)}}$. An important consequence of the phase $e^{i(\vartheta_R + \theta)}$ discussed for bilayers is that the strength $\lambda^{(tls)}_{R}$ of the induced Bychkov-Rashba SOC in trilayer stacks can be affected by quantum interference effects if $\vartheta^{(b)}_{R} + \theta^{(b)}$ and/or $\vartheta^{(t)}_{R} + \theta^{(t)}$ are non-zero. This can be interpreted as an interference of the virtual hopping processes to the two TMDC layers that give rise to the induced Rashba SOC. Thus,

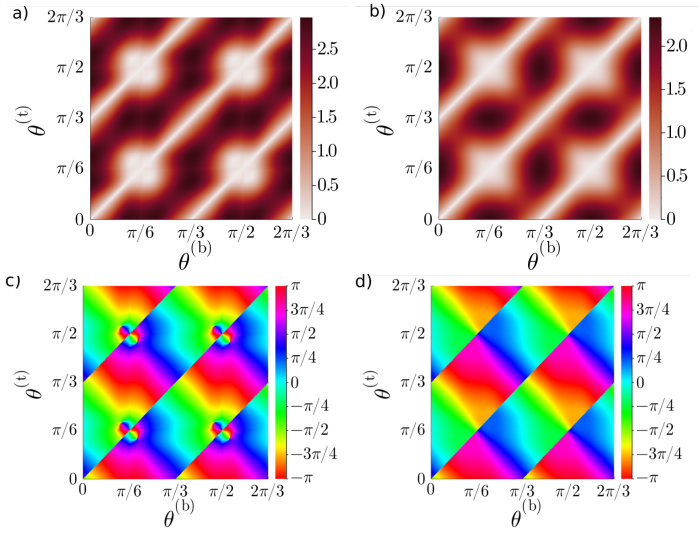

Figure 8.6: Calculations of the induced Bychkov-Rashba SOC for TMDC/graphene/TMDC trilayers as a function of the twist angles $\theta^{(t)}$ and $\theta^{(b)}$. a) and b) $\lambda^{(tls)}_{R}$ for two-sided encapsulation of graphene by MoS_2 and WSe_2, respectively. c) and d) the angle $\vartheta^{(tls)}$ for MoS_2 and WSe_2 two-sided encapsulation. We used parameters from DFT band structure calculations. Adapted from Ref. [283].

λ_R can be changed not only by external electric field, known from studies on 2DEG [216, 294], or by pressure, as it has recently been demonstrated for graphene/TMDC proximity structures [295], but in trilayers λ_R can also be effected by quantum interference effects. In Fig. 8.6 we show the

results of numerical calculations for $\bar{\lambda}_R^{(tls)}$ as a function of the twist angles $\theta^{(t)}$ and $\theta^{(b)}$. As one can see in Figs. 8.6(a) and (b), there are extended regions where $\lambda_R^{(tls)}$ is very small. This is due to the fact that for those twist angles the λ_R and ϑ_R contributions of both layers change slowly and they approximately cancel in Eq. (8.13). Regarding the phase $\vartheta^{(tls)}$, the apparent lines Figs. 8.6(c) and (d) correspond to $\lambda_R^{(tls)} = 0$, where $\vartheta^{(tls)}$ is not defined.

Experimental detection of the induced SOC in trilayers

We now briefly outline one of the possible approaches that can help to detect the twist angle dependence of the induced SOC in TMDC/graphene/TMDC heterostructures. It is based on the measurement of the anisotropy of the out-of-plane $\tau_\perp$ and in-plane $\tau_\parallel$ spin lifetimes. As already mentioned in Sec. 1.6.1, assuming a strong intervalley scattering in graphene, the ratio of the spin lifetimes in a graphene/TMDC bilayer is given by $\tau_\perp/\tau_\parallel = (\lambda_{vZ}/\lambda_R)^2(\tau_{iv}/\tau_p)+1/2$, where τ_{iv} (τ_p) is the intervalley (momentum) scattering time [155]. Taking now, e.g., a WSe_2/graphene/WSe_2 heterostructure, one can consider a case where $\theta^{(b)}$ is kept fixed while $\theta^{(t)}$ is changed. The ratio λ_{vZ}/λ_R can, in principle, be tuned in a wide range in such trilayer heterostructures. For example, λ_R is never zero for graphene/TMDC whereas one can choose $\theta^{(b)}$ and $\theta^{(t)}$ such that $\lambda_{vZ}^{(tls)} \neq 0$ and $\lambda_R^{(tls)} = 0$. Using $\tau_{iv}/\tau_p \approx 5$ [155], $\tau_\perp/\tau_\parallel$ as a function of $\theta^{(t)}$ is plotted for $\theta^{(b)} = 0°$ and $\theta^{(b)} = 30°$ in Fig. 8.7. When $\theta^{(b)} = 0$ and $1° < \theta^{(t)} \lesssim 15°$, then $\lambda_R^{(tls)}$ becomes small but $\lambda_{vZ}^{(tls)}$

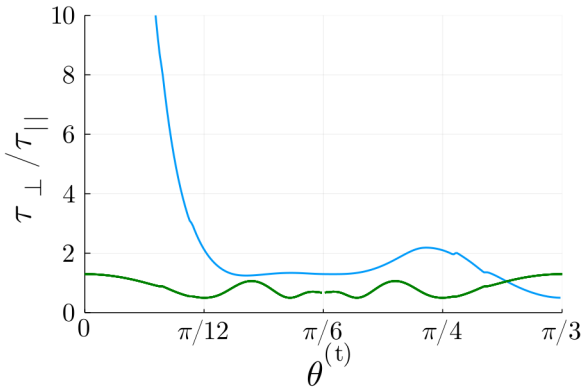

Figure 8.7: Calculated spin lifetime anisotropy in a WSe_2/graphene/WSe_2 heterostructure as a function of $\theta^{(t)}$ for $\theta^{(b)} = 0°$ (blue) and $\theta^{(b)} = 30°$ (green).

is finite, therefore $\tau_\perp/\tau_\parallel$ strongly increases as a function of $\theta^{(t)}$. In contrast, if $\theta^{(b)} = 30°$ then $\tau_\perp/\tau_\parallel$ remains finite for all $\theta^{(t)}$ angles. This shows that spin relaxation anisotropy measurements can help to obtain clear indications of the twist angle dependence of the induced SOC.

8.5 Summary

In summary we studied the induced SOC in graphene/TMDC and TMDC/graphene/TMDC heterostructures. We developed a theoretical framework based on virtual band-to-band tunneling to explain the microscopic mechanism of the induced SOC. This framework simplifies the study of heterobilayers where coupling between the layers is weak and the band structure of the constituent layers is well known and understood. It also helps to understand the role of the intrinsic properties of the individual layers, as well as the role of the energy alignment of the energy bands. We found that one can induce valley Zeeman and Bychkov-Rashba type SOC in graphene. In contrast, the strength of the intrinsic SOC cannot be changed by TMDC substrate. The valley Zeeman SOC is characterized by the SOC constant λ_{vZ}, which gives its strength. The induced Rashba type SOC

in twisted hexagonal bilayers can be parameterized by the strength λ_R and a spin-rotation angle ϑ_R. Our methodology allows to map out the interlayer twist angle dependence of the induced SOC. Using numerical calculations we found that both λ_{vZ} and λ_R can be significantly enhanced as a function of the interlayer twist angle. The parameter ϑ_R can also be changed, which affects the spin polarization of the graphene states such that it may not be tangential to the Fermi surface. Regarding TMDC/graphene/TMDC trilayers, we pointed out that quantum interference effects can affect the strength $\lambda_R^{(tls)}$ as well as the phase $\theta^{(tls)}$ of the Rashba SOC. We showed that the twist angle dependence of λ_{vZ} and λ_R could be detected through spin anisotropy measurements in TMDC/graphene/TMDC trilayers.

The methodology based on band-to-band tunneling to describe the induced SOC in graphene was published in Ref. [165]. Numerical calculations for the twist angle dependence of λ_{vZ} and λ_R were published in Refs. [165, 283]. The importance of ϑ_R and the related interference effects in trilayer structures were discussed in Ref. [283].

Chapter 9

Thesis Statements

1. We derived the general form of the intrinsic SOC for flat ABC trilayer graphene. Using a combination of group-theoretical and tight-binding approaches we showed that for the calculation of the SOC constants the d_{xz}, d_{yz} and d_{z^2} atomic orbitals need to be taken into account in addition to the usually considered p_z atomic orbitals. We determined that the intrinsic SOC can be described by seven SOC constants. Four of these SOC constant can be characterized as interlayer SOC. One of them lifts the otherwise four-fold degeneracy of the high-energy split-off bands. The remaining two SOC constants are intralayer ones and they due to the fact that the two carbon atoms in the top and bottom graphene layer of the ABC graphene have different atomic environment. We expressed the SOC constants in terms of atomic orbital energy differences and wavefunction overlaps. This allowed us to give an estimate for the values of the SOC constants of ABC graphene by making use of previously known results for AB stacked bilayer graphene. From the original model for ABC graphene we derived an effective low-energy Hamiltonian which is usually more convenient to use. We showed that the interlayer SOC parameters of the original model determine the leading momentum dependent SOC term in the effective model.

   The results were published in Ref. [1].

2. We derived the general form of the $\mathbf{k} \cdot \mathbf{p}$ Hamiltonian for monolayer TMDCs at the high symmetry $\pm K$, Γ, Q and M points in the BZ. To this end we determined the symmetry properties of several bands below and above the band gap of monolayer TMDCs. We then set up a seven-band model (fourteen-band, if spin is explicitly counted) for the $\pm K$ points, which takes into account the coupling between the VB and CB as well as couplings of these two bands to other, in energy more remote bands. We also determined the non-zero matrix elements of the intrinsic SOC in this seven-band model. Because of the lack of inversion symmetry, the intrinsic SOC leads to spin-orbit splitting of the bands at a general point in the BZ. We used these results to obtain an effective two-band model that describes the dispersion of the CB and the VB. We pointed out that off-diagonal SOC matrix elements of the original, seven band model can help to understand the details of the spin-orbit splitting of the CB in the low-energy model. Using a symmetry analysis of the bands and considering an external, out-of-plane electric field we derived the general form of the Bychkov-Rashba type SOC in monolayer TMDCs and the matrix elements that determine its strength. We showed that the Hamiltonian of the Bychkov-Rashba SOC contains two terms, one of which is not present in the corresponding Hamiltonian of III-V semiconductors.

   The results were published in Refs. [2, 3, 4].

3. We used the $\mathbf{k} \cdot \mathbf{p}$ Hamiltonian developed for the $\pm K$ valleys of monolayer TMDCs and the Luttinger prescription to calculate the Landau level spectrum. We found that the LLs in

the K and $-K$ valleys are not degenerate. This valley degeneracy breaking is linear in the magnetic field and can be characterized by an effective valley g-factor. We showed how to calculate the valley g-factors using the band structure parameters of the zero-magnetic field $\mathbf{k}\cdot\mathbf{p}$ Hamiltonian. We then used the LL spectrum to calculate the Shubnikov-de Haas oscillations of the longitudinal magnetoconductance σ_{xx}. We showed that the valley degeneracy breaking affects σ_{xx} in a similar way to the Zeeman spin-splitting in a two dimensional electron gas. We calculated the total σ_{xx} as the sum of the conductances coming from the occupied spin-orbit split bands. By comparison to experimental results we found that our results, which relied on single-particle considerations, present a useful starting point to interpret the SdH measurements in monolayer MoS_2. For temperatures 1K $\lesssim$ T $\lesssim$ 1.7K the main effect of the electron-electron interaction can be taken into account by a re-normalized value of the valley g-factor and the intrinsic SOC with respect to the values obtained in the single particle picture. At lower temperatures (T $< 1K$) the measurements gave clear indications that the single-particle picture is not sufficient and signatures of strong electron-electron interactions become apparent.

The results were published in Refs. [5] and [6].

4. We studied the properties of gate defined single and double quantum dots in monolayer TMDCs. Considering a circular QD in the non-interacting limit we calculated the spectrum of the QD as a function of out-of-plane magnetic field. We pointed out that the valley degeneracy breaking due to the magnetic field offers the possibility to use lowest energy Kramer's pair as spin-valley qubit. We also studied double quantum dots in the $(1,1)$ charge configuration. We assumed that each QD hosts a single energy level and that the Coulomb repulsion of electrons can be modeled by a Hubbard Hamiltonian. We investigated how the interplay of the valley degree of freedom, the strong SOC, the Coulomb interaction, the detuning of the QD levels and the interdot tunneling affect the low-energy spectrum of these DQDs. In the limit when the Coulomb interaction dominates the intrinsic SOC, we constructed an effective Hamiltonian that takes into account all states of the $(1,1)$ charge configuration and we determined the ground state in this model. In the opposite case, when the intrinsic SOC is large with respect to the Coulomb repulsion, we showed that the low-energy subspace is four-dimensional. In this subspace we defined spin-valley operators. We showed that in terms of these spin-valley operators the effective Hamiltonian is formally identical to the Heisenberg exchange Hamiltonian between two localized spins.

   The results were published in Refs. [4] and [7].

5. We studied the Berry curvature properties and the corresponding valley and spin Hall conductivities of bilayer TMDCs, in particular, of bilayer MoS_2. By developing a $\mathbf{k}\cdot\mathbf{p}$ model for the $\pm K$ valleys, we showed that there are intralayer as well as interlayer contributions to the Berry curvature. An important consequence of the interlayer contribution is that the Berry curvature is tunable by an out-of-plane electric field. This is a rare example where a topological property of a material can be changed by an external parameter. We pointed out that the stacking order also has important effects on the Berry curvature and therefore 3R and 2H stacked bilayers have very different Berry curvature properties. We studied the intrinsic contribution to the valley and spin Hall effect and calculated the corresponding conductivities σ_{xy}^{vH} and σ_{xy}^{sH} in n-doped bilayer MoS_2. Since they are closely related to the Berry curvature, they are tunable by external out-of-plane electric field. In particular, we found that in 2H bilayers σ_{xy}^{vH}, in leading order, a linear function of the interlayer potential difference, whereas σ_{xy}^{sH} is finite even in the absence of an out-of-plane electric field. We showed that there can be a sign change in σ_{xy}^{vH} and σ_{xy}^{sH} when the interlayer potential difference, which is due to an out-of-plane electric field, becomes larger than the intrinsic SOC in the CB. This is reminiscent of the physics in Chern insulators, where the sign change signals a

topological transition. However, we pointed out that in bilayer TMDCs these off-diagonal conductivities are not quantized and the material does not become a topological insulator.

The results were published in Ref. [8].

6. We developed a theoretical framework for the microscopic mechanisms of the induced SOC in graphene/TMDC heterostructures. We used a band-to-band tunneling picture between the two layers and a perturbation theory approach where the small parameter of the perturbation theory is the interlayer coupling. We found that two types of SOC, the valley Zeeman and Bychkov-Rashba SOC can be induced in graphene, while the intrinsic SOC of graphene cannot be enhanced by the TMDC layer. We showed that the magnitude of the induced valley Zeeman SOC depends on the diagonal elements of the intrinsic SOC matrix of the TMDC layer. On the other hand, the induced Bychkov-Rashba SOC can be explained by a three step virtual process, whereby a spin-independent tunneling between graphene and the TMDC bands is followed by a spin-flip tunneling between certain TMDCs bands and finally a spin-independent tunneling from the TMDC back to the graphene layer takes place. We also pointed out that the energy alignment of the electronic bands of the two layers affects the magnitude of the induced SOC constants λ_{vZ} and λ_R. We used our methodology to investigate the effects of the twist angle between the layers on the magnitude of the induced SOC. Our numerical calculations showed that the interlayer twist can significantly enhance the induced SOC, which we explained by features in the band structure of the TMDC layer.

   The results were published in Refs. [9] and [10].

7. We showed that for a general interlayer twist angle the induced Bychkov-Rashba type SOC in graphene/TMDC heterostructures is characterized not only by its amplitude λ_R, but also by a spin-rotation angle ϑ_R. The value of ϑ_R depends on the interlayer twist angle θ and it affects the spin polarization of the graphene bands. When $\vartheta_R + \theta$ is not an integer multiple of π, the spin polarization of the graphene states is not tangential to the Fermi surface as in a 2DEG, but it has a component which is perpendicular to the Fermi surface. We found that in TMDC/graphene/TMDC trilayers the quantum phase factor associated with ϑ_R can lead to interference effects between the contributions of the two TMDC layers. This interference affects the strength $\lambda_R^{(tls)}$ as well as the spin-rotation angle $\vartheta^{(tls)}$ of the induced Bychkov-Rashba SOC in such trilayer structures. According to our calculations the twist angle dependence of $\lambda_{vZ}^{(tls)}$ and $\lambda_R^{(tls)}$ can be detected using spin relaxation anisotropy measurements in TMDC/graphene/TMDC trilayers.

   The results were published in Ref. [10].

Publications referenced in the thesis statements

[1] Andor Kormányos and Guido Burkard. "Intrinsic and substrate induced spin-orbit interaction in chirally stacked trilayer graphene". *Phys. Rev. B* 87 (4 Jan. 2013), p. 045419.

[2] Andor Kormányos, Viktor Zólyomi, Neil D. Drummond, Péter Rakyta, Guido Burkard, and Vladimir I. Fal'ko. "Monolayer MoS_2: Trigonal warping, the Γ valley, and spin-orbit coupling effects". *Phys. Rev. B* 88 (4 July 2013), p. 045416.

[3] Andor Kormányos, Guido Burkard, Martin Gmitra, Jaroslav Fabian, Viktor Zólyomi, Neil D Drummond, and Vladimir Fal'ko. "$\mathbf{k} \cdot \mathbf{p}$ theory for two-dimensional transition metal dichalcogenide semiconductors". *2D Materials* 2.2 (2015), p. 022001.

[4] Andor Kormányos, Viktor Zólyomi, Neil D. Drummond, and Guido Burkard. "Spin-Orbit Coupling, Quantum Dots, and Qubits in Monolayer Transition Metal Dichalcogenides". *Phys. Rev. X* 4 (1 Mar. 2014), p. 011034.

[5] Andor Kormányos, Péter Rakyta, and Guido Burkard. "Landau levels and Shubnikov-de Haas oscillations in monolayer transition metal dichalcogenide semiconductors". *New Journal of Physics* 17.10 (2015), p. 103006.

[6] Riccardo Pisoni, Andor Kormányos, Matthew Brooks, Zijin Lei, Patrick Back, Marius Eich, Hiske Overweg, Yongjin Lee, Peter Rickhaus, Kenji Watanabe, Takashi Taniguchi, Atac Imamoglu, Guido Burkard, Thomas Ihn, and Klaus Ensslin. "Interactions and Magnetotransport through Spin-Valley Coupled Landau Levels in Monolayer MoS_2". *Phys. Rev. Lett.* 121 (24 Dec. 2018), p. 247701.

[7] Alessandro David, Guido Burkard, and Andor Kormányos. "Effective theory of monolayer TMDC double quantum dots". *2D Materials* 5.3 (June 2018), p. 035031.

[8] Andor Kormányos, Viktor Zólyomi, Vladimir I. Fal'ko, and Guido Burkard. "Tunable Berry curvature and valley and spin Hall effect in bilayer MoS_2". *Phys. Rev. B* 98 (3 July 2018), p. 035408.

[9] Alessandro David, Péter Rakyta, Andor Kormányos, and Guido Burkard. "Induced spin-orbit coupling in twisted graphene–transition metal dichalcogenide heterobilayers: Twistronics meets spintronics". *Phys. Rev. B* 100 (8 Aug. 2019), p. 085412.

[10] Csaba G. Péterfalvi, Alessandro David, Péter Rakyta, Guido Burkard, and Andor Kormányos. "Quantum interference tuning of spin-orbit coupling in twisted van der Waals trilayers". *Phys. Rev. Research* 4 (2 May 2022), p. L022049.

Chapter 10

Acknowledgements

First of all, I am gratefull for my family for their support during my carreer.

Most of the research projects presented in this thesis were completed during my postdoc time at University of Konstanz and I thank Prof. Guido Burkard for providing ideal circumstances for my work. I benefitted a lot from the collaboration with Viktor Zólyomi, Martin Gmitra, Neil D. Drummond, Vladimir Fa'lko and Klaus Ensslin, which lead to several important results discussed in this thesis. I worked closely with Alessandro David, my former PhD student at University of Konstanz, on two papers discussed in this thesis and the collaboration with Csaba G. Péterfalvi was very important concerning the last publication presented here. Last but not least I would like to thank my colleagues József Cserti, Péter Rakyta, András Csordás, János Koltai and Gábor Vattay at Eötvös Loránd University for their help and support.

During the writing of this thesis I was supported by the ÚNKP-21-5 New National Excellence Program of the Ministry for Innovation and Technology from the source of the National Research, Development and Innovation Fund. I also acknowledge support from the Hungarian Scientific Research Fund (OTKA) Grant No. K134437 the Hungarian Academy of Sciences through the Bólyai János Stipendium (BO/00603/20/11).

References

[1] K. S. Novoselov, A. K. Geim, S. V. Morozov, D. Jiang, Y. Zhang, S. V. Dubonos, I. V. Grigorieva, and A. A. Firsov. "Electric Field Effect in Atomically Thin Carbon Films". *Science* 306.5696 (2004), pp. 666–669.

[2] K. S. Novoselov, A. K. Geim, S. V. Morozov, D. Jiang, M. I. Katsnelson, I. V. Grigorieva, S. V. Dubonos, and A. A. Firsov. "Two-dimensional gas of massless Dirac fermions in graphene". *Nature* (Nov. 2005), pp. 197–200.

[3] A. H. Castro Neto, F. Guinea, N. M. R. Peres, K. S. Novoselov, and A. K. Geim. "The electronic properties of graphene". *Rev. Mod. Phys.* 81 (1 Jan. 2009), pp. 109–162.

[4] K. S. Novoselov, E. McCann, S. V. Morozov, V. I. Fal'ko, M. I. Katsnelson, U. Zeitler, D. Jiang, F. Schedin, and A. K. Geim. "Unconventional quantum Hall effect and Berry's phase of 2π in bilayer graphene". *Nature Physics* 2.3 (Mar. 2006), pp. 177–180.

[5] W. Bao, L. Jing, J. Velasco, Y. Lee, G. Liu, D. Tran, B. Standley, M. Aykol, S. B. Cronin, D. Smirnov, M. Koshino, E. McCann, M. Bockrath, and C. N. Lau. "Stacking-dependent band gap and quantum transport in trilayer graphene". *Nature Physics* 7.12 (Dec. 2011), pp. 948–952.

[6] Liyuan Zhang, Yan Zhang, Jorge Camacho, Maxim Khodas, and Igor Zaliznyak. "The experimental observation of quantum Hall effect of $l = 3$ chiral quasiparticles in trilayer graphene". *Nature Physics* 7.12 (Dec. 2011), pp. 953–957.

[7] Chun Hung Lui, Zhiqiang Li, Kin Fai Mak, Emmanuele Cappelluti, and Tony F. Heinz. "Observation of an electrically tunable band gap in trilayer graphene". *Nature Physics* 7.12 (Dec. 2011), pp. 944–947.

[8] Kin Fai Mak, Changgu Lee, James Hone, Jie Shan, and Tony F. Heinz. "Atomically Thin MoS_2: A New Direct-Gap Semiconductor". *Phys. Rev. Lett.* 105 (13 Sept. 2010), p. 136805.

[9] Andrea Splendiani, Liang Sun, Yuanbo Zhang, Tianshu Li, Jonghwan Kim, Chi-Yung Chim, Giulia Galli, and Feng Wang. "Emerging Photoluminescence in Monolayer MoS_2". *Nano Letters* 10.4 (2010), pp. 1271–1275.

[10] Qing Hua Wang, Kourosh Kalantar-Zadeh, Andras Kis, Jonathan N. Coleman, and Michael S. Strano. "Electronics and optoelectronics of two-dimensional transition metal dichalcogenides". *Nature Nanotechnology* 7 (11 Nov. 2012).

[11] Xiaodong Xu, Wang Yao, Di Xiao, and Tony F. Heinz. "Spin and pseudospins in layered transition metal dichalcogenides". *Nature Physics* 10 (5 May 2014).

[12] Xiaoxiang Xi, Zefang Wang, Weiwei Zhao, Ju-Hyun Park, Kam Tuen Law, Helmuth Berger, Lászó Forró, Jie Shan, and Kin Fai Mak. "Ising pairing in superconducting $NbSe_2$ atomic layers". *Nature Physics* 12 (Nov. 2015).

[13] Fengnian Xia, Han Wang, James C. M. Hwang, A. H. Castro Neto, and Li Yang. "Black phosphorus and its isoelectronic materials". *Nature Reviews Physics* 1 (May 2019), pp. 306–317.

[14] Denis A. Bandurin et al. “High electron mobility, quantum Hall effect and anomalous optical response in atomically thin InSe”. *Nature Nanotechnology* 12 (Nov. 2016).

[15] Li Song, Lijie Ci, Hao Lu, Pavel B. Sorokin, Chuanhong Jin, Jie Ni, Alexander G. Kvashnin, Dmitry G. Kvashnin, Jun Lou, Boris I. Yakobson, and Pulickel M. Ajayan. “Large Scale Growth and Characterization of Atomic Hexagonal Boron Nitride Layers”. *Nano Letters* 10.8 (2010), pp. 3209–3215.

[16] Bevin Huang, Genevieve Clark, Efrén Navarro-Moratalla, Dahlia R. Klein, Ran Cheng, Kyle L. Seyler, Ding Zhong, Emma Schmidgall, Michael A. McGuire, David H. Cobden, Wang Yao, Di Xiao, Pablo Jarillo-Herrero, and Xiaodong Xu. “Layer-dependent ferromagnetism in a van der Waals crystal down to the monolayer limit”. *Nature* 546 (June 2017).

[17] Yujun Deng, Yijun Yu, Yichen Song, Jingzhao Zhang, Nai Zhou Wang, Zeyuan Sun, Yangfan Yi, Yi Zheng Wu, Shiwei Wu, Junyi Zhu, Jing Wang, Xian Hui Chen, and Yuanbo Zhang. “Gate-tunable room-temperature ferromagnetism in two-dimensional Fe_3GeTe_2”. *Nature* 563 (Nov. 2018), pp. 94–99.

[18] Kangwon Kim, Soo Yeon Lim, Jae-Ung Lee, Sungmin Lee, Tae Yun Kim, Kisoo Park, Gun Sang Jeon, Cheol-Hwan Park, Je-Geun Park, and Hyeonsik Cheong. “Suppression of magnetic ordering in XXZ-type antiferromagnetic monolayer $NiPS_3$”. *Nature Communications* 10 (Jan. 2019).

[19] Xiaofeng Qian, Junwei Liu, Liang Fu, and Ju Li. “Quantum spin Hall effect in two-dimensional transition metal dichalcogenides”. *Science* 346.6215 (2014), pp. 1344–1347.

[20] Sanfeng Wu, Valla Fatemi, Quinn D. Gibson, Kenji Watanabe, Takashi Taniguchi, Robert J. Cava, and Pablo Jarillo-Herrero. “Observation of the quantum spin Hall effect up to 100 kelvin in a monolayer crystal”. *Science* 359.6371 (2018), pp. 76–79.

[21] Cui-Zu Chang et al. “Experimental Observation of the Quantum Anomalous Hall Effect in a Magnetic Topological Insulator”. *Science* 340.6129 (2013), pp. 167–170.

[22] Chang Liu, Yongchao Wang, Hao Li, Yang Wu, Yaoxin Li, Jiaheng Li, Ke He, Yong Xu, Jinsong Zhang, and Yayu Wang. “Robust axion insulator and Chern insulator phases in a two-dimensional antiferromagnetic topological insulator”. *Nature Materials* 19.5 (May 2020), pp. 522–527.

[23] Andrew J. Mannix, Zhuhua Zhang, Nathan P. Guisinger, Boris I. Yakobson, and Mark C. Hersam. “Borophene as a prototype for synthetic 2D materials development”. *Nature Nanotechnology* 13.6 (June 2018), pp. 444–450.

[24] Yi-Lun Hong, Zhibo Liu, Lei Wang, Tianya Zhou, Wei Ma, Chuan Xu, Shun Feng, Long Chen, Mao-Lin Chen, Dong-Ming Sun, Xing-Qiu Chen, Hui-Ming Cheng, and Wencai Ren. “Chemical vapor deposition of layered two-dimensional MoSi2N4 materials”. *Science* 369.6504 (2020), pp. 670–674.

[25] Kostya S Novoselov. “Discovery of 2D van der Waals layered MoSi2N4 family”. *National Science Review* 7.12 (Aug. 2020), pp. 1842–1844.

[26] A. K. Geim and I. V. Grigorieva. “van der Waals heterostructures”. *Nature* 499.7459 (July 2013), pp. 419–425.

[27] K. S. Novoselov, A. Mishchenko, A. Carvalho, and A. H. Castro Neto. “2D materials and van der Waals heterostructures”. *Science* 353.6298 (2016).

[28] Rebeca Ribeiro-Palau, Changjian Zhang, Kenji Watanabe, Takashi Taniguchi, James Hone, and Cory R. Dean. “Twistable electronics with dynamically rotatable heterostructures”. *Science* 361.6403 (2018), pp. 690–693.

[29] Yuan Cao, Valla Fatemi, Ahmet Demir, Shiang Fang, Spencer L. Tomarken, Jason Y. Luo, Javier D. Sanchez-Yamagishi, Kenji Watanabe, Takashi Taniguchi, Efthimios Kaxiras, Ray C. Ashoori, and Pablo Jarillo-Herrero. "Correlated insulator behaviour at half-filling in magic-angle graphene superlattices". *Nature* 556 (Mar. 2018), 80 EP.

[30] C. R. Dean, L. Wang, P. Maher, C. Forsythe, F. Ghahari, Y. Gao, J. Katoch, M. Ishigami, P. Moon, M. Koshino, T. Taniguchi, K. Watanabe, K. L. Shepard, J. Hone, and P. Kim. "Hofstadter's butterfly and the fractal quantum Hall effect in moiré superlattices". *Nature* 497.7451 (2013), pp. 598–602.

[31] L. A. Ponomarenko et al. "Cloning of Dirac fermions in graphene superlattices". *Nature* 497.7451 (2013), pp. 594–597.

[32] D. I. Indolese, R. Delagrange, P. Makk, J. R. Wallbank, K. Wanatabe, T. Taniguchi, and C. Schönenberger. "Signatures of van Hove Singularities Probed by the Supercurrent in a Graphene-hBN Superlattice". *Phys. Rev. Lett.* 121 (13 Sept. 2018), p. 137701.

[33] Yaping Yang, Jidong Li, Jun Yin, Shuigang Xu, Ciaran Mullan, Takashi Taniguchi, Kenji Watanabe, Andre K. Geim, Konstantin S. Novoselov, and Artem Mishchenko. "In situ manipulation of van der Waals heterostructures for twistronics". *Science Advances* 6.49 (2020).

[34] Rafi Bistritzer and Allan H. MacDonald. "Moiré bands in twisted double-layer graphene". *PNAS* 108.30 (July 2011), pp. 12233–12237.

[35] Fengcheng Wu, Timothy Lovorn, Emanuel Tutuc, and A. H. MacDonald. "Hubbard Model Physics in Transition Metal Dichalcogenide Moiré Bands". *Phys. Rev. Lett.* 121 (2 July 2018), p. 026402.

[36] Lei Wang et al. "Correlated electronic phases in twisted bilayer transition metal dichalcogenides". *Nature Materials* 19.8 (Aug. 2020), pp. 861–866.

[37] Aaron L. Sharpe, Eli J. Fox, Arthur W. Barnard, Joe Finney, Kenji Watanabe, Takashi Taniguchi, M. A. Kastner, and David Goldhaber-Gordon. "Emergent ferromagnetism near three-quarters filling in twisted bilayer graphene". *Science* 365.6453 (2019), pp. 605–608.

[38] M Serlin, C. L. Tschirhart, H. Polshyn, Y. Zhang, J. Zhu, K. Watanabe, T. Taniguchi, L. Balents, and A. F. Young. "Intrinsic quantized anomalous Hall effect in a moiré heterostructure". *Science* 367.6480 (2020), pp. 900–903.

[39] Emma C. Regan et al. "Mott and generalized Wigner crystal states in WSe2/WS2 moiré superlattices". *Nature* 579.7799 (Mar. 2020), pp. 359–363.

[40] Dante M. Kennes, Martin Claassen, Lede Xian, Antoine Georges, Andrew J. Millis, James Hone, Cory R. Dean, D. N. Basov, Abhay N. Pasupathy, and Angel Rubio. "Moiré heterostructures as a condensed-matter quantum simulator". *Nature Physics* 17.2 (Feb. 2021), pp. 155–163.

[41] Immanuel Bloch, Jean Dalibard, and Sylvain Nascimbène. "Quantum simulations with ultracold quantum gases". *Nature Physics* 8.4 (Apr. 2012), pp. 267–276.

[42] M. I. Katsnelson. "Zitterbewegung, chirality, and minimal conductivity in graphene". *The European Physical Journal B - Condensed Matter and Complex Systems* 51.2 (May 2006), pp. 157–160.

[43] József Cserti. "Minimal longitudinal dc conductivity of perfect bilayer graphene". *Phys. Rev. B* 75 (3 Jan. 2007), p. 033405.

[44] A. K. Geim and K. S. Novoselov. "The rise of graphene". *Nature Materials* 6.3 (Mar. 2007), pp. 183–191.

[45] M. I. Katsnelson, K. S. Novoselov, and A. K. Geim. "Chiral tunnelling and the Klein paradox in graphene". *Nature Physics* 2.9 (Sept. 2006), pp. 620–625.

[46] Vadim V. Cheianov and Vladimir I. Fal'ko. "Selective transmission of Dirac electrons and ballistic magnetoresistance of $n-p$ junctions in graphene". *Phys. Rev. B* 74 (4 July 2006), p. 041403.

[47] Andrea F. Young and Philip Kim. "Quantum interference and Klein tunnelling in graphene heterojunctions". *Nature Physics* 5.3 (Mar. 2009), pp. 222–226.

[48] József Cserti and Gyula Dávid. "Unified description of Zitterbewegung for spintronic, graphene, and superconducting systems". *Phys. Rev. B* 74 (17 Nov. 2006), p. 172305.

[49] V. P. Gusynin, S. G. Sharapov, and J. P. Carbotte. "Unusual Microwave Response of Dirac Quasiparticles in Graphene". *Phys. Rev. Lett.* 96 (25 June 2006), p. 256802.

[50] R. R. Nair, P. Blake, A. N. Grigorenko, K. S. Novoselov, T. J. Booth, T. Stauber, N. M. R. Peres, and A. K. Geim. "Fine Structure Constant Defines Visual Transparency of Graphene". *Science* 320.5881 (2008), pp. 1308–1308.

[51] Changgu Lee, Xiaoding Wei, Jeffrey W. Kysar, and James Hone. "Measurement of the Elastic Properties and Intrinsic Strength of Monolayer Graphene". *Science* 321.5887 (2008), pp. 385–388.

[52] Jannik C. Meyer, A. K. Geim, M. I. Katsnelson, K. S. Novoselov, T. J. Booth, and S. Roth. "The structure of suspended graphene sheets". *Nature* 446.7131 (Mar. 2007), pp. 60–63.

[53] Hidekatsu Suzuura and Tsuneya Ando. "Crossover from Symplectic to Orthogonal Class in a Two-Dimensional Honeycomb Lattice". *Phys. Rev. Lett.* 89 (26 Dec. 2002), p. 266603.

[54] Edward McCann and Vladimir I. Fal'ko. "Landau-Level Degeneracy and Quantum Hall Effect in a Graphite Bilayer". *Phys. Rev. Lett.* 96 (8 Mar. 2006), p. 086805.

[55] Yuanbo Zhang, Tsung-Ta Tang, Caglar Girit, Zhao Hao, Michael C. Martin, Alex Zettl, Michael F. Crommie, Y. Ron Shen, and Feng Wang. "Direct observation of a widely tunable bandgap in bilayer graphene". *Nature* 459.7248 (June 2009), pp. 820–823.

[56] B. M. Hunt, J. I. A. Li, A. A. Zibrov, L. Wang, T. Taniguchi, K. Watanabe, J. Hone, C. R. Dean, M. Zaletel, R. C. Ashoori, and A. F. Young. "Direct measurement of discrete valley and orbital quantum numbers in bilayer graphene". *Nature Communications* 8.1 (Oct. 2017), p. 948.

[57] L. C. Campos, A. F. Young, K. Surakitbovorn, K. Watanabe, T. Taniguchi, and P. Jarillo-Herrero. "Quantum and classical confinement of resonant states in a trilayer graphene Fabry-PÃ©rot interferometer". *Nature Communications* 3.1 (Dec. 2012), p. 1239.

[58] Mikito Koshino and Edward McCann. "Gate-induced interlayer asymmetry in ABA-stacked trilayer graphene". *Phys. Rev. B* 79 (12 Mar. 2009), p. 125443.

[59] Mikito Koshino and Edward McCann. "Trigonal warping and Berry's phase $N\pi$ in ABC-stacked multilayer graphene". *Phys. Rev. B* 80 (16 Oct. 2009), p. 165409.

[60] Fan Zhang, Bhagawan Sahu, Hongki Min, and A. H. MacDonald. "Band structure of *ABC*-stacked graphene trilayers". *Phys. Rev. B* 82 (3 July 2010), p. 035409.

[61] Maksym Serbyn and Dmitry A. Abanin. "New Dirac points and multiple Landau level crossings in biased trilayer graphene". *Phys. Rev. B* 87 (11 Mar. 2013), p. 115422.

[62] Sergej Konschuh. *Spin-orbit coupling effects: from graphene to graphite*. Dec. 2011.

[63] Roland Winkler. *Spin–Orbit Coupling Effects in Two-Dimensional Electron and Hole Systems*. Springer-Verlag Berlin Heidelberg, 2003.

[64] Edward McCann. "Asymmetry gap in the electronic band structure of bilayer graphene". *Phys. Rev. B* 74 (16 Oct. 2006), p. 161403.

[65] J.A. Wilson and A.D. Yoffe. "The transition metal dichalcogenides discussion and interpretation of the observed optical, electrical and structural properties". *Advances in Physics* 18.73 (1969), pp. 193–335.

[66] L. F. Mattheiss. "Band Structures of Transition-Metal-Dichalcogenide Layer Compounds". *Phys. Rev. B* 8 (8 Oct. 1973), pp. 3719–3740.

[67] B. Sipos, A. F. Kusmartseva, A. Akrap, H. Berger, L. Forró, and E. Tutiš. "From Mott state to superconductivity in 1T-TaS_2". *Nature Materials* 7.12 (Dec. 2008), pp. 960–965.

[68] A. H. Castro Neto. "Charge Density Wave, Superconductivity, and Anomalous Metallic Behavior in 2D Transition Metal Dichalcogenides". *Phys. Rev. Lett.* 86 (19 May 2001), pp. 4382–4385.

[69] Gui-Bin Liu, Di Xiao, Yugui Yao, Xiaodong Xu, and Wang Yao. "Electronic structures and theoretical modelling of two-dimensional group-VIB transition metal dichalcogenides". *Chem. Soc. Rev.* 44 (9 2015), pp. 2643–2663.

[70] Di Xiao, Gui-Bin Liu, Wanxiang Feng, Xiaodong Xu, and Wang Yao. "Coupled Spin and Valley Physics in Monolayers of MoS_2 and Other Group-VI Dichalcogenides". *Phys. Rev. Lett.* 108 (19 May 2012), p. 196802.

[71] Habib Rostami, Ali G. Moghaddam, and Reza Asgari. "Effective lattice Hamiltonian for monolayer MoS_2: Tailoring electronic structure with perpendicular electric and magnetic fields". *Phys. Rev. B* 88 (8 Aug. 2013), p. 085440.

[72] Gui-Bin Liu, Wen-Yu Shan, Yugui Yao, Wang Yao, and Di Xiao. "Three-band tight-binding model for monolayers of group-VIB transition metal dichalcogenides". *Phys. Rev. B* 88 (8 Aug. 2013), p. 085433.

[73] Shiang Fang, Rodrick Kuate Defo, Sharmila N. Shirodkar, Simon Lieu, Georgios A. Tritsaris, and Efthimios Kaxiras. "Ab initio tight-binding Hamiltonian for transition metal dichalcogenides". *Phys. Rev. B* 92.20 (Nov. 2015), p. 205108.

[74] Andor Kormányos, Guido Burkard, Martin Gmitra, Jaroslav Fabian, Viktor Zólyomi, Neil D Drummond, and Vladimir Fal'ko. "$\mathbf{k} \cdot \mathbf{p}$ theory for two-dimensional transition metal dichalcogenide semiconductors". *2D Materials* 2.2 (2015), p. 022001.

[75] Hualing Zeng, Junfeng Dai, Wang Yao, Di Xiao, and Xiaodong Cui. "Valley polarization in MoS_2 monolayers by optical pumping". *Nature Nanotechnology* 7 (8 Aug. 2012), p. 490.

[76] Kin Fai Mak, Keliang He, Jie Shan, and Tony F. Heinz. "Control of valley polarization in monolayer MoS_2 by optical helicity". *Nature Nanotechnology* 7 (8 Aug. 2012), p. 494.

[77] Ting Cao, Gang Wang, Wenpeng Han, Huiqi Ye, Chuanrui Zhu, Junren Shi, Qian Niu, Pingheng Tan, Enge Wang, Baoli Liu, and Ji Feng. "Valley-selective circular dichroism of monolayer molybdenum disulphide". *Nature Communications* 3 (June 2012), p. 887.

[78] B. Radisavljevic, A. Radenovic, J. Brivio, V. Giacometti, and A. Kis. "Single-layer MoS_2 transistors". *Nature Nanotechnology* 6.3 (Mar. 2011), pp. 147–150.

[79] Hui Fang, Steven Chuang, Ting Chia Chang, Kuniharu Takei, Toshitake Takahashi, and Ali Javey. "High-Performance Single Layered WSe2 p-FETs with Chemically Doped Contacts". *Nano Letters* 12.7 (2012). PMID: 22697053, pp. 3788–3792.

[80] Jiahao Kang, Wei Liu, and Kaustav Banerjee. "High-performance MoS2 transistors with low-resistance molybdenum contacts". *Applied Physics Letters* 104.9 (2014), p. 093106.

[81] Branimir Radisavljevic, Michael Brian Whitwick, and Andras Kis. "Integrated Circuits and Logic Operations Based on Single-Layer MoS2". *ACS Nano* 5.12 (2011). PMID: 22073905, pp. 9934–9938.

[82] Han Wang, Lili Yu, Yi-Hsien Lee, Yumeng Shi, Allen Hsu, Matthew L. Chin, Lain-Jong Li, Madan Dubey, Jing Kong, and Tomas Palacios. "Integrated Circuits Based on Bilayer MoS2 Transistors". *Nano Letters* 12.9 (2012). PMID: 22862813, pp. 4674–4680.

[83] L P Kouwenhoven, D G Austing, and S Tarucha. "Few-electron quantum dots". *Reports on Progress in Physics* 64.6 (May 2001), pp. 701–736.

[84] R. C. Ashoori. "Electrons in artificial atoms". *Nature* 379.6564 (Feb. 1996), pp. 413–419.

[85] R. Hanson, L. P. Kouwenhoven, J. R. Petta, S. Tarucha, and L. M. K. Vandersypen. "Spins in few-electron quantum dots". *Rev. Mod. Phys.* 79 (4 Oct. 2007), pp. 1217–1265.

[86] Guido Burkard, Thaddeus D. Ladd, John M. Nichol, Andrew Pan, and Jason R. Petta. *Semiconductor Spin Qubits*. 2021.

[87] M. D. Shulman, O. E. Dial, S. P. Harvey, H. Bluhm, V. Umansky, and A. Yacoby. "Demonstration of Entanglement of Electrostatically Coupled Singlet-Triplet Qubits". *Science* 336.6078 (2012), pp. 202–205.

[88] J. Medford, J. Beil, J. M. Taylor, S. D. Bartlett, A. C. Doherty, E. I. Rashba, D. P. DiVincenzo, H. Lu, A. C. Gossard, and C. M. Marcus. "Self-consistent measurement and state tomography of an exchange-only spin qubit". *Nature Nanotechnology* 8.9 (Sept. 2013), pp. 654–659.

[89] Dohun Kim, D. R. Ward, C. B. Simmons, John King Gamble, Robin Blume-Kohout, Erik Nielsen, D. E. Savage, M. G. Lagally, Mark Friesen, S. N. Coppersmith, and M. A. Eriksson. "Microwave-driven coherent operation of a semiconductor quantum dot charge qubit". *Nature Nanotechnology* 10.3 (Mar. 2015), pp. 243–247.

[90] D. M. Zajac, A. J. Sigillito, M. Russ, F. Borjans, J. M. Taylor, G. Burkard, and J. R. Petta. "Resonantly driven CNOT gate for electron spins". *Science* 359.6374 (2018), pp. 439–442.

[91] W. Huang, C. H. Yang, K. W. Chan, T. Tanttu, B. Hensen, R. C. C. Leon, M. A. Fogarty, J. C. C. Hwang, F. E. Hudson, K. M. Itoh, A. Morello, A. Laucht, and A. S. Dzurak. "Fidelity benchmarks for two-qubit gates in silicon". *Nature* 569.7757 (May 2019), pp. 532–536.

[92] Xiao Xue, Maximilian Russ, Nodar Samkharadze, Brennan Undseth, Amir Sammak, Giordano Scappucci, and Lieven M. K. Vandersypen. "Quantum logic with spin qubits crossing the surface code threshold". *Nature* 601.7893 (Jan. 2022), pp. 343–347.

[93] Nico W. Hendrickx, William I. L. Lawrie, Maximilian Russ, Floor van Riggelen, Sander L. de Snoo, Raymond N. Schouten, Amir Sammak, Giordano Scappucci, and Menno Veldhorst. "A four-qubit germanium quantum processor". *Nature* 591.7851 (Mar. 2021), pp. 580–585.

[94] A. Kurzmann, M. Eich, H. Overweg, M. Mangold, F. Herman, P. Rickhaus, R. Pisoni, Y. Lee, R. Garreis, C. Tong, K. Watanabe, T. Taniguchi, K. Ensslin, and T. Ihn. "Excited States in Bilayer Graphene Quantum Dots". *Phys. Rev. Lett.* 123 (2 July 2019), p. 026803.

[95] Marius Eich, Franti šek Herman, Riccardo Pisoni, Hiske Overweg, Annika Kurzmann, Yongjin Lee, Peter Rickhaus, Kenji Watanabe, Takashi Taniguchi, Manfred Sigrist, Thomas Ihn, and Klaus Ensslin. "Spin and Valley States in Gate-Defined Bilayer Graphene Quantum Dots". *Phys. Rev. X* 8 (3 July 2018), p. 031023.

[96] L. Banszerus, S. Möller, C. Steiner, E. Icking, S. Trellenkamp, F. Lentz, K. Watanabe, T. Taniguchi, C. Volk, and C. Stampfer. "Spin-valley coupling in single-electron bilayer graphene quantum dots". *Nature Communications* 12.1 (Sept. 2021), p. 5250.

[97] Fang-Ming Jing, Zhuo-Zhi Zhang, Guo-Quan Qin, Gang Luo, Gang Cao, Hai-Ou Li, Xiang-Xiang Song, and Guo-Ping Guo. "Gate-Controlled Quantum Dots Based on 2D Materials". *Advanced Quantum Technologies* n/a.n/a (2021), p. 2100162.

[98] Riccardo Pisoni, Zijin Lei, Patrick Back, Marius Eich, Hiske Overweg, Yongjin Lee, Kenji Watanabe, Takashi Taniguchi, Thomas Ihn, and Klaus Ensslin. "Gate-tunable quantum dot in a high quality single layer MoS_2 van der Waals heterostructure". *Applied Physics Letters* 112.12 (2018), p. 123101.

[99] S. Davari, J. Stacy, A.M. Mercado, J.D. Tull, R. Basnet, K. Pandey, K. Watanabe, T. Taniguchi, J. Hu, and H.O.H. Churchill. "Gate-Defined Accumulation-Mode Quantum Dots in Monolayer and Bilayer WSe_2". *Phys. Rev. Applied* 13 (5 May 2020), p. 054058.

[100] Justin Boddison-Chouinard, Alex Bogan, Norman Fong, Kenji Watanabe, Takashi Taniguchi, Sergei Studenikin, Andrew Sachrajda, Marek Korkusinski, Abdulmenaf Altintas, Maciej Bieniek, Pawel Hawrylak, Adina Luican-Mayer, and Louis Gaudreau. "Gate-controlled quantum dots in monolayer WSe_2". *Applied Physics Letters* 119.13 (2021), p. 133104.

[101] Xiang-Xiang Song, Di Liu, Vahid Mosallanejad, Jie You, Tian-Yi Han, Dian-Teng Chen, Hai-Ou Li, Gang Cao, Ming Xiao, Guang-Can Guo, and Guo-Ping Guo. "A gate defined quantum dot on the two-dimensional transition metal dichalcogenide semiconductor WSe_2". *Nanoscale* 7 (40 2015), pp. 16867–16873.

[102] Ke Wang, Kristiaan De Greve, Luis A. Jauregui, Andrey Sushko, Alexander High, You Zhou, Giovanni Scuri, Takashi Taniguchi, Kenji Watanabe, Mikhail D. Lukin, Hongkun Park, and Philip Kim. "Electrical control of charged carriers and excitons in atomically thin materials". *Nature Nanotechnology* 13.2 (2018), pp. 128–132.

[103] Chit Siong Lau et al. "Gate-Defined Quantum Confinement in CVD 2D WS2". *Advanced Materials* n/a.n/a (2021), p. 2103907.

[104] Zhuo-Zhi Zhang, Xiang-Xiang Song, Gang Luo, Guang-Wei Deng, Vahid Mosallanejad, Takashi Taniguchi, Kenji Watanabe, Hai-Ou Li, Gang Cao, Guang-Can Guo, Franco Nori, and Guo-Ping Guo. "Electrotunable artificial molecules based on van der Waals heterostructures". *Science Advances* 3.10 (2017), e1701699.

[105] J. M. Luttinger and W. Kohn. "Motion of Electrons and Holes in Perturbed Periodic Fields". *Phys. Rev.* 97 (4 Feb. 1955), pp. 869–883.

[106] Lok C Lew Yan Voon and Morten Willatzen. *The* $\mathbf{k}\cdot\mathbf{p}$ *Method*. Springer-Verlag Berlin Heidelberg, 2009.

[107] Gerald Bastard. *Wave Mechanics Applied to Semiconductor Heterostructures*. Wiley-Interscience, 1991.

[108] Ahmet El çi and Eric D. Jones. "Some consequences of the closure of the momentum Bloch functions". *Phys. Rev. B* 34 (12 Dec. 1986), pp. 8611–8615.

[109] M. S. Dresselhaus, G. Dresselhaus, and A. Jorio. *Group Theory (Application to the Physics of Condensed Matter)*. Springer-Verlag Berlin Heidelberg, 2008.

[110] Michael Tinkham. *Group Theory and Quantum Mechanics*. Dover Publications, inc, 1992.

[111] Jenő Sólyom. *Fundamentals of the Physics of Solids*. Springer, Berlin, Heidelberg, 2007.

[112] Michael Victor Berry. "Quantal phase factors accompanying adiabatic changes". *Proceedings of the Royal Society of London. A. Mathematical and Physical Sciences* 392.1802 (1984), pp. 45–57.

[113] D. J. Thouless, M. Kohmoto, M. P. Nightingale, and M. den Nijs. "Quantized Hall Conductance in a Two-Dimensional Periodic Potential". *Phys. Rev. Lett.* 49 (6 Aug. 1982), pp. 405–408.

[114] Shigeki Onoda, Naoyuki Sugimoto, and Naoto Nagaosa. "Intrinsic Versus Extrinsic Anomalous Hall Effect in Ferromagnets". *Phys. Rev. Lett.* 97 (12 Sept. 2006), p. 126602.

[115] R. D. King-Smith and David Vanderbilt. "Theory of polarization of crystalline solids". *Phys. Rev. B* 47 (3 Jan. 1993), pp. 1651–1654.

[116] Raffaele Resta. "Macroscopic polarization in crystalline dielectrics: the geometric phase approach". *Rev. Mod. Phys.* 66 (3 July 1994), pp. 899–915.

[117] Ganesh Sundaram and Qian Niu. "Wave-packet dynamics in slowly perturbed crystals: Gradient corrections and Berry-phase effects". *Phys. Rev. B* 59 (23 June 1999), pp. 14915–14925.

[118] Di Xiao, Ming-Che Chang, and Qian Niu. "Berry phase effects on electronic properties". *Rev. Mod. Phys.* 82 (3 July 2010), p. 1959.

[119] Zhong Fang, Naoto Nagaosa, Kei S. Takahashi, Atsushi Asamitsu, Roland Mathieu, Takeshi Ogasawara, Hiroyuki Yamada, Masashi Kawasaki, Yoshinori Tokura, and Kiyoyuki Terakura. "The Anomalous Hall Effect and Magnetic Monopoles in Momentum Space". *Science* 302.5642 (2003), pp. 92–95.

[120] Yugui Yao, Leonard Kleinman, A. H. MacDonald, Jairo Sinova, T. Jungwirth, Ding-sheng Wang, Enge Wang, and Qian Niu. "First Principles Calculation of Anomalous Hall Conductivity in Ferromagnetic bcc Fe". *Phys. Rev. Lett.* 92 (3 Jan. 2004), p. 037204.

[121] Wanxiang Feng, Yugui Yao, Wenguang Zhu, Jinjian Zhou, Wang Yao, and Di Xiao. "Intrinsic spin Hall effect in monolayers of group-VI dichalcogenides: A first-principles study". *Phys. Rev. B* 86 (16 Oct. 2012), p. 165108.

[122] Robert Karplus and J. M. Luttinger. "Hall Effect in Ferromagnetics". *Phys. Rev.* 95 (5 Sept. 1954), pp. 1154–1160.

[123] Frank Wilczek and A. Zee. "Appearance of Gauge Structure in Simple Dynamical Systems". *Phys. Rev. Lett.* 52 (24 June 1984), pp. 2111–2114.

[124] Naoto Nagaosa, Jairo Sinova, Shigeki Onoda, A. H. MacDonald, and N. P. Ong. "Anomalous Hall effect". *Rev. Mod. Phys.* 82 (2 May 2010), p. 1539.

[125] F. D. M. Haldane. "Berry Curvature on the Fermi Surface: Anomalous Hall Effect as a Topological Fermi-Liquid Property". *Phys. Rev. Lett.* 93 (20 Nov. 2004), p. 206602.

[126] B. Andrei Bernevig and Taylor S. Hughes. *Topological insulators and topological superconductors*. Princeton and Oxford: Princeton University Press, 2013.

[127] Wei Han, Roland K. Kawakami, Martin Gmitra, and Jaroslav Fabian. "Graphene spintronics". *Nature Nanotechnology* 9.10 (Oct. 2014), pp. 794–807.

[128] Igor Žuti ć, Jaroslav Fabian, and S. Das Sarma. "Spintronics: Fundamentals and applications". *Rev. Mod. Phys.* 76 (2 Apr. 2004), pp. 323–410.

[129] Jairo Sinova, Sergio O. Valenzuela, J. Wunderlich, C. H. Back, and T. Jungwirth. "Spin Hall effects". *Rev. Mod. Phys.* 87 (4 Oct. 2015), pp. 1213–1260.

[130] Juan F. Sierra, Jaroslav Fabian, Roland K. Kawakami, Stephan Roche, and Sergio O. Valenzuela. "Van der Waals heterostructures for spintronics and opto-spintronics". *Nature Nanotechnology* 16.8 (Aug. 2021), pp. 856–868.

[131] A. Avsar, H. Ochoa, F. Guinea, B. Özyilmaz, B. J. van Wees, and I. J. Vera-Marun. "Colloquium: Spintronics in graphene and other two-dimensional materials". *Rev. Mod. Phys.* 92 (2 June 2020), p. 021003.

[132] Marc Drögeler, Christopher Franzen, Frank Volmer, Tobias Pohlmann, Luca Banszerus, Maik Wolter, Kenji Watanabe, Takashi Taniguchi, Christoph Stampfer, and Bernd Beschoten. "Spin Lifetimes Exceeding 12 ns in Graphene Nonlocal Spin Valve Devices". *Nano Lett.* 16.6 (June 2016), pp. 3533–3539.

[133] Simranjeet Singh, Jyoti Katoch, Jinsong Xu, Cheng Tan, Tiancong Zhu, Walid Amamou, James Hone, and Roland Kawakami. "Nanosecond spin relaxation times in single layer graphene spin valves with hexagonal boron nitride tunnel barriers". *Appl. Phys. Lett.* 109.12 (Sept. 2016), p. 122411.

[134] J. Ingla-Aynés, M. H. D. Guimaães, R. J. Meijerink, P. J. Zomer, and B. J. van Wees. "24μm spin relaxation length in boron nitride encapsulated bilayer graphene". *Phys. Rev. B* 92.20 (Nov. 2015), 201410(R).

[135] H. Dery, P. Dalal, Ł Cywiński, and L. J. Sham. "Spin-based logic in semiconductors for reconfigurable large-scale circuits". *Nature* 447.7144 (May 2007), pp. 573–576.

[136] M. Venkata Kamalakar, Christiaan Groenveld, André Dankert, and Saroj P. Dash. "Long distance spin communication in chemical vapour deposited graphene". *Nature Communications* 6.1 (Apr. 2015), p. 6766.

[137] Hua Wen, Hanan Dery, Walid Amamou, Tiancong Zhu, Zhisheng Lin, Jing Shi, Igor Žutić, Ilya Krivorotov, L. J. Sham, and Roland K. Kawakami. "Experimental Demonstration of XOR Operation in Graphene Magnetologic Gates at Room Temperature". *Phys. Rev. Applied* 5 (4 Apr. 2016), p. 044003.

[138] M. Gmitra, S. Konschuh, C. Ertler, C. Ambrosch-Draxl, and J. Fabian. "Band-structure topologies of graphene: Spin-orbit coupling effects from first principles". *Phys. Rev. B* 80.23 (Dec. 2009), p. 235431.

[139] Zhe Wang, Dong-Keun Ki, Hua Chen, Helmuth Berger, Allan H. MacDonald, and Alberto F. Morpurgo. "Strong interface-induced spin-orbit interaction in graphene on WS_2". *Nat. Comm.* 6 (Sept. 2015), p. 8339.

[140] Zhe Wang, Dong-Keun Ki, Jun Yong Khoo, Diego Mauro, Helmuth Berger, Leonid S. Levitov, and Alberto F. Morpurgo. "Origin and Magnitude of 'Designer' Spin-Orbit Interaction in Graphene on Semiconducting Transition Metal Dichalcogenides". *Phys. Rev. X* 6.4 (Oct. 2016), p. 041020.

[141] Bowen Yang, Mark Lohmann, David Barroso, Ingrid Liao, Zhisheng Lin, Yawen Liu, Ludwig Bartels, Kenji Watanabe, Takashi Taniguchi, and Jing Shi. "Strong electron-hole symmetric Rashba spin-orbit coupling in graphene/monolayer transition metal dichalcogenide heterostructures". *Phys. Rev. B* 96.4 (July 2017), 041409(R).

[142] Simon Zihlmann, Aron W. Cummings, Jose H. Garcia, Máté Kedves, Kenji Watanabe, Takashi Taniguchi, Christian Schönenberger, and Péter Makk. "Large spin relaxation anisotropy and valley-Zeeman spin-orbit coupling in WSe_2/graphene/hBN heterostructures". *Phys. Rev. B* 97.7 (Feb. 2018), p. 075434.

[143] T. Wakamura, F. Reale, P. Palczynski, S. Guéron, C. Mattevi, and H. Bouchiat. "Strong Anisotropic Spin-Orbit Interaction Induced in Graphene by Monolayer WS_2". *Phys. Rev. Lett.* 120.10 (Mar. 2018), p. 106802.

[144] Martin Gmitra and Jaroslav Fabian. "Graphene on transition-metal dichalcogenides: A platform for proximity spin-orbit physics and optospintronics". *Phys. Rev. B* 92.15 (Oct. 2015), p. 155403.

[145] Martin Gmitra, Denis Kochan, Petra Högl, and Jaroslav Fabian. "Trivial and inverted Dirac bands and the emergence of quantum spin Hall states in graphene on transition-metal dichalcogenides". *Phys. Rev. B* 93.15 (Apr. 2016), p. 155104.

[146] Debora Pierucci, Hugo Henck, Jose Avila, Adrian Balan, Carl H. Naylor, Gilles Patriarche, Yannick J. Dappe, Mathieu G. Silly, Fausto Sirotti, A. T. Charlie Johnson, Maria C. Asensio, and Abdelkarim Ouerghi. "Band Alignment and Minigaps in Monolayer MoS_2 -Graphene van der Waals Heterostructures". *Nano Letters* 16.7 (July 2016), pp. 4054–4061.

[147] H. Nakamura et al. "Spin splitting and strain in epitaxial monolayer WSe_2 on graphene". *Phys. Rev. B* 101 (16 Apr. 2020), p. 165103.

[148] Jose H. Garcia, Marc Vila, Aron W. Cummings, and Stephan Roche. "Spin transport in graphene/transition metal dichalcogenide heterostructures". *Chem. Soc. Rev.* 47 (9 2018), pp. 3359–3379.

[149] Manuel Offidani, Mirco Milletari, Roberto Raimondi, and Aires Ferreira. "Optimal Charge-to-Spin Conversion in Graphene on Transition-Metal Dichalcogenides". *Phys. Rev. Lett.* 119 (19 Nov. 2017), p. 196801.

[150] Talieh S. Ghiasi, Alexey A. Kaverzin, Patrick J. Blah, and Bart J. van Wees. "Charge-to-Spin Conversion by the Rashba-Edelstein Effect in Two-Dimensional van der Waals Heterostructures up to Room Temperature". *Nano Letters* 19.9 (2019). PMID: 31408607, pp. 5959–5966.

[151] L. Antonio Benítez, Williams Savero Torres, Juan F. Sierra, Matias Timmermans, Jose H. Garcia, Stephan Roche, Marius V. Costache, and Sergio O. Valenzuela. "Tunable room-temperature spin galvanic and spin Hall effects in van der Waals heterostructures". *Nature Materials* 19.2 (Feb. 2020), pp. 170–175.

[152] M. I. D'yakonov and V. I. Perel'. "Spin relaxation of conduction electrons in noncentrosymmetric semiconductors". *Sov. Phys. Solid State* 13 (1972), p. 3023.

[153] D. Huertas-Hernando, F. Guinea, and Arne Brataas. "Spin-Orbit-Mediated Spin Relaxation in Graphene". *Phys. Rev. Lett.* 103 (14 Sept. 2009), p. 146801.

[154] Péter Boross, Balázs Dóra, Annamária Kiss, and Ferenc Simon. "A unified theory of spin-relaxation due to spin-orbit coupling in metals and semiconductors". *Scientific Reports* 3.1 (Nov. 2013), p. 3233.

[155] Aron W. Cummings, Jose H. Garcia, Jaroslav Fabian, and Stephan Roche. "Giant Spin Lifetime Anisotropy in Graphene Induced by Proximity Effects". *Phys. Rev. Lett.* 119 (20 Nov. 2017), p. 206601.

[156] Talieh S. Ghiasi, Joseph Ingla-Aynés, Alexey A. Kaverzin, and Bart J. van Wees. "Large Proximity-Induced Spin Lifetime Anisotropy in Transition-Metal Dichalcogenide/Graphene Heterostructures". *Nano Letters* 17.12 (Dec. 2017), pp. 7528–7532.

[157] L. Antonio Benítez, Juan F. Sierra, Williams Savero Torres, Aloïs Arrighi, Frédéric Bonell, Marius V. Costache, and Sergio O. Valenzuela. "Strongly anisotropic spin relaxation in graphene-transition metal dichalcogenide heterostructures at room temperature". *Nature Physics* 14.3 (2018), pp. 303–308.

[158] Edward McCann and Vladimir I. Fal'ko. "$z \rightarrow -z$ Symmetry of Spin-Orbit Coupling and Weak Localization in Graphene". *Phys. Rev. Lett.* 108 (16 Apr. 2012), p. 166606.

[159] T. Wakamura, F. Reale, P. Palczynski, M. Q. Zhao, A. T. C. Johnson, S. Guéron, C. Mattevi, A. Ouerghi, and H. Bouchiat. "Spin-orbit interaction induced in graphene by transition metal dichalcogenides". *Phys. Rev. B* 99 (24 June 2019), p. 245402.

[160] Dongying Wang, Shi Che, Guixin Cao, Rui Lyu, Kenji Watanabe, Takashi Taniguchi, Chun Ning Lau, and Marc Bockrath. "Quantum Hall Effect Measurement of SpinâOrbit Coupling Strengths in Ultraclean Bilayer Graphene/WSe_2 Heterostructures". *Nano Letters* 19.10 (2019). PMID: 31525877, pp. 7028–7034.

[161] Denis Kochan, Susanne Irmer, and Jaroslav Fabian. "Model spin-orbit coupling Hamiltonians for graphene systems". *Phys. Rev. B* 95 (16 Apr. 2017), p. 165415.

[162] C. L. Kane and E. J. Mele. "Quantum Spin Hall Effect in Graphene". *Phys. Rev. Lett.* 95 (22 Nov. 2005), p. 226801.

[163] Sergej Konschuh, Martin Gmitra, and Jaroslav Fabian. "Tight-binding theory of the spin-orbit coupling in graphene". *Phys. Rev. B* 82 (24 Dec. 2010), p. 245412.

[164] Yang Li and Mikito Koshino. "Twist-angle dependence of the proximity spin-orbit coupling in graphene on transition-metal dichalcogenides". *Phys. Rev. B* 99.7 (Feb. 2019), p. 075438.

[165] Alessandro David, Péter Rakyta, Andor Kormányos, and Guido Burkard. "Induced spin-orbit coupling in twisted graphene–transition metal dichalcogenide heterobilayers: Twistronics meets spintronics". *Phys. Rev. B* 100 (8 Aug. 2019), p. 085412.

[166] B. Hunt, J. D. Sanchez-Yamagishi, A. F. Young, M. Yankowitz, B. J. LeRoy, K. Watanabe, T. Taniguchi, P. Moon, M. Koshino, P. Jarillo-Herrero, and R. C. Ashoori. "Massive Dirac Fermions and Hofstadter Butterfly in a van der Waals Heterostructure". *Science* 340.6139 (2013), pp. 1427–1430.

[167] M.I. Dyakonov and V.I. Perel. "Current-induced spin orientation of electrons in semiconductors". *Physics Letters A* 35.6 (1971), pp. 459–460.

[168] Sasikanth Manipatruni, Dmitri E. Nikonov, Chia-Ching Lin, Tanay A. Gosavi, Huichu Liu, Bhagwati Prasad, Yen-Lin Huang, Everton Bonturim, Ramamoorthy Ramesh, and Ian A. Young. "Scalable energy-efficient magnetoelectric spin–orbit logic". *Nature* 565.7737 (Jan. 2019), pp. 35–42.

[169] Jairo Sinova, Dimitrie Culcer, Q. Niu, N. A. Sinitsyn, T. Jungwirth, and A. H. MacDonald. "Universal Intrinsic Spin Hall Effect". *Phys. Rev. Lett.* 92 (12 Mar. 2004), p. 126603.

[170] Jun-ichiro Inoue, Gerrit E. W. Bauer, and Laurens W. Molenkamp. "Suppression of the persistent spin Hall current by defect scattering". *Phys. Rev. B* 70 (4 July 2004), p. 041303.

[171] Ol'ga V. Dimitrova. "Spin-Hall conductivity in a two-dimensional Rashba electron gas". *Phys. Rev. B* 71 (24 June 2005), p. 245327.

[172] G. Dresselhaus. "Spin-Orbit Coupling Effects in Zinc Blende Structures". *Phys. Rev.* 100 (2 Oct. 1955), pp. 580–586.

[173] Shuichi Murakami, Naoto Nagaosa, and Shou-Cheng Zhang. "Dissipationless Quantum Spin Current at Room Temperature". *Science* 301.5638 (2003), pp. 1348–1351.

[174] A. Dyrdal, V. K. Dugaev, and J. Barnaś. "Spin Hall effect in a system of Dirac fermions in the honeycomb lattice with intrinsic and Rashba spin-orbit interaction". *Phys. Rev. B* 80 (15 Oct. 2009), p. 155444.

[175] Mirco Milletari, Manuel Offidani, Aires Ferreira, and Roberto Raimondi. "Covariant Conservation Laws and the Spin Hall Effect in Dirac-Rashba Systems". *Phys. Rev. Lett.* 119 (24 Dec. 2017), p. 246801.

[176] Jose H. Garcia, Aron W. Cummings, and Stephan Roche. "Spin Hall Effect and Weak Antilocalization in Graphene/Transition Metal Dichalcogenide Heterostructures". *Nano Letters* 17.8 (2017). PMID: 28715194, pp. 5078–5083.

[177] Jose H. Garcia, Marc Vila, Aron W. Cummings, and Stephan Roche. "Spin transport in graphene/transition metal dichalcogenide heterostructures". *Chem. Soc. Rev.* 47.9 (May 2018), pp. 3359–3379.

[178] J. Wunderlich, B. Kaestner, J. Sinova, and T. Jungwirth. "Experimental Observation of the Spin-Hall Effect in a Two-Dimensional Spin-Orbit Coupled Semiconductor System". *Phys. Rev. Lett.* 94 (4 Feb. 2005), p. 047204.

[179] Y. K. Kato, R. C. Myers, A. C. Gossard, and D. D. Awschalom. "Observation of the Spin Hall Effect in Semiconductors". *Science* 306.5703 (2004), pp. 1910–1913.

[180] S. O. Valenzuela and M. Tinkham. "Direct electronic measurement of the spin Hall effect". *Nature* 442.7099 (July 2006), pp. 176–179.

[181] J. Salfi, J. A. Mol, R. Rahman, G. Klimeck, M. Y. Simmons, L. C. L. Hollenberg, and S. Rogge. "Spatially resolving valley quantum interference of a donor in silicon". *Nature Materials* 13.6 (June 2014), pp. 605–610.

[182] Y. P. Shkolnikov, E. P. De Poortere, E. Tutuc, and M. Shayegan. "Valley Splitting of AlAs Two-Dimensional Electrons in a Perpendicular Magnetic Field". *Phys. Rev. Lett.* 89 (22 Nov. 2002), p. 226805.

[183] Jan Isberg, Markus Gabrysch, Johan Hammersberg, Saman Majdi, Kiran Kumar Kovi, and Daniel J. Twitchen. "Generation, transport and detection of valley-polarized electrons in diamond". *Nature Materials* 12.8 (Aug. 2013), pp. 760–764.

[184] Zengwei Zhu, Aurélie Collaudin, Benoît Fauqué, Woun Kang, and Kamran Behnia. "Field-induced polarization of Dirac valleys in bismuth". *Nature Physics* 8.1 (Jan. 2012), pp. 89–94.

[185] A. Rycerz, J. Tworzydlo, and C. W. J. Beenakker. "Valley filter and valley valve in graphene". *Nature Physics* 3.3 (Mar. 2007), pp. 172–175.

[186] Jing Li, Rui-Xing Zhang, Zhenxi Yin, Jianxiao Zhang, Kenji Watanabe, Takashi Taniguchi, Chaoxing Liu, and Jun Zhu. "A valley valve and electron beam splitter". *Science* 362.6419 (2018), pp. 1149–1152.

[187] Ivar Martin, Ya. M. Blanter, and A. F. Morpurgo. "Topological Confinement in Bilayer Graphene". *Phys. Rev. Lett.* 100 (3 Jan. 2008), p. 036804.

[188] Zhenhua Qiao, Jeil Jung, Qian Niu, and Allan H. MacDonald. "Electronic Highways in Bilayer Graphene". *Nano Letters* 11.8 (2011). PMID: 21766817, pp. 3453–3459.

[189] Wang Yao, Di Xiao, and Qian Niu. "Valley-dependent optoelectronics from inversion symmetry breaking". *Phys. Rev. B* 77 (23 June 2008), p. 235406.

[190] John R. Schaibley, Hongyi Yu, Genevieve Clark, Pasqual Rivera, Jason S. Ross, Kyle L. Seyler, Wang Yao, and Xiaodong Xu. "Valleytronics in 2D materials". *Nature Reviews Materials* 1 (Aug. 2016).

[191] Ziliang Ye, Dezheng Sun, and Tony F. Heinz. "Optical manipulation of valley pseudospin". *Nature Physics* 13.1 (Jan. 2017), pp. 26–29.

[192] Edbert J. Sie, James W. McIver, Yi-Hsien Lee, Liang Fu, Jing Kong, and Nuh Gedik. "Valley-selective optical Stark effect in monolayer WS2". *Nature Materials* 14.3 (Mar. 2015), pp. 290–294.

[193] Jonghwan Kim, Xiaoping Hong, Chenhao Jin, Su-Fei Shi, Chih-Yuan S. Chang, Ming-Hui Chiu, Lain-Jong Li, and Feng Wang. "Ultrafast generation of pseudo-magnetic field for valley excitons in WSe_2 monolayers". *Science* 346.6214 (2014), pp. 1205–1208.

[194] R. V. Gorbachev, J. C. W. Song, G. L. Yu, A. V. Kretinin, F. Withers, Y. Cao, A. Mishchenko, I. V. Grigorieva, K. S. Novoselov, L. S. Levitov, and A. K. Geim. "Detecting topological currents in graphene superlattices". *Science* 346.6208 (2014), pp. 448–451.

[195] Di Xiao, Wang Yao, and Qian Niu. "Valley-Contrasting Physics in Graphene: Magnetic Moment and Topological Transport". *Phys. Rev. Lett.* 99 (23 Dec. 2007), p. 236809.

[196] Jieun Lee, Kin Fai Mak, and Jie Shan. "Electrical control of the valley Hall effect in bilayer MoS_2 transistors". *Nature Nano* 11 (5 May 2016), p. 421.

[197] Y. Shimazaki, M. Yamamoto, I. V. Borzenets, K. Watanabe, T. Taniguchi, and S. Tarucha. "Generation and detection of pure valley current by electrically induced Berry curvature in bilayer graphene". *Nature Physics* 11 (12 Dec. 2015).

[198] D. A. Abanin, A. V. Shytov, L. S. Levitov, and B. I. Halperin. "Nonlocal charge transport mediated by spin diffusion in the spin Hall effect regime". *Phys. Rev. B* 79 (3 Jan. 2009), p. 035304.

[199] Mengqiao Sui, Guorui Chen, Liguo Ma, Wen-Yu Shan, Dai Tian, Kenji Watanabe, Takashi Taniguchi, Xiaofeng Jin, Wang Yao, Di Xiao, and Yuanbo Zhang. "Gate-tunable topological valley transport in bilayer graphene". *Nature Physics* 11 (12 Dec. 2015).

[200] J M Marmolejo-Tejada, J H García, M D Petrović, P-H Chang, X-L Sheng, A Cresti, P Plecháč, S Roche, and B K Nikolić. "Deciphering the origin of nonlocal resistance in multiterminal graphene on hexagonal-boron-nitride with ab initio quantum transport: Fermi surface edge currents rather than Fermi sea topological valley currents". *Journal of Physics: Materials* 1.1 (Sept. 2018), p. 015006.

[201] Thomas Aktor, Jose H. Garcia, Stephan Roche, Antti-Pekka Jauho, and Stephen R. Power. "Valley Hall effect and nonlocal resistance in locally gapped graphene". *Phys. Rev. B* 103 (11 Mar. 2021), p. 115406.

[202] A. Aharon-Steinberg, A. Marguerite, D. J. Perello, K. Bagani, T. Holder, Y. Myasoedov, L. S. Levitov, A. K. Geim, and E. Zeldov. "Long-range nontopological edge currents in charge-neutral graphene". *Nature* 593.7860 (May 2021), pp. 528–534.

[203] K. F. Mak, K. L. McGill, J. Park, and P. L. McEuen. "The valley Hall effect in MoS_2 transistors". *Science* 344.6191 (2014), p. 1489.

[204] Elyse Barré, Jean Anne C. Incorvia, Suk Hyun Kim, Connor J. McClellan, Eric Pop, H.-S. Philip Wong, and Tony F. Heinz. "Spatial Separation of Carrier Spin by the Valley Hall Effect in Monolayer WSe_2 Transistors". *Nano Letters* 19.2 (2019), pp. 770–774.

[205] M M Glazov. "Valley and spin accumulation in ballistic and hydrodynamic channels". *2D Materials* 9.1 (Dec. 2021), p. 015027.

[206] Cui-Zu Chang, Chao-Xing Liu, and Allan H. MacDonald. *Quantum anomalous Hall effect.* 2022.

[207] Samir Abdelouahed, A. Ernst, J. Henk, I. V. Maznichenko, and I. Mertig. "Spin-split electronic states in graphene: Effects due to lattice deformation, Rashba effect, and adatoms by first principles". *Phys. Rev. B* 82 (12 Sept. 2010), p. 125424.

[208] S. Konschuh, M. Gmitra, D. Kochan, and J. Fabian. "Theory of spin-orbit coupling in bilayer graphene". *Phys. Rev. B* 85 (11 Mar. 2012), p. 115423.

[209] J. C. Slater and G. F. Koster. "Simplified LCAO Method for the Periodic Potential Problem". *Phys. Rev.* 94 (6 June 1954), pp. 1498–1524.

[210] Andor Kormányos and Guido Burkard. "Intrinsic and substrate induced spin-orbit interaction in chirally stacked trilayer graphene". *Phys. Rev. B* 87 (4 Jan. 2013), p. 045419.

[211] F Guinea. "Spin–orbit coupling in a graphene bilayer and in graphite". *New Journal of Physics* 12.8 (Aug. 2010), p. 083063.

[212] J. Sichau, M. Prada, T. Anlauf, T. J. Lyon, B. Bosnjak, L. Tiemann, and R. H. Blick. "Resonance Microwave Measurements of an Intrinsic Spin-Orbit Coupling Gap in Graphene: A Possible Indication of a Topological State". *Phys. Rev. Lett.* 122 (4 Feb. 2019), p. 046403.

[213] Andor Kormányos, Viktor Zólyomi, Neil D. Drummond, Péter Rakyta, Guido Burkard, and Vladimir I. Fal'ko. "Monolayer MoS_2: Trigonal warping, the Γ valley, and spin-orbit coupling effects". *Phys. Rev. B* 88 (4 July 2013), p. 045416.

[214] Andor Kormányos, Viktor Zólyomi, Neil D. Drummond, and Guido Burkard. "Spin-Orbit Coupling, Quantum Dots, and Qubits in Monolayer Transition Metal Dichalcogenides". *Phys. Rev. X* 4 (1 Mar. 2014), p. 011034.

[215] Kai-Qiang Lin, Sebastian Bange, and John M. Lupton. "Quantum interference in second-harmonic generation from monolayer WSe_2". *Nature Physics* 15.3 (2019), pp. 242–246.

[216] Junsaku Nitta, Tatsushi Akazaki, Hideaki Takayanagi, and Takatomo Enoki. "Gate Control of Spin-Orbit Interaction in an Inverted $In_{0.53}Ga_{0.47}As/In_{0.52}Al_{0.48}As$ Heterostructure". *Phys. Rev. Lett.* 78 (7 Feb. 1997), pp. 1335–1338.

[217] J. B. Miller, D. M. Zumbühl, C. M. Marcus, Y. B. Lyanda-Geller, D. Goldhaber-Gordon, K. Campman, and A. C. Gossard. "Gate-Controlled Spin-Orbit Quantum Interference Effects in Lateral Transport". *Phys. Rev. Lett.* 90 (7 Feb. 2003), p. 076807.

[218] David MacNeill, Colin Heikes, Kin Fai Mak, Zachary Anderson, Andor Kormányos, Viktor Zólyomi, Jiwoong Park, and Daniel C. Ralph. "Breaking of Valley Degeneracy by Magnetic Field in Monolayer $MoSe_2$". *Phys. Rev. Lett.* 114 (3 Jan. 2015), p. 037401.

[219] G. Aivazian, Zhirui Gong, Aaron M. Jones, Rui-Lin Chu, J. Yan, D. G. Mandrus, Chuanwei Zhang, David Cobden, Wang Yao, and Xiaodong Xu. "Magnetic control of valley pseudospin in monolayer WSe_2". *Nature Physics* 11 (2 Feb. 2012), p. 148.

[220] Ajit Srivastava, Meinrad Sidler, Adrien V. Allain, Dominik S. Lembke, Andras Kis, and A. Imamoğlu. "Valley Zeeman effect in elementary optical excitations of monolayer WSe_2". *Nature Physics* 11 (2 Feb. 2012), p. 141.

[221] Yilei Li, Jonathan Ludwig, Tony Low, Alexey Chernikov, Xu Cui, Ghidewon Arefe, Young Duck Kim, Arend M. van der Zande, Albert Rigosi, Heather M. Hill, Suk Hyun Kim, James Hone, Zhiqiang Li, Dmitry Smirnov, and Tony F. Heinz. "Valley Splitting and Polarization by the Zeeman Effect in Monolayer $MoSe_2$". *Phys. Rev. Lett.* 113 (26 Dec. 2014), p. 266804.

[222] Nasser Alidoust, Guang Bian, Su-Yang Xu, Raman Sankar, Madhab Neupane, Chang Liu, Ilya Belopolski, Dong-Xia Qu, Jonathan D. Denlinger, Fang-Cheng Chou, and M. Zahid Hasan. "Observation of monolayer valence band spin-orbit effect and induced quantum well states in MoX2". *Nature Communications* 5.1 (Aug. 2014), p. 4673.

[223] J. M. Riley et al. "Direct observation of spin-polarized bulk bands in an inversion-symmetric semiconductor". *Nature Physics* 10.11 (Nov. 2014), pp. 835–839.

[224] Jill A. Miwa, Søren Ulstrup, Signe G. Sørensen, Maciej Dendzik, Antonija Grubić Čabo, Marco Bianchi, Jeppe Vang Lauritsen, and Philip Hofmann. "Electronic Structure of Epitaxial Single-Layer MoS_2". *Phys. Rev. Lett.* 114 (4 Jan. 2015), p. 046802.

[225] Y. J. Zhang, T. Oka, R. Suzuki, J. T. Ye, and Y. Iwasa. "Electrically Switchable Chiral Light-Emitting Transistor". *Science* 344.6185 (2014), pp. 725–728.

[226] Ermin Malic, Malte Selig, Maja Feierabend, Samuel Brem, Dominik Christiansen, Florian Wendler, Andreas Knorr, and Gunnar Berghäuser. "Dark excitons in transition metal dichalcogenides". *Phys. Rev. Materials* 2 (1 Jan. 2018), p. 014002.

[227] Piotr Kapuściński, Alex Delhomme, Diana Vaclavkova, Artur O. Slobodeniuk, Magdalena Grzeszczyk, Miroslav Bartos, Kenji Watanabe, Takashi Taniguchi, Clément Faugeras, and Marek Potemski. "Rydberg series of dark excitons and the conduction band spin-orbit splitting in monolayer WSe2". *Communications Physics* 4.1 (Aug. 2021), p. 186.

[228] Satoshi Kusaba, Kenji Watanabe, Takashi Taniguchi, Kazuhiro Yanagi, and Koichiro Tanaka. "Role of dark exciton states in the relaxation dynamics of bright 1s excitons in monolayer WSe2". *Applied Physics Letters* 119.9 (2021), p. 093101.

[229] Y. A. Bychkov and E. I. Rasbha. "Properties of a 2D electron gas with lifted spectral degeneracy". *JETP Lett.* 39 (2 1984), p. 78.

[230] Y. A. Bychkov and E. I. Rashba. "Oscillatory effects and the magnetic susceptibility of carriers in inversion layers". *Journal of Physics C: Solid State Physics* 17.33 (1984), p. 6039.

[231] Takaaki Koga, Junsaku Nitta, Tatsushi Akazaki, and Hideaki Takayanagi. "Rashba Spin-Orbit Coupling Probed by the Weak Antilocalization Analysis in InAlAs/InGaAs/InAlAs Quantum Wells as a Function of Quantum Well Asymmetry". *Phys. Rev. Lett.* 89 (4 July 2002), p. 046801.

[232] A. M. Gilbertson, M. Fearn, J. H. Jefferson, B. N. Murdin, P. D. Buckle, and L. F. Cohen. "Zero-field spin splitting and spin lifetime in n-InSb-$In_{1-x}Al_xSb$ asymmetric quantum well heterostructures". *Phys. Rev. B* 77 (16 Apr. 2008), p. 165335.

[233] Jing Zhang, Shuai Jia, Iskandar Kholmanov, Liang Dong, Dequan Er, Weibing Chen, Hua Guo, Zehua Jin, Vivek B. Shenoy, Li Shi, and Jun Lou. "Janus Monolayer Transition-Metal Dichalcogenides". *ACS Nano* 11.8 (Aug. 2017), pp. 8192–8198.

[234] Yang Song and Hanan Dery. "Transport Theory of Monolayer Transition-Metal Dichalcogenides through Symmetry". *Phys. Rev. Lett.* 111 (2 July 2013), p. 026601.

[235] Kristen Kaasbjerg, Kristian S. Thygesen, and Karsten W. Jacobsen. "Phonon-limited mobility in n-type single-layer MoS_2 from first principles". *Phys. Rev. B* 85 (11 Mar. 2012), p. 115317.

[236] Samuel Brem, Malte Selig, Gunnar Berghaeuser, and Ermin Malic. "Exciton Relaxation Cascade in two-dimensional Transition Metal Dichalcogenides". *Scientific Reports* 8.1 (May 2018), p. 8238.

[237] G. Bir and G. Pikus. *Symmetry and Strain-Induced Effects in Semiconductors*. Wiley, New York, 1974.

[238] F Geissler, J C Budich, and B Trauzettel. "Group theoretical and topological analysis of the quantum spin Hall effect in silicene". *New Journal of Physics* 15.8 (Aug. 2013), p. 085030.

[239] Csaba G. Péterfalvi, Andor Kormányos, and Guido Burkard. "Boundary conditions for transition-metal dichalcogenide monolayers in the continuum model". *Phys. Rev. B* 92 (24 Dec. 2015), p. 245443.

[240] Xu Cui et al. "Multi-terminal transport measurements of MoS_2 using a van der Waals heterostructure device platform". *Nature Nanotechnology* 10 (6 June 2015), p. 534.

[241] Riccardo Pisoni, Andor Kormányos, Matthew Brooks, Zijin Lei, Patrick Back, Marius Eich, Hiske Overweg, Yongjin Lee, Peter Rickhaus, Kenji Watanabe, Takashi Taniguchi, Atac Imamoglu, Guido Burkard, Thomas Ihn, and Klaus Ensslin. "Interactions and Magnetotransport through Spin-Valley Coupled Landau Levels in Monolayer MoS_2". *Phys. Rev. Lett.* 121 (24 Dec. 2018), p. 247701.

[242] Babak Fallahazad, Hema C. P. Movva, Kyounghwan Kim, Stefano Larentis, Takashi Taniguchi, Kenji Watanabe, Sanjay K. Banerjee, and Emanuel Tutuc. "Shubnikovde Haas Oscillations of High-Mobility Holes in Monolayer and Bilayer WSe_2: Landau Level Degeneracy, Effective Mass, and Negative Compressibility". *Phys. Rev. Lett.* 116 (8 Feb. 2016), p. 086601.

[243] G. Wang, L. Bouet, M. M. Glazov, T. Amand, E. L. Ivchenko, Palleau E., X. Marie, and B. Urbaszek. "Magneto-optics in transition metal diselenide monolayers". *2D Materials* 2.3 (2015), p. 034002.

[244] Andor Kormányos, Péter Rakyta, and Guido Burkard. "Landau levels and Shubnikov-de Haas oscillations in monolayer transition metal dichalcogenide semiconductors". *New Journal of Physics* 17.10 (2015), p. 103006.

[245] Tsuneya Ando. "Theory of Quantum Transport in a Two-Dimensional Electron System under Magnetic Fields. IV. Oscillatory Conductivity". *Journal of the Physical Society of Japan* 37.5 (1974), pp. 1233–1237.

[246] H. Schmidt, I. Yudhistira, L. Chu, A. H. Castro Neto, B. Özyilmaz, S. Adam, and G. Eda. "Quantum Transport and Observation of Dyakonov-Perel Spin-Orbit Scattering in Monolayer MoS_2". *Phys. Rev. Lett.* 116 (4 Jan. 2016), p. 046803.

[247] Kristen Kaasbjerg, Tony Low, and Antti-Pekka Jauho. "Electron and hole transport in disordered monolayer MoS_2: atomic vacancy-induced short-range and Coulomb disorder scattering". *arXiv:1612.00469* (2016).

[248] Fedir T. Vasko and Oleg E. Raichev. *Quantum Kinetic Theory and Applications*. New York: Springer, 2005.

[249] Henrik Bruus and Karsten Flensberg. *Many-Body Quantum Theory in Condensed Matter Physics*. Oxford University Press, 2004.

[250] Martin V. Gustafsson, Matthew Yankowitz, Carlos Forsythe, Daniel Rhodes, Kenji Watanabe, Takashi Taniguchi, James Hone, Xiaoyang Zhu, and Cory R. Dean. "Ambipolar Landau levels and strong band-selective carrier interactions in monolayer WSe_2". *Nature Materials* 17.5 (May 2018), pp. 411–415.

[251] Stefano Larentis, Hema C. P. Movva, Babak Fallahazad, Kyounghwan Kim, Armand Behroozi, Takashi Taniguchi, Kenji Watanabe, Sanjay K. Banerjee, and Emanuel Tutuc. "Large effective mass and interaction-enhanced Zeeman splitting of K-valley electrons in $MoSe_2$". *Physical Review B* 97.20 (May 2018), p. 201407.

[252] Jiangxiazi Lin, Tianyi Han, Benjamin A. Piot, Zefei Wu, Shuigang Xu, Gen Long, Liheng An, Patrick Cheung, Peng-Peng Zheng, Paulina Plochocka, Xi Dai, Duncan K. Maude, Fan Zhang, and Ning Wang. "Determining Interaction Enhanced Valley Susceptibility in Spin-Valley-Locked MoS_2". *Nano Letters* 19.3 (2019), pp. 1736–1742.

[253] Ying Zhang and S. Das Sarma. "Density-dependent spin susceptibility and effective mass in interacting quasi-two-dimensional electron systems". *Physical Review B* 72.7 (Aug. 2005), p. 075308.

[254] Hema C. P. Movva, Babak Fallahazad, Kyounghwan Kim, Stefano Larentis, Takashi Taniguchi, Kenji Watanabe, Sanjay K. Banerjee, and Emanuel Tutuc. "Density-Dependent Quantum Hall States and Zeeman Splitting in Monolayer and Bilayer WSe_2". *Physical Review Letters* 118.24 (June 2017), p. 247701.

[255] A. Isihara and L. Smřcka. "Density and magnetic field dependences of the conductivity of two-dimensional electron systems". en. *Journal of Physics C: Solid State Physics* 19.34 (1986), p. 6777.

[256] J. R. Petta, A. C. Johnson, J. M. Taylor, E. A. Laird, A. Yacoby, M. D. Lukin, C. M. Marcus, M. P. Hanson, and A. C. Gossard. "Coherent Manipulation of Coupled Electron Spins in Semiconductor Quantum Dots". *Science* 309.5744 (2005), pp. 2180–2184.

[257] Floris A. Zwanenburg, Andrew S. Dzurak, Andrea Morello, Michelle Y. Simmons, Lloyd C. L. Hollenberg, Gerhard Klimeck, Sven Rogge, Susan N. Coppersmith, and Mark A. Eriksson. "Silicon quantum electronics". *Rev. Mod. Phys.* 85 (3 July 2013), pp. 961–1019.

[258] D. M. Zajac, A. J. Sigillito, M. Russ, F. Borjans, J. M. Taylor, G. Burkard, and J. R. Petta. "Resonantly driven CNOT gate for electron spins". *Science* 359.6374 (2018), pp. 439–442.

[259] M. R. Buitelaar, A. Bachtold, T. Nussbaumer, M. Iqbal, and C. Schönenberger. "Multiwall Carbon Nanotubes as Quantum Dots". *Phys. Rev. Lett.* 88 (15 Mar. 2002), p. 156801.

[260] F. Kuemmeth, S. Ilani, D. C. Ralph, and P. L. McEuen. "Coupling of spin and orbital motion of electrons in carbon nanotubes". *Nature* 452.7186 (2008), pp. 448–452.

[261] Milton Abramowitz and Irene A. Stegun. *Handbook of Mathematical Functions*. New York: National Institute of Standards, 1970.

[262] S. Schnez, K. Ensslin, M. Sigrist, and T. Ihn. "Analytic model of the energy spectrum of a graphene quantum dot in a perpendicular magnetic field". *Phys. Rev. B* 78 (19 Nov. 2008), p. 195427.

[263] Patrik Recher, Johan Nilsson, Guido Burkard, and Björn Trauzettel. "Bound states and magnetic field induced valley splitting in gate-tunable graphene quantum dots". *Phys. Rev. B* 79 (8 Feb. 2009), p. 085407.

[264] Patrik Recher and Björn Trauzettel. "Quantum dots and spin qubits in graphene". *Nanotechnology* 21.30 (2010), p. 302001.

[265] S. Nadj-Perge, S. M. Frolov, E. P. A. M. Bakkers, and L. P. Kouwenhoven. "Spin-orbit qubit in a semiconductor nanowire". *Nature* 468 (7327 Dec. 2010).

[266] Karsten Flensberg and Charles M. Marcus. "Bends in nanotubes allow electric spin control and coupling". *Phys. Rev. B* 81 (19 May 2010), p. 195418.

[267] S. Weiss, E. I. Rashba, F. Kuemmeth, H. O. H. Churchill, and K. Flensberg. "Spin-orbit effects in carbon-nanotube double quantum dots". *Phys. Rev. B* 82 (16 Oct. 2010), p. 165427.

[268] András Pályi and Guido Burkard. "Spin-valley blockade in carbon nanotube double quantum dots". *Phys. Rev. B* 82 (15 Oct. 2010), p. 155424.

[269] Alessandro David, Guido Burkard, and Andor Kormányos. "Effective theory of monolayer TMDC double quantum dots". *2D Materials* 5.3 (June 2018), p. 035031.

[270] Niklas Rohling and Guido Burkard. "Universal quantum computing with spin and valley states". *New Journal of Physics* 14.8 (Aug. 2012), p. 083008.

[271] Daniel Loss and David P. DiVincenzo. "Quantum computation with quantum dots". *Phys. Rev. A* 57 (1 Jan. 1998), pp. 120–126.

[272] G Széchenyi, L Chirolli, and A Pályi. "Impurity-assisted electric control of spin-valley qubits in monolayer MoS2". *2D Materials* 5.3 (Apr. 2018), p. 035004.

[273] J. Pawlowski, D. Zebrowski, and S. Bednarek. "Valley qubit in a gated MoS_2 monolayer quantum dot". *Phys. Rev. B* 97 (15 Apr. 2018), p. 155412.

[274] Sanfeng Wu, Jason S. Ross, Gui-Bin Liu, Grant Aivazian, Aaron Jones, Zaiyao Fei, Wenguang Zhu, Di Xiao, Wang Yao, David Cobden, and Xiaodong Xu. "Electrical tuning of valley magnetic moment through symmetry control in bilayer MoS_2". *Nature Physics* 9 (3 Mar. 2013).

[275] Aaron M. Jones, Hongyi Yu, Jason S. Ross, Philip Klement, Nirmal J. Ghimire, Jiaqiang Yan, David G. Mandrus, Wang Yao, and Xiaodong Xu. "Spin-layer locking effects in optical orientation of exciton spin in bilayer WSe_2". *Nature Physics* 10 (2 Feb. 2014).

[276] Andor Kormányos, Viktor Zólyomi, Vladimir I. Fal'ko, and Guido Burkard. "Tunable Berry curvature and valley and spin Hall effect in bilayer MoS_2". *Phys. Rev. B* 98 (3 July 2018), p. 035408.

[277] Suzuki R., Sakano M., Zhang Y. J., Akashi R., Morikawa D., Harasawa A., Yaji K., Kuroda K., Miyamoto K., Okuda T., Ishizaka K., Arita R., and Iwasa Y. "Valley-dependent spin polarization in bulk MoS_2 with broken inversion symmetry". *Nature Nanotechnology* 9 (8 Aug. 2014).

[278] Zhirui Gong, Gui-Bin Liu, Hongyi Yu, Di Xiao, Xiaodong Cui, Xiaodong Xu, and Wang Yao. "Magnetoelectric effects and valley-controlled spin quantum gates in transition metal dichalcogenide bilayers". *Nature Communications* 4 (June 2013).

[279] Takahiro Fukui, Yasuhiro Hatsugai, and Hiroshi Suzuki. "Chern Numbers in Discretized Brillouin Zone: Efficient Method of Computing (Spin) Hall Conductances". *Journal of the Physical Society of Japan* 74.6 (2005), p. 1674.

[280] D. Sercombe, S. Schwarz, O. Del Pozo-Zamudio, F. Liu, B. J. Robinson, E. A. Chekhovich, I. I. Tartakovskii, O. Kolosov, and A. I. Tartakovskii. "Optical investigation of the natural electron doping in thin MoS_2 films deposited on dielectric substrates". *Scientific Reports* 3 (Dec. 2013).

[281] János Asbóth, László Oroszlány, and András Pályi. *A Short Course on Topological Insulators*. Lecture Notes in Physics. Springer, 2017.

[282] Zhigang Song, Ruge Quhe, Shunquan Liu, Yan Li, Ji Feng, Yingchang Yang, Jing Lu, and Jinbo Yang. "Tunable Valley Polarization and Valley Orbital Magnetic Moment Hall Effect in Honeycomb Systems with Broken Inversion Symmetry". *Scientific Reports* 5.1 (Sept. 2015), p. 13906.

[283] Csaba G. Péterfalvi, Alessandro David, Péter Rakyta, Guido Burkard, and Andor Kormányos. "Quantum interference tuning of spin-orbit coupling in twisted van der Waals trilayers". *Phys. Rev. Research* 4 (2 May 2022), p. L022049.

[284] Mikito Koshino. "Interlayer interaction in general incommensurate atomic layers". *New J. Phys.* 17.1 (2015), p. 015014.

[285] J. C. Slater and G. F. Koster. "Simplified LCAO Method for the Periodic Potential Problem". *Phys. Rev.* 94.6 (June 1954), pp. 1498–1524.

[286] Hongki Min, J. E. Hill, N. A. Sinitsyn, B. R. Sahu, Leonard Kleinman, and A. H. MacDonald. "Intrinsic and Rashba spin-orbit interactions in graphene sheets". *Phys. Rev. B* 74.16 (Oct. 2006), p. 165310.

[287] Klaus Zollner, Aron W. Cummings, Stephan Roche, and Jaroslav Fabian. "Graphene on two-dimensional hexagonal BN, AlN, and GaN: Electronic, spin-orbit, and spin relaxation properties". *Phys. Rev. B* 103 (7 Feb. 2021), p. 075129.

[288] Xuhui Yang, Baisheng Sa, Peng Lin, Chao Xu, Qiang Zhu, Hongbing Zhan, and Zhimei Sun. "Tunable Contacts in Graphene/InSe van der Waals Heterostructures". *The Journal of Physical Chemistry C* 124.43 (2020), pp. 23699–23706.

[289] Klaus Zollner, Marko D. Petrovi ć, Kapildeb Dolui, Petr Plechá č, Branislav K. Nikoli ć, and Jaroslav Fabian. "Scattering-induced and highly tunable by gate damping-like spin-orbit torque in graphene doubly proximitized by two-dimensional magnet $Cr_2Ge_2Te_6$ and monolayer WS_2". *Phys. Rev. Research* 2 (4 Oct. 2020), p. 043057.

[290] Klaus Zollner and Jaroslav Fabian. "Single and bilayer graphene on the topological insulator Bi_2Se_3: Electronic and spin-orbit properties from first principles". *Phys. Rev. B* 100 (16 Oct. 2019), p. 165141.

[291] Konrád Kandrai, Péter Vancsó, Gergő Kukucska, János Koltai, György Baranka, Ákos Hoffmann, Áron Pekker, Katalin Kamarás, Zsolt E. Horváth, Anna Vymazalová, Levente Tapasztó, and Péter Nemes-Incze. "Signature of Large-Gap Quantum Spin Hall State in the Layered Mineral Jacutingaite". *Nano Letters* 20.7 (2020). PMID: 32551708, pp. 5207–5213.

[292] Lorenzo Camosi, Josef Světlík, Marius V Costache, Williams Savero Torres, Iván Fernández Aguirre, Vera Marinova, Dimitre Dimitrov, Marin Gospodinov, Juan F Sierra, and Sergio O Valenzuela. "Resolving spin currents and spin densities generated by charge-spin interconversion in systems with reduced crystal symmetry". *2D Materials* 9.3 (June 2022), p. 035014.

[293] Josep Ingla-Aynés, Inge Groen, Franz Herling, Nerea Ontoso, C K Safeer, Fernando de Juan, Luis E Hueso, Marco Gobbi, and Fèlix Casanova. "Omnidirectional spin-to-charge conversion in graphene/$NbSe_2$ van der Waals heterostructures". *2D Materials* 9.4 (June 2022), p. 045001.

[294] Lorenz Meier, Gian Salis, Ivan Shorubalko, Emilio Gini, Silke Schön, and Klaus Ensslin. "Measurement of Rashba and Dresselhaus spin–orbit magnetic fields". *Nature Physics* 3.9 (Sept. 2007), pp. 650–654.

[295] Bálint Fülöp, Albin Márffy, Simon Zihlmann, Martin Gmitra, Endre Tóvári, Bálint Szentpéteri, Máté Kedves, Kenji Watanabe, Takashi Taniguchi, Jaroslav Fabian, Christian Schönenberger, Péter Makk, and Szabolcs Csonka. "Boosting proximity spin–orbit coupling in graphene/WSe2 heterostructures via hydrostatic pressure". *npj 2D Materials and Applications* 5.1 (Sept. 2021), p. 82.